Design Principles for Six Degrees-of-Freedom MEMS-based Precision Manipulators

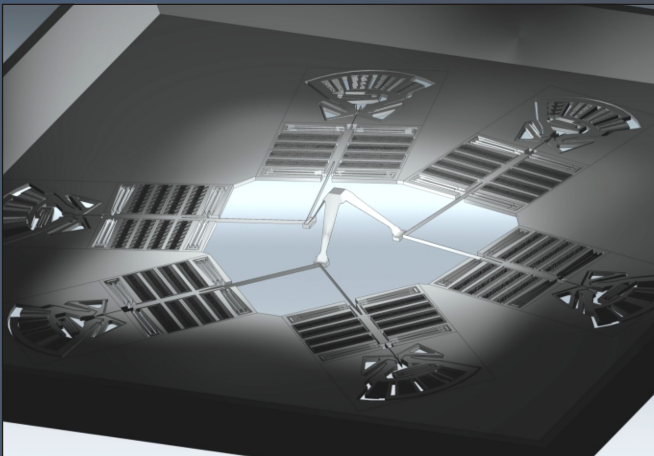
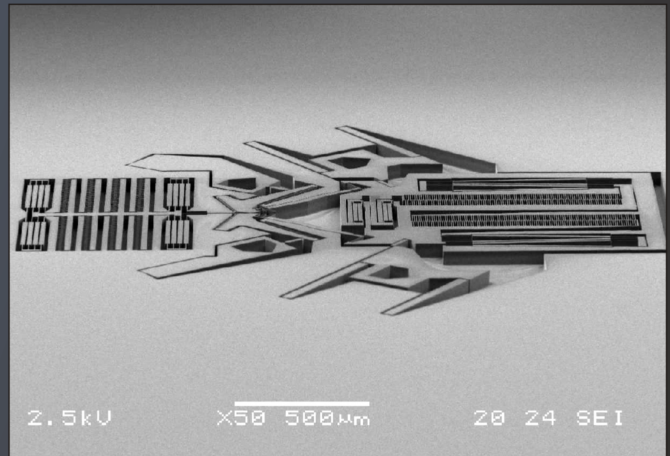

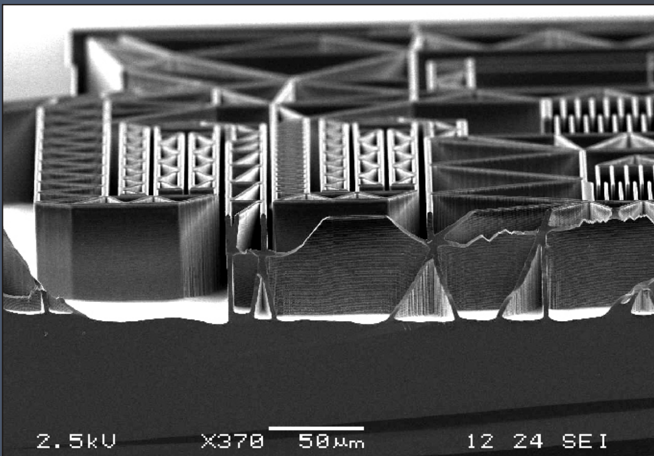

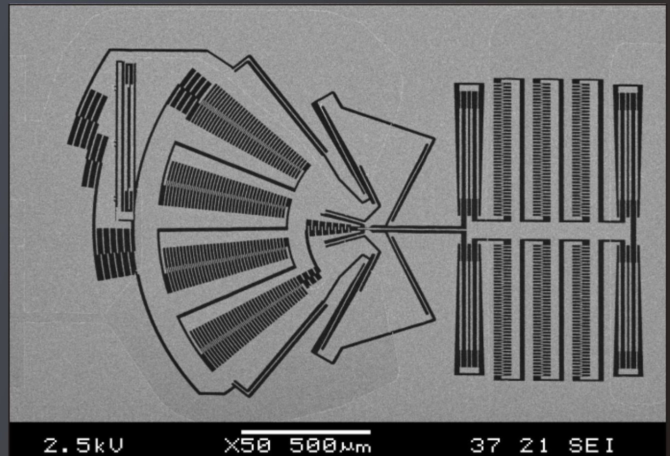

Dannis Brouwer

Design Principles for Six Degrees-of-Freedom MEMS-based Precision Manipulators

Dannis Brouwer

DESIGN PRINCIPLES FOR SIX DEGREES-OF-FREEDOM MEMS-BASED PRECISION MANIPULATORS

PROEFSCHRIFT

ter verkrijging van
de graad van doctor aan de Universiteit Twente,
op gezag van de rector magnificus,
prof.dr. W.H.M. Zijm
volgens besluit van het College voor Promoties
in het openbaar te verdedigen
op donderdag 14 juni 2007 om 16:45 uur

door

Dannis Michel Brouwer

geboren op 11 juli 1973
te Eindhoven, Nederland

Design Principles for Six Degrees-of-Freedom MEMS-based Precision Manipulators

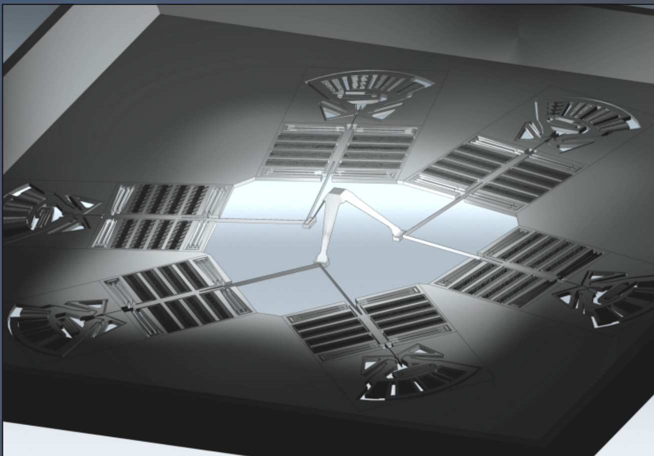

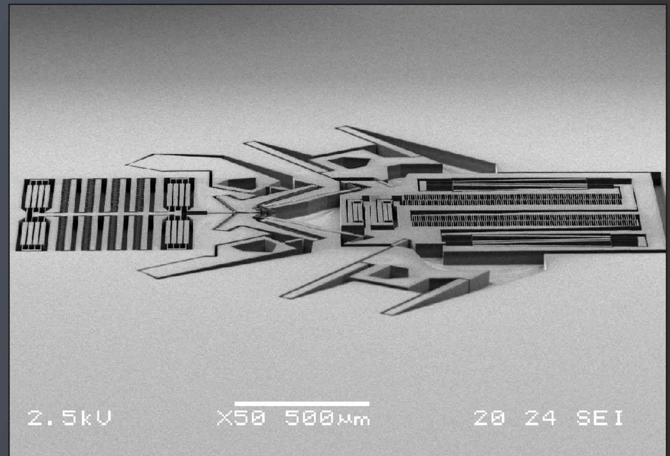

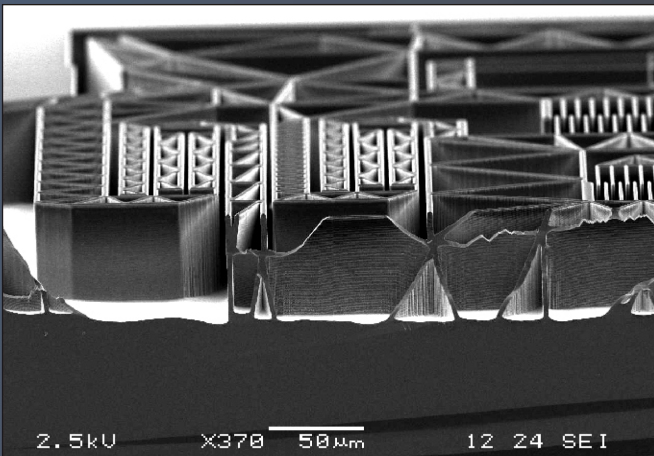

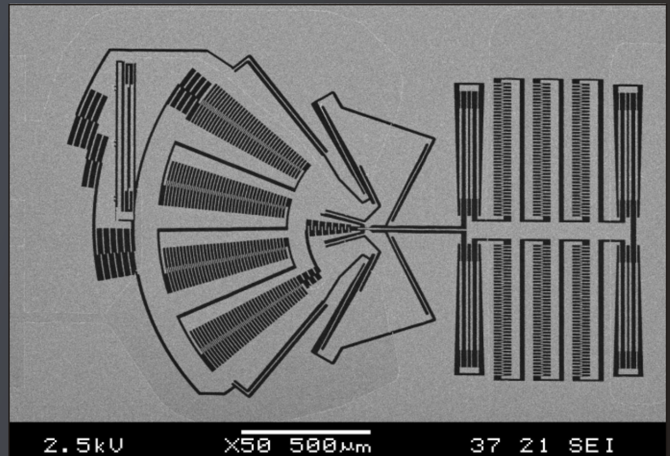

Dannis Brouwer

Design Principles for Six Degrees-of-Freedom MEMS-based Precision Manipulators

Dannis Brouwer

De promotiecommissie:

Voorzitter en secretaris	Prof. dr. C. Hoede	Universiteit Twente
Promotor	Prof. ir. H.M.J.R. Soemers	Universiteit Twente
Promotor	Prof. dr. M.C. Elwenspoek	Universiteit Twente
Assistent promotor	Dr. ir. J. van Dijk	Universiteit Twente
Leden	Prof. ir. R.H. Munnig Schmidt	Technische Universiteit Delft
	Prof. dr. ir. D. Reynaerts	Katholieke Universiteit Leuven
	Prof. dr. ir. P.H.J. Schellekens	Technische Universiteit Eindhoven
	Prof. dr. ir. J.B. Jonker	Universiteit Twente
	Prof. dr. ir. S. Stramigioli	Universiteit Twente

The research described in this thesis is part of the Multi Axes Micro Stage (MAMS) project and has been conducted at the chair of Mechanical Automation and Mechatronics of the department of Mechanical Engineering at the University of Twente, Enschede, the Netherlands. The research has been financially supported by the Innovative Oriented Research Program (IOP) Precision Technology (project IPT02308) from the Dutch Ministry of Economic Affairs.

Design Principles for Six Degrees-of-Freedom MEMS-based Precision Manipulators
D.M. Brouwer
Ph.D Thesis, University of Twente, Enschede, the Netherlands
ISBN: 978-90-365-2510-7

Cover:
Pictures on front cover in clockwise direction, starting top left: design of a 6 DOFs MEMS-based manipulator with 6 clamping mechanisms, SEM photo of 1st built clamping mechanism with linear comb-drive actuator, SEM photo of a rotational clamping mechanism, SEM photo of a Deep Reactive Ion Etched silicon structure.
Checkered transition: Starting something (at the roots of the author), finishing it.

Printed by: Wöhrmann Print Service, Zutphen, the Netherlands
© D.M. Brouwer, Enschede, the Netherlands, 2007

DESIGN PRINCIPLES FOR SIX DEGREES-OF-FREEDOM MEMS-BASED PRECISION MANIPULATORS

PROEFSCHRIFT

ter verkrijging van
de graad van doctor aan de Universiteit Twente,
op gezag van de rector magnificus,
prof.dr. W.H.M. Zijm
volgens besluit van het College voor Promoties
in het openbaar te verdedigen
op donderdag 14 juni 2007 om 16:45 uur

door

Dannis Michel Brouwer

geboren op 11 juli 1973
te Eindhoven, Nederland

Dit proefschrift is goedgekeurd door:

Prof. ir. H.M.J.R. Soemers (promotor)
Prof. dr. M.C. Elwenspoek (promotor)
Dr. ir. J. van Dijk (assistent-promotor)

Aan mijn ouders Wim en Gerda

PREFACE

There are many people who, directly and indirectly, enabled me to complete this work. I would like to thank those individuals who were especially helpful.

Herman made it possible for me to start in the first place. This involved quite a bit of turmoil. I would like to thank him for enabling me to participate in the MAMS project. The route we have taken was not standard. Therefore, it required a lot of evaluation and adjustment at times. In this respect, I would also like to thank the cooperative mentality of the members of IOP precision technology: Lou Hulst and Casper Langerak.

From the group of Mechanical Automation and Mechatronics, I would like to thank several individuals. The dedication of Ben in fundamental modeling made me learn many, until now, unrevealed aspects of non-linear mechanics. Johannes taught me the thoroughness of thesis writing and he helped me understand the results of modeling. Ronald adapted the SPACAR modeling program many times for the ever-changing questions I posed. Furthermore, I would like to thank Martine, Jeroen Old B., Benno, Menno, Toon, Dimi, Jonathan, Tjeerd and Jeroen for the nice time I experienced at WA.

Many people from the Transducer Science and Technology group contributed to the project. This group taught me the fundamentals of micro systems and the fabrication of these micro devices. I would like to thank the members of the MAMS team, Gijs and Boudewijn. Discussions with Gijs, a man not easily convinced, often made me think about the true fundamentals of designing. Macro engineering rules are usually not applicable in the micro domain. Boudewijn, working with you in ‘project room T517’ was great. You have been a true companion throughout the project. Apart from work time, the discussions and practical jokes during mountain biking, fitness and our Greek vacation were fruitful. Meint, Henrie and Erwin taught me to design MEMS fabrication processes. Meint also demonstrated the similarity between getting operational devices out of the clean room and the mentality necessary for being successful in bike races. Toon, our discussions on many levels were productive. Miko, your physical background is sometimes an

eye-opener for mechanical engineers. Your group is very special because of the open atmosphere. I have always felt most welcome at the TST group. Furthermore, I would like to thank: Remco S., Theo, Niels, Remco W., Dennis, Marcel, Marcus, Duy, Srini, Laura, Doekle and Jeroen.

Stefano and Wei participated in the MAMS team from the Control Engineering group. Stefano, your fundamental mathematical view on modeling was often revealing. Wei, I wish you success with the last part of the project.

Work in the clean room proved to be an important but often unpredictable factor in the success of the project. I would like to thank the clean room staff for their support throughout the project.

Twan, discussing the TEM sample manipulator with you helped to focus the project. Thanks for your commitment.

The assistance of Matthias and Jurre during their Master's thesis is gratefully acknowledged.

I would like to thank my friends and family for your ongoing support and encouragement when I needed it. 'Oma', thank you for offering me housing during the first five months. Jan, thank you for giving me advice and assistance.

I express my love and gratitude to my girlfriend Karin for her support and companionship, especially during the last part of the writing. Finally, I would like to thank my parents for their continued love, support and sacrifice.

Dannis Brouwer
Enschede, May 2007

NOMENCLATURE

Latin Symbols

a	Acceleration	m/s^2
a	Thermal diffusivity	m^2/s
A	Cross sectional area	m^2
A_c	Area of the coil perpendicular to the heat flow	m^2
A_s	Area of the substrate perpendicular to the heat flow	m^2
AR	Aspect Ratio of etching	-
B_{avg}	Average flux density in coil	T
B_r	Remanent flux density	T
c	Linear stiffness	N/m
c_1	Linear stiffness	N/m
c_2	Linear stiffness	N/m
c_{11}	Coefficient coupling longitudinal stress to strain in piezo	N/m^2
c_{act}	Stiffness at actuator	N/m
c_d	Drive stiffness	N/m
c_l	Stiffness of a load	N/m
c_m	Stiffness of mechanical spring	N/m
c_{piezo}	Stiffness of piezo	N/m
c_{act}	Stiffness at platform	N/m
c_x	Stiffness in x-direction	N/m
c_{x0}	Stiffness in x-direction at zero deflection	N/m
C	Stiffness matrix	N/m, N, Nm
C_{act}	Stiffness matrix for actuation	N/m, N, Nm
C_p	Specific heat capacitance	J kg^{-1} K^{-1}
$C_{pl,bl}$	Stiffness matrix for platform with blocked actuators	N/m, N, Nm
$C_{pl,unbl}$	Stiffness matrix for platform with unblocked actuators	N/m, N, Nm
D	Depth of Focus of optical system	m
d_{31}	Piezoelectric coefficient	m/V
e_f	Finger approach to each other	m
e_{pl}	Platform errors	m, -
E_y	Young's modulus	N/m^2

E_e	Electrical field	V/m
E_3	Electrical field in direction 3	V/m
EMF	Electromotive force	V
f	Deflection	m
fe	Vibration mode frequency	Hz
F	Force	N
$\underline{F}$	Force matrix	N
F_{act}	Actuator force	N
$\underline{F}_{act}$	Actuation force matrix	N
F_{bl}	Blocking force, max. force at zero displacement	N
F_{comb}	Comb-drive force	N
F_e	Electric force	N
F_m	Force created by a mechanical spring	N
F_{pl}	External force on platform	N
$\underline{F}_{pl}$	External force on platform matrix	N, Nm
g	Acceleration of gravitation field	m/s^2
g_a	Gap between the arms of a comb-drive actuator	m
g_f	Gap between the fingers of a comb-drive actuator	m
h	Height	m
h_c	Convection coefficient	W/(m^{2}K)
h_{comb}	Height of the comb-drive actuator	m
h_{pl}	Height of platform	m
h_{si}	Height of the silicon leaf-spring	m
i	Transmission ratio, linearized geometric transfer	-
I	Identity matrix	-
I	Area moment of inertia	m^4
I_e	Electrical current	A
J	Current density	A/m^2
k	Angular stiffness	Nm/rad
k_1	Coefficient of optical system	-
k_2	Coefficient of optical system	-
k_m	Motor constant of Lorentz actuator	N/A
l	Length	m
l_0	Initial length	m
l_a	Length of the arms of a comb-drive	m
l_f	Length of the fingers of a comb-drive	m
l_{ff}	Length of the folded flexure	m
$l_{i,pl}$	Inner platform length	m

l_{pl}	Platform length	m
l_{ov}	Finger overlap in a comb-drive	m
l_{si}	Si-leaf-spring length	m
l_{sl}	Slanted leaf-spring length	m
l_w	Length of the winding	m
L	Self induction of coil	H
m	Mass	kg
M	Moment	Nm
n	Number of finger pairs in a comb-drive actuator	-
N	Number of turns of coil winding	-
NA	Numerical Aperture	-
os	Offset distance	m
P	Power	W
P_d	Dissipated power	W
q_{cond}	Heat transport by conduction	W
q_{conv}	Heat transport by convection	W
q	Distributed force	N/m
q_{comb}	Distributed force along comb-arm due to finger force	N/m
q_{pp}	Distributed force along comb-arm due to parallel plate force	N/m
r	Linear characteristic dimension used for scaling	m
rx	Rotation around x-axis	rad
ry	Rotation around y-axis	rad
rz	Rotation around z-axis	rad
R	Resolution	m
R_c	Electrical resistance of coil	Ω
R_s	Electrical resistance of substrate	Ω
s	Stroke	m
$\underline{S}$	Compliance matrix	m
t	Thickness	m
t_a	Thickness of arms	m
t_f	Thickness of fingers	m
t_{ff}	Thickness of folded flexure	m
t_r	Thickness of reinforcement	m
t_s	Thickness of shuttle	m
t_{si}	Thickness of silicon leaf-spring	m
t_{sl}	Thickness of slanted leaf-spring	m
T	Temperature	K
T	Linearized geometric transfer function	-, 1/m

T_c	Temperature of the coil	K
T_i	Temperature of the interface	K
T_{amb}	Temperature of the ambient	K
U	Voltage	V
v	Velocity	m/s
V_a	Volume of arms of a comb-drive	m^3
V_c	Volume of a coil (total)	m^3
V_{cm}	Volume of a coil directly opposing the magnet	m^3
V_f	Volume of fingers of a comb-drive	m^3
V_{ga}	Volume of the space between the comb-arms	m^3
V_s	Volume of the shuttle of a comb-drive	m^3
V_t	Volume of the total comb-drive	m^3
w	Width	m
$w_{i,pl}$	Inner width of platform	m
w_{pl}	Width of platform	m
w_{sl}	Width of slanted leaf-spring	m
W	Work	J
x	Displacement	m
x_{act}	Actuator displacement	m
x_{pl}	Platform displacement	m, -
$\underline{X}$	Displacement matrix	m

Greek Symbols

α	Expansion coefficient	1/K
α	Angle	-
δ	Dielectric loss factor for piezo	-
Δl	Elongation	m
ΔT	Temperature difference	K
ε	Permittivity (8.854 10^{-12} for vacuum)	F/m
ζ	Ratio of force: parallel plate / force comb-drive	-
η	Efficiency	-
κ	Voltage factor for transition from stable to unstable	-
λ	Wavelength	m
λ	Max. stable displacement / deflection parallel plate actuator	-
λ	Thermal conduction coefficient	W/ (m K)
λ_c	Thermal conductance of a coil	W/ (m K)
λ_s	Thermal conductance of a substrate	W/ (m K)
μ	Permeability (1.256 10^{-6} for vacuum)	N/A^2
ν	Poisson's contraction coefficient	-
ξ	Factor to relate actuator volume to work	J/m^3
ρ	Density	kg/m^3
ρ_e	Specific electrical resistance	Ω m
σ	Stress	N/m^2
τ	Time constant	s
φ	Angle	rad
φ_a	Angle of comb-arm	rad

Abbreviations and frequently used terms

Actuation direction	Compliant, *y*-direction of mechanism, Figure 2.10	2.5.1
AFM	Atomic Force Microscopy [92]	1.1
AlN	Aluminum Nitride type of piezo material [68]	C.4
ARCE	Aspect Ratio Compensated Etching (DRIE)	2.2
ARDE	Aspect Ratio Dependent Etching (DRIE)	2.2
Back-etch release	Process developed by Sarajlic [112]	2.2
Bent-beam actuator	Type of thermal actuator with motion amplifier integrated [105]	C.5

Bimorph	Cantilever consisting of two layers, one active thermal or piezo	C.4,C.5
Blocking force	The maximum force the clamp mechanism has to block	5.6
Bosch etching	DRIE using Bosch recipe	2.2
Bulk micro machining	Process using SCS as structural layer	1.3.1
CAGR	Compounded Annual Growth Rate [107]	1.1
CCD	Charged Coupled Device	A.2
Cold Trap	Vacuum quality enhancing cold metal device in TEM	1.7.1
Comb-drive	Electrostatic actuator [81]	C.3
Compensation structure	Special mask for KOH etching in SCS [4]	4.2
Compliant mechanism	Flexure mechanism or elastic mechanism [8,56,62,76,121,122]	1.3
CVD	Chemical Vapor Deposition [92]	2.2
Design Principles	Design rules and best practices for precision engineering [76]	2.3
Determinism	Understandable cause and effect relationship [56]	2.3
DMD	Digital Mirror Device [71]	1.1
DOF(s)	Degree(s)-of-Freedom [8,76]	1.2.3
DRIE	Deep Reactive Ion Etching [92]	2.2
Drive stiffness	Actuation stiffness of a mechanism excluding actuator guidance	2.4.2
Dual Beam	Machine combining E-beam (SEM) & FIB	B
E-Beam	Electron beam	1.2.2
Elastic mechanism	Flexure or compliant mechanism [8,56,62,76,121,122]	1.3
Exact kinematic constraint design	Constraining exactly the correct amount of DOFs [8,76]	2.3
FIB	Focused Ion Beam	A.3
Flexure mechanism	Compliant or elastic mechanism [8,56,62,76,121,122]	1.3
Folded flexure	Straight guiding mechanism in MEMS, Figure 2.10	2.5.1
Hexapod	6 DOFs parallel kinematic manipulator	
HF	Hydrofluoric acid, etches silicon oxide	3.4
Hinge	1 Rotational DOF releasing element (roller or friction hinge)	3.3
Hinge flexure	1 Rotational DOF releasing flexure element	3.4
Hot-leg/cold-leg	Thermal actuator using 1 hot leg to extend w.r.t. 1 cold leg [34]	C.5
IC	Integrated Circuit	1.1
In-plane	Direction in the plane of the wafer	1.3
KOH	Potassium hydroxide [92]	2.2
Lateral comb-drive	Comb-drive actuating in longitudinal finger direction	C.3.1
Leaf-spring	Elastic element constraining 3 DOFs [76]	2.4.1
Longitudinal direction	Length direction of beam or leaf-spring, x-direction Fig. 2.10	2.5.1
LPCVD	Low Pressure Chemical Vapor Deposition [92]	2.2
MAMS	Multi Axis Micro Stage (name of this project)	1.1
MEMS	Micro Electro-Mechanical Systems [93]	1.1
MST	Micro Systems Technology [93]	1.1
NA	Numerical Aperture of an optical system	3.5
Out-of-plane	Direction perpendicular to the wafer plane	1.3
Parallel mechanism	>1 kinematic chain of links between the end-effector and base	3.2.5
Passive stability	Stability depending on material properties	3.2.6
Power density	Work per volume per second	C.1
Precision Engineering	Method to develop a precision machine	1.4

Pull-in	Typical behavior of instability of a comb-drive [81]	C.3.1
PZT	Lead Zirconacte Titanate type of piezo material [52,101]	C.4
Reinforced leaf-spring	Leaf-spring thickened in the middle [76] , Figure 2.11	2.5.2
Repeatability	How well a position can be reproduced	3.2.6
RIE	Reactive Ion Etching [92]	2.2
Scaling	Rate of physical quantity change w.r.t. linear dimension [92,45]	2.2
Scratch-drive	Type of stepping electrostatic actuator [92]	1.3.2
SCS	Singe Crystal Silicon [92]	1.3.1
Serial manipulator	One kinematic chain of links between the end-effector and base	3.2.5
SiRN	Silicon Rich Nitride [92]	2.2
Shuttle	Straight guided body (translator), Figure 2.10	2.5.1
SOI	Silicon On Insulator, Si-SiO_2-Si wafer [92]	1.3.3
SPACAR	Mechanical multi body Finite Element Modeling program	F
Stability	Deviation from a certain reference over time	3.2.6
Stage	Manipulator	1.1
Stewart platform	Certain symmetric version of a parallel kinematic manipulator	
Stiction	Force parallel to contact surface required to overcome cohesion	2.2
STM	Scanning Tunneling Microscope [92]	1.1
Surface micro machining	Process using added thin layers for structural mechanics	1.3.3
TEM	Transmission Electron Microscope	1.2.1
TEOS	Tetraethoxysilane, ingredient to create SiO_2 [92]	2.2
TMAH	Etchant, like KOH, etches along <111> planes [92]	1.1
Transverse comb-drive	Comb-drive actuating by changing the gap between fingers	C.3.2
TWIN	1 mask DRIE and release process [63, 112]	2.2
UV	Ultra Violet (light)	1.1
Work density	Work per volume	C.1
<100>	SCS crystal plane [92]	2.2
<110>	SCS crystal plane [92]	2.2
<111>	SCS crystal plane [92]	2.2

CONTENTS

PREFACE .... **i**
NOMENCLATURE .... **iii**
Latin Symbols iii
Greek Symbols vii
Abbreviations and frequently used terms vii
CONTENTS .... **xi**

CHAPTER 1:
INTRODUCTION **1**
1.1 Introduction to MEMS 1
1.2 Transmission Electron Microscope 3
1.2.1 Electron microscopy 3
1.2.2 TEM 3
1.2.3 The TEM sample manipulator 4
1.2.4 Miniaturizing the TEM sample manipulator 6
1.3 Overview of existing research about Multi-DOFs positioning in MEMS . 6
1.3.1 In-plane positioning 7
1.3.2 Out-of-plane positioning 9
1.3.3 Combinations of in- and out-of-plane manipulation 10
1.3.4 Assembly of MEMS devices 11
1.3.5 Conclusion regarding existing research 11
1.4 Precision Engineering 12
1.5 The goal of this research 12
1.6 Specifications of a TEM sample manipulator 13
1.7 TEM sample manipulator concept 15
1.7.1 Two stage concept 15
1.8 Thesis outline 17

CHAPTER 2:
DESIGN PRINCIPLES FOR MEMS-BASED COMPLIANT MECHANISMS

MECHANISMS ... **19**
2.1 Introduction ... 19
2.2 Background of MEMS design ... 20
2.3 Design principles with respect to MEMS design ... 29
2.4 Influence of a large deflection on leaf-spring behavior ... 35
2.4.1 Behavior of height restricted leaf-springs ... 35
2.4.2 Influence of drive stiffness on leaf-spring behavior ... 42
2.5 Straight guiding in MEMS ... 46
2.5.1 Types of straight guiding ... 46
2.5.2 Influence of reinforcement on folded flexure behavior ... 49
2.5.3 Non-linearity of actuation compliance ... 53
2.5.4 Improved straight guiding designs for MEMS ... 57
2.5.5 Design rules for straight guiding in MEMS ... 62
2.6 Conclusion ... 62

CHAPTER 3:
CONCEPTS FOR FABRICATION & DESIGN OF A SIX DOFs MEMS-BASED MANIPULATOR

BASED MANIPULATOR ... **65**
3.1 Introduction ... 65
3.2 MEMS-based Mechatronic System Design ... 66
3.2.1 Differences between MEMS and macro mechatronic design ... 66
3.2.2 Basis of design: Design principles and bulk micro machining ... 66
3.2.3 Motion in- and out-of-plane of the wafer ... 67
3.2.4 Actuator principle ... 68
3.2.5 Serial versus parallel kinematic mechanism ... 68
3.2.6 Position control ... 69
3.2.7 Conclusions regarding MEMS-based mechatronic design ... 72
3.3 The Kinematic Concept ... 73
3.4 Concept 1: Planar hinge flexure concept ... 76
3.5 Concept 2: Slanted hinge flexure concept ... 80
3.6 Concept 3: Slanted leaf-spring concept ... 88
3.7 Slanted leaf-spring concept with clamping mechanisms ... 92
3.8 Conclusions ... 93

CHAPTER 4:
DESIGN AND MODELING OF THE SIX DOFs MEMS-BASED MANIPULATOR 95
4.1 Introduction 95
4.2 Process design 96
4.3 Changes to the slanted leaf-spring design 104
4.4 Dimensioning the manipulator 105
4.5 Modeling the manipulator 108
4.5.1 Two DOFs model 109
4.5.2 Linearized system model of the manipulator 112
4.5.3 Geometric transfer function and actuation stiffness matrix $\underline{F}_{pl} = \underline{0}$; $\underline{F}_r = \underline{0}$ 114
4.5.4 Errors due to the use of a first-order model 117
4.5.5 Actuation force and stroke 120
4.5.6 Platform stiffness blocked and unblocked 123
4.5.7 Modal analysis 126
4.5.8 Vibration mode frequency shift due to platform displacement 130
4.5.9 Robustness: Elastic stability and stress 132
4.5.10 Thermal Stability 134
4.6 Conclusions and recommendations 138

CHAPTER 5:
DESIGN, FABRICATION AND TESTING OF A CLAMPING MECHANISM 141
5.1 Introduction 141
5.2 Conceptual design of the Clamping Mechanism 143
5.3 Clamp mechanism design 146
5.4 Modeling the clamping mechanism 151
5.5 Process design 157
5.6 Measurement results 165
5.7 Conclusions and recommendations 171

CHAPTER 6:
CONCLUSIONS 173
6.1 Research objective 173
6.1.1 Designing and manufacturing a 6 DOFs manipulator 174
6.1.2 Principle solutions for MEMS-based kinematic constraint design 176
6.2 The strong and weak points of MEMS-based micro manipulators 177

APPENDIX A:
ADDITIONAL BACKGROUND ON THE TEM 179
A.1 Introduction to electron microscopy 179
A.2 TEM 179
A.3 TEM applications 180

APPENDIX B:
CONCEPT FOR LOADING A SAMPLE IN A TEM 183

APPENDIX C:
MEMS-BASED ACTUATORS FOR PRECISION MANIPULATION 185
C.1 Introduction 185
C.2 Electro-magnetic actuators 188
C.2.1 Lorentz actuator 188
C.2.2 Conclusion regarding Electromagnetic actuators 195
C.3 Electrostatic actuation 196
C.3.1 Comb-drive actuator (lateral) 197
C.3.2 Transverse comb-drive actuator 203
C.3.3 Conclusion regarding electrostatic actuation 209
C.4 Piezo actuators 210
C.5 Thermal actuators 215
C.6 Steppers 220
C.7 Conclusion regarding actuation principles for MEMS 220

APPENDIX D:
SCALING OF FLUX DENSITY 225

APPENDIX E:
THERMAL CONDUCTION IN A MEMS LORENTZ ACTUATOR 229

APPENDIX F:
MULTIBODY SYSTEMS MODELED BY FINITE ELEMENTS 233

APPENDIX G:
PROCESS DOCUMENT OF THE MANIPULATOR 235

APPENDIX H:
PROCESS DOCUMENT OF THE CLAMPING MECHANISM 261

REFERENCES **271**
ABSTRACT **281**
SAMENVATTING **285**
ABOUT THE AUTHOR **289**

Chapter 1

INTRODUCTION

To explain the title of this thesis, this chapter gives a short introduction regarding the fields of Micro Electromechanical Systems (MEMS) and Precision Engineering. The Transmission Electron Microscope (TEM) sample manipulator is introduced as a suitable carrier for a MEMS-based 6 Degrees-of-Freedom (DOFs) manipulator. An overview of the existing literature regarding multi DOFs MEMS-based manipulators is given. The two main goals of the research are presented. The research described in this thesis focuses on a small displacement 6 DOFs MEMS-based precision manipulator.

1.1 Introduction to MEMS

MEMS is the acronym for Micro Electro Mechanical Systems (abbreviations and frequently used terms are listed from page vii onwards). It is often referred to as Micro Systems Technology (MST) [93] as well, but conventional electric integrated circuits (IC) are also covered by the term MST. MEMS devices comprise sensors, actuators, micro-fluidic systems and mechanical mechanisms. They are typically manufactured using lithography based processing similar to semiconductor processes. These devices generally range in size from a micrometer to several millimeters. MEMS are fabricated using modified silicon fabrication technology (originally used to make electronics), molding and plating, wet etching (KOH, TMAH) and dry etching (RIE and DRIE), electro discharge machining (EDM), and other technologies capable of manufacturing very small devices.

Systems in general potentially benefit from miniaturization. Not only does the size of devices decrease, but as a consequence they can become faster and cheaper and in many cases greater functionality is offered [93]. In a keynote paper in Annals of the CIRP 2000, Corbett et al. discuss most of the fields mentioned hereafter that will benefit increasingly from Microsystems [29]: High density data storage projects like the Millipede project from IBM [132], where a thermal probe array is used for read/write data storage, require precise planar *x/y*-scanning and displacement in the out-of-plane direction. Furthermore, a high vibration resonance frequency of deformation modes and low mass is required for fast data storage. For future ground-based telescope applications, deformable micro mirrors for adaptive optics are required. Adaptive optics is used to correct for perturbations in the wavefronts of the incoming light caused by atmospheric turbulence. Conventional deformable mirrors are very expensive, whereas MEMS based deformable mirrors potentially offer a low cost alternative [33]. In the field of space applications, there is a need for robust accelerometers, gyroscopes and sensor applications to monitor and control the harsh conditions in space. To enable further advances in nano-technology, ultra precision machines and instruments (with large through-put and reduced cycle-time) are required. These include the various probe techniques like atomic force microscopy (AFM), scanning tunneling microscopy (STM) or magnetic, thermal and chemical reactive probes, but also energy beam tools like UV optical, ion-beam, e-beam and X-ray for structuring and Scanning Electron Microscopy (SEM) and Transmission Electron Microscopy (TEM) for characterization. Pril [103] for example shows a hybrid MEMS/precision engineered mechanical probe with several nm repeatability. Overall, in many fields, systems potentially benefit from miniaturization.

MEMS have the ability to integrate several functions in a small package. For example, a MEMS acceleration sensor is equipped with self diagnostics and a digital output. MEMS become commercially attractive if they provide cost reduction or enable new functionality. Automotive applications like pressure, acceleration and rate sensors replace or are replacing multi-part, assembled, precision engineered counterparts because of cost reduction. Cost reduction can also be established by cutting maintenance costs. New functionality is enabled by MEMS, for example, by mirror arrays as demonstrated by Texas Instruments' Digital Mirror Device (DMD) [71]. Or as shown in the biomedical industry, where micro pumps, micro valves and micro sensors for fast analysis of liquids are integrated. The potential for future penetration in a broad range of applications is real. In terms of shipment, the worldwide market for Microsystems technology has

experienced a compounded annual growth rate (CAGR) in dollars of 21.0% between 2000 and 2004 according to Roger Grace Associates and Nexus [107].
MEMS could offer new functionality when it comes to precision manipulation within a confined space. In that case, MEMS technology is used for achieving miniaturization of precision manipulators. An application where a small precision manipulator is required is a next generation Transmission Electron Microscope (TEM). In this thesis, as part of the Multi Axis Micro Stage (MAMS) project, a small precision manipulator for a TEM will be researched.

1.2 Transmission Electron Microscope

To provide some background information on the manipulator used to position a sample in a TEM, the TEM will be briefly described. In Appendix A, more detailed information on the background of the TEM can be found.

1.2.1 Electron microscopy

Electron microscopes provide a resolution far better than that which is possible with optical light microscopes, and with improved depth of field. Additional background regarding the TEM is given in Appendix A. Basically, two types of electron microscopes exist:

- The scanning electron microscope (SEM) examines an object by scanning the surface with a fine electron beam and measuring the reflection. It produces surface images with good depth of focus at a resolution down to less than a nanometer.

- In transmission electron microscopy (TEM) electrons pass completely through the sample. It can produce images with resolutions down to 0.08 nm at magnifications of 50 million. However, the samples need to be prepared specially to become extremely thin. The TEM has the ability to determine the positions of atoms within materials.

1.2.2 TEM

A TEM consists of a long column which is isolated from floor vibrations. The column features an electron gun, a number of electromagnetic lenses, the sample manipulator, a diaphragm, a fluorescent screen and a camera system (see Figure 1.1). The electrons in a TEM are accelerated by an electric field and focused onto a sample by electromagnetic lenses. Just like optical lenses, electromagnetic lenses exhibit aberrations. To minimize aberrations, the gap between the lens pole pieces

focusing the electron beam onto the sample (see Figure 1.2) is only about 5 mm. As a result, little space for a sample manipulator is left.

The TEM is typically applied in biological and materials science, and semiconductor analysis. The samples are prepared in such a way that some portion of the sample is thin enough for the beam to penetrate it. In materials science, generally the thickness of a sample is less than 300 nm. Semiconductor samples are shown in Appendix A, Figure A.1.

1.2.3 The TEM sample manipulator

The maximum achievable image resolution is the most important characteristic of a TEM. Currently the sample manipulators' lack of stability mainly determines the maximum image resolution, making the manipulator one of the most critical mechanical parts of a TEM. This lack of stability is caused primarily by external heat and vibration sources. Currently a typical sample manipulator controls 5 Degrees-of-Freedom (DOFs) over displacements in the mm-range. A DOF is a motion in a direction that is free or relatively compliant in comparison to other, stiff directions [8,76]. There are two rotational DOFs of several tens of degrees. Currently the drift rate, the low frequent position deterioration, is typically in the tens of nanometers per minute directly after the positioning of the sample [138]. The drift decreases to less than 1 nanometer per minute if the TEM is left to homogenize for as long as half an hour. This drift rate and the time lost with homogenization, however, remain a major drawback. They result from the large size of the manipulator, which is about 10^{-4}-10^{-3} m^3. A large manipulator is intrinsically less stable than a small manipulator in terms of thermal drift. Moreover, because of the small gap of about 5 mm (see Figure 1.2) between the TEM pole pieces, the present manipulator is mounted onto the exterior of the TEM column. Therefore, the surroundings combine thermal and acoustic noise into the column and the manipulator.

The highest resolution images are currently obtained by mounting a sample onto a passive holder and placing the holder with sample on top of the lower pole piece using a manipulator. The manipulator is detached from the holder, and the holder rests passively on the lower pole piece. The thermal drift and vibrations of the sample with respect to the E-beam are small, because the sample is not directly connected to the exterior of the TEM. Therefore, the stability of the sample with respect to the E-beam is high. However, there is no tilt freedom and z-translation possible and the *x*- and *y*-translations have poor resolution.

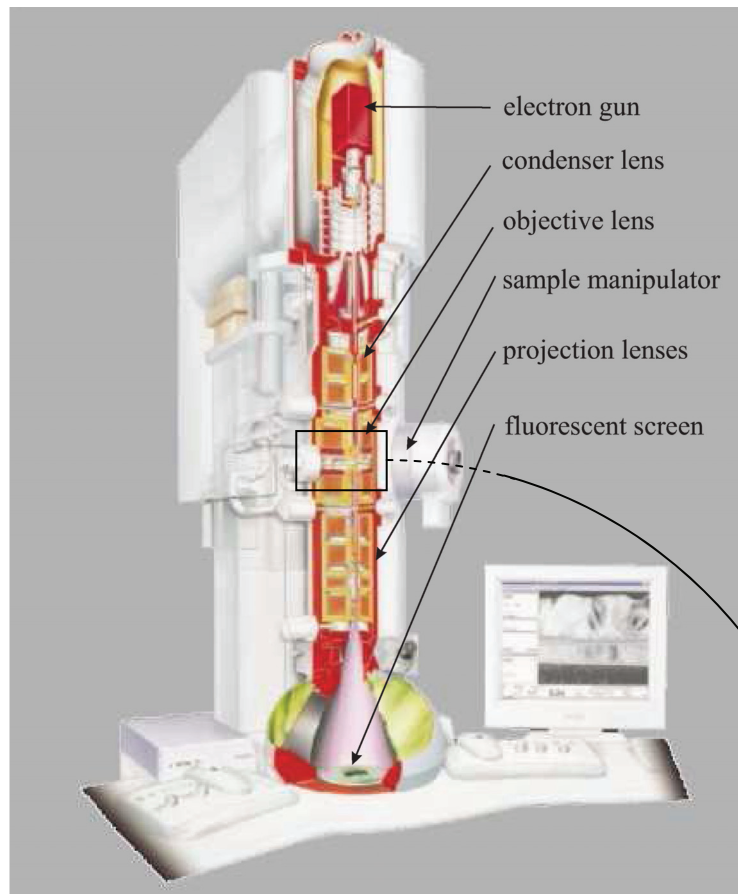

Figure 1.1: Cross-section of a TEM column (Courtesy of

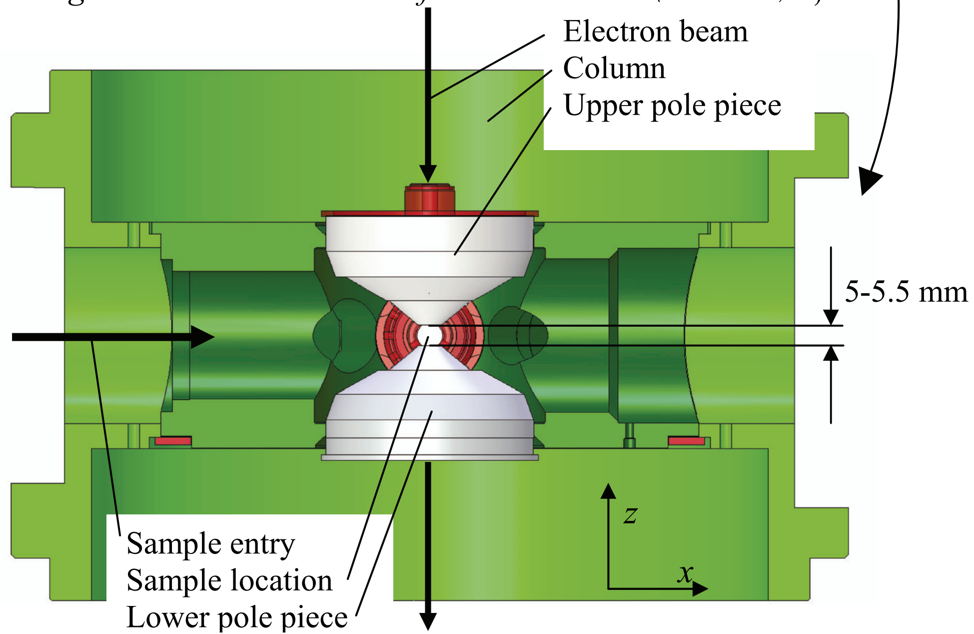

Figure 1.2: Cross-section of the pole pieces of the objective lens of a TEM (Courtesy of FEI).

The combination of miniaturizing the manipulator and attaching it directly to one of the pole pieces could greatly enhance the stability of the sample with respect to the E-beam. The micro manipulator is able to position the sample accurately and in a stable manner at the same time. This results in improved image resolution.

1.2.4 Miniaturizing the TEM sample manipulator

Miniaturizing the manipulator potentially increases the stability in two ways. It creates the opportunity to mechanically ”short-circuit” the manipulator to the column – the heart of the electron beam source, shown in Figure 1.2 – by fixing it to one of the TEM pole pieces, isolating external thermal and vibration noise. Secondly, the manipulator itself can be made more stable. Miniaturizing potentially increases the vibration mode frequencies, decreases the thermal expansion and also decreases the thermal time constant of the manipulator. Increasing the vibration mode frequencies of the manipulator helps to minimize vibration amplitudes of the sample with respect to the TEM column. More details will be given in section 1.6, where the specifications are explained. For these reasons MEMS-based manipulators, enabling miniaturization, will be investigated. An overview of the literature on MEMS manipulators will be presented in the next paragraph.

1.3 Overview of existing research about Multi-DOFs positioning in MEMS

To develop an idea of the state of the art of precision positioning in MEMS, a small survey is done with respect to existing examples of multi-DOFs devices in MEMS and whether or not the techniques used for these devices are suitable for a precision system. Because in many practical cases it seems easiest to confine a system to either planar or out-of-plane positioning, in this case MEMS manipulators are distinguished with respect to systems for planar positioning (paragraph 1.3.1), systems for out-of-plane positioning (paragraph 1.3.2) and combinations of both (paragraph 1.3.3). Combinations often pose a much larger challenge, because they generally require a larger sequence of fabrication processes. The stiffness requirements for the mechanism are also more complex. A different approach to creating 6 DOFs in MEMS is using assembly to stack manipulators or manipulator systems on top of each other (paragraph 1.3.4).

In MEMS design and fabrication, the characterization of MEMS devices, like positioning resolution, position stability, stroke, speed and force, is challenging and therefore often not specified in the literature. Although the reasons for this absence

are very real, it complicates the valuation of the potential of reported MEMS manipulators with respect to precision applications. In Table 1.1 typical multi-DOFs MEMS manipulators found in literature are presented and distinguished with respect to the amount of DOFs and obtainable strokes, the type of actuator used, and the kind of mechanism on which the manipulator is based. The linkages of the mechanism creating the DOFs are divided in hinges (friction, play) and compliant elements. A second distinction is made between mechanisms using parallel or series coupling of the linkages. The entire table is split up in systems for in-plane positioning, systems for out-of-plane positioning and systems combining in-plane and out-of-plane positioning.

For positioning repeatability it is important that the mechanism used in a manipulator does not have friction, play or backlash [8,56,62,76,121,122]. Many solutions for multi-DOFs hinges offering large freedom of movement show play and friction in the hinges [61, 102, 134 , 142]. This is a large drawback for precision applications. Compliant mechanisms generally do not suffer from friction, play and backlash and are far more suited to precision manipulation. However, the displacements are limited compared to the size of the mechanism. Hardly any data is found on position stability. Thermal drift and thermo-mechanical noise are important stability characteristics. Within the articles used for this survey only Chu et al. [27] give an analysis of the expected thermo-mechanical position noise.

1.3.1 In-plane positioning

An example of a 2 DOFs planar manipulation platform is presented by Sarajlic et al. in [114]. The platform is actuated by electrostatic comb-drives. The system is fabricated by a bulk micro machining process in single crystal silicon (SCS) allowing for high aspect-ratio structures and electrical insulation. Etching in the bulk wafer is called bulk micro machining. In the case of a silicon wafer, it results in SCS as a structural material. In general, 2 DOFs planar concepts can be expanded relatively easy to concepts for 3 DOFs planar manipulation. Using comparable technology, an example of a parallel 3 DOFs planar manipulator is fabricated as part of the MAMS project [64]. The vertexes of a triangular platform are displaced in tangential direction by comb-drives. Based on the same kinematic principle a three DOFs planar precision manipulator driven by piezoelectric bimorph actuators is presented in [58]. This system is made in quartz with hinge flexures made out of polyimide. The actuators are PZT elements assembled on top of the quartz.

Reference	DOFs & strokes*	actuation	mechanism	remarks
In-plane				
[114]	2 translations +/- 20 µm	comb-drives	compliant; parallel	
[64]	2 translations; 1 rotation +/- 10 µm; 4°	comb-drives	compliant; parallel	
[58]	2 translations; 1 rotation - 10 µm; -°	PZT	compliant; parallel	assembled actuators
[27]	2 translations 19 µm	thermal bent-beam	compliant; parallel	cap. position sensing sub-nm resolution
[125], [113]	1 translations / 2 translations "infinite"	electrostatic parallel plate	compliant; inchworm	nm resolution obtainable
Out-of-plane				
[80], [70]	2 tilt angles up to 20°	comb-drives vertical	compliant; series	
[95]	1 translation; 2 tilt angles +/-10 µm; 20°	comb-drives vertical	compliant; series/paral.	
[119]	1 translation; 2 tilt angles - µm; +/- 10°	thermal bimorph	compliant; parallel	
[33]	3 x 1 translation out-of-plane 23 µm	electrostatic parallel plate	compliant; parallel	adapt. optics deform mirror
[26]	1 translation; 2 tilt angles - µm; -°	thermal bimorph	compliant; parallel	linear motor friction
[130]	1 translation; 2 tilt angles - µm; -°	comb-drives	compliant; parallel	PDMS mechanism
[36], [35]	1 translation tens of µm	thermal bimorph	compliant	enable large forces
Combinations				
[48]	2 transl. in-pl.; 1transl. o.o.p. 120 µm; 250 µm	electrostatic scratch-drive	hinges; parallel	play in hinges
[22]	2 transl. in-pl.; 1tilt angle 1 µm; -°	comb-drives	compliant	
[28]	various - µm; -°	comb-drives	compliant	
[140]	6 DOF max. 2 µm; -°	PZT	compliant; parallel	diced grooves PZT filled
[134], [61]	6 DOF max. 150 µm; +/- 5°	comb-drives	hinges; parallel	play in hinges
[115]	various 13 µm; 2°	thermal bimorph	compliant	application SEM/TEM
[24]	6 DOF max. 13 µm; 2°	thermal hot-leg /cold-leg	compliant; parallel	application SEM/TEM

* The reported strokes are for static displacements and rotations.

Table 1.1 Survey of multi-DOF MEMS-based manipulators.

A 2 DOFs position stage with thermal “bent-beam” (a type of stroke amplifier) actuation and nanometer range 2 DOFs capacitive position sensing is discussed in [27]. A compliant stroke amplifier is applied to amplify the capacitance change of the sensor.

Stepper or inchworm actuators are also found in the micro-domain. Examples applying electrostatic parallel plate actuators for clamping and displacement are given in [125] for single DOF displacement and in [113] for 2 DOFs displacement. Theoretically, inchworms enable manipulation over an unlimited range while displacements in the nanometer range are obtainable. Practically, the range is often restricted by the maximum stress and deflection tolerable by the suspension beams. In most cases the limited actuator force to deflect the suspension beams limits the displacement also.

1.3.2 Out-of-plane positioning

Mechanisms for out-of-plane positioning are often found in adaptive optics [33] or scanning mirror applications. Generally, scanning mirror devices are capable of 2 DOFs tilt motion applied to deflect a laser beam or to project an image. In [80, 70, 95, 119] 2 DOFs tilt mechanisms as well as complete out-of-plane 3 DOFs mechanisms based on flexures are presented for micro mirrors and other optical elements like (Fresnel) lenses and gratings. Most scanning mirrors are driven by out-of-plane comb-drives. The tilting motion is realized with a compliant torsion suspension. Many scanning mirrors are meant to be driven in resonance, which allows for much larger tilt angles than those obtained at low frequencies. In the case of a manipulator, manipulation is low frequent and the system is not applied in resonance.

Out-of-plane stages for positioning of a platform are also reported. In [26] a 3 DOFs out-of-plane manipulation stage is presented applying three identical linear motors consisting of a slider and a pair of thermal bimorph actuators. The motors are radially positioned around a platform with 120° pitch and push radially inward. The propulsion is based on friction, which is a large drawback for precision positioning. Another 3 DOFs out-of-plane stage applying the same kinematic principle is presented in [48]. Here electrostatic scratch-drive actuators are applied. A scratch-drive actuator is a kind of stepping electrostatic actuator. For this stage, hinges are used with play instead of hinge flexures. A 3 DOFs out-of-plane stage with compliant hinges made from polydimethylsiloxane (PDMS) is presented in

[130]. Out-of-plane actuation is based on a mechanism, built up out of PDMS, transforming the in-plane motion of comb-drives to out-of-plane displacements of a platform.

Deladi et al. present various combinations of thermal actuators optimized for in-plane and out-of-plane actuation with large forces in [35, 36]. These can be applied in a multi DOFs stage.

1.3.3 Combinations of in- and out-of-plane manipulation

A 3 DOFs manipulator with two planar translational DOFs and one out-of-plane tilt DOF combined with a gripper, is presented in [22]. It employs electrostatic comb-drive actuators for all DOFs including the gripper. The system is based on an elastic mechanism. In [140] various multi-DOFs flexure mechanisms fabricated in silicon on insulator (SOI) wafers and with surface micro machining are reported. In surface micro machining thin layers are added onto a substrate and used as a structural mechanical layer. A SOI wafer features an oxide layer and a silicon layer on top of the silicon base wafer. Out-of plane flexures are generally based on thin film deposition on the wafer or in molds etched into the wafer. This relatively simple process offers design freedom for a large variety of flexure geometries, but the stiffness in the out-of-plane direction of the wafer is limited due to the thin layers. In general, this is an aspect that complicates MEMS design and fabrication for out-of-plane precision manipulation.

Complete 6 DOFs manipulation stages are discussed in [61] and [134]. These stages are fabricated with surface micro machining and based on multi-DOFs (non-compliant) hinges. The manipulators allow strokes in the order of 100 μm, but are more suited to micrometer resolution positioning than to nanometer resolution positioning due to the play and friction in the hinges. In [115], Zyvex presents various multi-DOFs manipulators for inspection inside a TEM or SEM. These are based on compliant mechanisms and driven by thermo-mechanical bimorph actuators made in a surface micro machining process.

Culpeper has designed a symmetric flexure mechanism for 6 DOFs manipulation [32] called HexFlex. In [24] a MEMS version of this mechanism is presented driven by twelve thermo-mechanical actuators arranged in 6 pairs. Each pair is capable of in-plane and out-of-plane deflection. The thermal actuators are of the hot-leg/cold-leg type and are applied in a stack with a layer of oxide in between (double SOI wafer). If both actuators in the stack are powered equally, the

deflection is in-plane. If the upper and lower actuator are powered differentially, a motion in the out-of-plane deflection results. Driving the actuators in the correct combination and ratio allows movement in all 6 DOFs. However, the system is over-actuated. The choice for this type of thermo-mechanical actuators allows relatively simple fabrication.

1.3.4 Assembly of MEMS devices

A combination of in-plane and out-of-plane manipulators can also be created by assembly. The technology for fabricating different types of actuators can be separated by using different wafers and bonding the wafers on top of one another. This is often called wafer scale assembly. Separation of devices, usually dicing, is done later. This way the clean room technology can be kept relatively simple. It is a mass products compatible technique of combining the functionality of several wafers which are manufactured and processed individually.

The literature describes many examples of wafer bonding of MEMS devices. A very nice example of assembly by wafer-bonding is a micro-turbine presented in [49], where a total of five wafers are stacked on top of each other. Another example where four wafers are stacked is given in [70] for a 2 DOFs tilt mirror with buried actuators. An assembled magnetic induction machine is presented in [3] and [30]. Here, a rotor structure is assembled on top of a molded coil structure. Zyvex has developed modular construction elements made from silicon that are assembled with the aid of compliant connectors and sockets [129]. This assembly requires a macroscopic external precision manipulator system. Using this this technique, a micro SEM is developed [110].

Application of assembly relies much on the allowable tolerances. The smallest error in the alignment in wafer-bonding, for instance, is often in the micrometer range. Of course this depends on the equipment used for the alignment. The modular assembly used by Zyvex requires the development of an external macro manipulator system. Without a system such as this assembly is too time consuming and expensive.

1.3.5 Conclusion regarding existing research

None of the literature studied in the survey described above reports characterization with respect to stability and resolution. As mentioned before, this is typical of literature on MEMS systems and understandable, since obtaining the required measurement data is very challenging. However, it is also typical that hardly any of

the references report anything on the desired stability and resolution and how these have an effect on the mechanism design. Designing for precision is clearly a rather new discipline within the field of MEMS. There is, however, no fundamental reason why positioning in MEMS cannot be accomplished on a nanometer level. In the macro scale world, precision machines are usually designed by using Precision Engineering.

1.4 Precision Engineering

Precision engineering is the research and development, design, manufacture and measurement of high accuracy components and systems. It is related to mechanical, electronic, optical and production engineering, physics, chemistry, and computer and materials science [2]. Historically, precision engineering is associated with techniques such as turning, milling, honing, lapping, polishing, grinding and electro discharge machining. Although the geometric uncertainty of these machining techniques might be at a sub-micron level, the feature size is usually not below the 0.1 millimeter range. For accurate manipulation, often the so-called design principles [8, 56, 62, 76, 116, 121, 122] are used in precision engineering. In chapter 2 certain design principles that are relevant for MEMS especially will be discussed in detail.

A design synthesis of precision engineering, a proven design philosophy for creating precision machines, and MEMS, a technology for miniaturization, could lead to precision micro-scale manipulators.

1.5 The goal of this research

The goal of this research is twofold:

- Design and manufacture a 6 DOFs MEMS-based manipulator with nanometer resolution positioning.

- Derive principle solutions for the synthesis between Design Principles and MEMS fabrication technology for multi DOFs precision manipulation in the micro domain.

A next generation Transmission Electron Microscope (TEM) sample manipulator requires extreme stability, a small size and up to 5 DOFs of positioning (for specifications see section 1.6). It is therefore a suitable carrier for this research. It only concerns the slow manipulation of objects with a mass even smaller than the mass of the manipulator. For this reason, there is no need to deliver (large) forces other than required to deflect the mechanism of the manipulator. This in contrast to an application like micro assembly, where relatively large forces are expected, which in general are not easily predictable (one could think of adhesive or thermal bonding).

Multi DOFs precision manipulation in the micro domain is frequently based on the use of exact kinematic constraint flexure based design. Exact kinematic constraint design leads to the predictable (deterministic) behavior of a mechanism. Flexure based design minimizes friction and wear, and avoids play. Minimizing the friction in combination with high stiffness of the actuated structure leads to a good positional repeatability of a manipulator. The actuation stiffness should be low for reducing strain energy storage and thus minimizing the actuator size. Exact kinematic constraint design, flexure mechanism and designing for high stiffness are topics typically originating from the design principles [8, 56, 62, 76, 116, 121, 122]. These principles need to be combined with MEMS fabrication techniques with their restricted geometric design freedom. Fabrication process solutions to allow for a large variety of mechanical functions are required, in combination with the particular process limitations and forthcoming design rules.

Packaging in MEMS is important, because it should provide a reliable interface with regard to the surroundings. In the case of the TEM an electrical and mechanical interface should not harm or influence the performance of the manipulator. However, in this research the focus is on designing and fabricating MEMS for precision manipulation in the micro domain. In this thesis, design principles for accurate positioning in MEMS are derived.

1.6 Specifications of a TEM sample manipulator

The specifications of a next generation TEM sample manipulator are set by FEI Company. First, the manipulator has to operate in an ultra high vacuum (10^{-8} – 10^{-9} Torr) and should not interfere with the E-beam. The maximum displacement should be enough to examine a sample. A semiconductor sample is typically 20 x 10 x 0.2 μm^3. Therefore, the *x*- and *y*-strokes of the manipulator should be about 20 μm.

Samples are shown in Appendix A Figure A.1. For the focusing of the electron beam, the z-stroke should be about 20 μm also. Once an area of interest is found on the sample, the TEM sample manipulator should be able to find this area again with a translational repeatability of about 10 nm. Extremely fine positioning is possible by manipulating the E-beam itself. For biological applications, tomography is used to generate a three-dimensional reconstruction out of slices or sections through a three-dimensional object obtained with the TEM. Two large tilt angles, one of +/- 70° and one of +/- 30°, are necessary to generate the data for 3D reconstruction. The two rotation axes might be any two perpendicular ones. For certain single crystal materials, the E-beam needs to be aligned with one of the crystal directions. The rotational repeatability needs to be better than 0.05°.

Some TEMs can be used in a scanning TEM (STEM) mode, where the beam can be rastered across the sample to form the image. The rastering of the beam across the sample makes it possible to determine the elemental composition of the sample. Taking a picture in the STEM mode can take up to half a minute. This fact, combined with the possible image resolution of 0.08 nm, results in an extreme stability requirement of 0.1 nm/min for the sample with respect to the E-beam. This stability should be reached within 10 s after the manipulation of the sample. Because of the high resolution capability of the TEM, sound and the vibrating surroundings cause the TEM column to vibrate, which could lead to unclear images. Therefore, the sample needs to be fixed dynamically stable to the column to result in small vibration amplitudes of the sample with respect to the column. A combination of a stiff coupling and a relatively small mass (high vibration mode frequencies) with regard to the manipulator is needed. Current manipulators show a first vibration mode frequency of several hundreds of Hz. For a next generation manipulator, a lowest vibration mode frequency of more than 1 kHz is required by FEI Company. A summary of the specifications is given in Table 1.2.

Property	**value**
Stroke x, y, z	±10 μm
Repeatability x, y, z	10 nm
Rotational stroke (any 2 DOFs)	1 x 30° & 1 x 70°
Rotational repeatability	0.05°
Stability *	0.1 nm/min
1st vibration mode frequency	> 1kHz

* Value should be reached within 10 seconds after manipulation.

Table 1.2: Specifications for a next generation TEM sample manipulator for FEI.

1.7 TEM sample manipulator concept

In this section, the decision to split the manipulator into two separate manipulators - a 2 DOFs large angle tilt stage and a 6 DOFs MEMS stage – will be explained. The loading concept of a sample and a manipulator in a TEM is briefly explained in Appendix B.

1.7.1 Two stage concept

Elastic mechanisms enable high positional repeatability through their deterministic behavior. Elastic mechanisms in general incorporate low hysteresis, no friction, no play and no wear [76]. All are necessary properties in precision manipulation. However, large rotation angles require non-elastic mechanisms, because the elastic hinges or leaf-springs deflected over a large displacement do not constrain any DOF, as will be explained in section 2.4. Therefore a separate tilt stage is to be developed which incorporates precision friction bearings for facilitating large rotations and high stiffness. A MEMS manipulator is mounted in the tilt-stage and offers fine positioning in up to 6 DOFs (Figure 1.3).

A rotation stage has been designed by Kruizinga [78] as part of the MAMS project, and is shown in Figure 1.3. It consists of two tilt axes perpendicular to each other (universal joint), resulting in a single rotation point. The *Rx*-axis has a stroke of +/-30°, the *Ry*-axis has a stroke of +/-70°. The stage rests on a ring on the lower TEM pole, and has a dimension smaller than the diameter of the entry which is used to insert the stage in the TEM. The actuation principle used is based on Inertia Sliding Motion [78] and shear piezo elements [101]. Due to the small steps of the piezo, the desired resolution of 0.05° is no problem. Sapphire on Silicon Nitride proved to be a low wear yet hard contact combination in high vacuum. The total energy produced in two full stroke operations of all rotation actuators, combined with the greatest thermal length, results in a maximum thermal drift of less than 0.05 nm. The first vibration mode frequency of the rotation stage is about 3.3 kHz. Two capacitive angular positions sensors are used for feedback.

In this thesis the design of the second stage, the small displacements MEMS-based stage, will be explained.

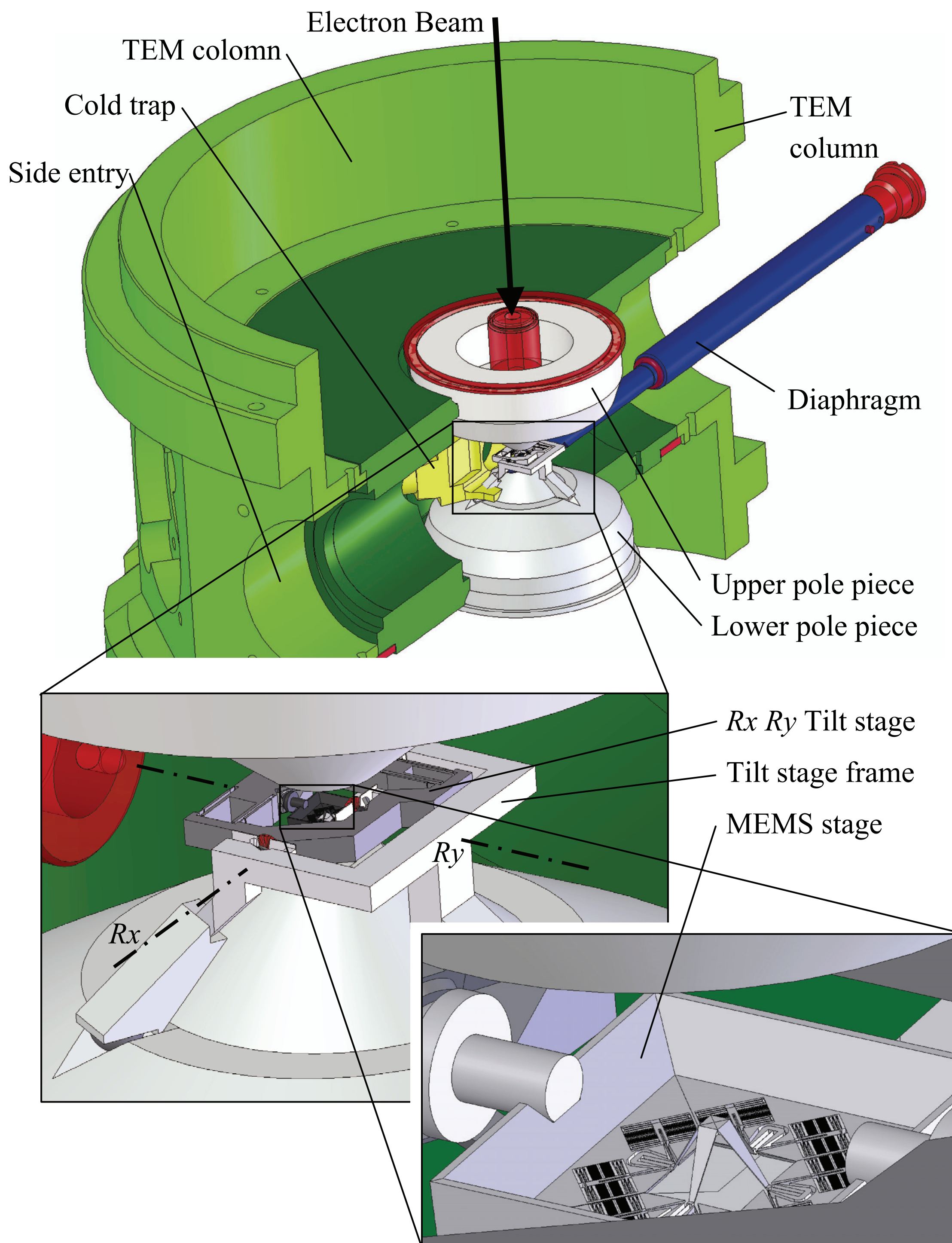

Figure 1.3: The two stage manipulation concept in the objective lens of the TEM column. The tilt stage is capable of making large rotations R_x and R_y. The MEMS stage is stacked on top of the tilt stage and is capable of making small displacements and rotations in 6 DOFs (Courtesy of FEI).

1.8 Thesis outline

The thesis consists of 4 main chapters, chapters 2, 3, 4 and 5. Appendix C elaborates on MEMS-based actuation, which is especially important in MEMS design. Appendix C may be considered an extra chapter.

In chapter 2 the use of design principles in MEMS design is discussed. Combining the knowledge of design principles and MEMS could lead to systems with more deterministic behavior, enhancing accurate positioning. However, the fabrication limitations of MEMS compromise the design principles. Therefore trade-offs need to be made.

In chapter 3 a MEMS-based mechatronic concept will be derived for 6 DOFs positioning. Three concepts, with trade-offs between fabrication and exact kinematic constraint structural design, are presented and evaluated. The total design process is the synthesis between these two.

In chapter 4 the concept for a parallel kinematic MEMS-based precision manipulator as proposed in chapter 3 will be detailed. The typical relatively large deformations of compliant mechanisms in MEMS result in relatively large displacements and large rigid body rotations. The actuator forces and displacements are derived. The first vibration mode frequencies, the stiffness and the buckling load of the manipulator are calculated.

In chapter 5 a fabricated and tested design of a relatively large force (0.5 mN) high precision MEMS clamping mechanism is presented. The clamping mechanism fixes the TEM sample manipulator unpowered once positioned. The elastic deformation of the clamp flexure has been optimized so as not to influence the TEM sample manipulator position during clamping. The device area of the mechanism has been optimized further by balancing the strain energy stored in the flexure elements with the actuator area.

In chapter 6 the conclusions are given. Research findings regarding the design and manufacture of a 6 DOFs MEMS-based manipulator and principle solutions for MEMS-based exact kinematic constraint design are discussed. The strong and weak points of MEMS-based precision manipulation are given.

In appendix C a ranking of actuation principles for actuators in micro dimensions is made. A numerical theoretical analysis of the four most relevant actuation principles - piezoelectric, thermal, electrostatic and magnetic actuators - for MEMS-based precision manipulation is summarized. The physical and practical limitations when designing actuators are briefly explained.

Chapter 2

DESIGN PRINCIPLES FOR MEMS-BASED COMPLIANT MECHANISMS

Combining design principles, a mature design philosophy for creating precision machines, and MEMS fabrication, a technology for miniaturization, could lead to micro systems with more deterministic behavior and enhanced accurate positioning. However, in MEMS design trade-offs need to be made between fabrication complexity and design principle requirements. In this chapter a brief background of MEMS design is presented. Basic design principles which are especially relevant for MEMS will be discussed. Special attention is given to leaf-spring behavior at large deflections, because compliant MEMS mechanisms often feature leaf-springs as elastic elements. Designs are presented for improved straight guiding with respect to the traditional folded flexure. This is important for the performance of comb-drive actuators.

2.1 Introduction

In the macro world the use of design principles for accurate positioning in precision engineering can be classified as a mature design philosophy. Several books from different sources exist that review (ultra) precision mechanism designs: Koster et al.[76] from Philips Electronics, Blanding [8] from Eastman Kodak Company, Slocum [121] and Hale [56], MIT, Jones [62], Wadham and Balliol Colleges, Oxford (UK), Smith and Chetwynd [122] from the University of North Carolina at Charlotte (USA) and the University of Warwick (UK). Schellekens et al. [116] from the Technical University of Eindhoven (NL) also show fundamental design principles. Combining the knowledge of design principles and MEMS could lead to systems with more deterministic behavior, enhancing accurate positioning. In MEMS design, however, the design principles are seldom used. In MEMS design

trade-offs need to be made between fabrication complexity and design principle requirements. In this chapter the fabrication limitations will be briefly discussed, pointing out the implications for the design principles. Compliant mechanisms play an important role in MEMS, and therefore leaf-springs are often applied. Exact kinematic constraint design with MEMS leaf-springs will be discussed. Straight guiding in MEMS is a second topic which has been researched because of its importance for the performance of comb-drive actuators.

2.2 Background of MEMS design

In this section a brief summary is given regarding MEMS design in general. The limited design freedom due to fabrication restrictions and limited actuator work density are discussed and the implications on MEMS design will be pointed out. The characteristics of typical MEMS materials will be compared to those of high strength steel and aluminum and low expansion Invar and Zerodur. The importance of compliant mechanism design for precision engineering in MEMS is briefly discussed. The typically fragile looking MEMS mechanisms, consisting of relatively long and slender elastic elements, will be briefly discussed based on scaling.

MEMS FABRICATION LIMITATIONS ON DESIGN

In short, the basic structuring in MEMS is achieved by depositing (adding) and etching (subtracting) material. A photolithographic step is used to transfer the pattern of a mask onto photosensitive material by selective exposure to a radiation source such as light (usually UV). This pattern transfer technology enables (sub) micron resolution feature sizes. A short background is presented, but it is by no means a complete overview. A more detailed explanation can be found in Madou [92].

For a designer in particular the layer thickness of deposited films is of interest, because the layers can be used as a mechanical structure. Depositing a film can be done roughly between a few nanometers and several tens of micrometers, depending on the material and process used. Commonly used deposition processes are: Sputtering, Electroplating, Physical Vapor Deposition (PVD) and Chemical Vapor Deposition (CVD). In the MESA$^+$ clean room Silicon rich Nitride (SiRN), SiO_2 and poly-silicon films are often used for structural layers. The maximum thickness is limited by stress due to the difference in the thermal expansion coefficient of Single Chrystal Silicon (SCS) and the deposited or grown layer.

SiRN can be deposited by Low Pressure Chemical Vapor Deposition (LPCVD) with a thickness ranging from 0.3 -2.5 μm. SiO_2 is often deposited by a LPCVD process in which tetraethoxysilane (TEOS) is used as a silicon source to deposit silicon dioxide with a thickness of 0.3-1.6 μm. Silicondioxide can also be thermally grown up to about 6 μm by oxidizing the wafer silicon. Poly-silicon deposited by LPCVD has a thickness of up to 5 μm. All layer thicknesses given are based on experiments performed at the $MESA^+$ clean room facility at the University of Twente.

There are basically two types of etching: wet and dry. In wet etching, the material is dissolved when immersed in a chemical solution. When dry etching is applied, the material is dissolved using reactive ions or a vapor phase etchant. A distinction needs to be made between isotropic and anisotropic etching. Some single crystal materials, such as silicon, exhibit anisotropic etching in certain chemicals. Anisotropic etching, in contrast to isotropic etching, means etching at different rates in different directions within the material. In the wet etching of silicon, a chemical such as potassium hydroxide (KOH) etches relatively slow in a certain crystal direction, perpendicular to the <111> direction in this case. It results in the appearance of <111> side walls during etching. In reactive ion etching (RIE), a combination of chemical reactions and physical bombardment of ions is used to remove material from a substrate. Deep reactive ion etching (DRIE), for example the Bosch process, makes use of RIE alternated with the deposition of a fluor carbon gas. The fluor carbon gas composition creates a film on the surface of the substrate. This film is etched by the physical part of the RIE, but only on the horizontal surfaces and not the sidewalls. Since the polymer dissolves very slowly in the chemical part of the etching, it builds up on the sidewalls and protects them from etching. As a result, etching aspect ratios of 1 to 20 can be achieved. The aspect ratio is the ratio of the width to the depth of an etched trench. Tapering is the unparallel in the depth etching of a trench. This tapering also limits the maximum thickness to height ratio of a leaf-spring to about 1 to 20.

Using SCS as a structural material for high aspect ratio devices requires DRIE. Because of Aspect Ratio Dependant Etching (ARDE) using DRIE, a design in general should not contain too much difference between the small and large gaps. The etching of wide gaps is faster than small gaps and may cause problems. Several processes exist to create high aspect ratio devices, but all suffer from ARDE. In the TWIN process for example, the release of the devices by isotropic underetch becomes difficult. The Twin process as described by Sarajlic [112] is a

bulk micro machining process resulting in a 35 μm thick structural layer. In another process, the back-etch release process [112], trenches run through the wafer. In that respect back-etched mechanisms are comparable to wire-spark eroded macro mechanisms. In the back-etch process devices are etched from the front side, and are released by etching the wafer from the backside. The release of wide gaps is earlier than the release of the small gaps because of the ARDE effect. As a result, the passivation of the wide gaps is exposed to a chemical isotropic etchant relatively long. In a Silicon On Insulator (SOI) wafer the oxide serves as an etch stop. However, the oxide layer is charged by the ions and therefore starts deflecting incoming ions. The side wall near the bottom is etched which is called footing or notching. In the manipulator design, chapter 4, and in the clamp design, chapter 5, an Aspect Ratio Compensated Etching (ARCE) recipe was used for Bosch etching of the devices. By using an ARCE recipe, the ARDE effect is reduced for certain trenches. Good results were obtained by limiting the gap variation between 3-20 μm in width. The depth varied between 42-52 μm.

The uncertainty of the etching and the resolution of the contact lithography mask limit the smallest feature size to about 2 μm. The overlay accuracy due to the alignment of one mask to the next is about 1 micron or more. The overall size (2-20 mm) to feature accuracy (2 μm) is limited to about $<10^4$.

In theory etching, depositing and pattern transfer using a mask can be performed over and over again. It is possible, for example, to combine in-plane (surface micro machined) with out-of-plane (bulk micro machined) leaf-springs. However, it requires a combination of process techniques that usually becomes complicated (current status). In MEMS, each step has influence on the previous steps and the previous steps have influence on the current one. Although each individual step might have been proven, the combination of steps is, in most cases, a unique sequence and therefore can (and usually will) display new difficulties. A general rule is: **Keep the process as simple as possible**. This does not necessarily also mean: Keep the number of mask steps as low as possible!

Currently the implications of the process limitations on structural design are:

- The maximum aspect ratio of gaps & trenches is 1:20.
- The maximum aspect ratio of out-of-plane DRIE leaf-springs is also about 1:20. These leaf-springs are built up out of single crystal silicon and therefore contain almost no stress.
- The smallest in-plane feature size is 2 µm.
- In-plane leaf-springs have a thickness between 0.3 and 10 µm, when built up out of poly, SiO_2 or SiRN. In contrast to SCS leaf-springs there is internal stress built up.
- Because of the ARDE effect, a device mask in general should not contain too much difference between small and large gaps (3-20µm).
- A limited overall size to feature accuracy of $<10^4$.
- Combining in-plane with out-of-plane leaf-springs requires a combination of process techniques that usually becomes complicated (current status).

MECHANISMS DESIGN IN MEMS

Freedom of motion in mechanisms in general is created by bearings (roller or friction) or by complaint elements. In MEMS, hinges (non-elastic) have been shown by, for example, Friedberger et al [50], Kiang et al [72] and Walraven [134]. Friedberger has measured the play to be between 1.3 and 2.0 µm, depending on the direction. Roller bearings have not been shown in MEMS yet. There are several problems in MEMS hinge and bearing fabrication. The first reason for this is that the overall size to feature accuracy is inadequate, resulting in inaccurate bearing shells and a relatively large play. The second reason is that the assembly, necessary for making a ball bearing for example, is difficult at micro scale. The third reason is that a controlled pre-tension is difficult to create. All together, for precision manipulation in MEMS, a mechanism has to rely on compliant elements as in general they incorporate low hysteresis, no friction, no play and no wear [76].

MEMS MATERIALS

In Table 2.1 the material properties of several structural materials for MEMS are compared to a strong aluminum alloy known as Al 7075T6, a strong steel alloy Stavax, a low thermal expansion nickel/iron alloy called Invar and an extremely low expansion ceramic known as Zerodur (used in wafer stages for example). The thermal parameters listed will be explained. α/λ reflects the sensitivity for expansion gradients due to spatial temperature gradients due to limited conductivity. $\rho\, Cp/\lambda$ is proportional to the time constant of the transient thermal behavior. Substances with low thermal time constant rapidly adjust their temperature to their surroundings, because they conduct heat quickly in comparison to their thermal 'bulk'.

SCS is a good construction material for micro devices because of its pureness, low hysteresis and high strength [100]. The pureness ensures that there are no inclusions in the material, which is necessary when etching thin (2 μm) features. In the single crystal structure there is no intergranular slip or movement of dislocations possible below 800°C, so there is no energy absorbing mechanism. Therefore, very high Q-factor mechanisms in a vacuum, which are mechanisms with extremely low damping, are possible. Q-factors exceeding 350,000 [54] have been reported. The low hysteresis implies that silicon-based elastic mechanisms, without external friction mechanisms, have no fundamental repeatability limiting mechanism. SCS is also insensitive to fatigue failure at high cyclic loads. However, SCS is very sensitive with regard to fracturing. SCS has a very high maximum tensile elongation compared to metals, although precautions need to be taken for notch stress concentration. Structural silicon mechanisms need rounding off at the edges to reduce the risk of notch fracture. Because of anisotropic behavior, the Young's modulus of SCS ranges from 130.4 to 169.7 GPa in the <100> and <110> direction, respectively. The Poisson's ratio ranges from 0.278 in the <100> direction to 0.061 and 0.362 in the <110> direction. SCS has two Poisson's ratios, which are exactly equal in the <100> direction. In general, the mechanical and thermal properties of SCS are good, as is shown in Table 2.1.

Property	Unit	SCS	SiO_2	Si_3N_4	Al 7075T6	Steel Stavax	Invar	Zerodur
Mechanical								
Young's modulus (E)	10^9 N/m^2	150	73	323	70	210	148	91
Yield strength (St)	10^9 N/m^2	7.0	8.4	14	0.48	1.61	0.25	0.80
Density (ρ)	kg/m^3	2400	2300	3100	2700	7800	8030	2530
Max. Strain (St/E)	%	4.7	11.5	4.3	0.7	0.8	0.2	0.1
Specific modulus (E/ρ)	10^6 m^2/s^2	63	32	104	26	27	18	36
Specific strength (St/ρ)	10^3 m^2/s^2	2917	3652	4516	178	206	31	32
Thermal								
Thermal expansion coeff. (α)	10^{-6} / K	2.6	0.55	2.8	25	11	1.2	0.05
Thermal cond. at 300K (λ)	W/(m K)	157	1.4	19	237	23	11	1.6
Specific heat (Cp)	J/(kg K)	700	1000	700	880	460	460	821
Expansion due to heat (α/λ)	10^{-9} m/W	17	393	147	105	478	109	31
Thermal diffuse time ($\rho Cp/\lambda$)	10^3 s/m^2	11	1643	114	10	156	336	1298

Table 2.1: Material properties of several structural materials for MEMS compared to a strong aluminum alloy, Al 7075T6, a strong steel alloy, Stavax, a low thermal expansion nickel/iron alloy, Invar and an extremely low expansion ceramic, Zerodur (used in wafer stages for example).

Other often used structural materials are silicon-rich nitride (SiRN) and silicon dioxide. All possess low expansion coefficient and high temperature stability when compared to metals in general. The amount of stress induced in the generally high temperature deposition or cleaning processes does not result in great stress or deterioration of the structural material when compared to metals in general. However, when the layer thickness increases, stress becomes the limiting factor.

SCALING

The often relatively large suspended geometries in MEMS, for example comb-drive shuttles, may look like terrible mechanical designs when the geometry dimensions are in the range of millimeters instead of micrometers. However, because of scaling effects this (macro) designer's intuition does not hold true.

Scaling is the rate at which a physical quantity changes when the 3D dimensions change proportionally. Scaling down to micron level feature size does not change the material properties significantly. The Young's modulus of single crystal silicon, for example, starts to change somewhere around feature sizes of 170 nm. Li et al [84] measured ultra thin resonant single crystalline silicon cantilevers ranging from 12 to 170 nm. The Young's modulus varied from 63-160 Nm^{-2}, respectively.

Scaling can be analyzed by studying the exponent of the length scale of linear dimensions r. An area then scales as: $A \sim r^2$. Mass scales as: $m \sim r^3$. With respect to stiffness, the compressive and tensile stiffness of a beam scale as:

$$c \sim \frac{E_y A}{l} \sim \frac{r^0 r^2}{r^1} = r^1 \tag{2.1}$$

where A is a cross-sectional area of the beam, l is the length of the beam and E_y is the Young's modulus. With respect to the bending stiffness of a beam the scaling is as follows:

$$c \sim \frac{E_y\, I}{l^3} \sim \frac{r^0 r^4}{r^3} = r^1 \tag{2.2}$$

where I is the area moment of inertia. Therefore both the tensile/compressive and the bending stiffness of beams scale as $c \sim r$. The vibration mode frequency then scales as:

$$fe \sim \sqrt{\frac{c}{m}} \sim \sqrt{\frac{r}{r^3}} \sim r^{-1} \tag{2.3}$$

The stress in (elastic) elements suspending a mass is a combination of tensile/compressive stress, bending stress, shear stress due to torsion and shear stress due to a shear force. With respect to tensile/compressive stress, the following holds true:

$$\sigma = \frac{F}{A} \sim \frac{m\, g}{A} \sim \frac{r^3 r^0}{r^2} = r \tag{2.4}$$

where F is the force due to the mass m, g is the gravitational acceleration and A is a cross-sectional area of the suspension. With respect to bending stress the scaling is as follows:

$$\sigma = \frac{0.5\, M\, t}{I} \sim \frac{r\, F\, t}{I} \sim \frac{r\, m\, g\, t}{I} \sim \frac{r^1\, r^3\, r^0\, r^1}{r^4} = r \tag{2.5}$$

where M is a bending moment caused by inertia and t is the thickness of an element suspending the mass. With respect to shear stress τ due to torsion:

$$\tau = \frac{M}{W_w} \sim \frac{r\,m\,g}{W_w} \sim \frac{r^1\,r^3\,r^0}{r^3} = r \tag{2.6}$$

where W_w is the section modulus for torsion. With respect to shear stress due to a shear force:

$$\tau = \frac{F}{A} \sim \frac{m\,g}{A} \sim \frac{r^3\,r^0}{r^2} = r \tag{2.7}$$

In all cases, the stress on (elastic) elements caused by inertia scales linearly. It means in the small scale world forces due to inertia cause relatively small stress on their suspending structures.

Another reason why micro mechanical structures are allowed to be relatively long and slender is because the buckling force is allowed to be relatively large. This can be shown by examining the scaling of the critical length l_{cr} with respect to the buckling of a compressively loaded beam. The critical length l_{cr} with respect to an external weight $m\,g$ scales as:

$$\begin{aligned} &F \sim \frac{E_y I}{l_{cr}^{\;2}} \quad ; \quad F \sim m\,g \\ &l_{cr} \sim \sqrt{\frac{E_y I}{m\,g}} \sim \sqrt{\frac{r^0 r^4}{r^3 r^0}} = r^{\frac{1}{2}} \end{aligned} \tag{2.8}$$

Therefore, with respect to buckling, beams may be relatively long and slender when loaded by a mass in the micro domain.

The combination of a low stress and a relatively large critical length allows relatively long and slender beams to suspend a mass in micro structures. The analogue with the animal kingdom is typical. Small animals, like spiders, have relatively long and slender legs loaded by a relatively inefficient bending stress [76]. In contrast large animals, like elephants, have relatively thick legs loaded mainly by an efficient compressive stress.

With respect to shock the maximum tolerable acceleration *a* scales as:

$$a \sim \frac{F}{m} \sim \frac{\sigma A}{m} \sim r^{-1} \qquad (2.9)$$

Micro structures can withstand large accelerations. However, shock can be a problem due to notch effects, which reduce the tolerable stress in SCS. It must be pointed out here that the real forces that may destruct devices are usually external forces stemming from: viscous forces during processing, wire bonding, probing and assembly.

Scaling also has an effect on thermal diffusion times. The diffusion time becomes small according to Elwenspoek [45]:

$$\tau \sim RC \sim r^{2} \qquad (2.10)$$

where the thermal resistance $R \sim r^{-1}$ and the thermal capacitance $C \sim r^{3}$ (see equations 4.38 and 4.39).

In the micro domain surface, forces become relatively large and adhesion is a significant force between two bodies making contact. The bodies in MEMS are often made of the same material which generally implies extra adhesion. Stiction or fusion bonding can become a problem for positioning. Stiction is the threshold of force parallel to the contact surface required to overcome static cohesion. Stiction is a threshold, not a continuous force.

Scaling down affects the signal to noise ratio of sensors badly, because in general the signal decreases more than the noise floor decreases. For example, the charge moved in capacitive or piezo sensors due to a certain displacement becomes small when scaling down, but the noise floor generated by the amplifier electronics, interference of the surroundings and parasitic capacitances does not change that much.

In general, stiffness scales linearly (equations 2.1 and 2.2). This would imply that the energy storage of a complaint mechanism would scale with the third power, which is equal to the work density scaling of electrostatic, thermal and piezo actuators (Appendix C, Figure C.8). However, in a compliant mechanism the (low) stiffness in the complaint actuation direction scales less than linear. This is beause the smallest feature size in MEMS limits the leaf-spring thickness to 2 μm.

Therefore, the leaf-spring thickness has scaled less than linear. In addition, the work density of typical electrostatic and thermal MEMS actuators is low compared to macro scale electromagnetic actuators. Given these two reasons, elastic elements in MEMS are made relatively long because the compliant energy storage is relatively large compared to the deliverable energy of MEMS actuators.

When scaling down to the sub-millimeter size and smallest feature size the micron level designers have to be aware of:

- Ratio: deliverable actuator work / compliant energy stored is low.
- Accuracy of sensing limited.
- Stiction.
- Stress due to inertia in a suspension is low.
- High vibration mode frequencies (even with compromised leaf-springs).
- Influence of thermal cross-talk is relatively small.
- Physical laws do not change.

2.3 Design principles with respect to MEMS design

The design principles for accurate positioning [8, 56, 62, 76, 116, 121, 122], although originating from the macro world, are also valid in the micro domain. As discussed earlier, applying them in MEMS can be troublesome because of process limitations. A few Design Principles which are especially relevant in MEMS design will be discussed:

- Determinism

Deterministic behavior is when machines obey cause and effect relationships that are within our ability to understand and therefore control. This rule promotes the use of compliant mechanisms because of their perfectly repeatable behavior. Friction during actuation, for example, should be minimized because it leads to virtual play [76]. It is therefore difficult to control the position of an object containing friction.

- Exact kinematic constraint design

The key concept of exact kinematic constraint design is a one-to-one relationship between applied constraints and compliant (or free) degrees-of-freedom [56]. A DOF is a motion in a relatively compliant (or free) direction in comparison to other stiff directions. There are at least three main motivations for the exact kinematic constraint design philosophy:

1) Internal stress is minimized by exact kinematic constraint design. A component that must remain stable at nanometers will not do so if it is joined in an over-constraint way to a structure that deforms by micrometers.

2) Behavior under load, mechanical or thermal, becomes highly predictable.

3) A divergence from exact kinematic constraint design often leads to an increase in cost because fitting parts together then relies on manufacturing tolerances.

It might be the case (and often is) that the best design is not an exact kinematic constraint design. However, it is a good starting point so that the implications of non-exact kinematic constraint design are fully considered and expected.

- Symmetry

Symmetry can help to reduce or even cancel errors in certain directions due to thermal or dynamic noise sources [76].

These design principles hold true in the micro domain also. However, due to fabrication limitations the design freedom is restricted in MEMS.

DESIGN FREEDOM IS RESTRICTED BY FABRICATION IN MEMS

In MEMS, mechanisms are often compromised with respect to exact kinematic constraint design because of fabrication limitations. It is difficult to constrain the exact number of DOFs needed. This is due to the fact that the geometry of “leaf-springs” in MEMS often does not result in constraining 3 DOFs per leaf-spring. This is because the ability to structure in three dimensions is limited. (The DOFs that a leaf-spring constrains in MEMS will be investigated in section 2.4.1.) Another example of fabrication limitations on exact kinematic constraint design is when exactly 1 compliant DOF, the rotation around an axis in the plane of the

wafer, is needed. An example of this is the suspension of deflection mirrors. Two types of mirror suspension are generally implemented in MEMS:

The first type of mirror suspension has three unconstraint DOFs and has been implemented in the Digital Mirror Device (DMD) [71]. However, only one DOF is intended to be compliant, which is the rotation *ry* schematically shown in Figure 2.1a. The two leaf-springs together effectively constrain only three DOFs, *x, y* and *rz*, which means the suspension is under-constrained times two. Two DOFs, which should have been constrained, are *z* and *rx*. The resulting uncontrolled movements of the mirror, especially *rx* movements, influence the beam path. However, in the DMD a lens with its focal point at the mirror surface projects the beam at the same spot regardless of small errors on the mirror angle r_x. Therefore, the DMD as a total design functions even though mechanically another suspension might be preferable.

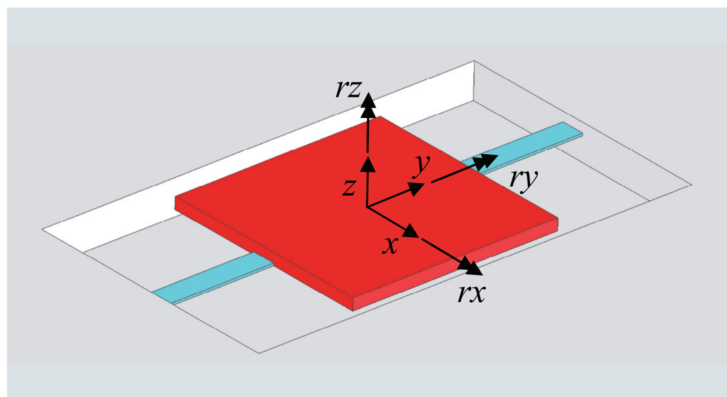

Figure 2.1a: Mirror suspension consisting of two horizontal leaf-springs. The mirror is under-constrained in two DOFs (z and rx).

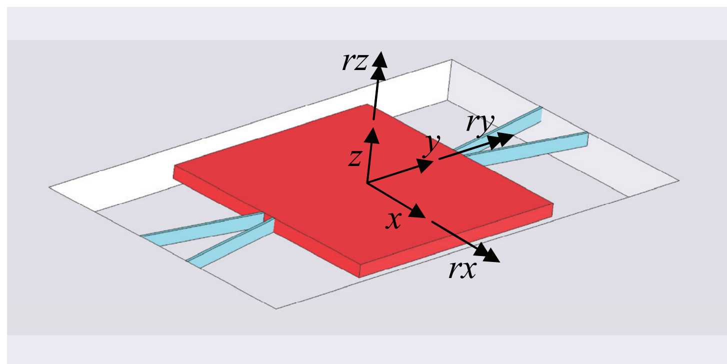

Figure 2.1b: Mirror suspension consisting of four vertical leaf-springs. The rotation ry is not very compliant compared to the constraint DOFs.

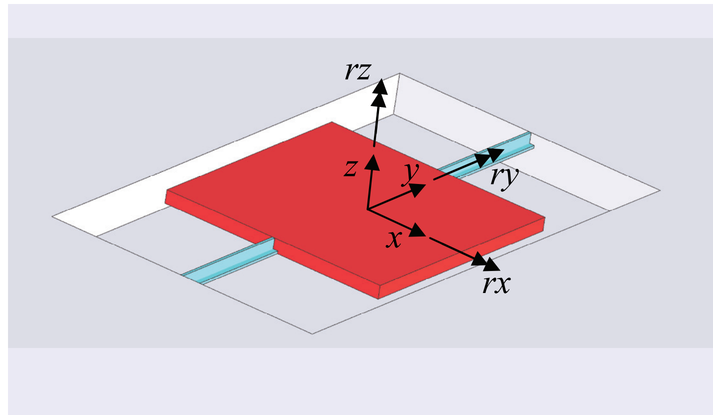

Figure 2.1c: T-shaped torsion hinge suspension consisting of 2 x 2 perpendicular leaf-springs results in exactly 1 compliant DOF: ry.

The second type of mirror suspension has two extra leaf-springs for constraining the two unwanted compliant DOFs, which is shown schematically in Figure 2.1b. An example is the out-of-plane stage as demonstrated by de Jong [63]. However, the stiffness in the originally intended compliant direction, *ry*, increases considerably. A mechanical solution is presented in Figure 2.1c, Figure 3.10 and also by de Jong [63]. A T-shaped torsion hinge suspension leaves *ry* compliant and the other DOFs relatively stiff. The two perpendicular leaf-springs can be made by a combination of DRIE and surface micro machining or TWIN [112] process. However, this combination of processes complicates fabrication significantly. This mechanical solution, therefore, is not described in literature regarding MEMS.

In general, the restrictions of the fabrication processes necessitate trade-offs in MEMS.

Compromising exact kinematic constraint design in MEMS

As mentioned in the previous section, exact kinematic constraint design is often compromised in MEMS because of fabrication limitations. Therefore, solutions for certain requirements such as stiffness or robustness are necessary, compromising the exact kinematic constraint design even more:

1. Creating stiffness can require an over-constraint design.

An example is the over-constraint design of 4 folded flexures suspending a shuttle, as shown in Figures 2.10 and 2.11. Two folded flexures suspending the shuttle would theoretically be enough. However, because of the restricted leaf-spring height in the out-of-plane direction (of the wafer), stiffness is low. Adding two

folded flexures increases the out-of-plane stiffness 2-8 times, depending on the design, while the stiffness in the actuation direction is increased only twofold.

2. For robustness, extra strength is needed by over-constraint design.

Although static and dynamic forces created internally in a system may be small, external forces created by processing especially can be large. An example are the viscous forces created by liquids during etching or cleaning. In general, over-constraint design increases internal stress. However, it can effectively reduce stress created by external forces. An example of this is the previously mentioned shuttle suspended by 4 folded flexures (Figures 2.10 and 2.11). Another example is the suspension of a clamp, as shown in Figure 5.2, which has an extra out-of-plane reinforcement by a folded leaf-spring.

3. Deformation as a result of stress can be compensated by symmetric design.

In surface micro machining the deposition of a thin film, such as polysilicon, results in stress within the structural layer. An example where the stress results in misalignment is a shuttle suspension consisting of two polysilicon folded flexures. The shuttle fingers have to stay aligned with the comb fingers of a comb-drive. By adding two folded flexures in a symmetric set-up as shown in Figure 2.10, the shuttle stays aligned better, although the flexures are subject to extra stress.

4. A symmetric suspension design for better dynamics

The suspension shown in Figure 2.1a consists of two co-linear leaf-springs. Using the exact kinematic constraint design principles, one leaf-spring would be enough to restrict exactly the same DOFs, *x, y, rz*. However, actuation forces excite deformation vibration modes which need to be restricted. Symmetry effectively changes the vibration modes to less harmful ones. In this case, symmetry forces an over-constraint design. Although compliant in the out-of-plane direction for small deformation, the two leaf-springs together effectively constrain large out-of-plane movements due to non-linear stiffening.

5. A symmetric suspension design for better thermodynamics

The location of a thermal center [76] can be better defined by using symmetry. In turn, the self-canceling displacement also holds true for dynamic thermal response.

Compromising exact kinematic constraint design has consequences that a designer should be aware of.

CONSEQUENCES OF COMPROMISING EXACT KINEMATIC CONSTRAINT DESIGN

The consequences of not exact kinematic constraint design for MEMS are the same as in the macro world. Over-constraint design in general leads to:

- Non-linear stiffness behavior of suspensions, sometimes called stiffening
- Coupling of deformation of the surroundings, for example a frame, into stress of an over-constraint suspended micro device. This changes the stiffness and dynamic behavior of a system.
- Stress build-up due to heat sources
- Unpredictable behavior under thermal load

Under-constraint design leads to:

- Vibrations in unwanted compliant directions
- Low stiffness in unconstraint directions

2.4 Influence of a large deflection on leaf-spring behavior

Precision mechanisms in MEMS usually consist of compliant mechanisms. These mechanisms themselves are mainly built up from leaf-springs and parts that are intended to be rigid bodies. The stiffness behavior of leaf-springs is important because they are used to constrain certain directions and leave others compliant. In the case of a comb-drive actuator, for example, the suspension stiffness needs to be high to prevent pull-in (typical instability of a comb-drive actuator, Appendix C, C.3.1). At the same time, the actuation stiffness needs to be low for minimizing energy storage in the actuation direction. There are two significant differences between the behavior of leaf-springs in MEMS and the behavior of leaf-springs at the macro scale:

1) The height of a leaf-spring is often restricted in MEMS.
2) The drive stiffness, the stiffness which a leaf-spring experiences in the actuation direction as part of a mechanism in MEMS, is low. In the macro world this stiffness is usually high because the motion in this direction is controlled, is driven by a stiff actuator or is driven by a stiff drive system like a lead-screw. In MEMS the drive stiffness is low especially with regard to electrostatic comb-drives and Lorentz actuators. In the case of thermal or piezo actuators with large transmission ratios the drive stiffness can be low as well.

Both differences influence the stiffness of the leaf-springs significantly. This will be explained in the next paragraphs.

2.4.1 Behavior of height restricted leaf-springs

The height restriction of a leaf-spring in MEMS influences the behavior of a leaf-spring. A leaf-spring is generally described as an elastic element, a plate, which constrains 3 DOFs [76]. In comparison to the three compliant deformations modes, the translation in the longitudinal or *x*-direction (Figure 2.2) and the two bending deformation modes in the *xz*-plane, the *z*-translation and *ry*-rotation, are relatively stiff. The three compliant deformation modes are torsion (*rx*-rotation) and the two bending deformation modes in the *xy*-plane, the *y*-translation and *rz*-rotation.

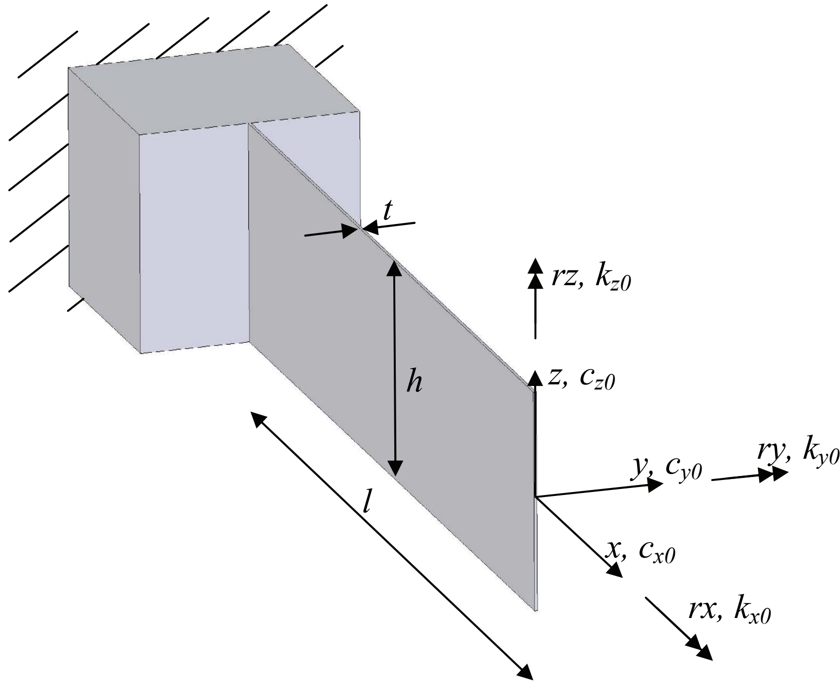

Figure 2.2: Undeformed leaf-spring. The cross-sectional area of the movable end of the leaf-spring remains undeformed. c_{x0}, c_{y0}, c_{z0} are the translational and k_{x0}, k_{y0}, k_{z0} the rotational stiffnesses of the leaf-spring in undeformed flat state. c_{x0} and k_{x0} are also known as the longitudinal and torsional stiffness, respectively. A flat leaf-spring constrains three Degrees-of-Freedom, meaning the directions x, z, ry are stiff in relation to the other three, y, rx, rz.

In MEMS, however, there are two reasons why a leaf-spring will not always constrain 3 DOFs. First, the implemented processes often limit the height of leaf-springs, resulting in compromised *ry*- and *z*-stiffness. Secondly, the relatively large displacements often used in MEMS significantly decrease the stiffness of the constraint DOFs due to geometric non-linearity. To investigate both effects, calculations are performed on three differently dimensioned leaf-springs which are loaded by a moment around the *rz*-direction. However, the deflection of leaf-springs in general is caused by a combination of a bending moment and a transverse force. The coordinate system is attached to the free end of the leaf-spring and rotates according to the possibly large rotation *rz*. At a certain rotation of interest $rz = Rz$, the coordinate system is fixed.

The free end is, at that instance, loaded by the moment necessary to create rotation *Rz*. Small forces or moments are superimposed on the moment to create *Rz* and the deflection is monitored in the directions as is shown in Figure 2.3. The stiffnesses of the end of the leaf-spring can then be defined as:

$$c_x = \frac{dF_x}{dx}, c_y = \frac{dF_y}{dy}, c_z = \frac{dF_z}{dz} \qquad (2.11)$$

$$k_x = \frac{dM_x}{drx}, k_y = \frac{dM_y}{dry}, k_z = \frac{dM_z}{drz} \qquad (2.12)$$

where, for example, dF_x is an infinitesimal small force in the x-direction and dx is the resulting small displacement in the x-direction.

To investigate the effect of a restricted height on the behavior of leaf-springs, three differently fabricated leaf-springs with typical corresponding geometrical ratios are examined. A macro sheet metal leaf-spring is compared to a Deep Reactive Ion Etched (DRIE) leaf-spring and a surface micro machined leaf-spring. Table 2.2 lists the dimensionless geometry. The geometry is represented dimensionless because the calculated stiffness and deflection are also shown dimensionless. As a consequence, the results hold for any scale (gravity not taken into account). Intuitively, a designer would expect the macro leaf-spring dimensions to be in mm, whereas the DRIE and surface micro machined leaf-spring typically could be read in μm.

	l	*h*	*t*	*l/h*	*l/t*	*h/t*	$h^2/(l\,t)$
Macro sheet metal	600	150	2	4	300	75	18.8
DRIE	600	35	2	17.1	300	17.5	1.0
Surface micro machined	600	5	2	120	300	2.5	0.0021

Table 2.2: Deflected leaf-spring by a moment. The leaf-spring's dimensionless geometry represents typical ratios of length to height to thickness found in three different fabrication methods. These ratios are used to create Figures 2.4, 2.5 and 2.6.

For the modeling of the relatively large deflections of leaf-springs SPACAR (Appendix F) was used. SPACAR is based on a non-linear finite element approach. The SPACAR beam element can be used to model a leaf-spring accurately if two conditions are met:

l >>h

The shear stress due to in-plane bending can be disregarded. For leaf-springs with $l = 4h$, the error of in-plane stiffness due to disregarding of shear stiffness is about 4%, according to Koster [76].

$h^2/(l\ t) \leq 1$

The out-of-plane bending stiffness is not increased considerably by transverse strain in the beams cross-section due to Poisson's contraction. As an example, Van Eijk [43] shows that the Poisson's contraction adds another 6% bending stiffness to a purely geometrical model for a straight guided leaf-spring with geometric ratio $h^2/(l\ t) = 25$ at a deflection $y/l = 0.10$. The implications of this are that the surface micro machined and DRIE leaf-spring are modeled well by SPACAR (Table 2.2 gives the $h^2/(l\ t)$ ratio). The SPACAR result for a macro sheet metal leaf-spring will be less accurate.

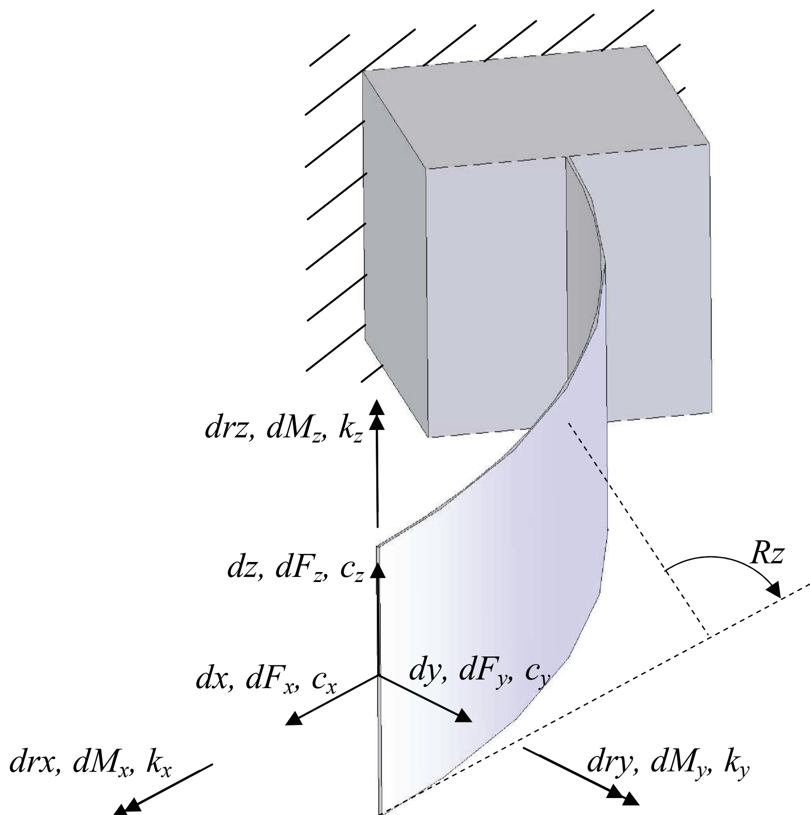

Figure 2.3: Deflected leaf-spring. The coordinate system is fixed at a certain Rz, after first traveling with the free end of the leaf-spring. The linearized stiffnesses are calculated in 6 DOFs for this rotation Rz.

Although the abovementioned conditions are not always met in the cases presented in Table 2.2, the errors made in the calculation of the stiffness ratios presented in Figures 2.4, 2.5 and 2.6 will not be large. The stiffness in the Figures is normed. The highest translational and rotational stiffness at zero deflection is set at 1. The other stiffnesses are scaled accordingly.

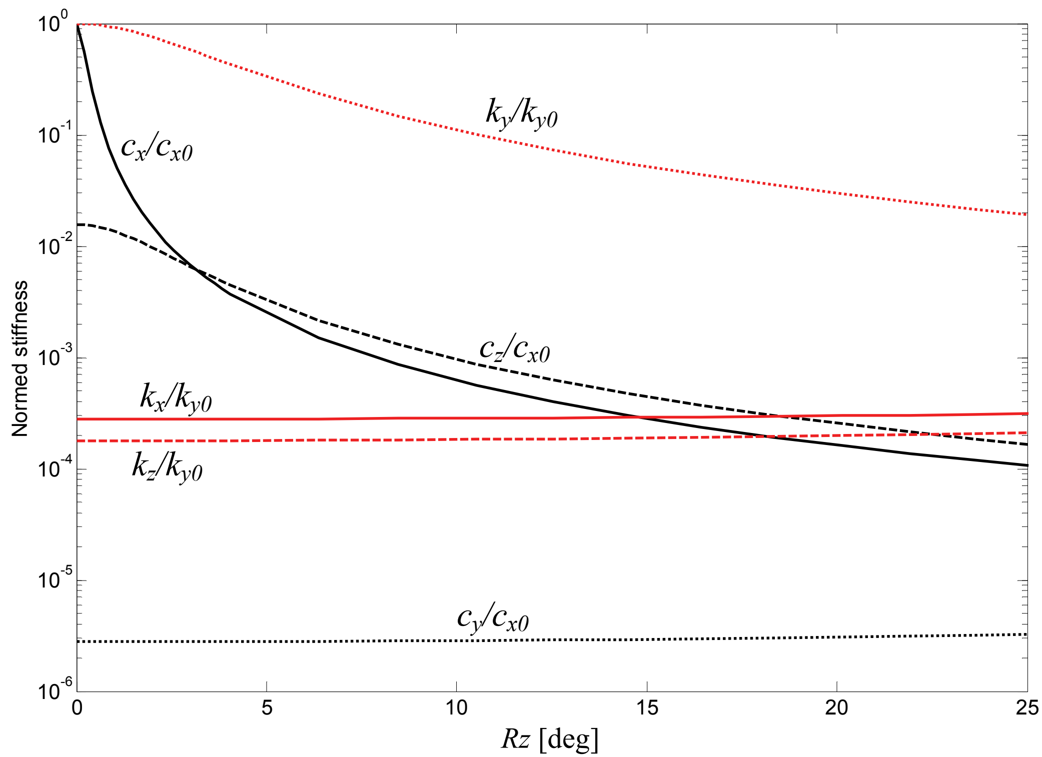

Figure 2.4: Normed stiffnesses of a macro sheet metal leaf-spring that is deflected in the Rz-direction. The relative dimension are: l/h = 4, l/t = 300, h/t = 75.

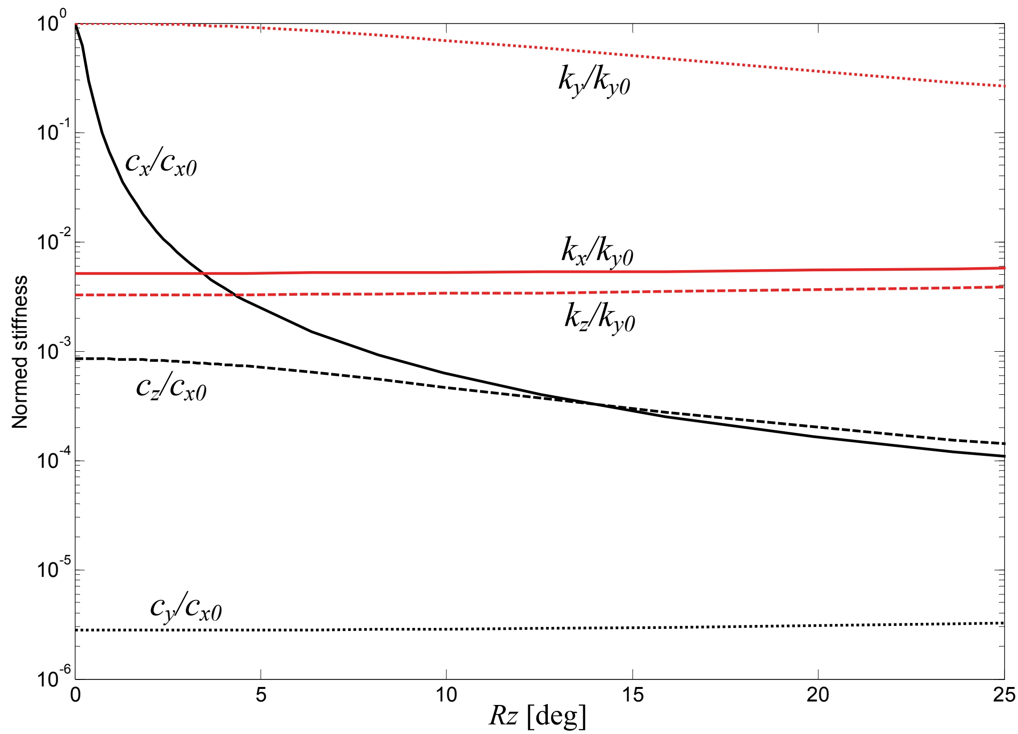

Figure 2.5: Normed stiffnesses of a DRIE leaf-springthat is deflected in the Rz-direction. The relative dimension are: l/h = 17.1, l/t = 300, h/t = 17.5.

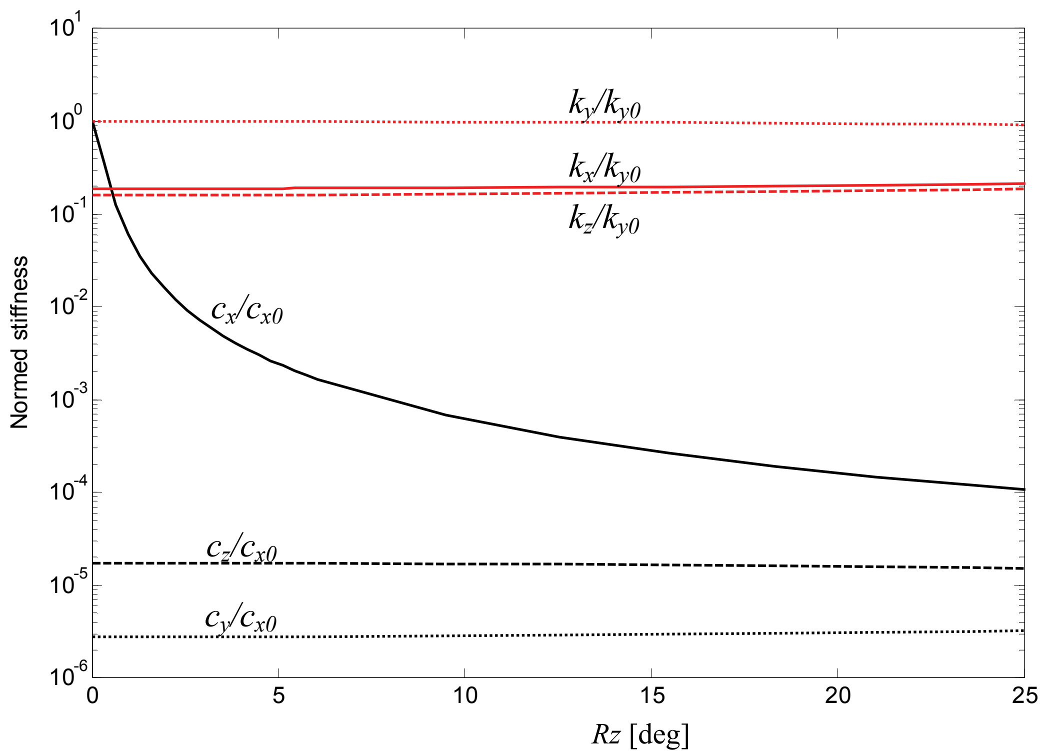

Figure 2.6: Normed stiffnesses of a surface micro machined "leaf-spring" that is deflected in the Rz-direction. The relative dimension are: l/h = 120, l/t = 300, h/t = 2.5.

Based on the Figures 2.4, 2.5 and 2.6 several conclusions can be drawn regarding the influence of *l/h* on the stiffness of leaf-springs at varying deflections:

- In all cases, the c_x-stiffness decreases the most during deflection in the *rz*-direction.
- k_x, k_z and c_y, the stiffnesses in the compliant DOFs, are more or less “constant” during deflection.
- Both the initial stiffness c_{z0} and k_{y0} and the decrease of c_z and k_y due to deflection in the *rz*-direction depend on the *l/h* ratio.
- Normed stiffnesses c_x/c_{x0} and c_y/c_{x0} are not influenced by *h* for any deflection, whereas c_z/c_{x0} changes.
- Leaf-springs with a high *h/t* ratio show a greater decrease in c_z- and k_y-stiffness during deflection in the *rz*-direction than leaf-springs with a small *h/t*. This can be explained as follows: during deflection the c_z- and k_y-stiffness become a series stiffness of bending and torsion stiffness. A large *h/t* results in a relatively high c_{z0}- and k_{y0}-stiffness in relation to torsion stiffness k_x, as the bending stiffness is proportional to t^1l^3 and the torsion stiffness is more or less proportional to t^3h^1 for these types of cross-sections. The high c_{z0}- and k_{y0}-stiffness of leaf-springs with a high *h/t* ratio is compromised more by the torsion stiffness at deflection than that of leaf-springs with a small *h/t.*
- A macro leaf-spring initially constrains 3 DOFs. The stiffness in the constraint directions is more than 3.5 orders higher then the stiffness in the compliant directions. At 10 degrees of deflection the constraint/compliant stiffness ratio is still 2.5 orders, usually enough to still consider it as constraining 3 DOFs.
- A Bosch etched leaf-spring can be seen as a leaf-spring constraining 3 DOFs up to about 10 degrees of rotation with a constraint/compliant stiffness ratio of 2 orders.
- Surface micro machined “leaf-springs” behave like slender beams constraining only 1 DOF for deflections up to about 10 degrees of rotation. Therefore, the term “leaf-spring” should be replaced by the term “beam” in the case of surface micro machined leaf-springs.
- In all cases, the stiffnesses in the “constraint” directions become less for large rotations in the *Rz*-direction.

When designing compliant mechanisms on any scale, one should be concerned with the loss of stiffness due to deflection. A second effect which is especially important in MEMS is the changed leaf-spring behavior due to the limited height of leaf-springs.

2.4.2 Influence of drive stiffness on leaf-spring behavior

Leaf-springs are often used in straight guiding mechanisms such as four bar parallel leaf-spring mechanisms [76]. A typical example in MEMS is a comb-drive straight guidance. The bending moment in the leaf-spring is zero exactly in the middle of the length direction of the leaf-spring. Therefore reinforcing the middle section does not increase the bending stiffness c_y as much as it increases the longitudinal stiffness c_x (Figure 2.7). The leaf-spring dimensions are set at *l* for length and *t* for thickness. A leaf-spring, prismatic or reinforced, is clamped at one end and constrained for rotation *rz* at the other. The reinforced section is often set at 5/7th of the total leaf-spring length. In this experiment, the reinforcement is considered to be rigid. In section 2.5.2 the reinforcement thickness influence on the overall stiffness will be studied in more detail.

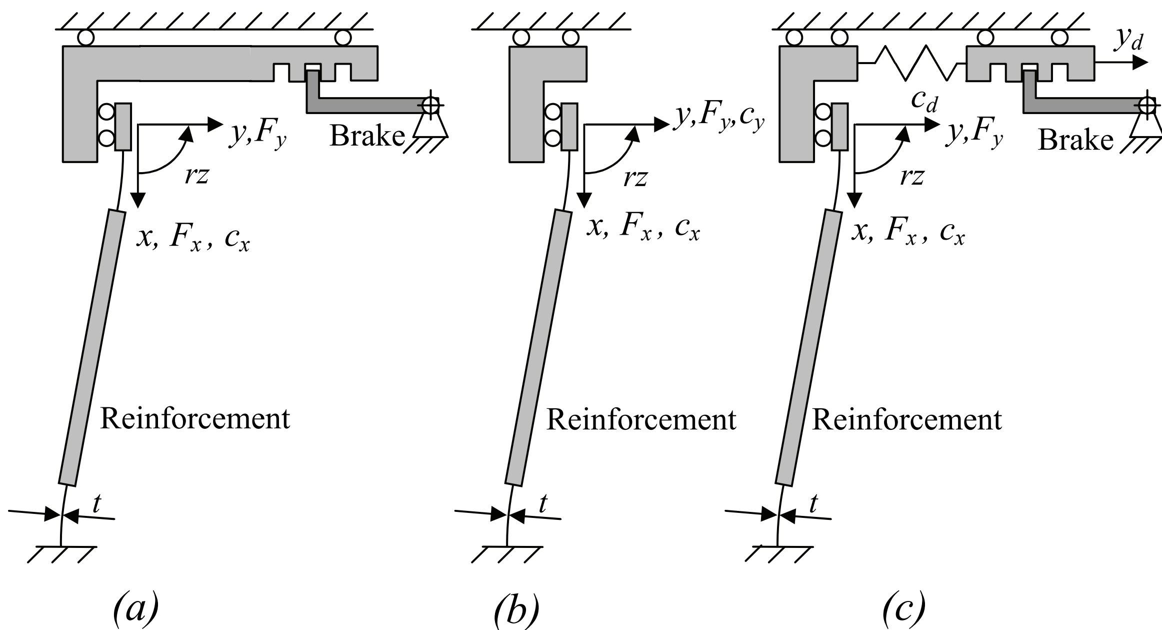

Figure 2.7: The drive stiffness. (a) In macro mechanisms the y-direction is usually constrained. (b) In MEMS mechanisms the y-direction is not constrained. (c) The y-direction is coupled to its surroundings by the drivestiffness c_d.

Figure 2.7a represents a model of a typical macro mechanism. The c_x-stiffness of a leaf-spring is calculated while the leaf-spring is constrained at the actuated end. First, the leaf-spring is loaded by a force in y-direction with the brake released. Secondly, the brake is activated, so the y-direction is constrained. The leaf-spring is then loaded by a force in the x-direction. The stiffness c_x is calculated by dividing the x-force by the x-displacement. This c_x-stiffness decreases during deflection in the y-direction. The situation of Figure 2.7a has been modeled by Van Eijk [43]. The model is appropriate if the y-direction is constrained by a very stiff actuator system. This could be a lead screw or a "stiff" controlled system or a brake.

In MEMS, however, the stiffness in the y-direction is often solely determined by the stiffness of the leaf-spring c_y. This situation is shown in Figure 2.7b. A force in the y-direction causes a deflection in the y-direction. However, loading a force in the x-direction causes the leaf-spring to deflect mainly in the y-direction and only a small x-displacement results. The leaf-spring describes an arc-like curve.

A general case is shown in Figure 2.7c, in which a so-called "drive stiffness" c_d couples the leaf-spring to the ground. There stiffness c_d acts in parallel with c_y on the leaf-spring end. The stiffness c_y is the stiffness of the leaf-spring only. The ratio c_x / c_{x0} at the relative displacement y/t has been calculated for different relative drive-stiffnesses c_d / c_y for reinforced and prismatic beams. The results are shown in Figure 2.8. In this figure c_{x0} is the stiffness in the x-direction when there is no deflection. Legtenberg [81] has calculated the c_x-stiffness with respect to the y-displacement for the situation shown in Figure 2.7b. The results are equivalent to Figure 2.8 with $c_d = 0$. Van Eijk's [43] results regarding the longitudinal stiffness with respect to the y-displacement are similar to the results shown in Figure 2.8 if $c_d / c_y = \infty$.

The stiffness c_{x0} of a leaf-spring being rigidly reinforced over $5/7^{th}$ of the total length, is 3.5 times larger than c_{x0} of a prismatic leaf-spring. This stiffness ratio increases during deflection in the y-direction for $c_d / c_y > 100$. The reason is that by constraining the y-displacement the leaf-spring is forced in a "buckling like bending-mode" when loaded in the x-direction. Reinforcement stiffens this "buckling like bending-mode" effectively, as the buckling length is shortened.

The c_x-stiffness of a reinforced leaf-spring is always higher than that of a prismatic leaf-spring with the same geometry (except for the reinforcement) and deflection. The c_{x0}-stiffness is increased by a factor of 3.5 due to reinforcing when there is no deflection. However, for a leaf-spring with $c_d / c_y < 100$ the factor becomes less during deflection in the y-direction. For the situation $c_d / c_y = 0$ at a relative deflection $y/t = 10$ the c_x-stiffness of a reinforced leaf-spring is only 1.9 greater than the c_x-stiffness of a prismatic leaf-spring. This in contrast to the same situation for $c_d / c_y = \infty$, where the c_x-stiffness increase factor due to reinforcement is 6.1. The reason is that loading a leaf-spring with $c_d / c_y << 100$ in the x-direction causes the leaf-spring to deflect mainly in the y-direction. The movement in the x-direction is a second-order effect. Therefore, the bending stiffness c_y dominates c_x for large y/t for $c_d / c_y << 100$. The c_y-stiffness of the reinforced leaf-spring, which is almost constant during deflection (van Eijk[43] and section 2.5.3), is however only 58% greater than that of a prismatic leaf-spring. The c_x-stiffness increase factor due to a rigid reinforcement of a leaf-spring with $c_d / c_y << 100$ at large y/t will therefore be closer to 1.58 than 3.5. For the situation $c_d / c_y < 10$, $y/t = 10$ the c_x-stiffness increase factor < 2.0, while the c_y-stiffness increase factor is 1.58. Therefore, the ratio $c_x / c_y < 1.26$, benefits marginally from reinforcement, whereas the actuation compliance is jeopardized by a factor 1.58.

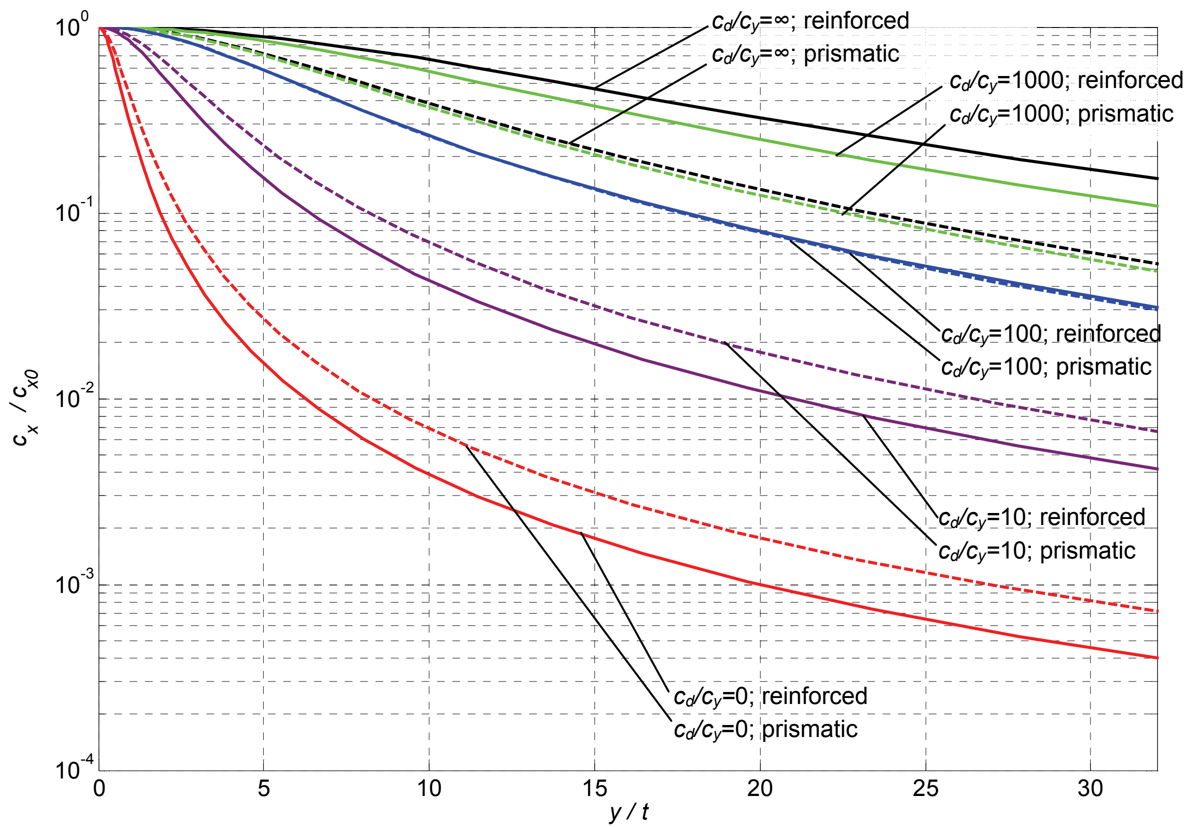

Figure 2.8: The relative longitudinal stiffness c_x / c_{x0} as a function of the relative deflection y/t in relation to the drive stiffness for prismatic and for reinforced leaf-springs. The reinforcement is modeled rigid and has a length $5/7^{th}$ of the total leaf-spring length.

Several conclusions can be drawn:

- The c_x-stiffness decreases substantially with the y-deflection.
- The smaller c_d/c_y, the greater the decrease of c_x-stiffness due to deflection.
- Reinforcing leaf-springs in a system with a $c_d/c_y > 1000$ results in a great increase of the ratio c_x/c_y at deflection.
- Reinforcing leaf-springs in a system with a $c_d/c_y < 10$ results in a small increase of the ratio c_x/c_y at deflections $y/t > 5$. However, the increased c_y-stiffness requires 58% larger actuator forces.

2.5 Straight guiding in MEMS

In MEMS, straight guiding mechanisms are often used to straight guide the shuttle of a comb-drive actuator. Many types of straight guiding mechanisms have been used. A brief overview is presented. Leaf-springs for straight guiding at the macro scale are often reinforced to increase the longitudinal to actuation stiffness ratio. The influence of reinforcing the leaf-springs is researched for typical MEMS geometry leaf-springs in a folded flexure. The non-linearity of the actuation compliance is studied. It will be shown that the longitudinal stiffness of a folded flexure decreases rapidly at increasingly large deflections. Therefore, two improved MEMS-based straight guiding mechanisms will be presented.

2.5.1 Types of straight guiding

In MEMS, straight guiding mechanisms are often used to straight guide the shuttle of a comb-drive actuator (see Figure 2.11). The displacement of the shuttle needs to be straight for minimizing pull-in effects and maximizing output displacement and force. The actuation direction of the suspension has to be compliant to minimize elastic energy storage. The other 5 DOFs are intended to be stiff in relation to the actuation direction, effectively constraining these 5 DOFs. For a comb-drive a high stiffness in the *x*-direction (Figure 2.9) of the shuttle is important to minimize the possibility of pull-in. In MEMS, many types of straight guiding mechanisms have been used. A brief overview is presented.

The parallel leaf-spring flexure of Figure 2.9a is often used in macro systems. Although the mechanism is almost exactly kinematic constraint, the mechanism does not straight guide very well. The shuttle moves over an “arc-like” curve and experiences displacement in the *x*-direction while moving in the *y*-direction. At a relative deflection $y/l = 0.02$ the straightness error is $0.012\ y$ [43]. Making the design symmetric as shown in Figure 2.9b, thus adding 2 extra leaf-springs, solves the straightness problem. However, the design - which is over-constraint in many ways - progressively builds up tensile stress at deflection, resulting in progressive stiffness in the actuation direction. For small deflections the design can be satisfactory. Analog Devices has used this suspension for its accelerometers of the ADXL family [23]. In Figure 2.9c, the over-constraint design is modified by adding flexures which are loaded in the compliant bending direction. Although the problem of the progressive actuation stiffness is solved, the design has become compliant in the *x*-, *y*- and *rz*-directions. A trade-off can be made between actuation stiffness progressiveness and the stiffness in the *x*-direction, but it will always

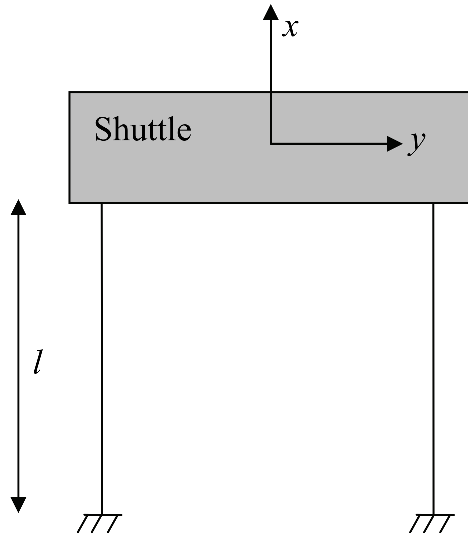

a) Parallel leaf-spring flexure

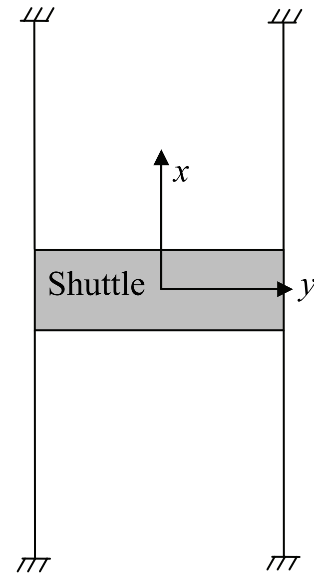

b) Double parallel leaf-spring flexure

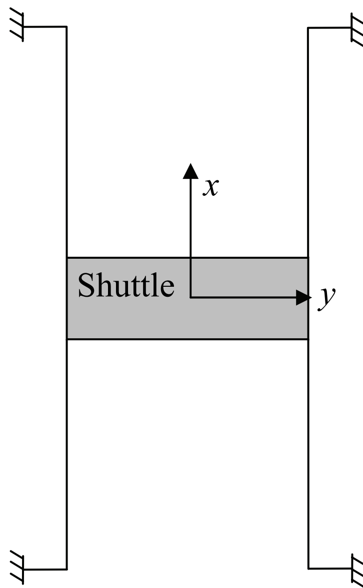

c) Crab-leg flexure

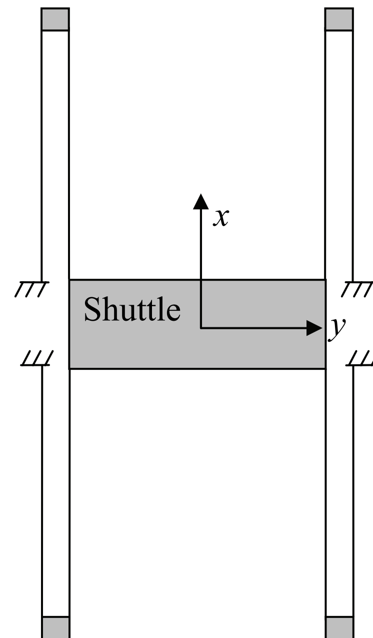

d) Back-folded leaf-spring flexure

Figure 2.9: Several commonly used straight guidance mechanisms.

result in a compromised stiffness ratio c_x / c_y. The back-folded leaf-spring flexure depicted in Figure 2.9d uses a second set of leaf-springs to compensate for the curve-like motion of the shuttle, such as the one shown in Figure 2.9a. NovaSensor uses this suspension in commercial accelerometers [38]. The weak point of this suspension is that the stiffness in the *x*-direction is strongly dependent on the

bending stiffness of the leaf-springs, even when there is no y-displacement. This reduces the stiffness in the x-direction. The folded flexure [124] design presented in Figure 2.10 does not suffer from this dependency of the stiffness in the x-direction on the leaf-spring bending stiffness in the y-direction when there is no y-displacement. This flexure design is capable of straight guiding a shuttle with reasonable stiffness over a medium length displacement. When deflected, however, the stiffness decreases rapidly as well. The main reason is that at a given y-displacement of the shuttle, a load in the x-direction on the shuttle will influence the y_i-position of the intermediate bodies. This means at large displacements there is a geometric coupling, a transmission ratio, between the x-position of the shuttle and the y_i-position of the intermediate bodies. Therefore, due to the transmission ratio the stiffness in the x-direction is coupled to the low stiffness in y-direction at large displacements. It will be shown that the influence of position y_i on x can be decreased.

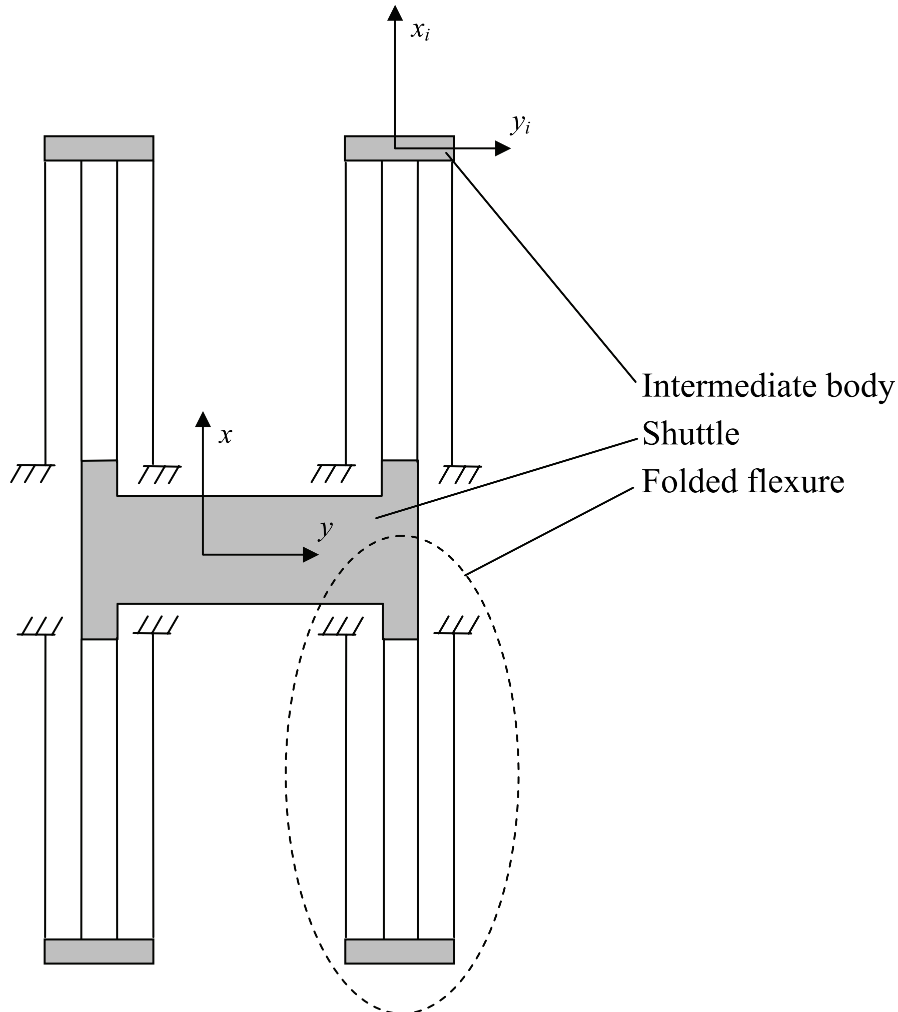

*Figure 2.10: 4*x *folded flexure straight guiding mechanism.*

2.5.2 Influence of reinforcement on folded flexure behavior

Although the reinforcement used in leaf-springs is often considered to be rigid, the compliance of the reinforcement influences the behavior of the leaf-spring and needs investigation. Figure 2.11 shows an application of the folded flexure design as shown in Figure 2.10. While a high c_x-stiffness is of importance for the stability of a comb-drive, the c_z-stiffness can be of importance for other applications and for robustness. The *z*-direction is the out-of-plane direction in Figure 2.11. It will be shown that the first vibration mode frequency of the manipulator presented in chapter 4 relies on the c_z-stiffness of the actuator shuttles. The stiffness c_y should be low to minimize elastic energy storage resulting in a reduced actuator area.

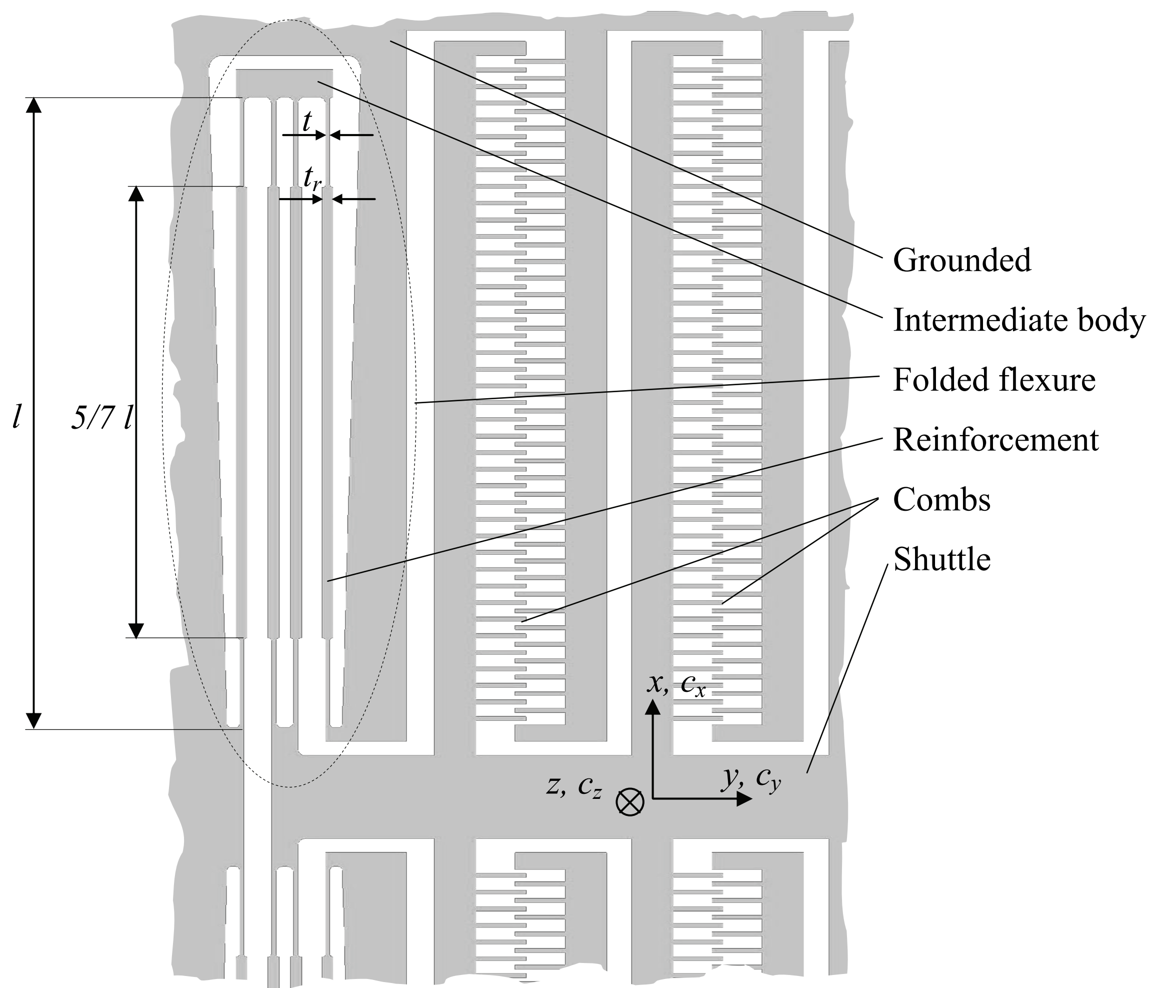

Figure 2.11: Reinforced folded flexure guiding a comb-drive actuator. The shuttle is suspended by 4 folded flexures as shown in Figure 2.10. Material is colored grey. The dimensions in this case are l = 406µm, h = 35µm, t =3µm and t_r = 8µm.

The c_x / c_y and c_z / c_y stiffness ratios (not c_{y0}) as a function of the relative deflection, in relation to the reinforcement thickness, have been modeled using SPACAR. The results are shown in Figure 2.12. For the c_z -stiffness the length l of the leaf-spring in relation to the height h is important.

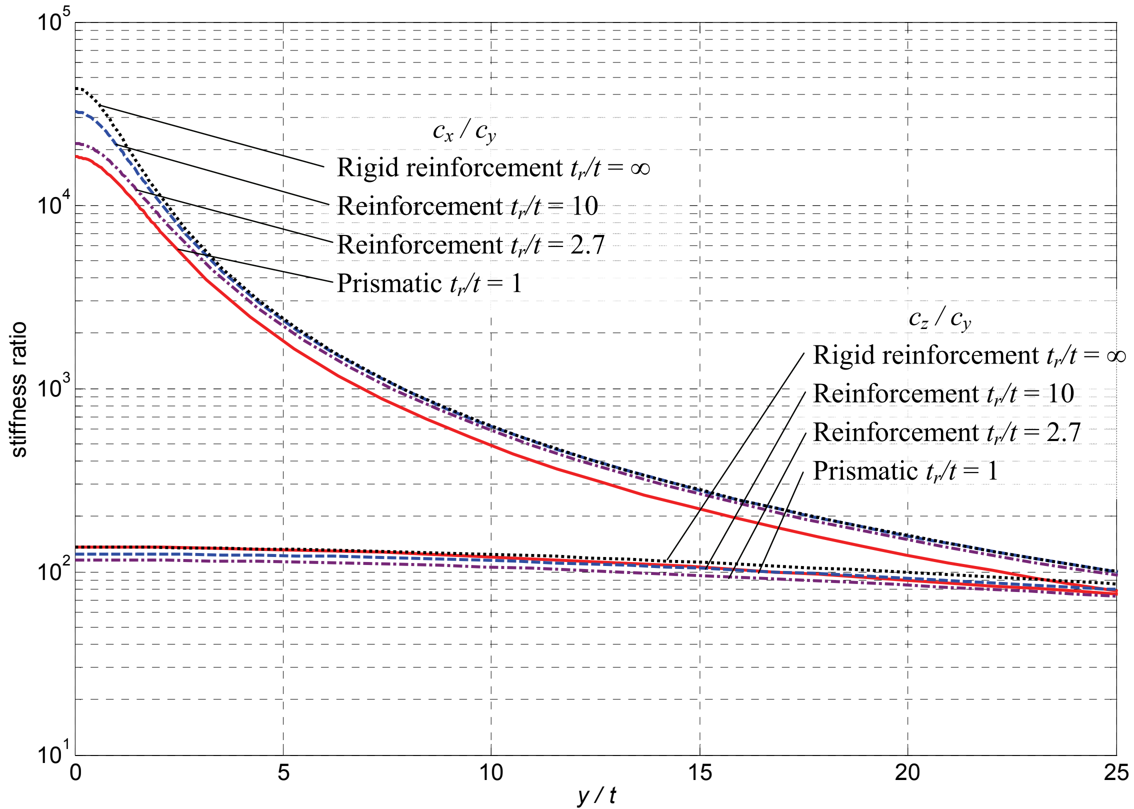

Figure 2.12: Stiffness ratios c_x / c_y and c_z / c_y for a 4x folded flexure suspension with dimensions l/h = 11.7 and l/t = 135 (Figure 2.11) as a function of the relative displacement y/t.

The c_z / c_y stiffness ratio hardly benefits from reinforcement. The c_z bending stiffness is increased the same amount as the c_y bending stiffness. In fact, reinforcing $t_r/t = 2.7$ shows a decrease in the c_z / c_y stiffness ratio when compared to a prismatic leaf-spring. This is because the c_y-stiffness initially increases faster than the c_z-stiffness when increasing the reinforcement thickness from $t_r = t$ to $t_r >> t$. The c_z / c_y stiffness ratio doesn't change much due to deflection, because l/h is relatively large [43]. A large l/h results in a relatively low c_z bending stiffness to torsion stiffness ratio of the leaf-springs themselves. Therefore, the c_z-stiffness does not greatly depend on the deflection as explained in section 2.4.1.

A folded flexure suspension of a comb-drive can benefit from reinforced leaf-springs if the leaf-springs are pre-curved and are straightened during actuation (Figures 2.13 and 2.14). At the point of maximum pull-in force the reinforced leaf-spring is then straight with maximum longitudinal stiffness [13].

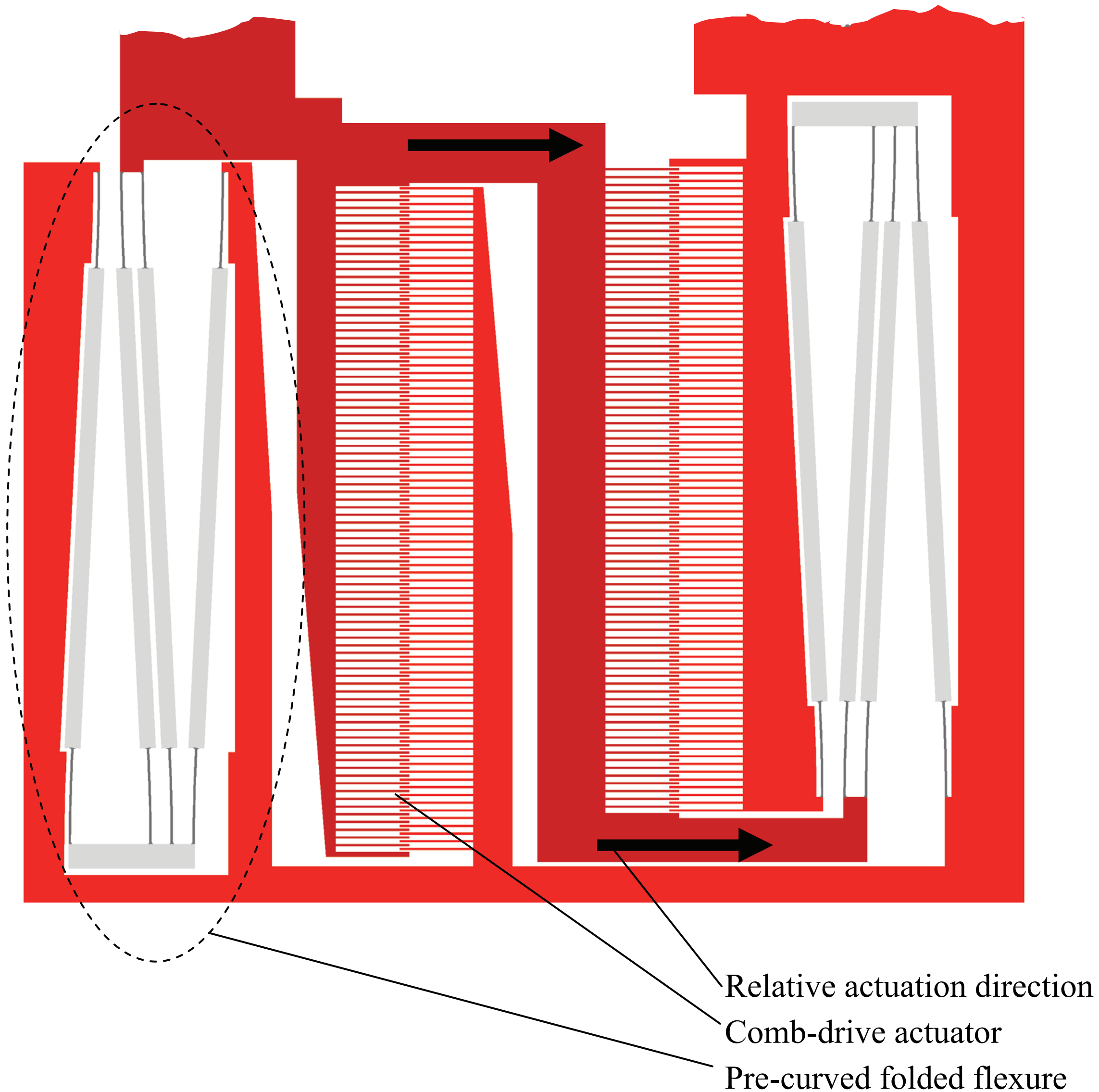

Figure 2.13: Reinforced leaf-springs in a pre-curved folded flexure design of a comb-drive actuator. This design was used in the first clamping mechanism design (chapter 5).

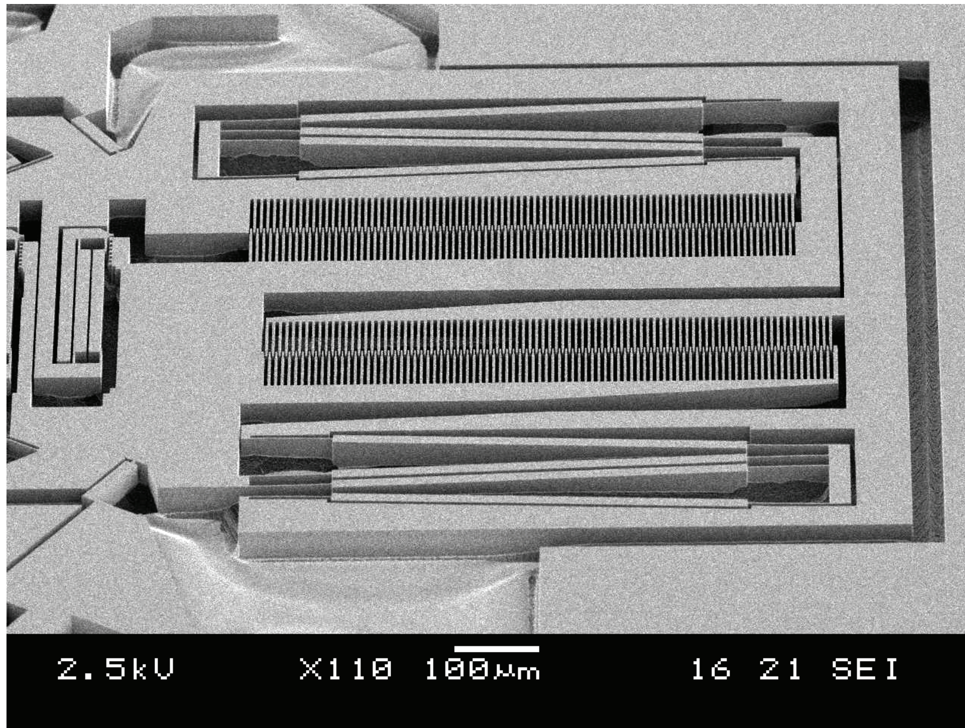

Figure 2.14: SEM picture of reinforced leaf-springs in a pre-curved folded flexure.

Several conclusions can be drawn with respect to a shuttle suspended by 4 folded flexures with l/h = 11.7 and l/t = 135 (see also Figure 2.12):

- The longitudinal stiffness c_x decreases strongly due to y-deflection.
- The out-of-plane stiffness c_z decreases up to a maximum of only 40% at a y-deflection of $y/t \leq 25$.
- Reinforcement does not help the out-of-plane stiffness ratio c_z / c_y much.
- The c_x / c_{x0} of a folded flexure at a relative displacement y/t (Figure 2.12) is equivalent to the c_x / c_{x0} of a single leaf-spring, as shown in Figure 2.7c, at relative displacement $y/2t$ and $c_d = 0$.
- If there is no y-deflection the longitudinal stiffness difference between a rigid and a t_r/t = 10 reinforced leaf-spring is still 25%. Modeling a reinforcement as a rigid is only accurate at a very thick reinforcement.
- At relative deflections $y/t > 5$ there is almost no difference in c_x / c_y and c_z / c_y stiffness ratio between a rigid reinforced or prismatic leaf-spring folded flexure.

Although reinforcing leaf-springs helps to increase the stiffness ratio c_x / c_y there is a fundamental difference between the macro scale and MEMS world. In the macro scale world, the question often is how to increase the stiffness ratio c_x / c_y. More generally speaking, the question is: how can DOFs which are intended to be constraint be made stiffer? In that case, reinforcing leaf-springs helps. In the MEMS world, the question often is not only how to increase the stiffness ratio c_x / c_y, but also how to increase compliance in the actuation direction. In that case, reinforcing leaf-springs can compromise the actuation compliance too much. This is especially important for low drive stiffness mechanisms where the increase of the c_x-stiffness due to reinforcement is relatively small at large deflections.

2.5.3 Non-linearity of actuation compliance

When designing a MEMS straight guidance mechanism, one should be aware of the non-linearity of the actuation compliance, which can result from various sources. In a first order approximation a folded flexure can be considered to have a constant compliance in the actuation direction. However, depending on the way a flexure is loaded, up to three sources of non-linearities can be distinguished:

- Curving of leaf-springs due to Poisson's contraction
- Geometrical non-linearity
- Compressive and tensile loading

CURVING OF LEAF-SPRINGS DUE TO POISSON'S CONTRACTION

An effect which is not taken into account by SPACAR calculations is leaf-spring stiffening by deformation of the rectangular cross-section of the leaf-spring due to transverse strain by Poisson's contraction. Bending causes a tensile stress at the elongated side and a compressive stress at the compressed side of a leaf-spring. The longitudinal tensile stress in a leaf-spring leads to contraction of the height of the leaf-spring. Compressive longitudinal stress leads to extension of the leaf-spring height. The combined effects cause the rectangular cross-section of a leaf-spring to curve. Van Eijk [43] has calculated the magnitude of this effect. Leaf-springs having a relatively large height show increasingly strong non-linearity. As a consequence a folded flexure with leaf-springs having a ratio $h^2/(l\ t) = 4$ shows an extra 1% increase in actuation force at a relative displacement of 0.2 y/l. However, for MEMS usually the leaf-springs have a geometry $h^2/(l\ t) < 1.5$. Therefore Poisson's contraction stiffening doesn't play a significant role in MEMS. For the macro leaf-spring with $h^2/(l\ t) = 18.8$ mentioned in section 2.4.1, the same situation would show an extra increase of the actuation force of 6%. So for MEMS leaf-spring dimensions SPACAR calculations can be applied without significant errors

in this respect. For macro-sized leaf-springs one must be cautious when relatively large deflections are modeled.

The combined effects of geometric non-linearity and compressive / tensile loading are modeled using SPACAR for the folded flexure shown in Figure 2.15. The results for various geometries are displayed in Figure 2.16.

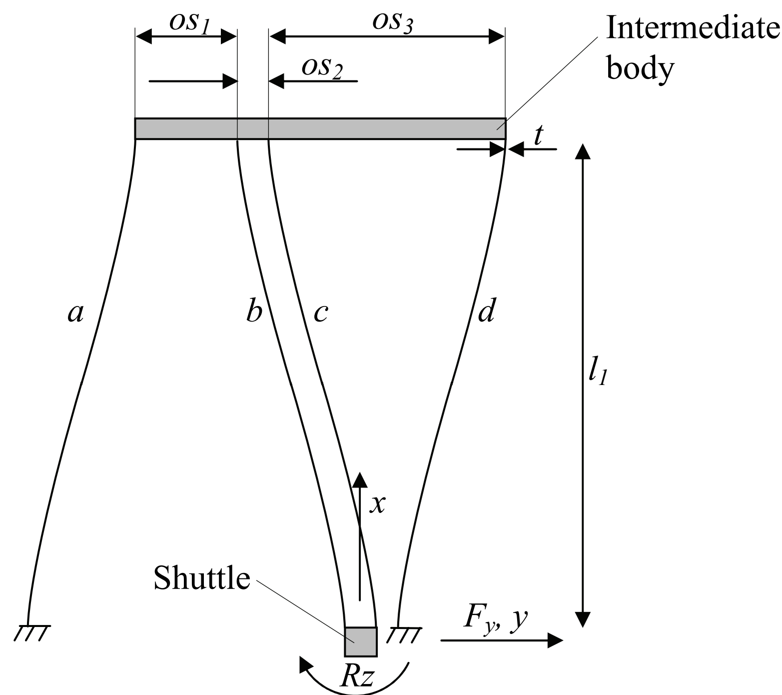

Figure 2.15: Schematic of a folded flexure. The y-direction is the compliant actuation direction.

GEOMETRIC NON-LINEARITY

For an increasing *y*-displacement of the shuttle, the bending of the leaf-springs increases more than proportionally with the displacement. The length of the arm l_1 (Figure 2.15) and the length of the leaf-springs will start to deviate from one another. These effects cause geometric non-linearity in the actuation stiffness. In Figure 2.16 the geometric non-linearity effect on the actuation stiffness is shown by the difference in actuation stiffness between 203 µm and 406 µm long leaf-springs (with the same off-sets os_1, os_2 and os_3) in the folded flexure. The 203 µm long folded-flexures show increased actuation stiffness with respect to 406 µm long folded-flexures when deflected.

COMPRESSIVE AND TENSILE LOADING

Loading the shuttle with a force F_y (Figure 2.15) causes a displacement in the *y*-direction. The resulting bending moments of the leaf-springs *b* and *c* on the shuttle cause a tensile force in leaf-spring *b* and a compressive force in leaf-spring *c*, as explained by Koster [76] and Jones [62]. At the same time leaf-spring *a* will be loaded by a compressive force and leaf-spring *d* will be loaded by a tensile force. The compressively loaded leaf-springs will decrease the actuation stiffness of the folded flexure, which is not entirely compensated for by the increase in stiffness due to the tensile loaded leaf-springs at large deflections. This effect is particularly large for long leaf-springs with small off-sets os_1, os_2 and os_3, as shown in Figure 2.16. If the rotation *Rz* is constrained, no actuation stiffness reduction due to displacement takes place. The reason is that the bending moments caused by the leaf-springs on the shuttle do not result in a rotation *Rz* of the shuttle. Therefore there are no compressive or tensile forces in the leaf-springs necessary to compensate the bending moments of the leaf-springs.

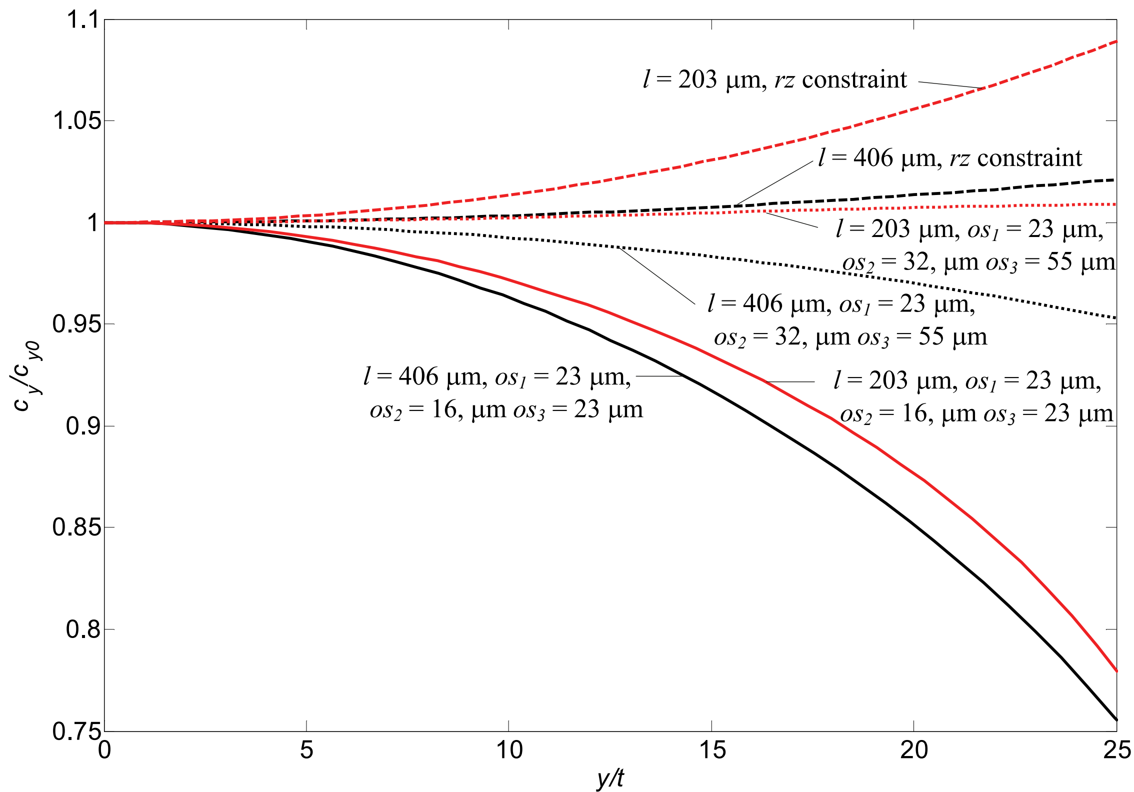

Figure 2.16: Combined influence of geometrical non-linearity, and compressive and tensile loading on the relative actuation stiffness for various geometries of folded flexures.

Usually a shuttle is guided by more than one folded flexure. Four folded flexures guiding a shuttle, as shown in Figure 2.10, compensate each other's bending moments. Therefore the leaf-springs are not loaded by a compressive or tensile force. The situation is equivalent to a shuttle with constraint *Rz*. Two folded flexures can also compensate each other's bending moment. An example is shown in Figure 2.13. The situation is also equivalent to a shuttle with constraint *Rz*, if the shuttle is stiff.

In general, over-constraint designs can cause unexpected non-linearities in stiffness behavior due to tensile or compressive loading of flexures. These non-linearities are hard to calculate as the tensile and compressive stress in the leaf-springs is usually unknown.

The following conclusions can be drawn with respect to non-linearity of the actuation compliance:

- Geometric non-linearity of the actuation c_y-stiffness in MEMS plays a minor role in mechanism design. In MEMS the deviation of the non-linear model from the linear model is usually less than 5% for deflections $y/t < 20$.
- Curving of leaf-springs due to Poisson's contraction does not play a significant role in the stiffness of MEMS flexures.
- Non-linear stiffness due to compressive and tensile loading of the leaf-springs can be high. However, usually this non-linear stiffness can be counteracted by using two folded flexures (Figure 2.13) or four folded flexures (Figure 2.10) compensating each other's bending moments. Otherwise large offsets os_1, os_2 and os_3 or a large offset between the folded flexures should be used.
- Over-constraint design with typical tensile and compressive stress in the leaf-springs causes non-linearity of stiffness at displacement. However, the magnitude of this effect is difficult to calculate.

2.5.4 Improved straight guiding designs for MEMS

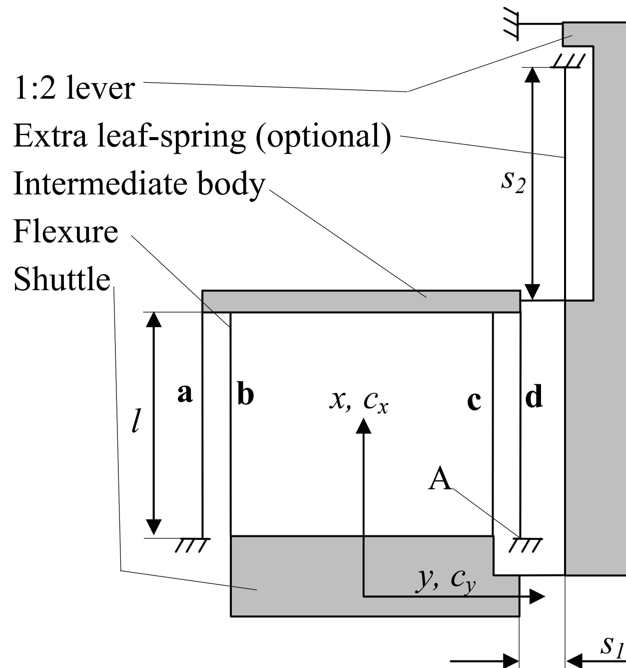

Figure 2.17: Improved straight guiding design using a guided intermediate body

In section 2.5.1, the loss of stiffness in the x-direction at large deflections of a folded flexure due to the coupling of the x-position (Figure 2.10) of the shuttle to the y_i-position of the intermediate body was described. In this paragraph two improved MEMS-based straight guiding mechanisms will be presented.

Loading a y-displaced shuttle of a folded flexure as shown in Figure 2.15 in the x-direction causes a negative y-force on the intermediate body by the slanted leaf-springs **b** and **c**. It also causes compressive stress in the two leaf-springs **b** and **c**, and tensile stress in leaf-springs **a** and **d**. Therefore, the leaf-springs **b** and **c** tend to deflect more in the y-direction than leaf-springs **a** and **d**. Both previously mentioned effects account for a misalignment of the intermediate body. This cross-talk of a force in the x-direction on the shuttle resulting in displacement of the intermediate body in the y-direction also affects the x-stiffness strongly. This problem could be solved by constraining the intermediate body to half the displacement of the shuttle [62, 76] by a 1:2 lever, as is shown in Figure 2.17. A second improvement could be to reinforce the leaf-springs **a**, **b**, **c** and **d** of the folded flexure. A third improvement could be to constrain the lever in the x-direction by adding an extra leaf-spring in the x-direction, as is shown in Figure

2.17. These three approaches have been modeled with SPACAR. The following dimensions have been used: l = 461 μm, s_1 = 263 μm and s_2 = 400 μm. The leaf-spring is reinforced over 5/7th of the length. The leaf-spring thickness is 3 μm, the reinforcement is 5 times the leaf-spring thickness and the leaf-spring height is 35 μm. The compliance of the reinforcement is taken into account. The results are shown in Figure 2.18.

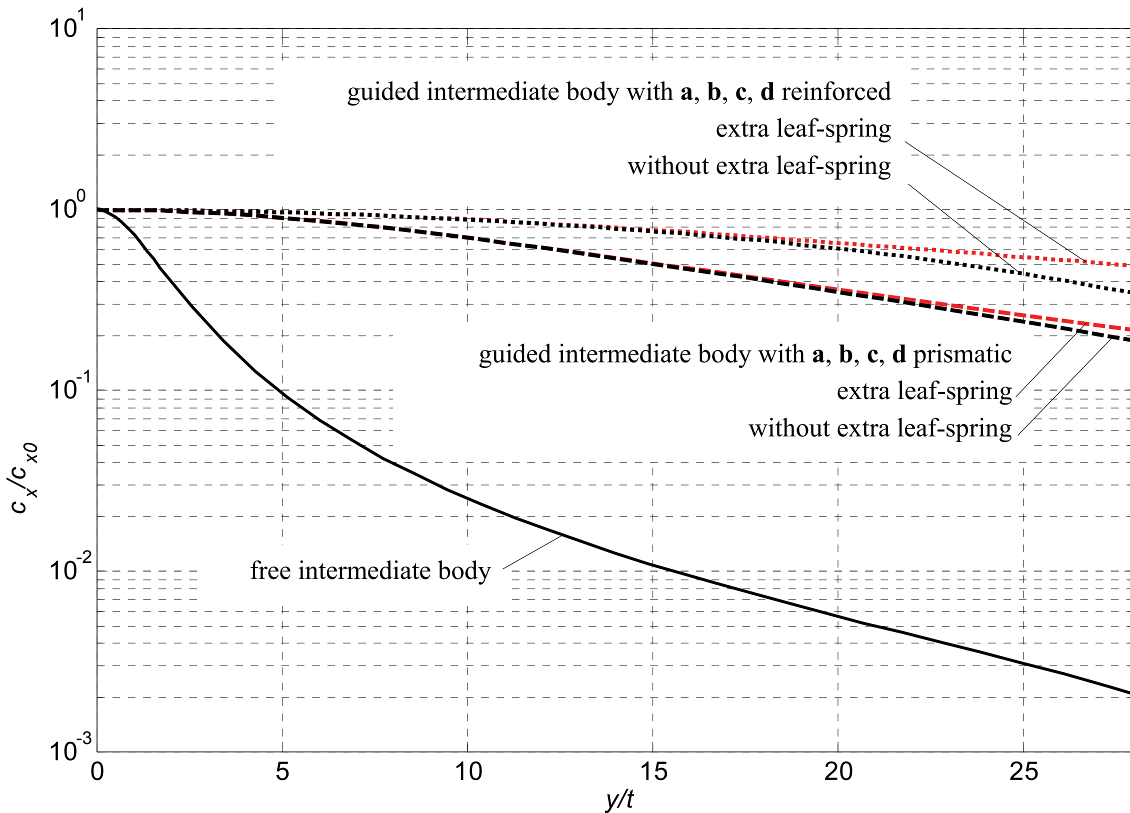

Figure 2.18: Comparison of the normed longitudinal stiffness c_x / c_{x0} of several improved folded flexure designs. Although the deflection is given in dimensionless y/t, the values are based on specific design dimensions

The following conclusions can be drawn from Figure 2.18:

- Constraining the displacement of the intermediate body in a 1 to 2 ratio with respect to the shuttle of a folded flexure increases the c_x / c_{x0} stiffness ratio at y-deflection considerably.
- Reinforcement helps to reduce the c_x / c_{x0}-stiffness ratio decrease with y-deflection, while also being stiffer initially then the prismatic leaf-spring design.
- For large deflections $y/t > 20$, constraining the 1:2 guidance lever by an extra leaf-spring in the x-direction, as shown in Figure 2.17, increases the c_x / c_{x0}-stiffness ratio.

The presented solutions can be implemented in assembled systems, in surface micro machined MEMS, TWIN [112] and SOI based devices. However, for back-etched [112] MEMS devices it is difficult to ground point **A** in Figure 2.17. Back-etched devices are etched through a thin portion of the wafer, which is comparable to wire spark eroded macro mechanisms which run through the workpiece as well. A possible solution is presented in Figure 2.19.

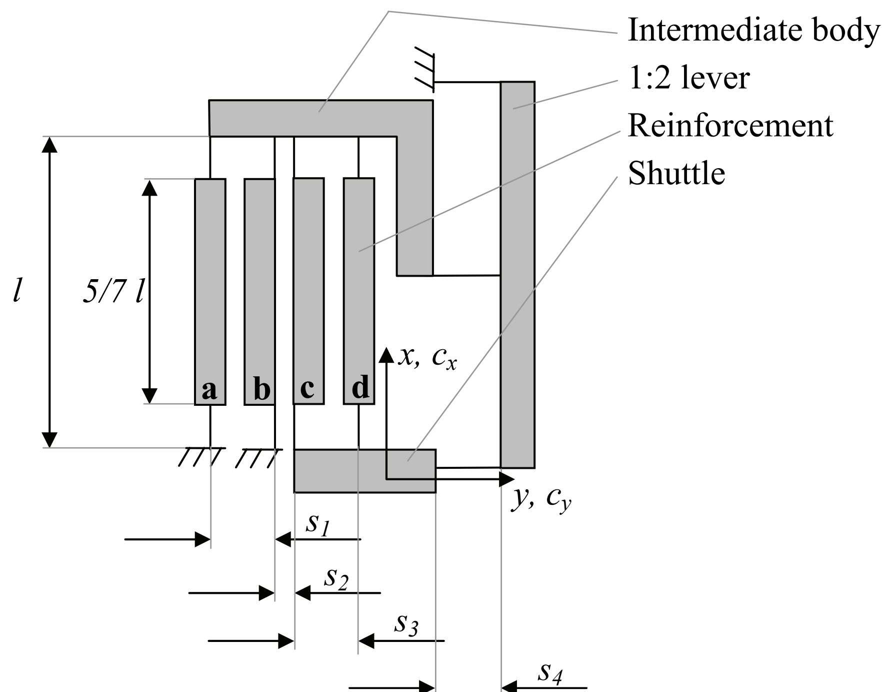

Figure 2.19: Back folded leaf-spring flexure with constraint intermediate body designed for back-etch processed leaf-springs.

A numerical comparison of a folded flexure (Figure 2.10), a reinforced folded flexure (Figure 2.11) and the design of Figure 2.19 has been carried out using SPACAR. The results are shown in Figure 2.20. The following dimensions of the folded flexure, the reinforced folded flexure and the design of Figure 2.19 are selected: l = 406 µm, the thickness of the leaf-springs (t) is 3 µm, the height (h) is 35 µm, and the thickness of the reinforcement is 4 times the leaf-spring thickness. The angles (*rx, ry & rz*) of the shuttle are considered to be constrained. A large longitudinal stiffness of the design of Figure 2.19 can be obtained by taking large values for s_1 and s_3 and a small one for s_2. For a high actuation compliance a large s_4 needs to be chosen. A trade-off needs to be made between the preferably large dimensions s_1, s_3 and s_4 and the total wafer area usage. A reasonable compromise for the previously mentioned dimensions is derived at s_1 = 23 µm, s_2 = 6 µm, s_3 = 23 µm and s_4 = 100 µm.

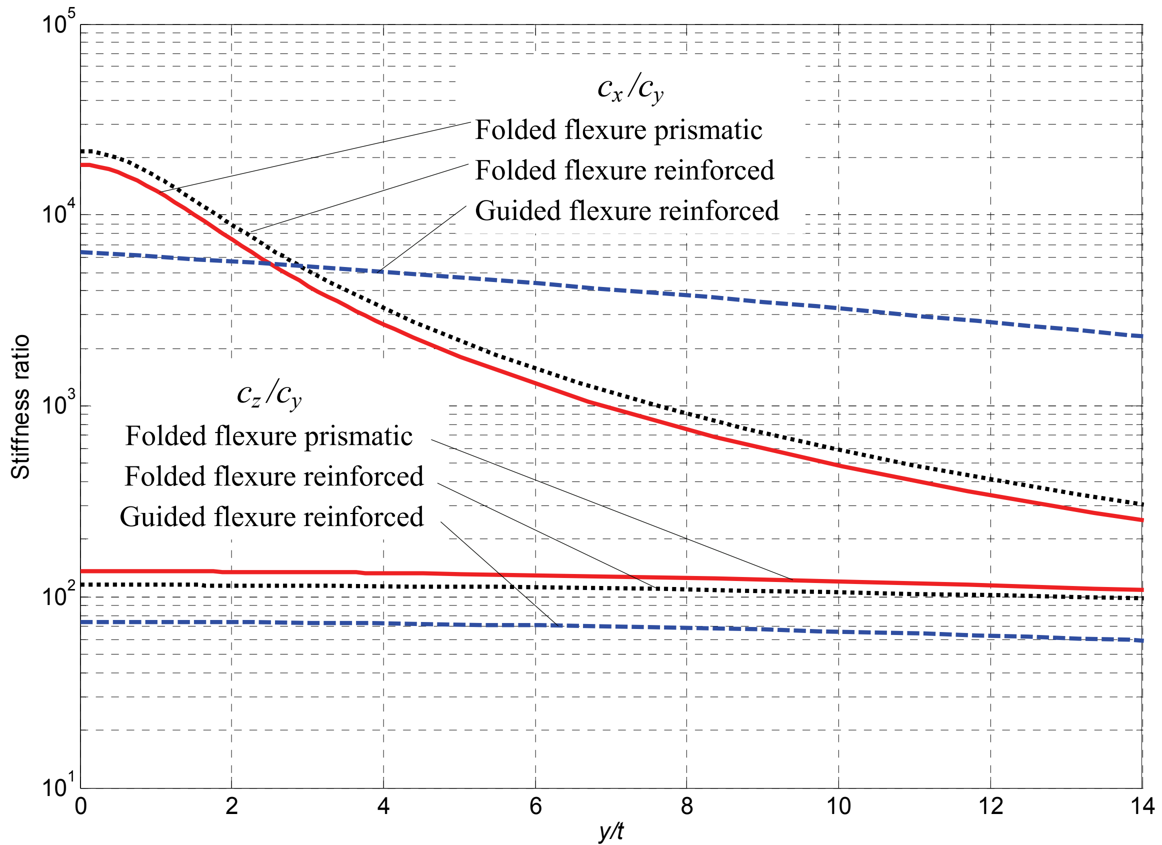

Figure 2.20: Comparison of stiffness ratios between a folded flexure, a reinforced folded flexure and the design of Figure 2.19. Although the deflection is given in dimensionless y/t, the values of the guided flexure are based on specific design dimensions shown in Figure 2.19.

Because Figure 2.20 shows stiffness ratios, some absolute values are given:

- At zero deflection the c_x-stiffness of the guided flexure is 0.88 times the c_x-stiffness of the prismatic folded flexure.
- At zero deflection the c_x-stiffness of the reinforced folded flexure is 1.8 times the c_x-stiffness of the prismatic folded flexure.
- The c_y-stiffness of all three flexures is almost constant.
- The energy storage of the guided flexure during deflection is large compared to that of the prismatic folded flexure design, leading to 2.5 times higher stiffness in the c_y-direction.
- The reinforced folded flexure is 1.5 times stiffer in the c_y-direction than the prismatic folded flexure.

The following conclusions can be drawn from Figure 2.20:

- The stiffness ratio c_x / c_y of the reinforced folded flexure is marginally (14% - 36%) better than that of the prismatic folded flexure, regardless of the deflection.
- The stiffness ratio c_z / c_y of the reinforced folded flexure is worse than that of the prismatic folded flexure! Increasing the c_z-stiffness requires thicker reinforcement.
- The guided flexure is less symmetric than a reinforced folded flexure, leading to less c_x stiffness when there is no y-deflection.
- The zero deflection stiffness ratio c_{x0} / c_{y0} of the guided flexure is about 2.9 times lower than the c_{x0} / c_{y0} of the prismatic folded flexure.
- At deflections $y/t > 3$, the guided flexure outperforms the folded flexures in terms of stiffness ratio c_x / c_y, though at the cost of more occupied area of the flexure mechanism and a 2.5 times larger actuation force.
- At $y/t = 14$ the stiffness c_x / c_y of the guided flexure is 7 times better than that of the reinforced folded flexure. The design is especially interesting for relatively large y-deflections, $y/t > 7$.

2.5.5 Design rules for straight guiding in MEMS

Based on the findings in this chapter the following design rules are advised for use with low drive stiffness MEMS-based mechanisms:

- For one way comb-drives, reinforced pre-curved leaf-spring folded flexures are a good option (Figure 2.13). The maximum mechanical stiffness is available at the point of maximum electrostatic pull-in force.

- For MEMS devices having a small drive stiffness (c_d / c_y < 10), which is usually the case in two way comb-drives:

  - Using SOI, TWIN and surface micro machined fabrication technology:
    - For relatively small deflections of $y/t < 3$, use prismatic folded flexures
    - For deflections of $y/t > 5$, use a design as presented in Figure 2.17 with reinforced leaf-springs (the area usage can be optimized).

  - Using Back-etch fabrication technology:
    - For deflections of $y/t < 7$, use prismatic folded flexures
    - For relatively large deflections of $y/t > 10$, use a design as shown in Figure 2.19.

However, a designer should realize that the designs depicted in Figures 2.17 and 2.19 require extra space and actuation force.

2.6 Conclusion

Single crystal silicon is a good structural material for micro devices because of its pureness, low hysteresis, high strength and high heat conductance. Other often used structural materials are polysilicon, silicon-rich nitride and silicon oxide. All possess a low expansion coefficient and high temperature stability, which offer many processing possibilities. The brittleness of the single crystal silicon structures needs to be taken into account, however.

When mechanical structures scale down to the sub millimeter level, a designer's intuitive sense of mechanics does not always hold true. Structures might seem relatively long and slender, and are therefore thought to posses low frequency vibration modes. In general, however, vibration mode frequencies are high, but the mechanisms are often compromised with respect to exact kinematic constraint design.

Large angle rotations with elastic mechanisms are not possible without compromising the dynamic behavior of a system. Contact bearings in MEMS, although enabling large angle rotations, incorporate play (micron level), hysteresis and wear, and are therefore unsuitable for precision manipulation. Creating hinges with the axis of rotation in the wafer plane requires a combination of technologies such as DRIE and surface micro machining, which makes processing challenging.

The limited aspect ratio of DRIE processed MEMS leaf-springs limits the ability to constrain DOFs with respect to compliant DOFs. Bosch etched leaf-springs can be seen as leaf-springs constraining 3 DOFs up to about 10 degrees of bending rotation. Surface micro machined vertical "leaf-springs" behave like a slender beam constraining only 1 DOF. Of all stiffness directions, the longitudinal direction of leaf-springs shows the largest decrease in stiffness under deflection. The stiffness decrease in the height direction at deflection of a leaf-spring is low in typical MEMS leaf-spring dimensions. The initially already compliant modes have a more or less constant compliance during deflection.

Geometric non-linearity of the compliant actuation direction in MEMS plays a minor role in mechanism design.

The longitudinal stiffness of leaf-springs which are deflected decreases substantially with the deflection, especially for low drive-stiffness (see section 2.4.2) systems. Reinforcing leaf-springs of folded flexures in MEMS with a low drive stiffness generally result in more negative effects than positive ones.

Constraining the displacement of the intermediate body in a 1 to 2 ratio with respect to the shuttle of a folded flexure increases the longitudinal stiffness ratio at deflection considerably. Two improved folded flexure designs incorporating a 1 to 2 lever are proposed for large deflections. However, the stiffness in the actuation direction also increases. Design rules are derived based on the technology used and the amount of relative deflection.

Chapter 3

CONCEPTS FOR FABRICATION & DESIGN OF A SIX DOFs MEMS-BASED MANIPULATOR

The key issue in this chapter is obtaining a concept for a 6 DOFs manipulator using the mainly planar fabrication technology of MEMS. A motion converting mechanism using only one type of actuator is chosen in favor of a combination of in- and out-of-plane actuators. Six electrostatic comb-drives will be used for actuation. A parallel kinematic mechanism is preferred over a serial mechanism. Feed-back versus feed-forward positioning strategy will be discussed. Based on these system design choices, three concepts are presented and evaluated. Each concept includes a fabrication process in conjunction with an exact kinematic constraint design. The total design process is a synthesis between these two. The most feasible concept is shown, including a clamping mechanism.

3.1 Introduction

The specifications of the manipulator are based on the requirements set by FEI Company and can be found in chapter 1, section 1.6. The concept proposed in section 1.7 consists of a 2 DOFs large tilt stage and a 6 DOFs MEMS stage. Manipulation in 6 DOFs requires in- and out-of-plane motion, which in MEMS is not straightforward. In this chapter three concepts will be proposed for the 6 DOFs MEMS stage. The most feasible one will be combined with a clamping mechanism.

3.2 MEMS-based Mechatronic System Design

In this section, basic design choices are made regarding the creation of 6 DOFs mobility in MEMS. Some differences between MEMS and macro mechatronic design will be mentioned. Six DOFs positioning requires both in- and out-of-plane (wafer-plane) motion. This can be achieved by using a combination of in- and out-of-plane actuators or by using 1 type of actuator and a motion converting mechanism. The actuator choice has to be made in conjunction with the decision whether to use a parallel or a serial kinematic set-up. The use of a feed-forward or feed-back positioning strategy will be discussed.

3.2.1 Differences between MEMS and macro mechatronic design

There are some important differences between a mechatronic design in MEMS and in the macro scale world:

- The influence of the fabrication technology on the design is large.
- Fabrication technology is often based on planar processes.
- The influence of the actuator choice is great.
- Sensing is relatively inaccurate.
- The repeatability of compliant mechanisms in Si-based technology is high.

Although in mechatronic system design error budgets are often used to systematically predict and/or control the (repeatable) errors of a machine, they will not be used. In this case an error budget is too strongly application driven and/or too specific goal driven.

3.2.2 Basis of design: Design principles and bulk micro machining

The derived concepts will be based on the design principles [76] in combination with mainly bulk micro machining based processes [92].

The design principles [8, 56, 62, 76, 116, 121, 122] are a design philosophy enabling or enhancing accurate positioning as explained in section 2.3. The design principles which are especially relevant in the MEMS-based 6 DOFs manipulator design are:

- Determinism, promotes the use of compliant mechanisms
  (no friction, no wear, low hysteresis, no play).
- Exact kinematic constraint design.
- Symmetry.

A bulk micro machining based process in SCS allows high aspect-ratio structures by DRIE in combination with electrical insulation. DRIE enables relatively high leaf-springs of 35-40 μm high and 2 μm thick. High leaf-springs are necessary for increasing the out-of-plane stiffness of the relatively large MEMS devices.

3.2.3 Motion in- and out-of-plane of the wafer

6 DOFs positioning requires both in- and out-of-plane (wafer-plane) motion. Basically there are two options for 6 DOFs motion generation:

- Combination of in- and out-of-plane actuators in one system.
- Use of a mechanism to convert in- to out-of-plane motion or vise versa.

COMBINATION OF IN- AND OUT-OF-PLANE ACTUATORS

Usually the technology used to fabricate in-plane actuators differs from the technology applied to fabricate out-of-plane actuators. Therefore, a combination between the two is a rarity. In chapter 1, for example, several MEMS-based multi DOFs positioning systems are discussed based on a literature study. None of these combine in- and out-of-plane actuators except for one described by de Jong [63]. De Jong has presented a concept for a combination of in- and out-of-plane actuation based on comb-drives. However, manipulation was demonstrated in 3DOFs only, by wafers containing either only in-plane or out-of-plane actuators. Therefore, combining in- and out-of-plane actuators in one system is difficult.

MOTION CONVERSION FROM IN- TO OUT-OF-PLANE

Conversion from in- to out-of-plane motion can be realized in many ways. Cheng [26], Fan [48] and Walraven [134] use counteracting in-plane actuators to push a platform out-of-plane. Others, like Culpepper [32], use a special double SOI wafer incorporating a stack of two in-plane thermal actuators on top of each other. When driven synchronously an in-plane motion results. Conversely, when driven differentially a deflection out-of-plane is generated. Although it is easier to fabricate six actuators of the same type than three in-plane and three out-of-plane actuators, the mechanism needed to convert motion usually also requires special additional process steps.

When considering the options ‘using two types of actuators’ or ‘using one type of actuator and a mechanism to convert motion’, the latter seems easier and will therefore probably be more successful. As a consequence, a combination of a motion converting mechanism with one type of actuator will be developed.

3.2.4 Actuator principle

The most common actuator principles for MEMS are discussed in appendix C. The actuator choice in MEMS design has even larger implications for the overall conceptual design than on a macro scale. There are several reasons for this:

- The actuator principle strongly influences the fabrication process.
- MEMS actuators are relatively large.
- The direction of motion, in- or out-of-plane, is actuator type specific. Typical out-of-plane actuators are thermal or piezo bimorphs. Typical in-plane actuators are electrostatic comb-drives, bent-beam thermal actuators and thermal extenders.
- The actuator suspension is actuator type specific.
- The suspension can be relatively large.

Magnetic actuators have a low energy density. Piezo (PZT) actuators are difficult to integrate in MEMS technology or need assembly. Thermal actuators can have an energy density comparable to electrostatic actuators. However, the thin film technology to fabricate uni-morph and multi-morph actuators conflicts with integration into a bulk micro-machined system. Simple extenders, as used by Paalvast [98], have a limited stroke and require strong stroke amplification. In general, thermal actuators lack thermal stability, causing position uncertainty at nano manipulation. An advantage of thermal actuators over electro-static actuators is the fact that they do not jeopardize the stability of the E-beam. However, the problem of the interaction of the E-beam with electrostatic actuators can be overcome by either blocking the actuators with a clamp (chapter 5) or by shielding. Regarding the necessary stroke and force of the manipulator a lateral comb-drive type electro-static actuator would suffice. This type of actuator integrates well into bulk micro machining.

3.2.5 Serial versus parallel kinematic mechanism

A distinction can be made between two main basic concepts with regard to the mechanism. One type is serial, the other is parallel. In a serial mechanism, there is one kinematic chain of links and joints between the end-effector and base. A typical example of a serial manipulator is the classic assembly robot as often used in the automotive industry. In a parallel mechanism, multiple independent kinematic chains exist parallel to each other between the end-effector and the base. An example of a parallel 6 DOFs mechanism is a Stewart platform, which is often used in flight-simulators.

Parallel kinematic robots at the macro scale combine a medium stiffness with a low moving mass, resulting in high vibration mode frequencies. The stiffness of a macro parallel kinematic manipulator is often determined by the bearings, which are typically universal or spherical joints. The stiffness of these bearings is generally not as high as that of an oil bearing or a large area air bearing system. The overall stiffness of a parallel manipulator can, however, be substantially higher than the stiffness of a cascaded robot, whose relatively long arms decrease the overall stiffness. The high vibration mode frequencies of parallel kinematic robots make them suitable for fast positioning. In MEMS a parallel mechanism can be used to convert motion from in-plane to out-of-plane. The high vibration mode frequencies in this case are convenient in the TEM application for a good coupling between the TEM column and the sample. At the macro scale, parallel kinematic robots are relatively large compared to their workspace. In MEMS, however, a serial robot is also quite large, as stacking one DOF on top of the other is actually embedding one actuator with its DOF in the next, making the total system occupy a relatively large area as well. A large advantage of a parallel set-up, especially in MEMS, is that the actuators are stationary. This makes routing of the electrical connections to the actuators (and sensors) easy. Electrical leads in MEMS are relatively large and are flexures which are usually part of the mechanism. Adding extra flexures in the case of a serial manipulator usually results in increased stiffness (especially in MEMS), which is counteracting the necessary compliance in the actuation direction.

3.2.6 Position control

Two specifications with respect to positioning need to be distinguished: the positional *repeatability* and the *stability*. The repeatability is the uncertainty at which the manipulator can reproduce a position each time. The repeatability is specified to be 10 nm (section 1.6). The stability of 0.1 nm specifies how well the position is kept constant relative to the electron beam over a certain amount of time, in this case 1 min. Because of the small speed nature position deterioration, it is also often referred to as drift.

SENSORS IN THE MANIPULATOR

Precision macro systems often rely on feedback for accurate position information. Measuring on the micro scale is less trivial. Capacitive sensor systems can provide relative good feedback, especially when combined with special techniques such as large structures, special patterns and motion amplifiers. Kuijpers [79] demonstrates that specific periodic patterns can be sensed with an estimated uncertainty of less

than 10 nm over a range in the order of 100 μm. The measurements are, however, performed far from real-time operation. Chu [27] uses a transmission ratio to increase the capacitive sensing resolution to values of over a nm. Comb-drive actuators can also be used for measuring if a high frequency measurement signal, for example 1 MHz, is superimposed on the actuation signal. The spacious comb-drive structures can be exploited in this way for sensing as well. In general, however, measuring with an uncertainty less than 10 nm over a range of 20 μm in MEMS is far from straightforward.

For achieving the highest positioning repeatability, measuring directly on the end-effector would be preferable. However, measuring an object, macro or micro, in 6 DOFs directly is not easy. In MEMS, given the confined dimensions of the end-effector and the surrounding space, there seems to be no practical solution available. Therefore, the sensors will be coupled to the actuators, or are part of the actuators. Feedback control based on sensors compared with feed-forward control of a fully compliant, no friction, MEMS mechanism only gives added value if the mechanism properties change. The vibration disturbances acting on the manipulator are too high frequent to measure and compensate for. Overall there are several reasons why the added value of sensors in the TEM application is small. However, in applications where substantial external forces exist, such as micro assembly, the sensors are probably a necessity to achieve sub-micron repeatability.

FEED-FORWARD CONTROL STRATEGY

In the TEM manipulator application there is no unknown external force loading the manipulator except for forces due to external vibrations. In addition, MEMS, especially SCS, is known for its low hysteresis, due to the monolithic and often single crystal mechanical structure. Combined with a fully compliant, no-friction mechanism the repeatability and stability of the system without feedback, only using feed-forward, can be excellent. However, because of manufacturing uncertainty the mechanism needs to be calibrated in a 6 DOFs set-up. For in-situ calibration the E-beam can be used.

E-BEAM AS A SENSOR

The only feedback source for sub-nm level uncertainty measurement regarding the TEM is the E-beam itself. However, the E-beam only gives accurate feedback of the planar *x*, *y*, *Rz*-position (top-view) of the sample (which is shown in Figure A.1). The feedback of the E-beam is also slow as building an STEM picture can take up to 30 s, which makes it difficult to use it in the feedback real time. It can be used in a learning feed-forward strategy, compensating the measured offset.

Theoretically, the drift can also be compensated for, but there are several issues involved in this. Actuators with reliable low speeds of 0.1 nm/min are required. Moreover, not blocking the compliant actuators like comb-drives results in low frequent vibration modes (blocking the system by clamping will be discussed in chapters 4 and 5). Also, actuating electrostatic actuators requires shielding of the actuators with respect to the E-beam. Overall, the E-beam can be used for a learning feed-forward control strategy, but compensating drift is hard. Therefore, the *stability* will need to rely on passive mechanical *stability*.

STABILITY

Passive mechanical *stability* of the manipulator means that the manipulator depends on material properties to counteract position deterioration due to temperature fluctuations and vibrations. The small dimensions of MEMS, a fully compliant mechanism without friction, combined with the good mechanical and thermal material properties make passive *stability* a feasible design solution. Therefore, the *stability* once the sample is positioned will rely on the passive *stability* of the mechanical structure.

CLAMPING

There are several reasons why the passive *stability* can be enhanced by unpowered blocking of the manipulator using a clamping mechanism once it has reached its targeted position:

- Cross-talk between the electron beam of the TEM and electric or magnetic fields from the actuators of the manipulator affects the stability of the E-beam and the manipulator. Clamping decreases this cross-talk.
- The two design objectives, a high actuation compliance and high frequency deformation vibration modes, are principally counteracting each other. A high actuation compliance is necessary for minimizing actuation forces, and requires low stiffness in the actuation direction. High frequency deformation vibration modes are necessary for reducing deformation mode amplitudes, and require high stiffness (in all directions). By using a clamping mechanism, the manipulator can be switched between compliant actuation modes for positioning, and high frequent deformation vibration modes during imaging.

A mechanical clamp with a locking device is investigated for that purpose in chapter 5. An overall conceptual design of the 6 DOFs manipulator and clamping mechanisms will be shown in section 3.7, Figure 3.16.

CONCLUSIONS REGARDING POSITION CONTROL

- Measuring with an uncertainty less than 10 nm over a range of 20 μm in MEMS real time is far from straightforward.
- Measuring directly on the end-effector in 6 DOFs in MEMS is extremely difficult.
- The added value of sensors in the TEM application is small, as there is no (unknown) external disturbance except for high frequency vibrations.
- With feedback, only the relatively low frequency disturbances can be compensated for.
- When using MEMS-based sensors, with their relatively large uncertainty and low sensing bandwidth, the bandwidth and uncertainty of feedback control is limited.
- The combination of no external load and the deterministic behavior of MEMS manipulators makes feed-forward control a good positioning option.
- The stiffness of the mechanics will be much higher than the "control stiffness", especially when the mechanism is blocked.
- Stability has to rely on the passive *stability* of the mechanical structure.
- The E-beam can be used for a learning feed-forward in 3 DOFs positioning.

The implications for the design are that there will be no extra sensors incorporated into the device. The E-beam can be used for learning feed-forward control, but this has no implications for the design.

3.2.7 Conclusions regarding MEMS-based mechatronic design

In the following sections, 3 conceptual designs will be presented based on:

- Parallel kinematics
- One type of actuator: a lateral comb-drive electrostatic actuator (in-plane).
- 6 DOFs mobility by a conversion mechanism from in- to out-of-plane.
- Clamping mechanisms compatible with the process technology of the manipulator.
- Fabrication technology preferably based on bulk micro machining in SCS.
- No extra sensing structures.

The concepts are presented in an order going from rough concept to more and more details. The last concept presented is also combined with clamping mechanisms. The three concepts are based on the same kinematics, more or less. This kinematic concept is explained by a macro version based on non-elastic joints and hinges to show the DOFs. This kinematic concept will be presented first.

3.3 The Kinematic Concept

In this section, the kinematic concept behind the 3 manipulator concepts discussed hereafter will be explained based on a macro version containing joints and hinges instead of elastic elements. The kinematics and DOFs of a 6 DOFs actuated platform will be explained (Figure 3.2). The manipulator consists of 3 equal legs. The next section will explain that each leg defines 2 DOFs of the platform leaving the other 4 DOFs free.

The manipulator has a **flat base** over which 3 **intermediate bodies** can move. Each **intermediate body** is actuated in 2 translational DOFs (*x* and *y* in Figure 3.1) and constrained in the other 4 DOFs (*z, Rx*, *Ry* and *R*z). The **ball joint** connecting the **intermediate body** with the **triangle** releases 3 DOFs. The **triangle** has 2 actuated, 3 free and 1 constraint DOFs therefore. The **hinge** releases another DOF. Therefore, the **platform** has 2 actuated and 4 free DOFs by one leg as shown in Figure 3.1. Table 3.1 summarizes the DOFs per component.

	free	actuated	constrained	
Intermediate body	0	2	4	
				Ball joint releases 3 DOFs
Triangle	3	2	1	
				Hinge releases 1 DOF
Platform	4	2	0	

Table 3.1: The DOFs of the rigid bodies of 1 leg of the manipulator.

The combination of 3 times 2 DOFs actuated per leg results in the platform having 6 DOFs actuated (Figure 3.2). Each of the individual DOFs of the platform is shown with the corresponding intermediate body *xy*-translations in Figure 3.3.

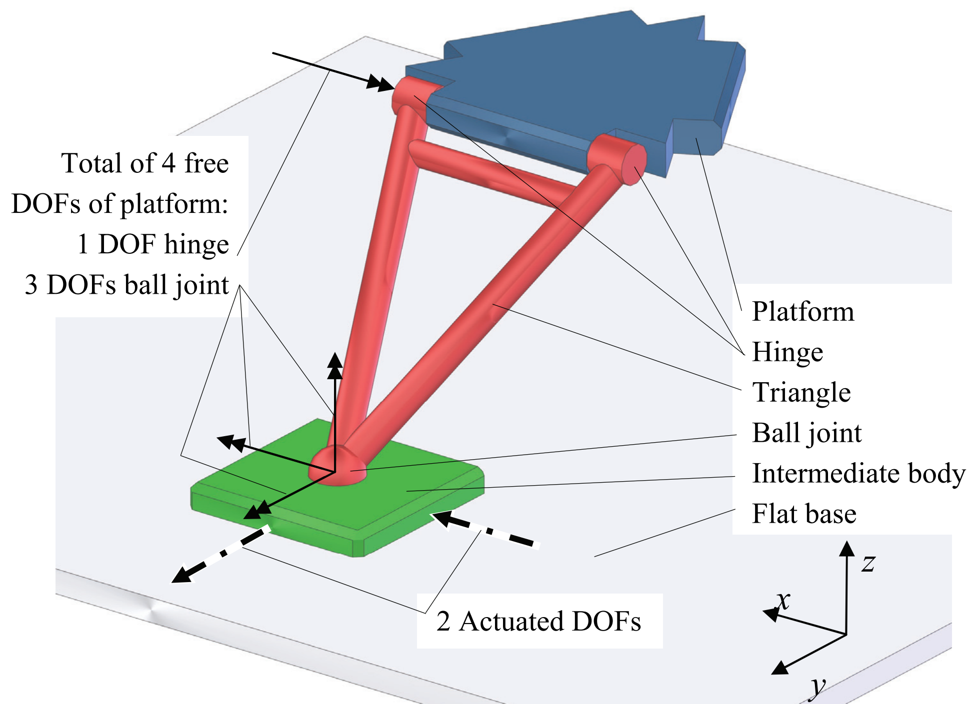

Figure 3.1: One of the three legs of the manipulator with the platform. The 6 DOFs of the platform, 4 free and 2 actuated, are indicated by the 6 arrows.

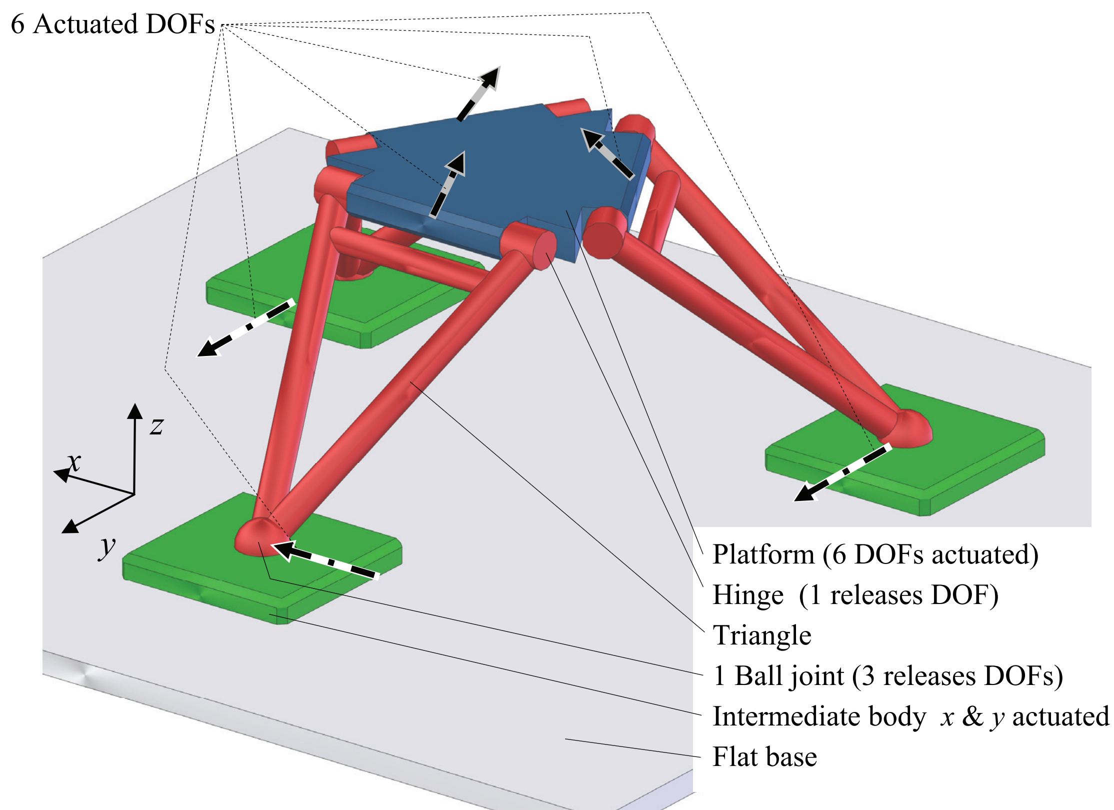

Figure 3.2: The 6 actuated DOFs of the platform are generated by the combination of 3 legs and 2 DOFs actuated per leg.

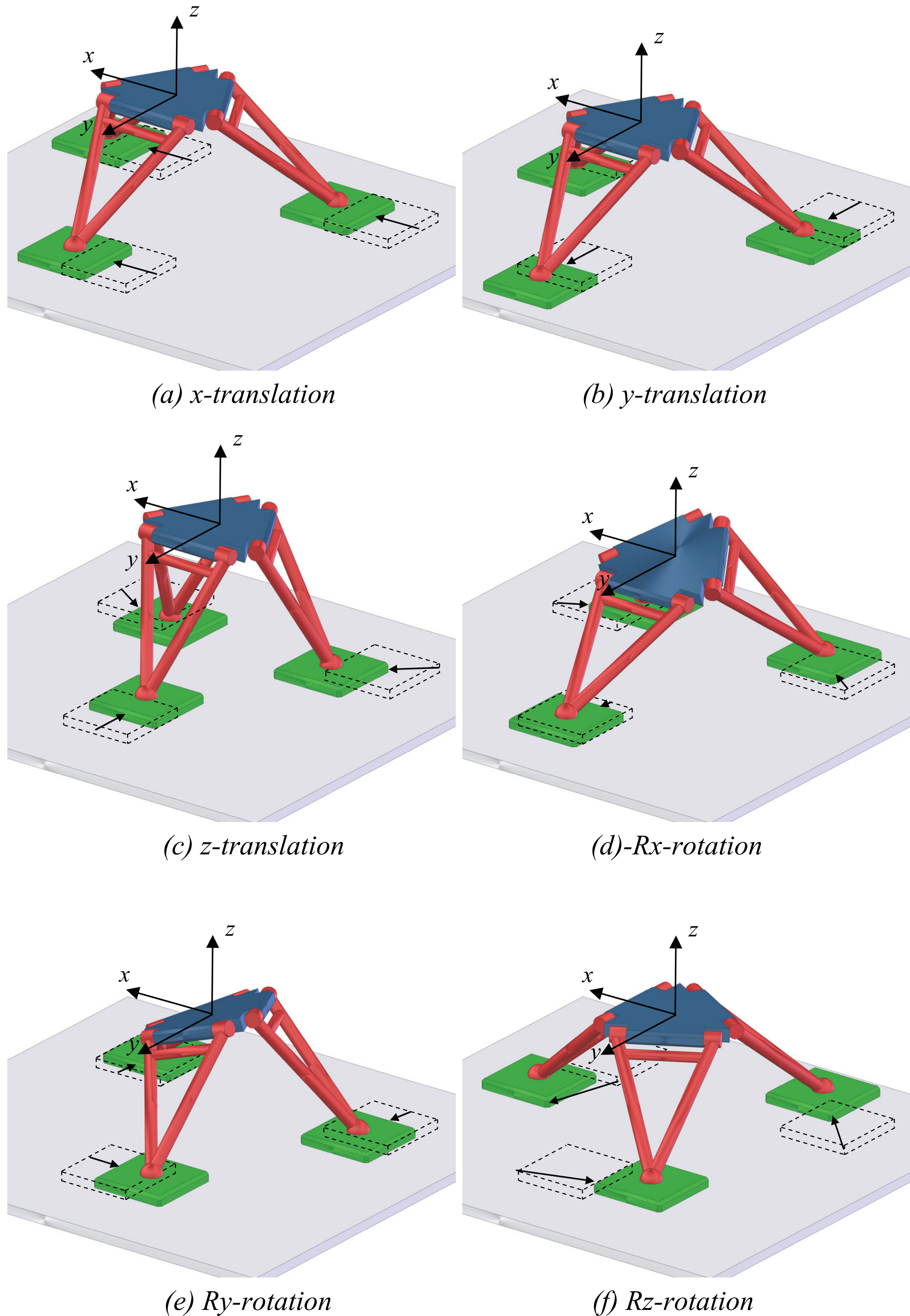

Figure 3.3: Each of the independent 6 DOFs of the platform are created by combinations of planar xy-displacements of the three intermediate bodies.

3.4 Concept 1: Planar hinge flexure concept

KINEMATIC DESIGN

The non-elastic joints and hinges used to explain the kinematic concept are replaced by elastic elements. The planar hinge flexure concept comprises planar leaf-springs at two levels in the wafer, converting in-plane to out-of-plane motion. The set-up is rotational symmetric. Because of robustness, buckling and stress, at this scale leaf-springs are prefered over slender elastic beams.

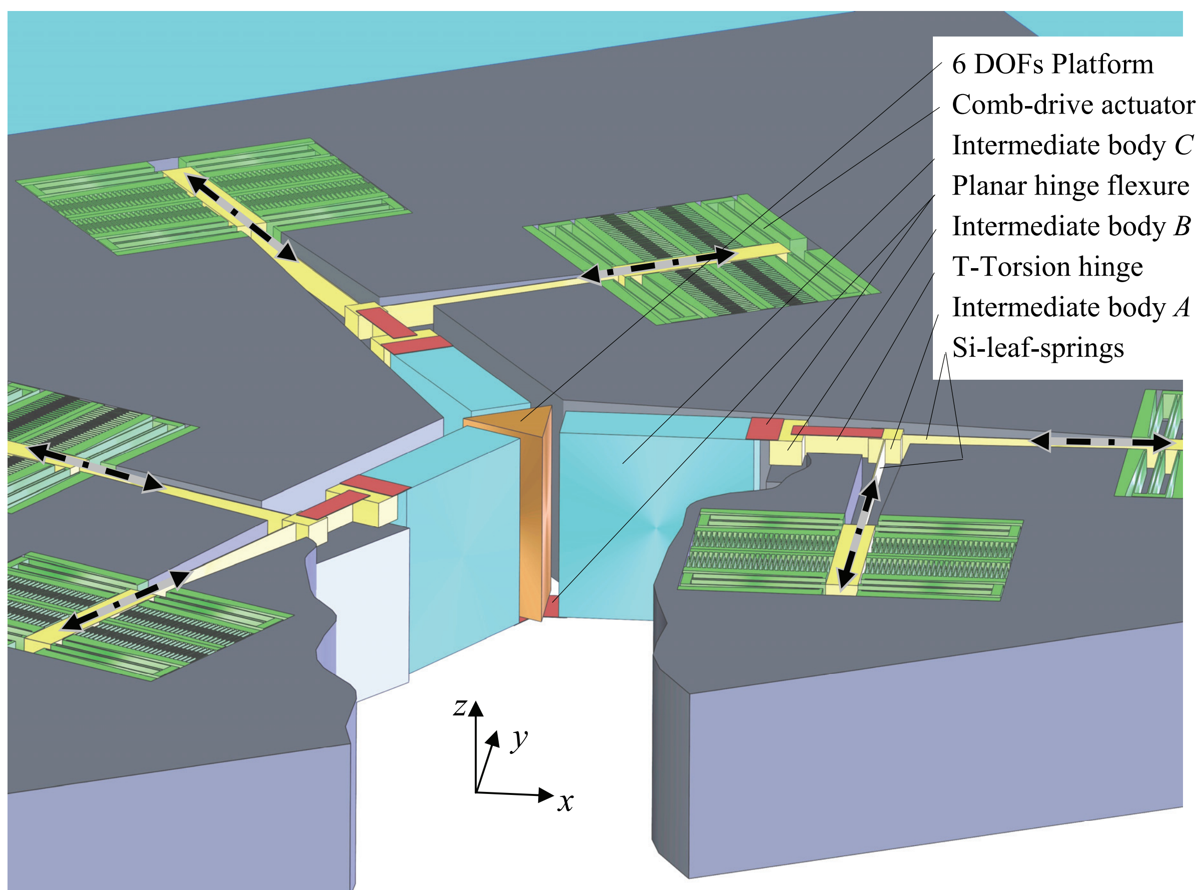

Figure 3.4: The planar hinge flexure concept. The dash-dotted arrows show the actuation direction of the 6 comb-drives.

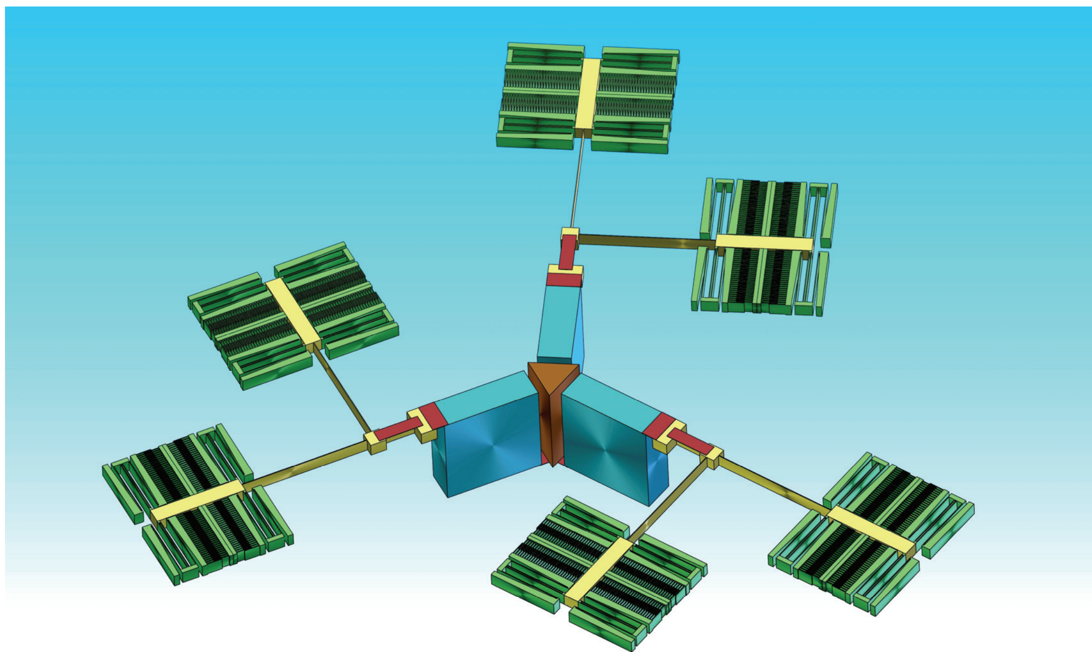

Figure 3.5: Overview of the movable parts in the planar hinge flexure concept.

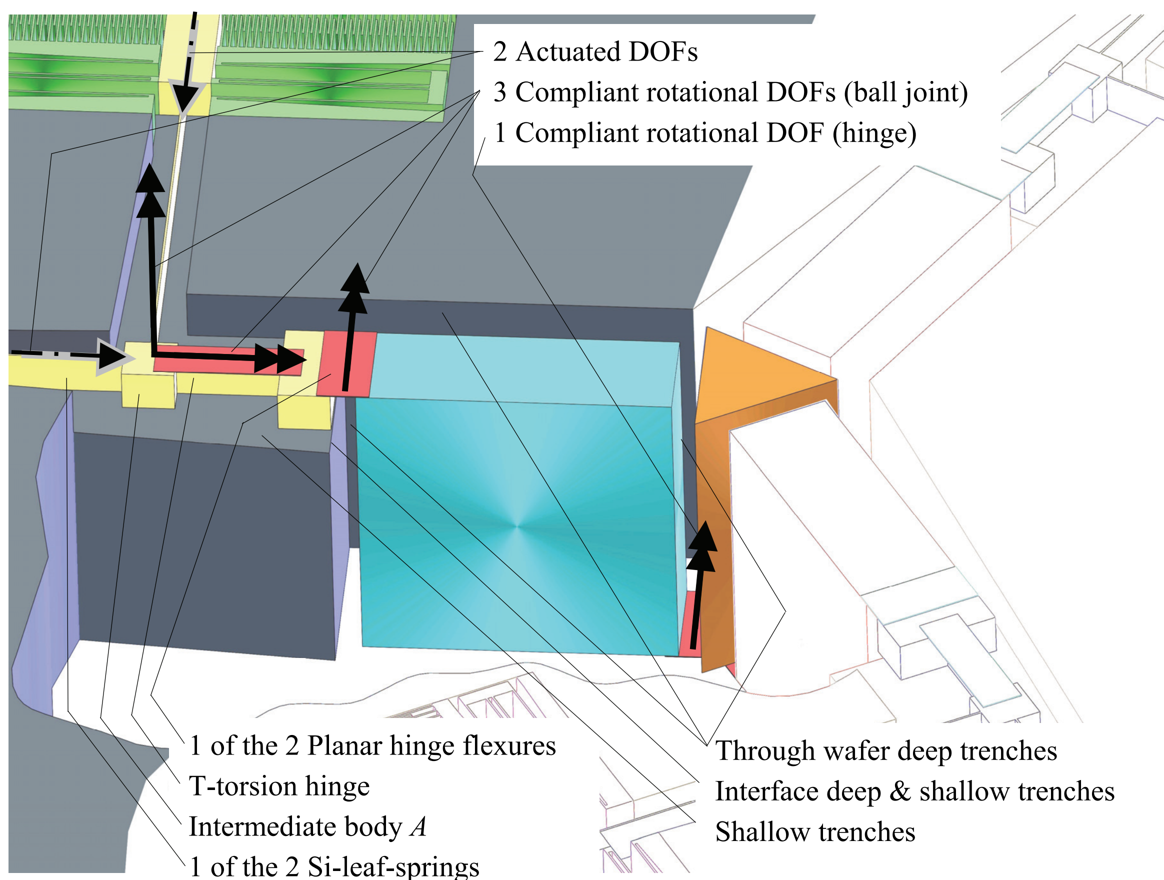

Figure 3.6: The DOFs of one of the three comb-pair sections. The 2 actuated and 4 compliant DOFs are shown. Combined with the other 2 comb-pair sections exactly 6 DOFs of the platform can be controlled.

Six comb-drives are arranged in 3 pairs, each pair controlling one of the 3 intermediate bodies *A* (Figure 3.4*)* in the two translational DOFs of the *xy*-wafer-plane. This is equivalent to the 2 DOFs *xy*-translational actuation of the intermediate bodies in Figure 3.2. The movable parts are shown without the stationary wafer in Figure 3.5. The movable parts are free of the wafer, being connected to the wafer only by the folded flexures of the straight guidance of the actuators. The comb-drives are connected by an Si-leaf-spring to the intermediate body *A*. The pair of Si-leaf-springs connected to the intermediate body *A* releases 1 DOF. This 1 DOF is the rotation around the intersection of the Si-leaf-springs (Figure 3.6). A T-torsion hinge, made out of one planar leaf-spring and a vertical leaf-spring, releases another DOF. The torsion hinge is mentioned in section 2.3. The relatively short leaf-springs “planar hinge flexures” of Figure 3.7 can be considered torsion hinges, leaving compliant only 1 DOF instead of 3 DOFs of a conventional leaf-spring as mentioned in section 2.4.

The compliant DOFs of the intersection of the 2 Si-leaf-springs, the T-torsion hinge and 1 hinge flexure together have 3 compliant perpendicular rotational DOFs, as shown in Figure 3.6. This makes them act like a ball joint, as shown in the kinematic concept of Figure 3.1. The second hinge flexure depicted in Figure 3.6 releases another DOF just like the hinge shown in Figure 3.1. In total, one of the three comb-pair sections leaves 4 DOFs compliant at the platform and actuates 2 DOFs. Combined with the other two comb-pair sections, exactly 6 DOFs have mobility and can be actuated, equivalent to the kinematic concept presented in section 3.3.

FABRICATION PROCESS

This concept does not include a fully detailed fabrication description. The process shown in Figure 3.7 is based on a SOI-wafer, which is preferably thinned to 300 μm. Roughly the process could include the following steps:

- Trench isolation (optional in a SOI wafer). Step 1, Figure 3.7. See section 5.5 for details.
- Deposition of the SiO_2 and SiRN front- and backside.
- Structuring the SiO_2 and SiRN front- and backside. Step 2.
- Deposition of an oxide buried mask for shallow and deep trenches. Step 3.
- Cover the front side buried mask shallow trenches with resist.
- DRIE backside deep trenches 100% through the wafer. Step 4.
- DRIE front side deep trenches 85% through the wafer.
- Open buried mask.

- DRIE front side shallow trenches and the remaining 15% of trenches. Step 5.
- Vapor HF oxide removal, release of devices. Step 6.

The SOI wafer could also be replaced by a TWIN [112] release step at the end.

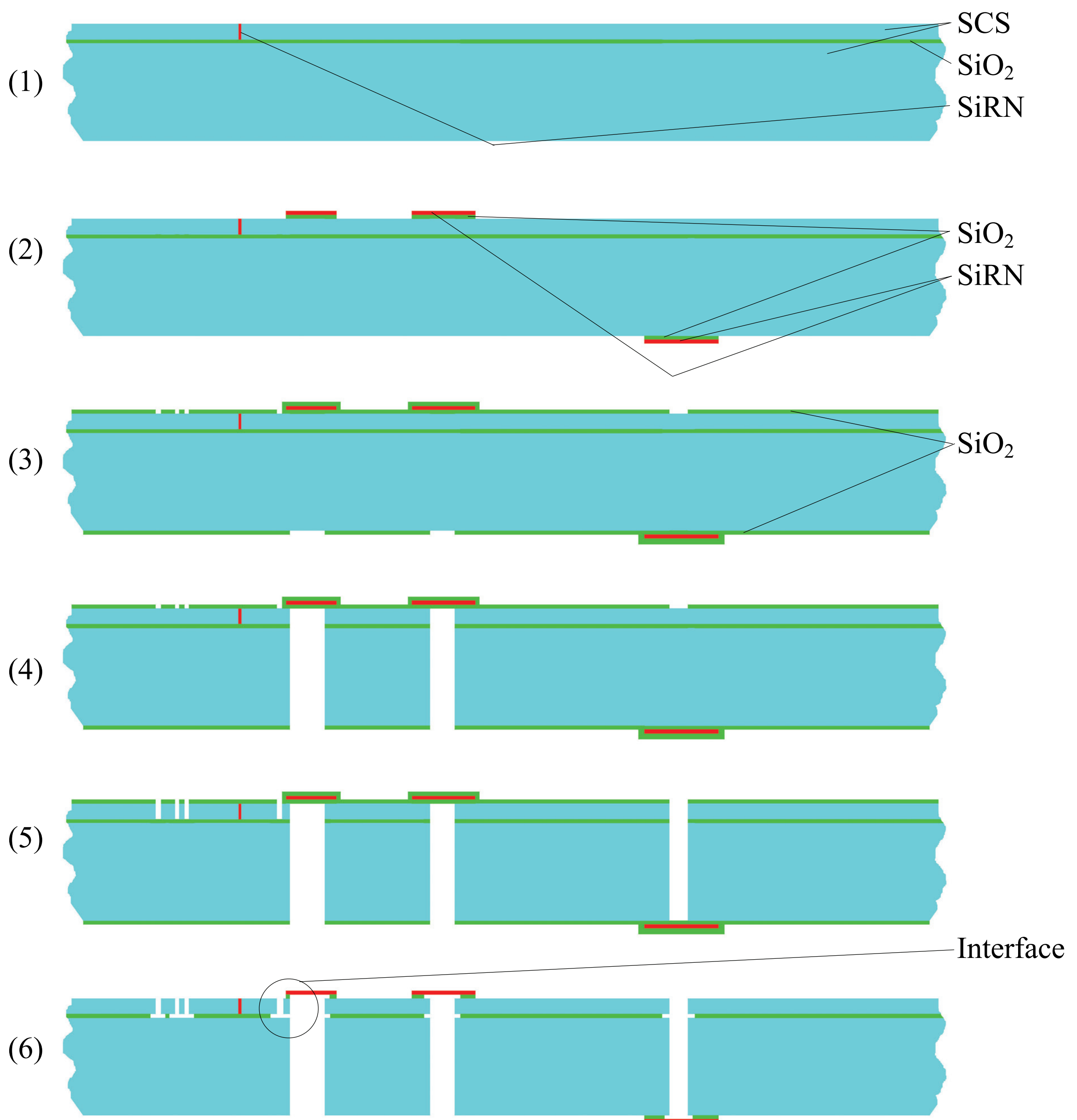

Figure 3.7: Fabrication process concept for the planar hinge flexure concept.

The weak points of the planar hinge flexure concept are:

- The interface, as shown in Step 6, Figure 3.7, between shallow and wafer deep trenches is difficult to fabricate. On one hand, the hinge flexure must stay attached to the SCS, on the other hand the SiO_2 of the SOI needs to be isotropically removed. Replacing the SOI wafer with TWIN technology does not help.
- Etching trenches through the wafer up to the leaf-springs at the other side does not result in precise dimensions at 300 μm deep.
- The trenches from the front- and backside connect. The wafer is perforated after the fabricating of the first deep DRIE trench. Heating during DRIE of the suspended parts can be a risk.
- There is a trade-off between the stiffness of the platform and the bending compliance of the planar hinge flexures. The platform needs to be stiff to reduce vibration mode amplitudes, which requires short leaf-springs. The leaf-springs need to be short as the low frequency vibration modes will load the hinge flexures with a bending moment. The bending compliance of the planar hinge flexures needs to be high to minimize actuation forces, requiring long hinge flexures.
- The suspended masses are quite large (also for MEMS).

3.5 Concept 2: Slanted hinge flexure concept

This concept makes use of the anisotropic etching properties of KOH on SCS [92] (section 2.2). KOH etching in SCS can result in a pyramid SCS structure if compensation structures are used [4] (section 4.2). The pyramid is used to deposit slanted hinge flexures on. The interface between the comb-drives in the device plate and the hinge flexures on the pyramid has been improved with respect to the interface of the planar hinge flexure concept. Since the hinge flexures are slanted, the stiffness of the platform has been increased, while the actuation compliance is kept high.

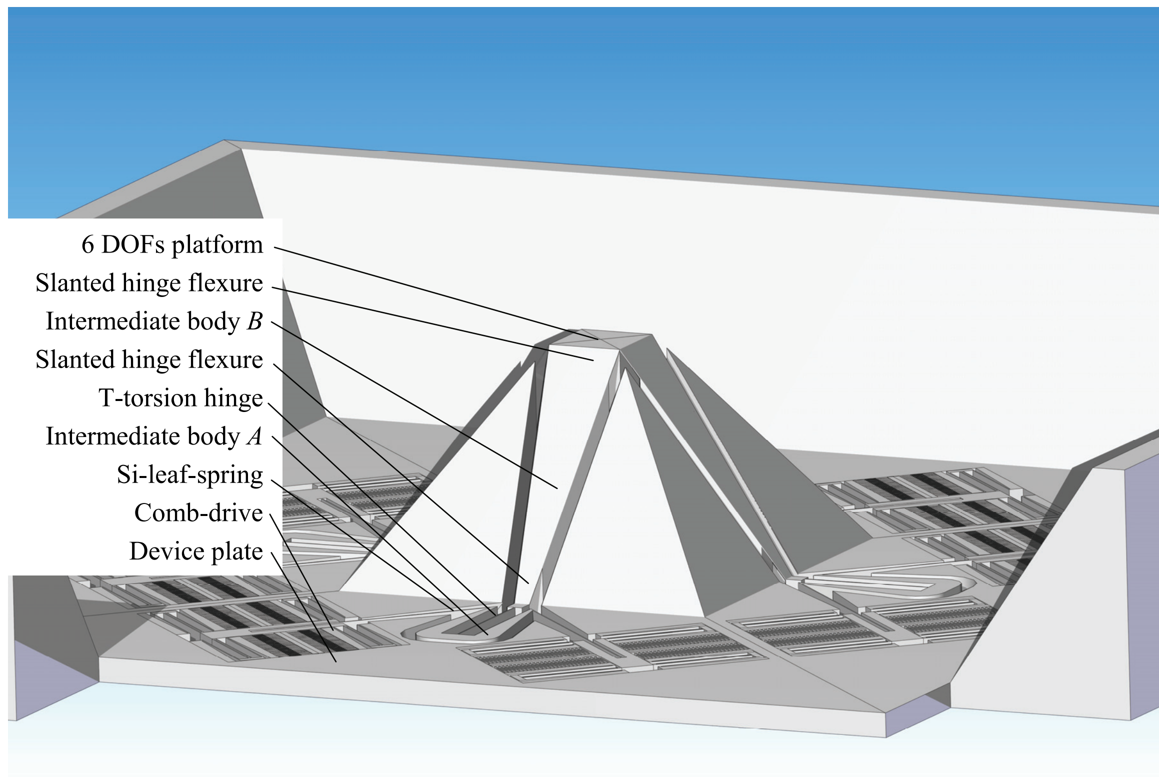

Figure 3.8: Side view of the slanted hinge flexure concept. For viewing purposes part of the side has been removed. 8 comb-drive actuators arranged in 4 pairs drive the stage.

KINEMATIC DESIGN

Eight comb-drives are arranged in 4 pairs. Each pair controls one of the 4 intermediate bodies *A* (Figures 3.8 & 3.9) in the two translational DOFs of the wafer-plane. The two Si-leaf-springs connecting at the intermediate body *A* are constraining 3 DOFs (Figure 3.10). 2 DOFs are actuated and one DOF, the rotation around the intersection of the leaf-springs, is compliant if there is no further attachment. A T-torsion hinge (Figure 3.11), made out of one planar leaf-spring and a vertical leaf-spring, releases another DOF (see section 2.3). The relatively short slanted leaf-springs, the “slanted hinge flexures”, have one compliant rotational DOF. External forces will load the hinges in a tensile direction. As a consequence, the platform stiffness will not be compromised by the bending compliance of the hinge flexures.

The kinematic concept is almost equivalent to the kinematic concept shown in section 3.3. The manipulator consists of 4 equivalent legs, as shown in Figure 3.9. Each leg consists of an elastic version of the ball joint and hinge. There are 3

compliant perpendicular DOFs: that of the intersection of the 2 Si-leaf-springs, the T-torsion hinge and 1 hinge flexure, as shown in Figure 3.10. This makes them act like a ball joint as shown in the kinematic concept of Figure 3.1. The second hinge flexure near the platform (Figure 3.10) releases another DOF just like the hinge in Figure 3.1. In total, one of the four legs leaves 4 DOFs compliant at the platform and actuates 2 DOFs. The combination with the other three legs results in an overactuated system being able to theoretically manipulate 8 DOFs. The 8 DOFS consists of 6 DOFs mobility of the platform and 2 internal deformation DOFs in the manipulator. However, the internal deformation will be limited, because the internal DOFs are relatively stiff and the actuator force is limited. Therefore the stress built up due to inaccuracies of the actuation will also be limited.

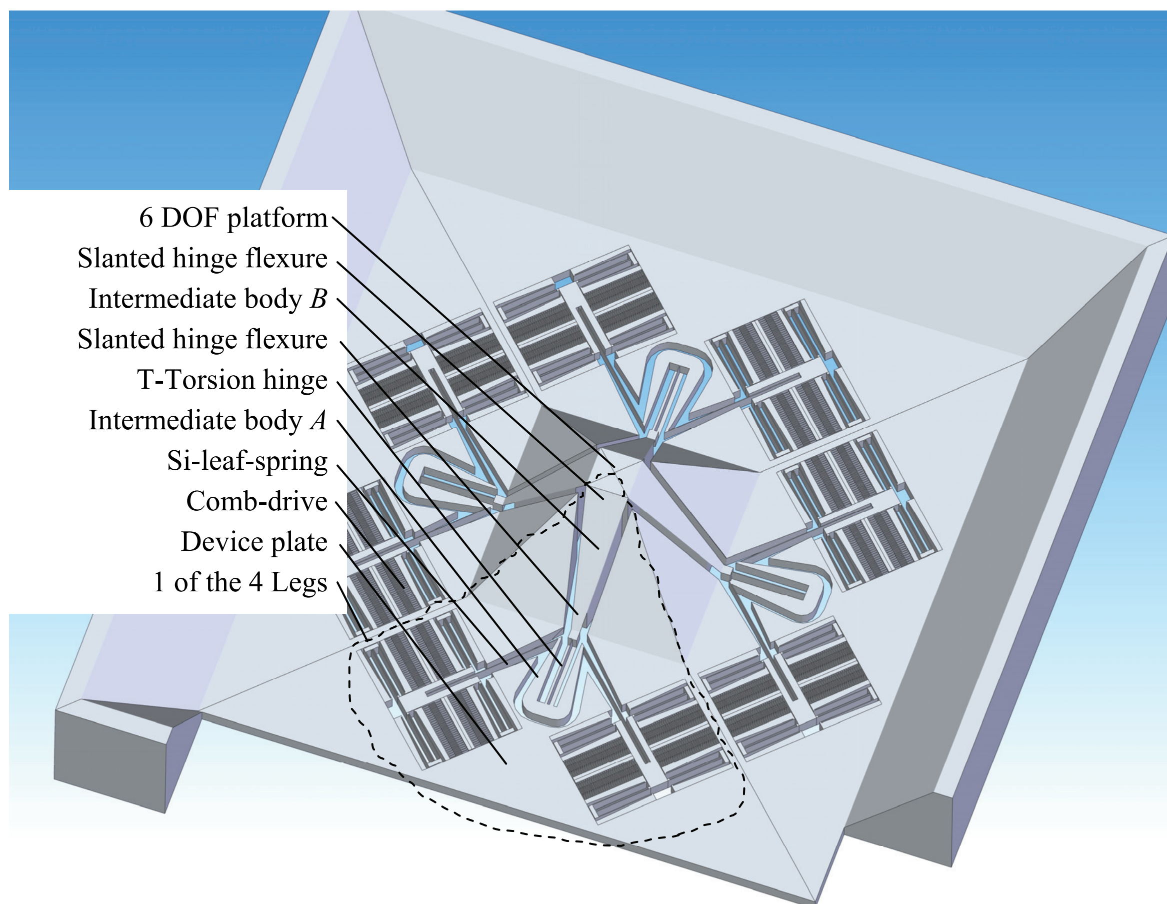

Figure 3.9: Top view of the slanted hinge flexure concept. For viewing purposes part of the side has been removed.

FABRICATION OF THE KOH PIT FOR THE SLANTED LEAF-SPRING

A KOH pit can conveniently supply a supporting mold for fabricating flat slanted leaf-springs. KOH etching of <100> SCS wafers results in pyramid-shaped pits. The flat sides are oriented along <111> planes. The depth of the pyramid depends on the etch time and the opening in the mask, which is the base of the pyramid. Pyramids out of SCS can also be made with KOH etching using compensation structures, as explained by Bao [4]. An example is shown in chapter 4, Figure 4.1. In this way, an SCS pyramid can remain within a KOH pit during etching (Step 1, Figure 3.12). The device plate structure between the SCS pyramid and the sides of the KOH pit can be a convenient device layer for the comb-drives and vertical leaf-springs. The interface between deep and shallow trenches as mentioned in the previous concept (Step 6, Figure 3.7) has been solved in this way. KOH pits in <100> SCS have rectangular shapes. Dividing 6 comb-drives over 4 sides results in asymmetry. Therefore, in this concept for reasons of symmetry 8 comb-drive actuators are incorporated (Figure 3.9).

STRUCTURING LEAF-SPRINGS IN THE KOH PIT

Basically, two ideas have been investigated for the purpose of structuring leaf-springs in a KOH pit:

- Shadow mask technology with metal evaporation.
- Spray resist combined with projection lithography.

Experiments using a shadow mask at Mesa$^+$ have been done by Burger et al. [17]. A combination of a low pressure evaporation technique, a small target and a long distance from the target to the wafer results in structures with a definition of 3 μm at a depth of 300 μm. The depth of the KOH pit in the wafer is 460 μm. The resolution at that depth is expected to be 5 μm.

Spray resist is sprayed instead of spun on the substrate, and has good coverage in KOH pits as well. The normal contact lithography, however, has limited depth of focus. A projection lens is used to enhance it. The capability of optical projection lithography may be calculated using the Rayleigh equations [92]:

$$R = \frac{k_1 \lambda}{NA} \tag{3.1}$$

where R [m] is the resolution, k_1 is a factor depending on the optical system, λ [m] is the wavelength and NA [-] is the Numerical Aperture.

$$D = \frac{k_2 \lambda}{NA^2} \tag{3.2}$$

where D [m] is the depth of focus and k_2 is a factor depending on the optical system. The depth of focus needs to be at least half the depth of the KOH pit, if the optical system is focused at half the KOH pit depth. A KOH pit in a normal <100> double sided polished wafer needs to be around 460 µm deep. According to Madou [92], current optical systems typically have a k_1 of 0.7 and a k_2 of 0.5. With the depth of focus known, the resolution can be calculated based on a certain wavelength as shown in Table 3.2.

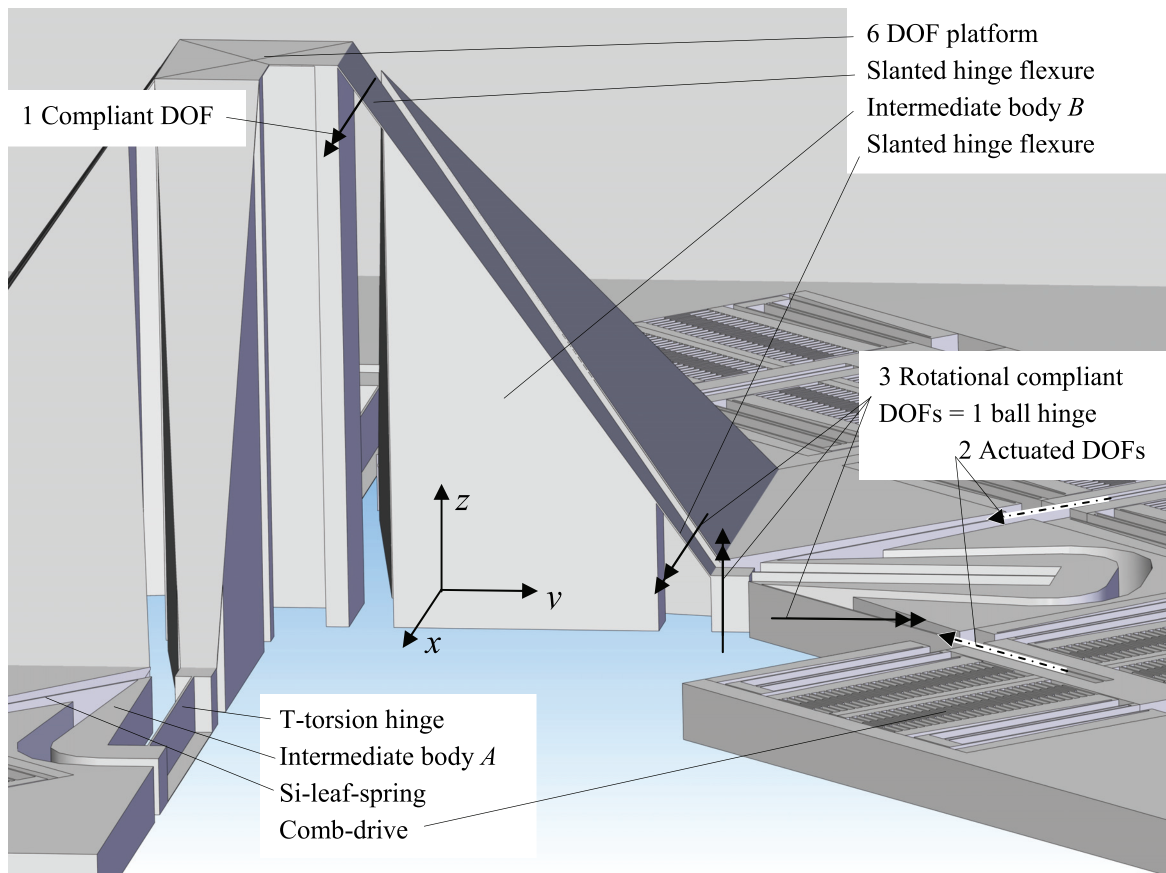

Figure 3.10: Side view of the slanted hinge flexure concept. For viewing purposes part of the pyramid, one of the comb-drives and one of the sides have been removed. Compared to the planar hinge flexure concept, the intersection of the Si-leaf-springs, which is the compliant DOF around the z-axis, is relatively close to platform. This enhances the Rz-rotation of the platform at a certain actuator displacement.

The spray resist in combination with projection lithography is a more feasible solution for mass production, as the shadow mask is contaminated during evaporation. However, the number of TEM manipulators produced each year is small. To match the resolution of the shadow mask technology an optical wavelength source of less than 192 nm is required. Although sources with this type of small wavelengths exist, they are expensive and are not present in a clean room facility. Therefore, the shadow mask technology will be used to structure the slanted hinge flexures.

λ	*NA*	k_1	k_2	**Resolution**	**Depth of Focus**
nm	-	-	-	µm	µm
632	0.0371	0.7	0.5	12	230
436	0.0308	0.7	0.5	10	230
365	0.0282	0.7	0.5	9	230
192	0.0205	0.7	0.5	7	230
13.5	0.0054	0.7	0.5	2	230

Table 3.2: The resolution and the depth of focus of an optical projection system based on the Rayleigh equations [92].

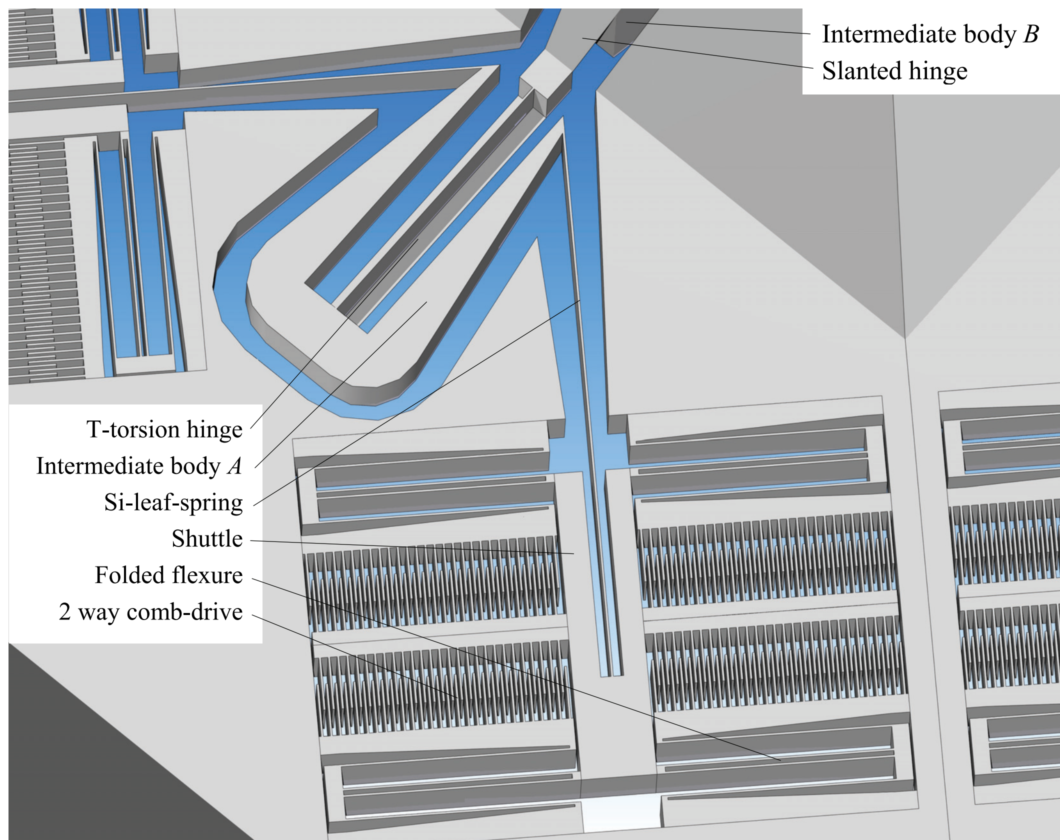

Figure 3.11: Top view of a detail of the slanted hinge flexure concept. The Si-leaf-spring has been extended in the comb-shuttle to gain compliance with the same overall dimensions. To gain space intermediate body A is horseshoe shaped.

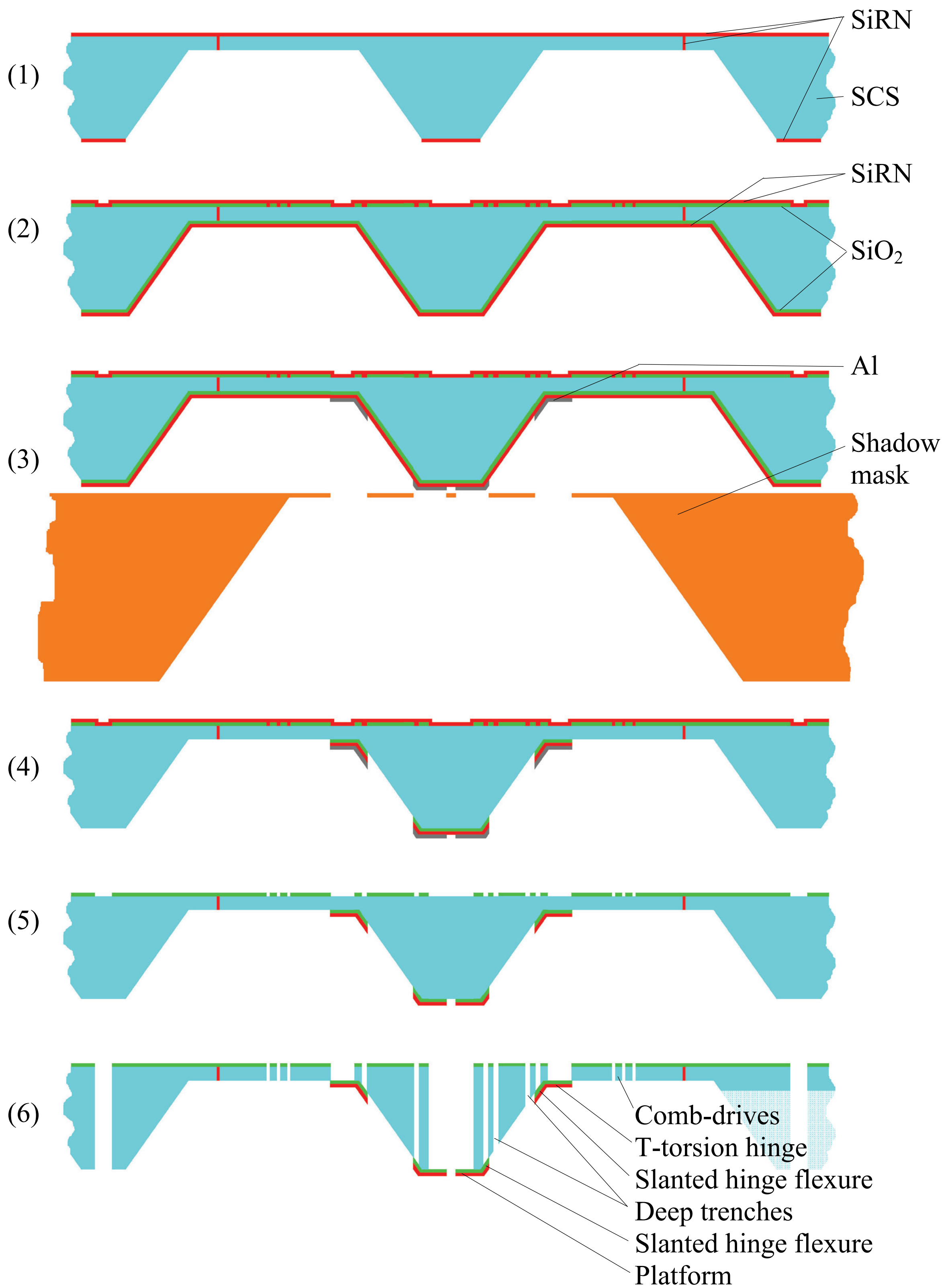

Figure 3.12: Fabrication process concept for the slanted hinge flexure concept.

FABRICATION PROCESS CONCEPT

This concept does not include a fully detailed fabrication description. The process is shown in Figure 3.12, and roughly could include the following steps:

- Trench isolation. See section 5.5 for details.
- Deposition of SiRN mask with compensation structures for KOH etching.
- KOH etching until trench isolation is reached. Step 1, Figure 3.12.
- Stripping of SiRN mask.
- Deposition of SiO_2 buried mask.
- Deposit SiRN layer (the slanted hinge flexures). Step 2.
- Evaporate Al through shadow mask. Step 3.
- RIE SiRN and SiO_2 backside. Step 4. (Structuring of the slanted hinge flexures).
- Strip Al backside, strip SiRN front side. Step 5.
- Use extra resist mask or second shadow mask for covering shallow trenches.
- DRIE deep trenches up to 90%.
- Remove resist or shadow mask.
- DRIE shallow and deep trenches last 10%. Step 6.
- Optionally use vapor HF oxide removal.

The strong points of the slanted hinge flexure in comparison with the planar hinge flexure concept are:

- The interface between shallow and wafer deep trenches is easier to make.
- Improved stiffness of the platform. External loads on the platform result in tensile or compressive loading of the slanted hinge flexures.
- The intersection of the Si-leaf-springs, which is the compliant DOF around the *z*-axis, is relatively close to the platform. This enhances the *Rz*-rotation of the platform at a certain actuator displacement.

This concept, however, has some weak points:

- The suspended masses are quite large (also for MEMS).
- The out-of-plane stiffness is jeopardized by the cascading of the Si-leaf-springs, T-torsion hinge and the two planar hinge flexures.
- The dynamic behavior will suffer from the compromised stiffness and relatively large masses.

- The cascading of elastic elements requires a lot of space.
- The robustness will also suffer from the cascading.
- Eight actuators require a lot of space and wiring.
- A special control strategy is necessary to manipulate in 6 DOFs.
- Etching trenches through the wafer up to the planar hinge flexures at the other side does not result in precise dimensions at 300-460 μm deep.
- The wafer is perforated during the last DRIE. Heating of the suspended parts by the ion bombardment from DRIE can be a risk as the heat has to flow through the leaf-spring to the surroundings.

3.6 Concept 3: Slanted leaf-spring concept

The slanted leaf-spring concept (Figure 3.13 & 3.14) is strongly based on the slanted hinge flexure concept. The main differences are:

- Reduction of the cascading of elastic elements.
- Reduction of the suspended mass.
- Making the hinge flexures much larger, by turning them into leaf-springs, decreases the relative dimensional uncertainty due to fabrication.
- Reduction of the number of actuators from 8 to 6.

KINEMATIC DESIGN

The kinematic concept is almost equivalent to the kinematic concept shown in Figures 3.1 and 3.2. Two Si-leaf-springs, which are connected at the intermediate body, leave 1 DOF compliant, the rotation around their intersection. The slanted leaf-spring releases 3 DOFs, which can be regarded as 3 rotational DOFs, as shown in Figure 3.15. The 3 compliant DOFs near the intermediate body can be regarded as a ball joint, equivalent to the ball joint in Figure 3.2. Although these three rotational compliant DOFs are not orthogonal, they do act as an elastic ball joint, because they do not coincide, are not parallel and intersect close to each other. The compliant DOF near the platform can be regarded as the hinge equivalent of Figure 3.2. The 3 slanted leaf-springs together determine the 6 DOFs position of the platform. To give an impression of the dimensions: the overall size is 4.9 x 5.2 mm. The platform is elevated 460 μm above the comb-drives, folded flexures and Si-leaf-springs. Figure 3.14 gives an additional impression of the design.

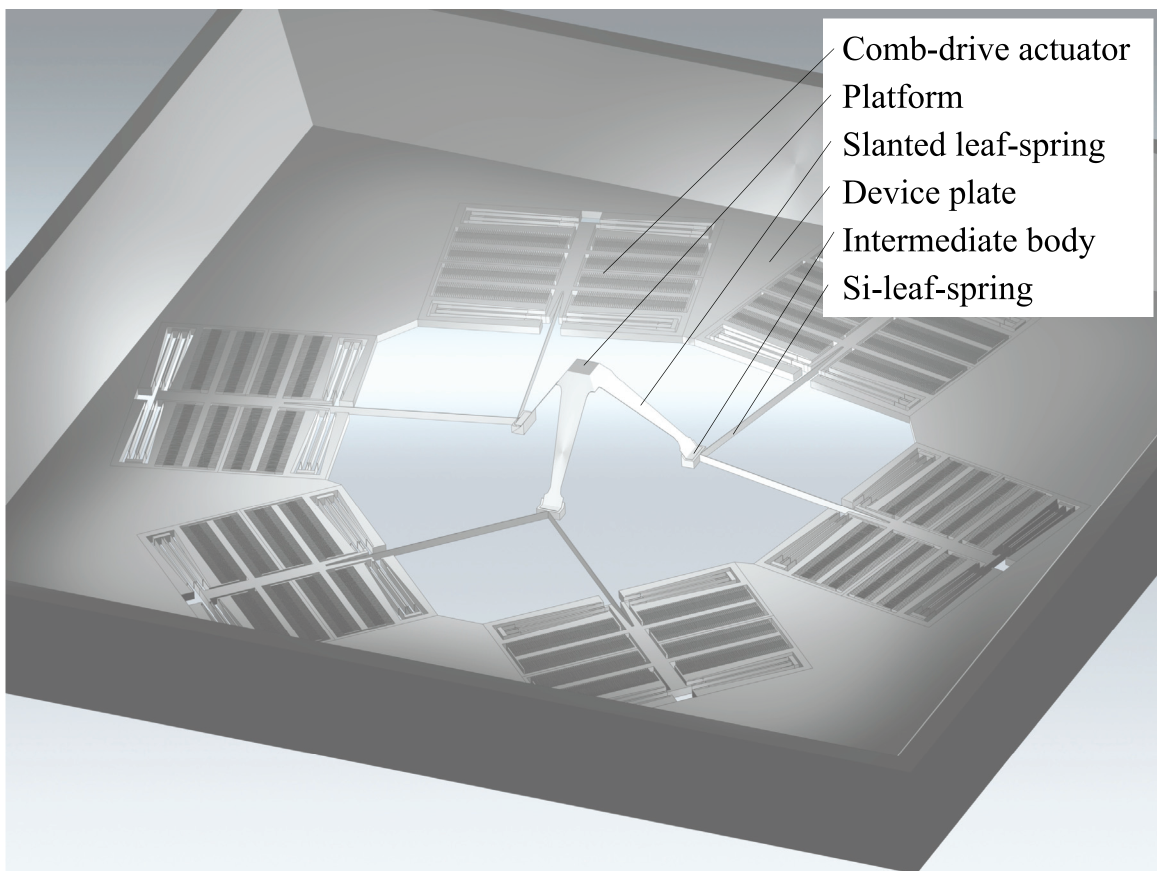

Figure 3.13: 3D-view of the slanted leaf-spring concept. The overall dimensions are 4.9 x 5.2 mm.

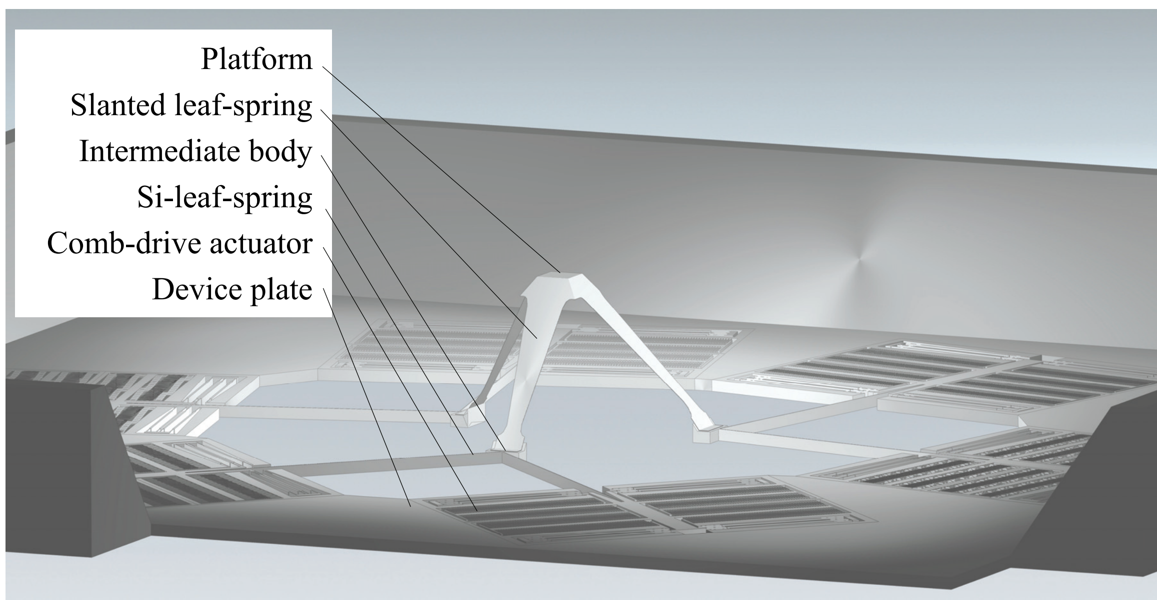

Figure 3.14: 3D-view of the slanted leaf-spring concept. For viewing purposes part of the side has been removed.

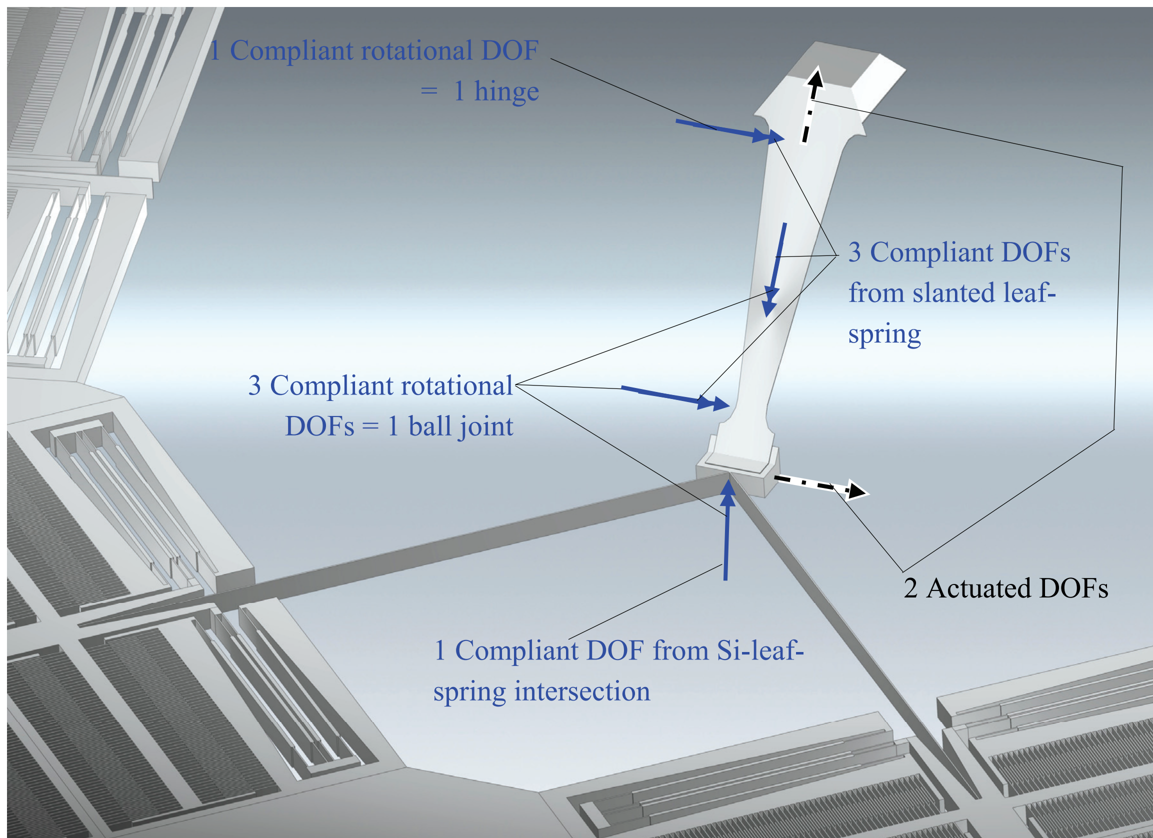

Figure 3.15: The 6 DOFs (2 actuated and 4 compliant) of the platform defined by 1 leg. The slanted leaf-spring releases 3 DOFs. The intersection of the Si-leaf-springs releases 1 DOF. The 3 compliant DOFs near the intermediate body can be regarded as a ball joint, equivalent to the ball joint in Figure 3.2. The compliant DOF near the platform can be regarded as the hinge equivalent of Figure 3.2.

FABRICATION PROCESS

The fabrication process of this design closely resembles that of the slanted hinge flexures concept shown in Figure 3.12. The main differences are the shape and the DRIE release of the SiRN slanted leaf-springs. Details of the fabrication process of this concept can be found in chapter 4, Figure 4.3. The process can be adapted for polysilicon or SiO_2 slanted leaf-springs. However, based on experience in the clean room SiRN is more robust. Polysilicon could have the advantage of electrically grounding the platform easily and providing the opportunity to measure the stress in the poly because it can be made piezo-resistive.

The strong points of the slanted hinge flexure in comparsion with the planar leaf-spring concept are:

- Less cascading of elastic elements.
- Improved stiffness.
- Lower suspended mass.
- Improved vibration mode frequencies.
- Less spacious design.
- Easier actuation with 6 instead of 8 actuators.
- The robustness of the platform when touched by an external manipulator of the slanted leaf-spring concept is better than the robustness of the slanted hinge flexure concept. During attachment of a sample by a probe tip, buckling of the slanted leaf-springs may occur. The buckling makes the manipulator robust for small misalignments of the probe tip with respect to the manipulator. The encountered stress is lower at a certain displacement when compared to the stress encountered in the slanted hinge flexure concept. The slanted hinge flexure will break easier during buckling.
- Uncertainty in releasing the slanted leaf-springs by DRIE does not result in relatively large geometrical uncertainties of the leaf-spring.

This concept, however, has some weak points:

- The presence of large open spaces between the Si-leaf-springs leads to ARDE effect (section 4.2).
- The wafer is perforated during the last DRIE. Heating of the suspended parts by the ion bombardment from DRIE can be a risk because the heat has to flow through the leaf-spring to the surroundings.
- The asymmetry due to a reduction from 8 to 6 actuators results in a lower buckling load (section 4.5.9).
- The compensation structures for KOH etching are rather wide and require a larger platform. See section 4.2 for details.

The abovementioned weak points have been taken into account in the final design, which is presented in chapter 4.

3.7 Slanted leaf-spring concept with clamping mechanisms

The passive *stability* of the manipulator can be enhanced by unpowered blocking of the manipulator using a clamping mechanism once it has reached its targeted position (see section 3.2.6 for details). The cross-talk between the electron beam of the TEM and electric or magnetic fields from the actuators of the manipulator can be decreased. Additionally, by using a clamping mechanism the manipulator can be switched between compliant actuation modes for positioning and high frequent deformation vibration modes during imaging. A mechanical clamp with a locking device is investigated for that purpose. Each of the 6 actuators of the manipulator should be clamped, as shown in Figure 3.16. The design of the clamping mechanism will be discussed in chapter 5.

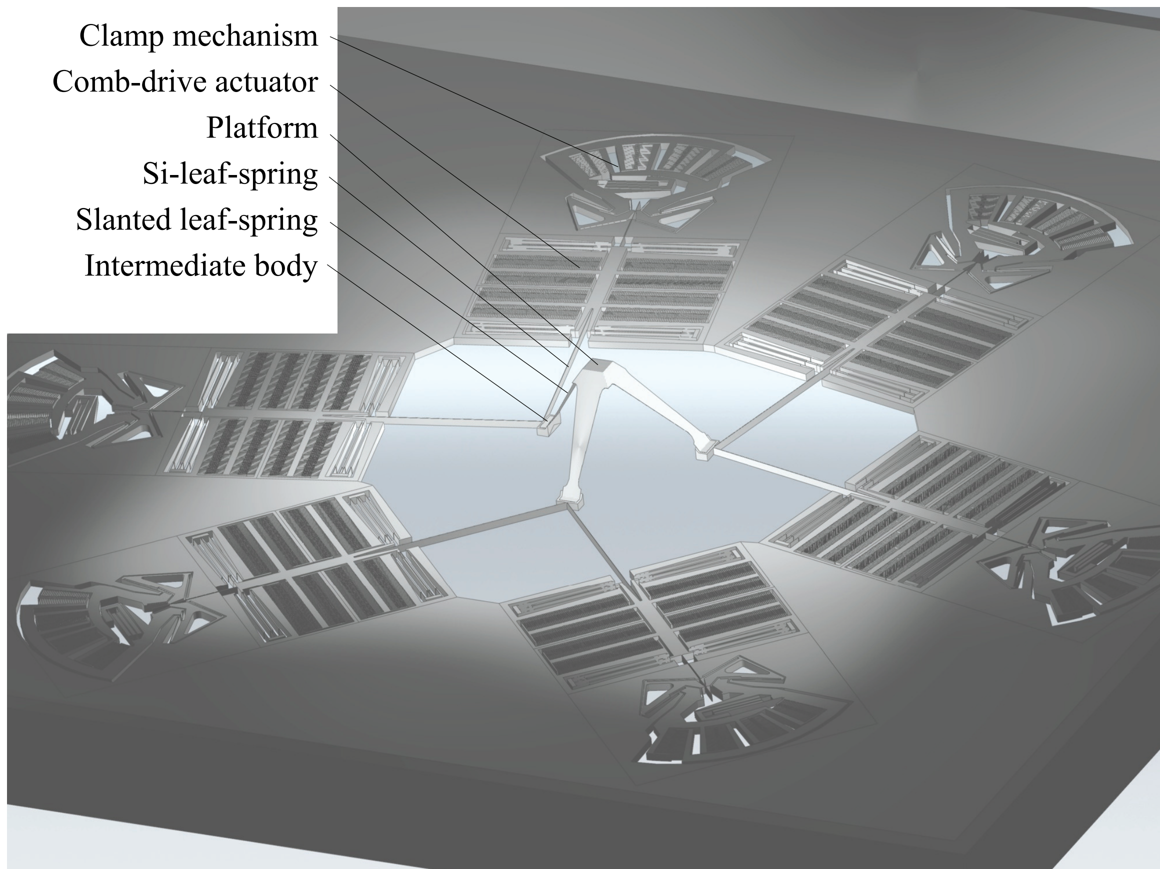

Figure 3.16: Concept of the 6 DOFs MEMS-based manipulator with clamping mechanisms on each of the actuators.

3.8 Conclusions

Although some drawbacks remain, the slanted leaf-spring concept offers the best synthesis of mechanical and fabrication technical design choices of the presented concepts. The following design choices have been made:

- The design is an exact kinematic constraint design (at least as much as possible).
- The mechanism is fully compliant (no friction, hysteresis, wear, play).
- The MEMS-based manipulator is designed like a parallel manipulator.
- 6 comb-drives actuate the system.
- One single technology can be used to manufacture six electrostatic lateral comb-drive actuators of the same type.
- 3 SiRN slanted leaf-springs deposited on the <111> sides of a KOH etch pit convert the in-plane actuator motion to the 6 DOFs motion of the platform.
- Symmetry has been compromised in favor of using less space.
- A KOH etch pit with compensation structures is used to create the slanted leaf-springs and a device plate (Figure 4.4) for the comb-drives, folded flexures and Si-leaf-springs.
- The KOH pit conveniently connects the slanted leaf-springs to the device plate.
- Trench isolation technology is used for electrical insulation.
- A shadow mask is used to structure the SiRN slanted leaf-springs in the KOH pit.
- The process is compatible with the clamp fabrication process.

In chapter 4 the slanted leaf-spring concept will be detailed and modeled.

Chapter 4

DESIGN AND MODELING OF THE SIX DOFs MEMS-BASED MANIPULATOR

The concept for a parallel kinematic MEMS-based precision manipulator as proposed in chapter 3 will be detailed in this chapter. A 5 mask fabrication process based on the slanted leaf-spring concept described in chapter 3 is presented. With the rough dimensions of the flexure elements known from the applied process, the manipulator is analyzed with geometric non-linearity taken into account. Exact kinematic constraint design is a necessity to obtain both a high actuation compliance and high vibration mode frequencies. Comb-drive actuator dimensions are derived. Although the design incorporates relatively long and slender leaf-springs, the first vibration mode frequency is 3.8 kHz with blocked actuators. The typically relatively large deflections of compliant mechanisms in MEMS result in position-dependent stiffness. The buckling force of the platform is 0.2 mN. Stress caused by internal or external causes is low. The 0.1 nm/min positional stability of the sample is not jeopardized by disturbances, as can be expected in a TEM. The total design is a synthesis of the fabrication process design and an exact kinematic constraint structural design.

4.1 Introduction

In the next section the 6 DOFs MEMS-based manipulator concept, as presented in chapter 3, will be developed into a design. The fabrication process will be detailed. With the fabrication processes known, the manipulator can be dimensioned. The positional errors made by calculating the actuation force and displacement using a first order geometrical linear transfer function are analyzed. Stability regarding high frequencies (see the specifications in section 1.6) is analyzed by calculating the first

vibration mode frequencies and corresponding vibration mode shapes. The first vibration mode frequency decrease relating to displacement of the platform is investigated. With respect to robustness the buckling load and the stress caused by internal deformation or external loading is discussed. The thermal stability is analyzed.

The MEMS-manipulator conceptual design was discussed in chapter 3. The slanted leaf-spring concept will be detailed in this chapter. The slanted leaf-spring concept (section 3.6) features the following design choices:

- The design is exactly kinematically constrained (at least as much as possible).
- The mechanism is fully compliant (no friction, hysteresis, wear, play).
- The MEMS-based manipulator is a parallel manipulator, kinematically.
- 6 comb-drives actuate the system.
- One single technology can be used to manufacture six electrostatic lateral comb-drive actuators of the same type.
- 3 SiRN slanted leaf-springs deposited on the <111> sides of a KOH etch pit convert the in-plane actuator motion to 6 DOFs.
- A KOH etch pit with compensation structures is used to create the slanted leaf-springs and a device plate (Figure 4.4) for the comb-drives, folded flexures and Si-leaf-springs.
- The KOH pit conveniently connects the slanted leaf-springs and device plate.
- Trench isolation technology is used for electrical insulation.
- A shadow mask is used to structure the SiRN slanted leaf-springs in the KOH pit.
- The process is compatible with the clamp fabrication process, as will be explained in sections 4.2 and 5.5.

First, the fabrication process will be detailed. Subsequently, a final design can be proposed.

4.2 Process design

The fabrication process consists of 5 masking steps. The 3 mask fabrication process of the clamp is compatible with the fabrication process of the manipulator. The process will be presented in the next section. The full process document is given in Appendix G.

The process starts with a highly doped (p^+) <100> double sided polished wafer. The resistivity varies between 0.15-0.19 Ωm. In Olin 907-17 resist the mask for the 2 μm wide trench isolation is developed (Figure 4.3, step 1). The trenches are etched to a depth of 40 μm by Bosch etching with an Adixen 100 SE plasma etch system. This step defines the thickness of the device plate (Figure 4.4) containing the comb-drives, folded flexures and Si-leaf-springs (h_{si} Figure 4.6). The device plate thickness will be a few μm less than the depth of the trench isolation. Next, the resist is stripped in a barrel etcher (O_2 plasma). Since the resist is annealed during the Bosch etching, the remaining fluor-carbon side wall protection is ashed in an oxidation oven at 800˚C. The remaining oxide is removed by 50% HF etching. In the trenches, a 0.8 μm thick layer of low stress SiRN by LPCVD is deposited (Figure 4.3, step 2). The SiRN is removed from the top side by selective dry etching on an Adixen 100 DE system. A dry oxidation at 800˚C removes all Fluor Carbon residue from etching. After removing the thermal oxide by HF 1% etching, a second layer of SiRN, 1.6 μm thick, is deposited to fill the trenches completely. A more detailed schematic of the two-step filling of the trenches is given in Figure 5.6a, with photos presented in Figure 5.7. At the backside an Olin 907-17 resist layer is spun. By lithography and development a backside KOH mask with compensation structures is transferred in the resist. The compensation structures are necessary to leave an SCS pyramid without the edges being etched. <100> compensation structures are used, which result in a pyramid with flat sides (Figure 4.2). The flat sides are necessary to obtain flat slanted leaf-springs. The size of the <100> structures are a drawback. The size of the platform is based on the compensation structure size (Figure 4.1). Although Bao [4] describes smaller compensation structures, they are sensitive to alignment. The width of the compensation structure requires the platform to be > 1.3 mm long and wide (l_{pl} and w_{pl}, Figure 4.6).

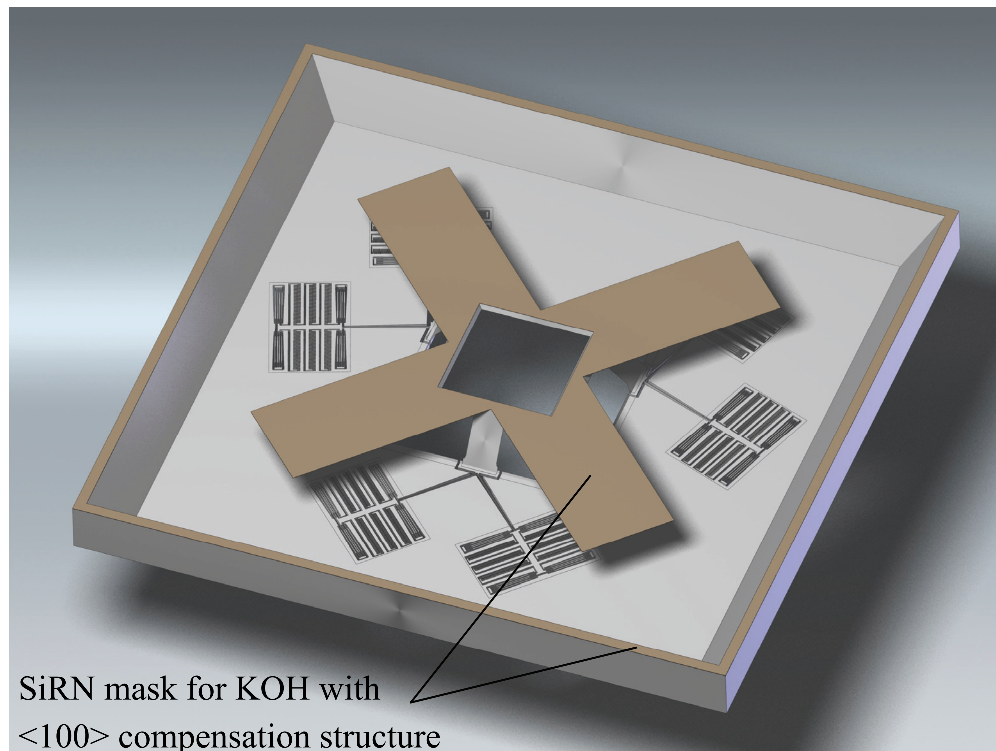

Figure 4.1: The compensation mask is shown in the final device. The width of the <100> compensation structure defines the smallest size of the platform.

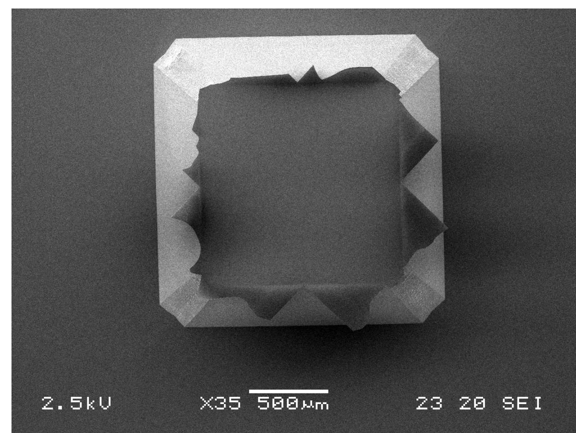

Figure 4.2: SEM picture of an SiRN mask for KOH with <100> compensation structure. The unsupported SiRN breaks during KOH etching. The pyramid has been overetched resulting in the <411> planes at the corners.

The Adix 100 DE system is used to transfer the mask from the resist into the SiRN (Figure 4.3, step 3). The polymers are stripped in HNO_3 fumic acid. A short HF 1% dip is used to remove the native oxide just before KOH etching. KOH is used to etch along the <111> planes until a plate thickness of 35 µm is left (h_{si}), and the SiRN filled trenches are visible from the backside (Figure 4.3, step 4). An RCA-2

cleaning is necessary to remove the potassium from the silicon. The SiRN is stripped both on the front- and backside with an Elektrotech PF310/340 system without a load-lock (Figure 4.3, step 5). Load-locks with their loading arm potentially damage the fragile thin plate wafer and are therefore used only if absolutely necessary. A 1.5 μm thick low-stress SiO_2 TEOS layer is deposited by LPCVD (Figure 4.3, step 6). The topside TEOS functions as a buried mask of the comb-drives and folded flexure. The bottom side acts as a protection layer for the slanted SiRN leaf-springs during etching later on. The TEOS is annealed at 900˚C for an outgassing of H_2 and to avoid cracking of the oxide layer when SiRN is deposited later on. Resist Olin 907-17 is spun on the topside. The resist is exposed and developed with a mask containing the comb-drive structures, folded flexures and Si-leaf-springs. A substrate wafer with cavities and air channels which are 150 μm deep is bonded to the device wafer with Fomlin oil. The air channels release the air of the KOH cavities when the substrate and device wafer assembly is put in an evacuated chamber. The resist mask is etched selectively in the oxide by an Adixen 100 DE etcher (Figure 4.3, step 7). Since the helium backside cooling is less with the extra substrate wafer, the electrode temperature is set at -20˚C. The substrate is removed and the device wafer is cleaned with IPA. The polymers are removed in a barrel etcher. By LPCVD a low stress 0.7 μm thick SiRN layer is deposited which will become the structural layer of the slanted leaf-springs (Figure 4.3, step 8). In this step, the thickness t_{sl} of the slanted leaf-springs is defined. The shadow mask is aligned and fixed with clamps to the backside. An aluminum layer of 0.3 μm is evaporated through the holes in the shadow mask, which have the shape of the slanted leaf-springs (Figure 4.3, step 9). The long distance from the aluminum target combined with the large mean free path makes copying the shadow mask to the bottom of the KOH etch pit possible within several microns [17]. The aluminum structure is transferred into the SiRN by cryogenic SF6 dry SiRN etching on the Adix 100 SE system (Figure 4.3, step 10), which is a process to selectively dry etch SiRN with respect to SiO_2. The substrate has to be used for this operation. Alternatively, the Electrotech PF310/340 can be used. An in-situ interferometer is used to detect the point at which the interface SiRN to SiO_2 is reached. The aluminum is stripped in a wet bench for aluminum etching (Figure 4.3, step 11). The topside SiRN is removed by cryogenic SF6 dry SiRN etching on the Adix 100 SE system (Figure 4.3, step 12) (or the Electrotech PF310/340 with interferometer is used). During this operation, the vertical walls of SiRN in the buried SiO_2 mask will remain. Compensation is therefore needed in the SiO_2 device mask. The Adix 100 SE is used with an Aspect Ratio Compensated Etching (B-ARCE-1) procedure to etch the buried mask into the silicon (Figure 4.3, step 13). The ARDE effect,

shown in Figure 5.9, needs to be minimized as much as possible. The SiO_2 layer at the back serves as an etch stop. The substrate wafer has to be used. Next, the second shadow mask is used to protect the comb-drive, folded flexure and Si-leaf-springs. An isotropic plasma is used on the Adix 100 SE with high selectivity for Si with respect to SiO_2, to etch the bulk silicon (Figure 4.3, step 14). The thickness of platform h_{pl} is defined. This procedure does not heat the device wafer considerably. Vapor HF is used to remove the SiO_2 (Figure 4.3, step 15). An option to fabricate horizontal leaf-springs in SiRN is also shown in step 15. Combined with vertical Bosch etched leaf-springs, torsion hinges can be made.

The substrate is fabricated using one mask. The Elektrotech PF310/340 is used for silicon etching, because the air channels have to connect all the way to the sides of the wafer (some etching machines use clamping rings, which prevent etching at the sides of the wafer). The cavities and air channels are 150 μm deep.

Fabrication of the two shadow masks (Figure 4.3, step 9 and step 14) requires three mask steps. A mask buried in SiO_2 is made. It will be used to etch a small step in depth in the silicon. The second mask step is a resist mask spun over the SiO_2-buried mask. It defines the structured holes in resist. The hole structure is etched with a Bosch process in silicon up to 20 μm depth. The resist is stripped and so the buried oxide mask is opened. By Bosch etching, both the hole structure and the small step are etched deeper into the silicon. A SiRN layer is deposited at the front- and backside.

The third mask is a KOH mask structured in SiRN at the backside. The KOH is used to etch through the wafer until the first SiRN structures of the front side can be seen from the backside of the wafer. The SiRN is removed. The second shadow mask, used for dry etching (Figure 4.3, step 14), is oxidized at the end of the process to better withstand the DRIE when used.

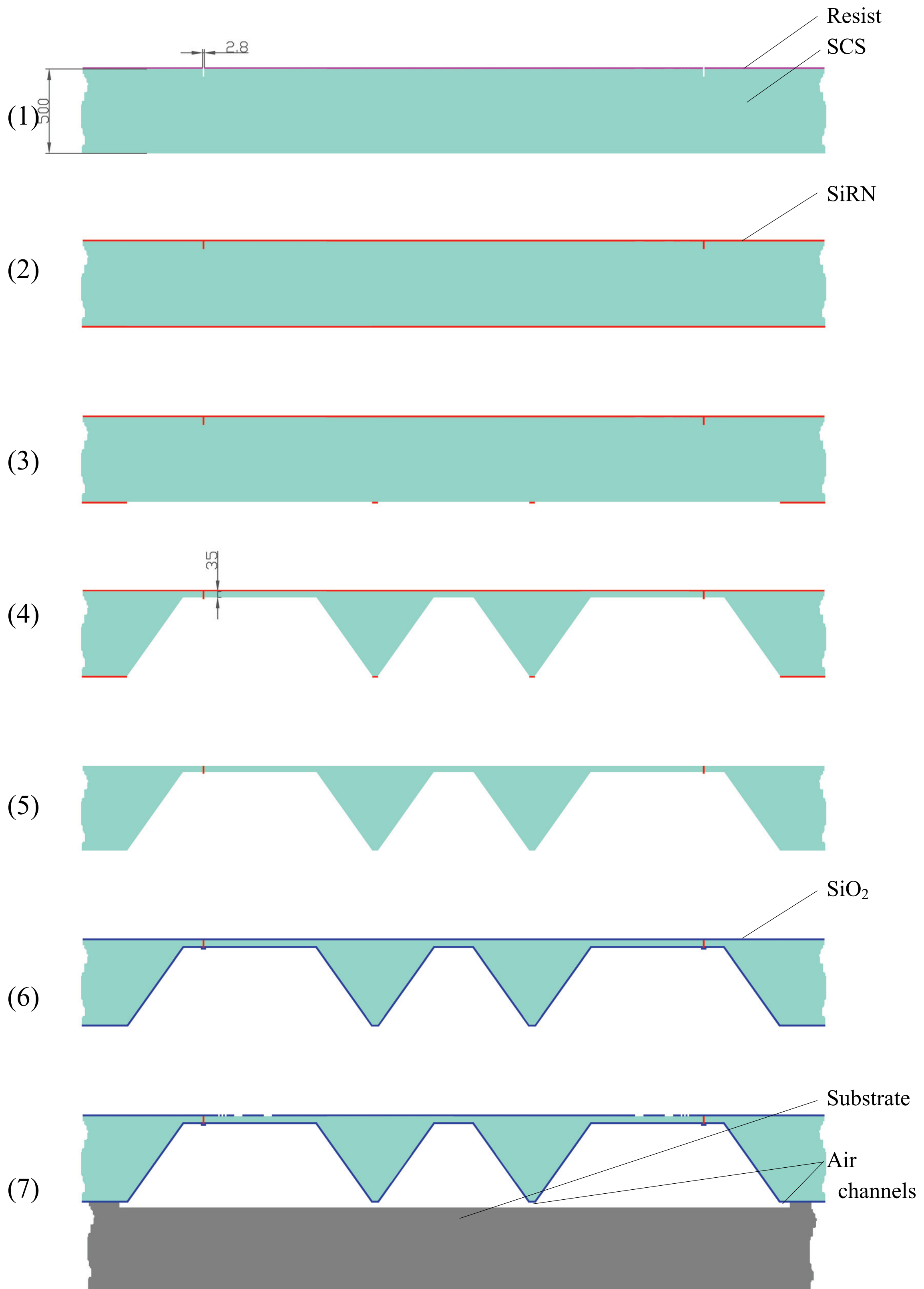

Figure 4.3a: The process for the fabrication of the 6 DOFs MEMS-based manipulator

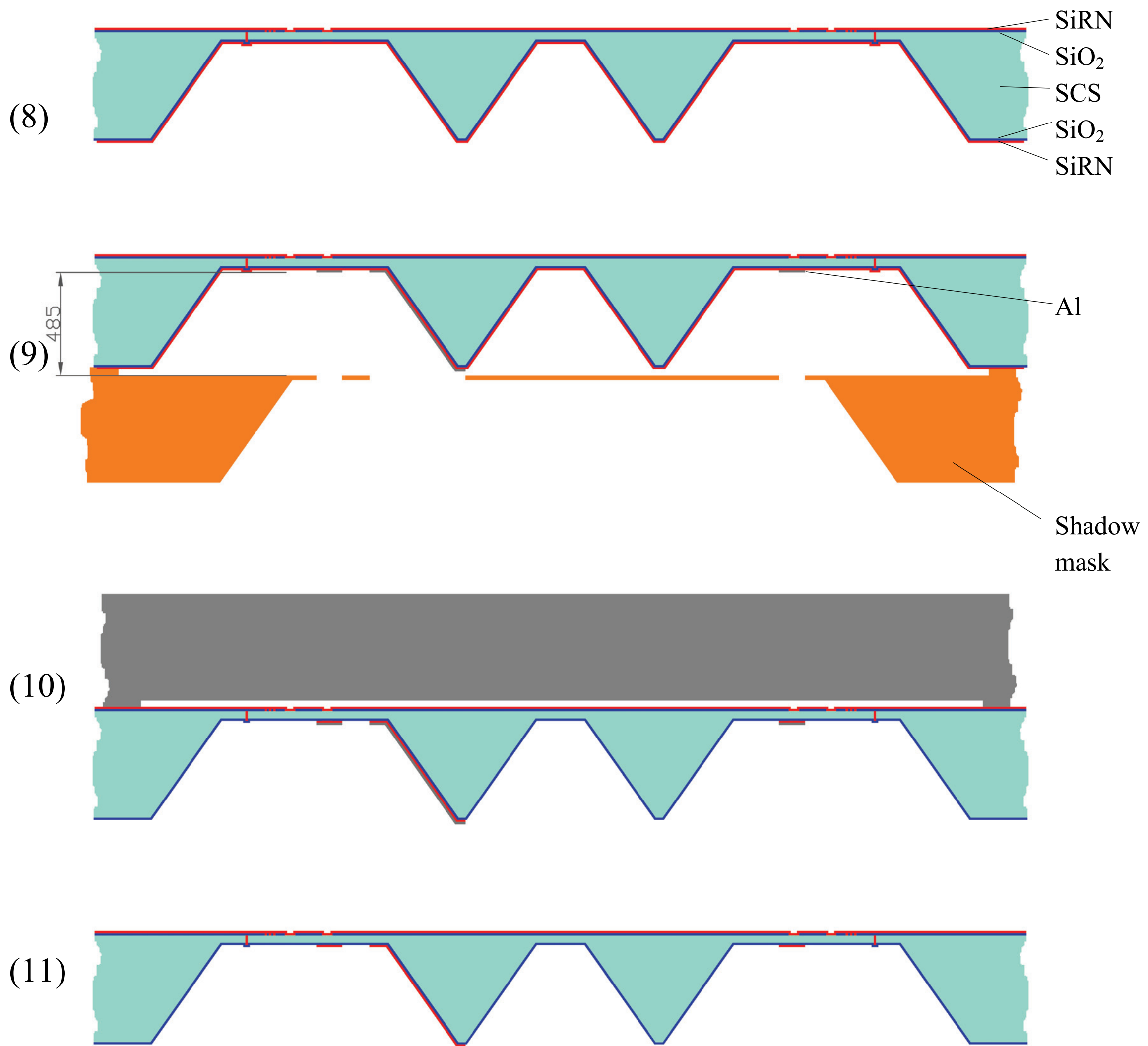

Figure 4.3b: The process for the fabrication of the 6 DOFs MEMS-based manipulator

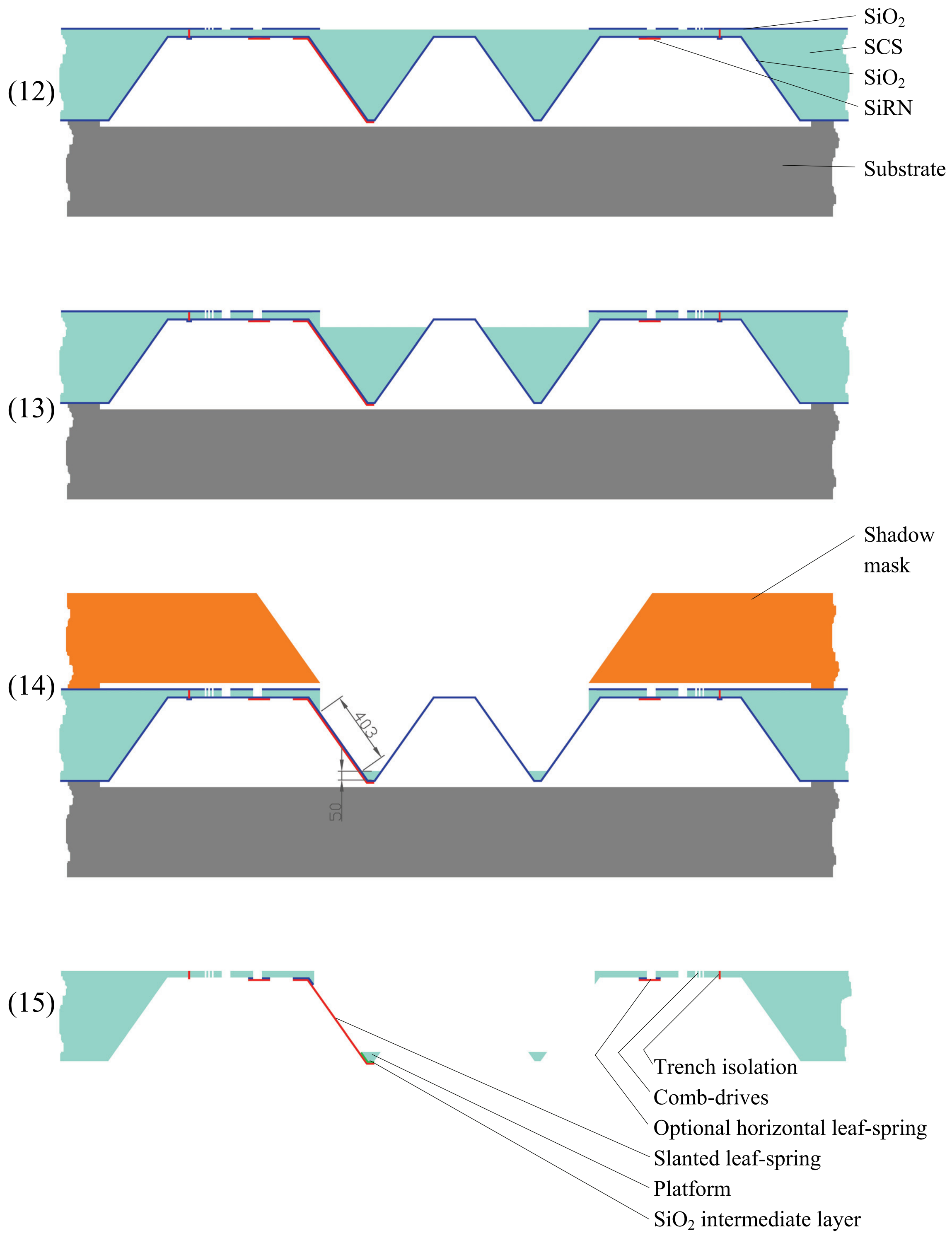

Figure 4.3c: The process for the fabrication of the 6 DOFs MEMS-based manipulator

4.3 Changes to the slanted leaf-spring design

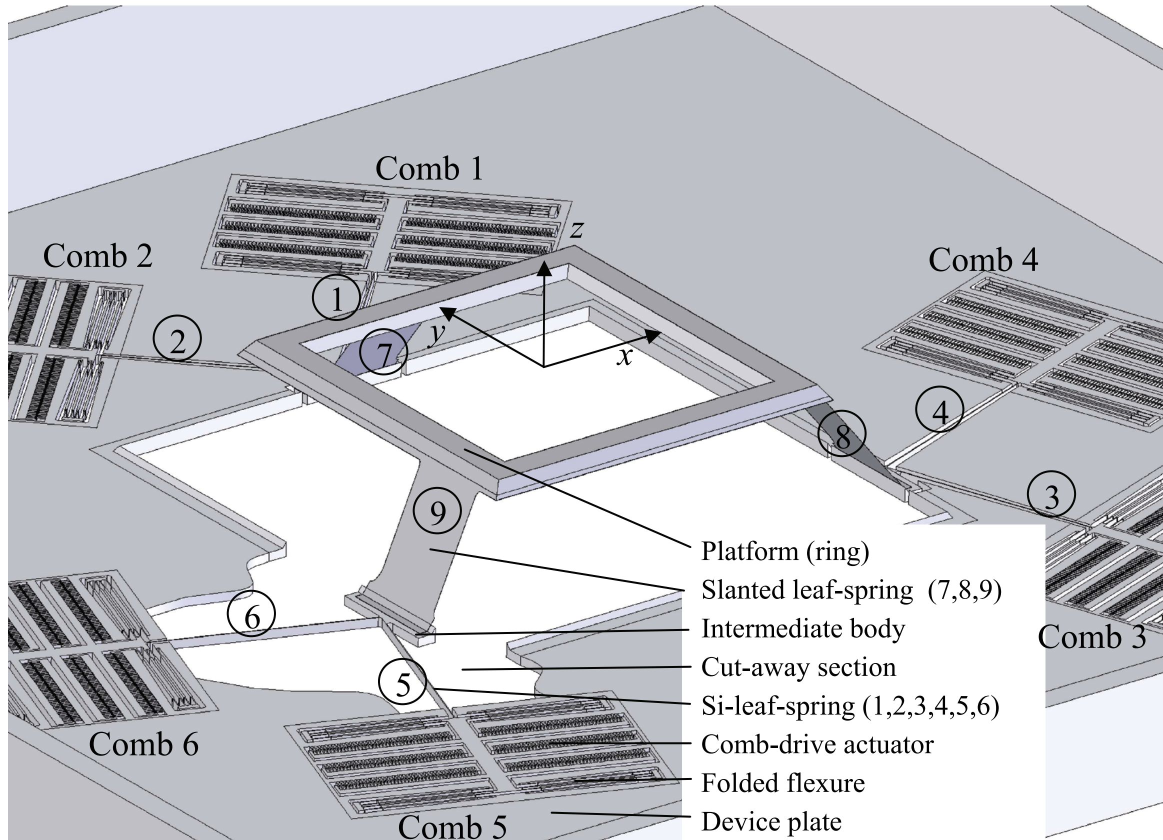

Figure 4.4: The MEMS-based 6 DOFs manipulator design. For viewing purposes a section has been cut away.

The manipulator concept is based on the slanted leaf-spring concept as discussed in section 3.6. Figures 4.4 and 4.5 present an overview of the final manipulator design. The main differences between the slanted leaf-spring concept and the final manipulator design are:

- All DRIE trenches in the device plate (Figure 4.4) have a width between 3 and 20 μm to minimize the ARDE effect (explained in section 2.2). Therefore, there are no large open spaces in the silicon device plate. See section 4.2 for details and Figure 5.9 for a SEM picture of the ARDE effect.
- Several KOH compensation structures were tested. However, the most feasible structure requires a large platform, as shown in Figure 4.1. See section 4.2 for details.
- The platform is ring shaped to reduce the suspended mass.
- Slanted leaf-springs are made wider to be more robust against buckling.

In the first design of the manipulator concept presented in this chapter the clamping mechanisms are not integrated to reduce risk during fabrication.

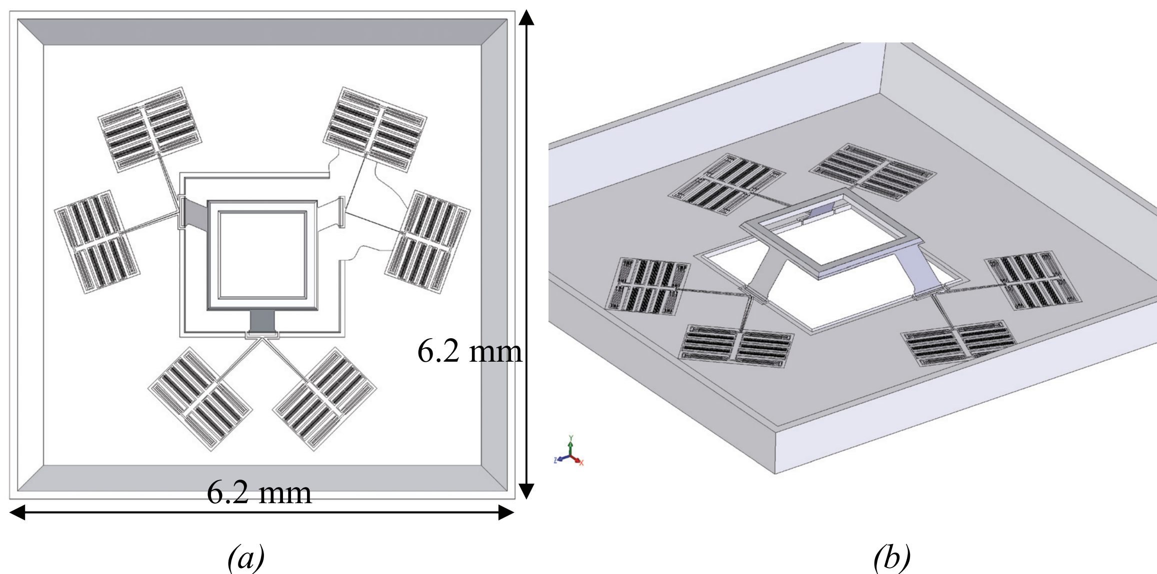

(a) (b)

Figure 4.5: a) Top view of the MEMS-based 6 DOFs manipulator design, displaying the layout of the comb-drive actuators. For viewing purposes a section has been cut away. b) A 3D-view offering a second perspective.

4.4 Dimensioning the manipulator

Many dimensions of the manipulator are determined by the process steps used, as is mentioned in section 4.2. Dimensioning the manipulator is an iterative process. The most important dimensions are the ones concerning the elastic elements: the folded flexures, the slanted leaf-springs and the Si-leaf-springs.

THE FOLDED FLEXURES

The design of the comb-drive suspension integrated in the first design of the manipulator is kept relatively conservative, so as not to accumulate risk. Therefore 4 reinforced folded flexures (Figures 2.10 and 2.11) suspend one comb-drive. The comb-drives actuate in one direction only to keep the number of electrical connections low in the first design. However, if large strokes are necessary, comb-drives actuating in two directions are preferred. This is because the total stroke is then divided over two directions. Therefore, the maximum deflection of the folded flexures of a two way comb-drive is half the maximum deflection of the folded flexures of a one way comb-drive given a certain specified stroke. Thus, the stiffness reduction of a two way comb-drive due to leaf-spring deflection is smaller (section 2.5.2). The leaf-spring thickness can be set at 2 μm. However, 3 μm is used

to make the mechanism more robust for processing. The reinforcement is 8 μm thick. The leaf-spring height is 35 μm and is determined by trench isolation technology as explained in section 4.2. The length is a trade-off between the amount of comb-drive energy stored in the leaf-springs and the amount of space needed for the flexures. The length is set at 406 μm.

THE SLANTED LEAF-SPRINGS

The slanted leaf-springs create a 54.7° angle with the device plate (Figure 4.4) resulting from KOH etching in SCS. The 54.7° angle in combination with the thickness of the wafer minus the thicknesses of the platform and the device plate results in a 403 μm length. The thickness of the slanted leaf-springs is determined by the LPCVD of SiRN which is generally between 0.3 and 2.5 μm. To keep the stress during processing low, the thickness is kept relatively small at 0.7 μm. The width of the leaf-spring is set at 300 μm. This is relatively large so as to ensure increased robustness against buckling.

THE SI-LEAF-SPRINGS

The height of the Si-leaf-springs is determined by the thickness of the device plate. The device plate thickness is determined by the maximum height for trench isolation, which is about 35-40 μm. The thickness of the Si-leaf-spring can be set at 2 μm. However, 3 μm is used to make the mechanism more robust for processing. The length of the leaf-springs needs to be long for a large actuation compliance and is set at 800 μm.

The dimensions shown in Figure 4.6 are listed in Table 4.1. The results of modeling presented in section 4.5 will be based on these dimensions.

OVERVIEW OF THE MOST IMPORTANT DIMENSIONS

Symbol	Size	Flexure geometry	Dimension constrained by
l_{pl}	1.32 mm	Platform length	min. length constrained by KOH compensation mask
w_{pl}	1.32 mm	Platform width	min. width constrained by KOH compensation mask
$l_{i,pl}$	1.12 mm	Inner platform length	free to choose
$w_{i,pl}$	1.12 mm	Inner platform width	free to choose
h_{pl}	50 μm	Platform height	free to choose, needs height for bending stiffness
l_{sl}	403 μm	Slanted leaf-spring length	defined by wafer thickness, KOH etch angle, platform thickness & the device plate thickness (h_{si})
w_{sl}	300 μm	Slanted leaf-spring width	free to choose, chosen wide w.r.t. buckling
t_{sl}	0.7 μm	Slanted leaf-spring thickness	between 0.3-2.5 SiRN layer thickness
l_{si}	800 μm	Silicon leaf-spring length	free to choose, chosen long for actuation compliance
h_{si}	35 μm	Silicon leaf-spring height	max. height determined by refilling of trench
t_{si}	3 μm	Si-leaf-spring thickness	thickness greater than 2 μm
l_{ff}	406 μm	Folded flexure length	free to choose, trade-off between space and actuation compliance
t_{ff}	3 μm	Folded flexure thickness	thickness greater than 2 μm
t_r	8 μm	Reinforcement thickness	free, thickened for process robustness
l_f	28 μm	Comb finger length	free, based on actuator displacement
g_f	3 μm	Comb finger gap	greater than 2 μm

Table 4.1: The most important dimensions of the manipulator design.

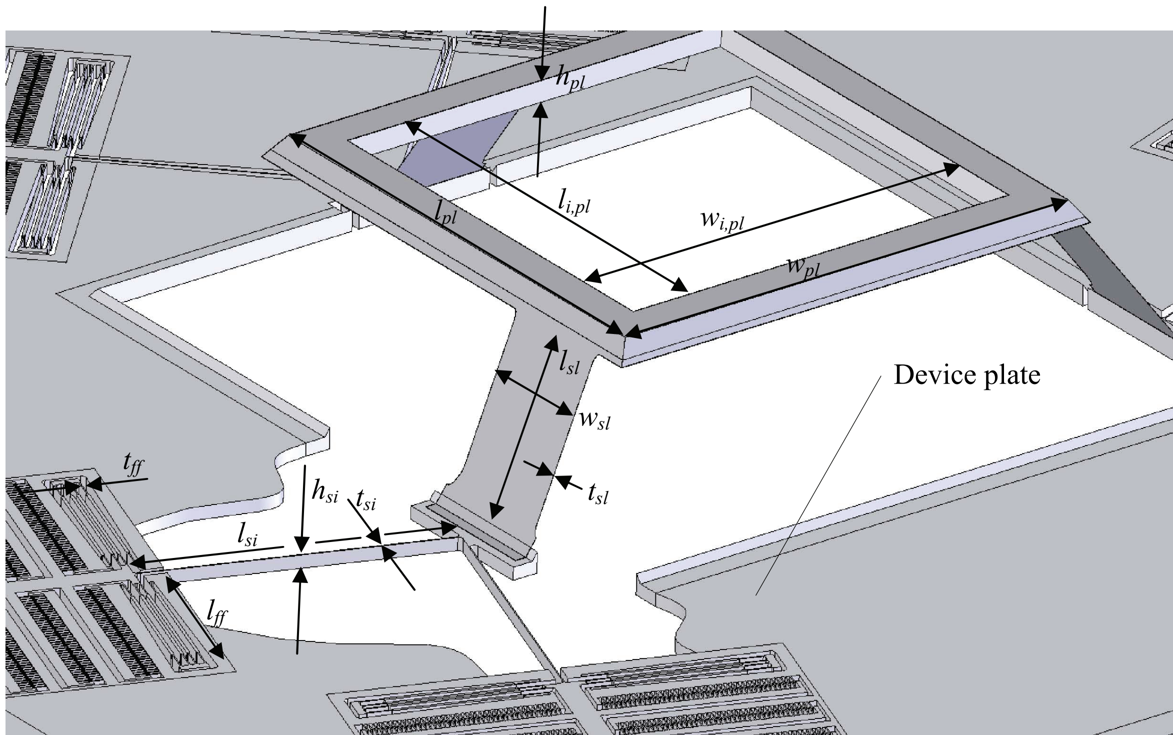

Figure 4.6: The dimensions of the manipulator.

4.5 Modeling the manipulator

In this section, the manipulator will be modeled. The modeling is done for the following reasons:

- To obtain the dimensions of the actuators by calculating the displacement and force output of the actuators.
- To obtain the first vibration mode frequencies of the manipulator and the corresponding vibration modes.
- The robustness needs to be determined by calculating buckling force on the platform and the accompanying stress in the flexures.
- To determine the stress level in the flexures due to deflection by actuation.
- The thermal stability has to be investigated.

Based on the results several recommendations will be made.

The manipulator is modeled with the aid of SPACAR. SPACAR [67] is based on a finite element theory for multi-degree of freedom mechanisms. SPACAR is able to quickly and accurately model the large deflection behavior of leaf-springs with a small number of elements. More details about SPACAR are given in Appendix F.

First a 2 DOFs example will be introduced to explain the similarity between a simple 2 DOFs system modeled by a single (scalar) stiffness, and the 198 deformation modes of the manipulator system modeled by a 6x6 geometrical transfer function and 6x6 stiffness matrices.

4.5.1 Two DOFs model

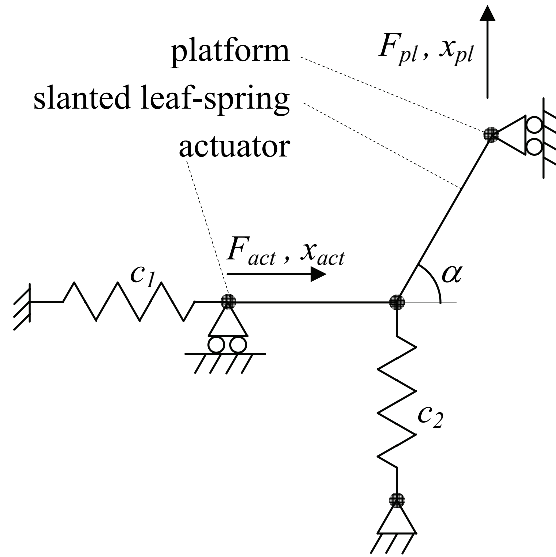

Figure 4.7: Models containing 2 DOFs.

For explanatory purposes (it is not used for calculating the manipulator), a 2 DOFs model of the manipulator with only 2 stiffnesses is introduced. Suppose that the stiffness c_1 shown in Figure 4.7 represents the stiffness of the folded flexures in the actuation direction and c_2 represents the out-of-plane (wafer-plane) bending stiffness of the Si-leaf-springs of the 6 DOFs manipulator. The following numerical values are substituted: $c_1 = 100$, $c_2 = 600$, $\tan(\alpha) = 2$. For explanatory purposes, the values in the models are represented dimensionless. The stiffness matrix is given by:

$$\underline{F} = C \cdot \underline{X} = \begin{bmatrix} c_{11} & c_{12} \\ c_{12} & c_{22} \end{bmatrix} \cdot \underline{X}$$

$$\begin{bmatrix} F_{act} \\ F_{pl} \end{bmatrix} = \begin{bmatrix} c_1 + \dfrac{c_2}{\tan^2(\alpha)} & -\dfrac{c_2}{\tan(\alpha)} \\ -\dfrac{c_2}{\tan(\alpha)} & c_2 \end{bmatrix} \cdot \begin{bmatrix} x_{act} \\ x_{pl} \end{bmatrix} = \begin{bmatrix} 250 & -300 \\ -300 & 600 \end{bmatrix} \cdot \begin{bmatrix} x_{act} \\ x_{pl} \end{bmatrix} \tag{4.1}$$

The inverse of the stiffness matrix, the compliance matrix, is:

$$\underline{X} = S \cdot \underline{F} = \begin{bmatrix} s_{11} & s_{12} \\ s_{12} & s_{22} \end{bmatrix} \cdot \underline{F}$$
$$\begin{bmatrix} x_{act} \\ x_{pl} \end{bmatrix} = \begin{bmatrix} \frac{1}{c_1} & \frac{1}{c_1 \tan(\alpha)} \\ \frac{1}{c_1 \tan(\alpha)} & \frac{1}{c_1 \tan^2(\alpha)} + \frac{1}{c_2} \end{bmatrix} \cdot \begin{bmatrix} F_{act} \\ F_{pl} \end{bmatrix} = \begin{bmatrix} \frac{1}{100} & \frac{1}{200} \\ \frac{1}{200} & \frac{1}{240} \end{bmatrix} \cdot \begin{bmatrix} F_{act} \\ F_{pl} \end{bmatrix} \tag{4.2}$$

The experienced stiffness is a phrase used in mechanics. This is the stiffness of a system at a certain location, if the external forces are unchanged, except the external force where the stiffness is determined. The external constant forces should be small, so the geometry will not change much: $\Delta\alpha \ll 1$. Therefore the stiffness experienced by the actuator, if F_{pl} = constant, can be derived from the compliance matrix:

$$c_{act} = \left.\frac{\partial F_{act}}{\partial x_{act}}\right|_{F_{pl}=\text{const}} = \left.\left(\frac{\partial x_{act}}{\partial F_{act}}\right)^{-1}\right|_{F_{pl}=\text{const}} = \left(\frac{\partial\left(s_{11}F_{act} + s_{12}F_{pl}\right)}{\partial F_{act}}\right)^{-1} =$$
$$= \left(s_{11}\right)^{-1} = c_1 = 100 \tag{4.3}$$

The stiffness experienced at the platform, if F_{act} = constant, is:

$$c_{pl} = \left.\frac{\partial F_{pl}}{\partial x_{pl}}\right|_{F_{act}=\text{const}} = \left(s_{22}\right)^{-1} = \left(\frac{1}{c_1 \tan(\alpha)} + \frac{1}{c_2}\right)^{-1} = 240 \tag{4.4}$$

The stiffness the actuator experiences contains c_1 only. Therefore, it differs clearly from the stiffness experienced by a force at the platform, which contains both c_1 and c_2.

SPECIAL CASE: PLATFORM FORCE IS ZERO

To calculate the displacement of the platform due to an actuator force, a geometric transfer is introduced, which is only valid if $F_{pl} = 0$. Equation 4.2 can then be simplified to:

$$\begin{bmatrix} x_{act} \\ x_{pl} \end{bmatrix} = \begin{bmatrix} s_{11} & \cdots \\ s_{12} & \cdots \end{bmatrix} \cdot \begin{bmatrix} F_{act} \\ 0 \end{bmatrix} = \begin{bmatrix} \dfrac{1}{c_1} & \cdots \\ \dfrac{1}{c_1 \tan(\alpha)} & \cdots \end{bmatrix} \cdot \begin{bmatrix} F_{act} \\ 0 \end{bmatrix} \tag{4.5}$$

results in:

$$x_{act} = \frac{1}{c_1} F_{act} \quad ; \qquad x_{pl} = \frac{1}{c_1 \tan(\alpha)} F_{act} \tag{4.6}$$

The geometric transfer i or, in this case, the transmission ratio, links the actuator displacement, due to actuator force, to the platform displacement:

$$x_{act} = i \cdot x_{pl} \tag{4.7}$$

Using equations 4.6 and 4.7 the linear geometric transfer can be determined for $F_{pl} = 0$:

$$i = s_{11} \cdot (s_{12})^{-1} = \tan(\alpha) = 2 \tag{4.8}$$

The actuator force resulting in a certain platform can be written as follows:

$$F_{act} = i \cdot c_{act} \cdot x_{pl} = 200 x_{pl} \tag{4.9}$$

The presented results will be used to explain the model of the manipulator.

4.5.2 Linearized system model of the manipulator

In SPACAR the 6 comb-drive suspensions and the manipulator are examined separately, because otherwise the model would become too large. Therefore, each comb-drive actuator suspension, consisting of four folded flexures (Figure 2.10 and 2.11), is substituted by a set of 6 trusses resulting in an equivalent compliance in 6 DOFs. A truss represents a single compliance between two points. A total of 36 trusses are used to model the 6 actuator suspensions. The trusses need to be chosen long enough to represent the geometrical straightness of a folded flexure guidance. The elastic elements in the model of the manipulator are the three slanted leaf-springs (Figure 4.4), the six Si-leaf-springs and the 36 trusses representing the folded flexures. Each leaf-spring is modeled by 3 SPACAR beam elements. Each beam element in SPACAR has 6 possible deformation modes. The 6 possible deformation modes of 1 beam element are 1 longitudinal mode, 1 torsional mode and 4 bending modes. Therefore, the total number of deformation modes for the system is 198. The varying Young's modulus and Poisson's ratio for different directions in SCS has been taken into account. The manipulator platform, the intermediate bodies and the comb-drive shuttles have been considered rigid in the SPACAR model.

Although linearized at a given position, the geometrical transfer function and the stiffness matrices will be handy to physically understand the motion of the platform due to actuation forces, or external forces on the platform. Therefore, in section 4.5.2, three 6x6 stiffness matrices and a 6x6 linear geometric transfer matrix will be derived.

The displacement matrices of the platform $\underline{X}_{pl}$,the actuators $\underline{X}_{act}$, and the force matrices of the platform $\underline{F}_{pl}$ and the actuators $\underline{F}_{act}$ are defined by:

$$\underline{X}_{pl} = \begin{bmatrix} x_{pl} \\ y_{pl} \\ z_{pl} \\ rx_{pl} \\ ry_{pl} \\ rz_{pl} \end{bmatrix} ;\ \underline{X}_{act} = \begin{bmatrix} x_{act\,1} \\ x_{act\,2} \\ x_{act\,3} \\ x_{act\,4} \\ x_{act\,5} \\ x_{act\,6} \end{bmatrix} ;\ \underline{F}_{pl} = \begin{bmatrix} F_{x,pl} \\ F_{y,pl} \\ F_{z,pl} \\ M_{x,pl} \\ M_{y,pl} \\ M_{z,pl} \end{bmatrix} ;\ \underline{F}_{act} = \begin{bmatrix} F_{act\,1} \\ F_{act\,2} \\ F_{act\,3} \\ F_{act\,4} \\ F_{act\,5} \\ F_{act\,6} \end{bmatrix} \tag{4.10}$$

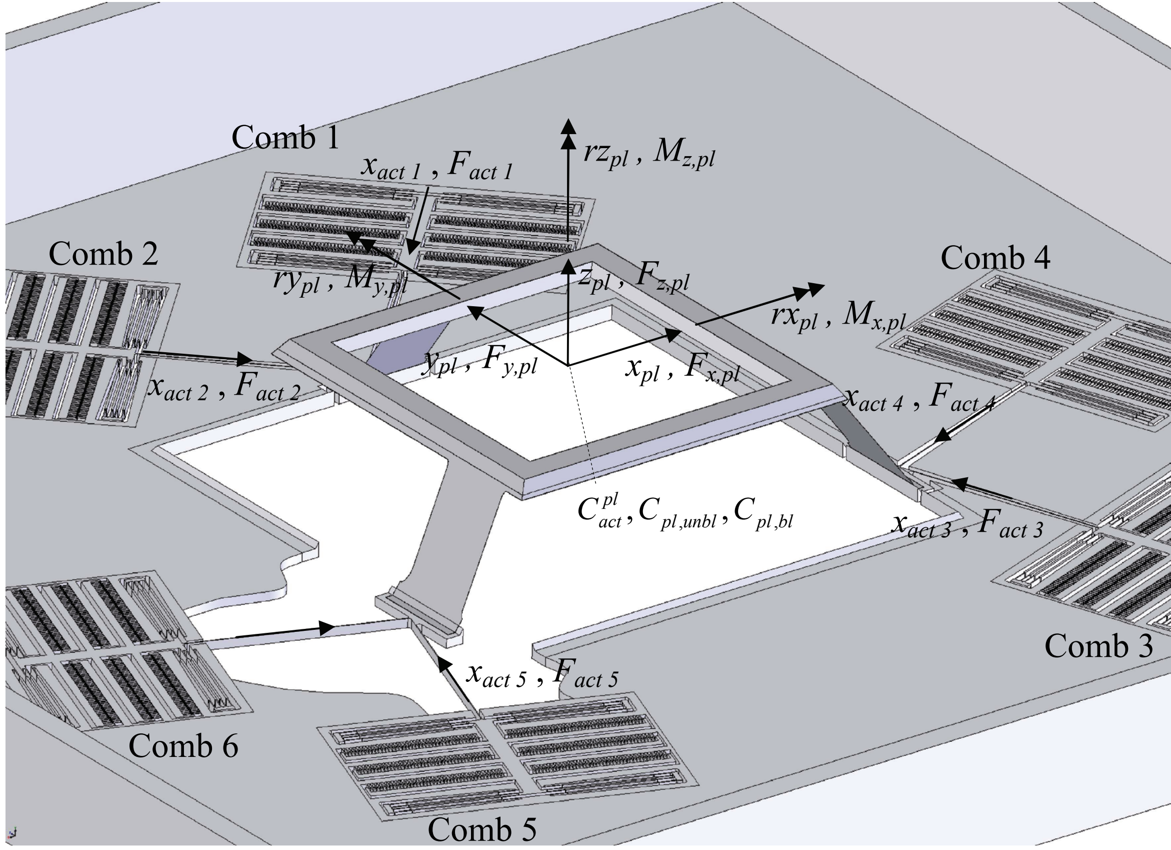

Figure 4.8: Definition of the 6 DOFs platform displacements $\underline{X}_{pl}$, platform forces $\underline{F}_{pl}$, actuator displacements $\underline{X}_{act}$ and actuator forces $\underline{F}_{act}$.

Equation 4.10 in combination with Figure 4.8 shows the definition of the displacement and force matrices. The displacement of the nodes in between the actuators and the platform are represented by matrix $\underline{X}_r$, with the dual external forces $\underline{F}_r$. In the SPACAR model used, these matrices have a dimension 184 x 1. The total static linear system model of the total manipulator is given by:

$$\begin{bmatrix} \underline{F}_{act} \\ \underline{F}_{pl} \\ \underline{F}_{r} \end{bmatrix} = \begin{bmatrix} C_{11} & C_{12} & C_{13} \\ C_{12}^{T} & C_{22} & C_{23} \\ C_{13}^{T} & C_{23}^{T} & C_{33} \end{bmatrix} \cdot \begin{bmatrix} \underline{X}_{act} \\ \underline{X}_{pl} \\ \underline{X}_{r} \end{bmatrix} \tag{4.11}$$

and:

$$\begin{bmatrix} \underline{X}_{act} \\ \underline{X}_{pl} \\ \underline{X}_{r} \end{bmatrix} = \begin{bmatrix} S_{11} & S_{12} & S_{13} \\ S_{12}^{T} & S_{22} & S_{23} \\ S_{13}^{T} & S_{23}^{T} & S_{33} \end{bmatrix} \cdot \begin{bmatrix} \underline{F}_{act} \\ \underline{F}_{pl} \\ \underline{F}_{r} \end{bmatrix} \tag{4.12}$$

4.5.3 Geometric transfer function and actuation stiffness matrix $\underline{F}_{pl} = \underline{0}\,; \underline{F}_r = \underline{0}$

In this section a 6x6 linear geometric transfer matrix T will be derived to map the actuator displacements, due to actuator forces, to the platform displacements. In addition a 6x6 stiffness matrix to model the stiffnesses, experienced by the 6 actuators, C_{act}, will be derived. Similar to the 2 DOFs model (equations 4.7 and 4.9), T and C_{act} are valid if the forces acting on the system are solely the actuation forces: $\underline{F}_{pl} = \underline{0}\,; \underline{F}_r = \underline{0}$. In this case only certain parts of equation 4.12 are of interest:

$$\begin{bmatrix} \underline{X}_{act} \\ \underline{X}_{pl} \\ \underline{X}_r \end{bmatrix} = \begin{bmatrix} S_{11} & \cdot & \cdot \\ S_{12}{}^T & \cdot & \cdot \\ S_{13}{}^T & \cdot & \cdot \end{bmatrix} \cdot \begin{bmatrix} \underline{F}_{act} \\ \underline{0} \\ \underline{0} \end{bmatrix} \tag{4.13}$$

The external forces on the actuators $\underline{F}_{act}$ result in a linear coupling of the displacement of the platform $\underline{X}_{pl}$ to the displacement of the actuators $\underline{X}_{act}$. The geometrical transfer function T can then be defined analogous to the transmission ratio i for the 2 DOFs model, equation 4.7:

$$\begin{aligned} \underline{X}_{act} &= T \cdot \underline{X}_{pl} \\ T &= S_{11} \cdot \left(S_{12}{}^T\right)^{-1} \end{aligned} \qquad \Leftarrow \underline{F}_{pl} = \underline{0}\,; \underline{F}_r = \underline{0} \tag{4.14}$$

Second order tensor transformation of equation 4.14 results in the transformation of the dual forces, the actuator forces and the platform forces:

$$T^T \cdot \underline{F}_{act} = \underline{F}_{pl} \qquad \Leftarrow \underline{F}_{pl} = \underline{0}\,; \underline{F}_r = \underline{0} \tag{4.15}$$

The actuator stiffness matrix C_{act} can be defined as follows:

$$\begin{aligned} \underline{F}_{act} &= C_{act} \cdot \underline{X}_{act} \\ C_{act} &= S_{11}{}^{-1} \end{aligned} \qquad \Leftarrow \underline{F}_{pl} = \underline{0}\,; \underline{F}_r = \underline{0} \tag{4.16}$$

The stiffness matrix C_{act} can be transformed to a stiffness matrix C_{act}^{pl} to act on the platform forces:

$$C_{act}^{pl} = T^T \cdot C_{act} \cdot T = S_{12}^{-1} \cdot S_{11}^{T} \cdot \left(S_{12}^{T}\right)^{-1} \qquad \Leftarrow \underline{F}_{pl} = \underline{0}\,;\, \underline{F}_r = \underline{0} \tag{4.17}$$

The actuator forces necessary to displace the platform can be written as:

$$\underline{F}_{act} = \left(T^T\right)^{-1} \cdot C_{act}^{pl} \cdot \underline{X}_{pl} = \left(S_{12}^{T}\right)^{-1} \cdot \underline{X}_{pl} \qquad \Leftarrow \underline{F}_{pl} = \underline{0}\,;\, \underline{F}_r = \underline{0} \tag{4.18}$$

Equation 4.18 is analogous to the following, which holds true for the 2 DOFs model of Figure 4.7:

$$F_{act} = i^{-1} \cdot c_{act}^{pl} \cdot x_{pl} \qquad \Leftarrow F_{pl} = 0 \tag{4.19}$$

where c_{act}^{pl} is the stiffness experienced by the actuator, and is located at the platform shown in Figure 4.7:

$$c_{act}^{pl} = i^2\, c_{act} = s_{12}^{-2} \cdot s_{11} = 400 \qquad \Leftarrow F_{pl} = 0 \tag{4.20}$$

Combining equations 4.19 and 4.20 yields equation 4.9.

In a similar way as for the 2 DOFs model with equations 4.6 and 4.7, the linear geometric transfer can be determined. However, in this case it is done numerically. As input in SPACAR, 6 times a different force matrix $\underline{F}_{act_I} ... \underline{F}_{act_{VI}}$ is used. The forces need to be small so that the displacements of the actuators and the displacements of the platform will be relatively small. In addition, the rank of the matrix $\left[\underline{F}_{act_I}, \underline{F}_{act_{II}} ... \underline{F}_{act_{VI}}\right]$ should be 6. In this case the following has been used:

$$\left[\underline{F}_{act_I}, \underline{F}_{act_{II}} ... \underline{F}_{act_{VI}}\right] = I \cdot 10^{-7} \tag{4.21}$$

where I is the 6x6 identity matrix. The force matrix $\underline{F}_{act_I}$ results in actuator displacement $\underline{X}_{act_I}$ and platform displacements $\underline{X}_{pl_I}$. By using the Gauss Jordan elimination method, the reduced row echelon form (rref) gives the geometric transfer T as follows:

$$[I,T]=\text{rref}\left[\underline{X}_{pl_I},\underline{X}_{pl_{II}}\ldots\underline{X}_{pl_{VI}},\underline{X}_{act_I},\underline{X}_{act_{II}}\ldots\underline{X}_{act_{VI}}\right] \tag{4.22}$$

The stiffness matrix C_{act}^{pl} can be derived:

$$\left[I,\left(T^T\right)^{-1}C_{act}^{pl}\right]=\text{rref}\left[\underline{X}_{pl_I},\underline{X}_{pl_{II}}\ldots\underline{X}_{pl_{VI}},\underline{F}_{act_I},\underline{F}_{act_{II}}\ldots\underline{F}_{act_{VI}}\right] \tag{4.23}$$

The geometric transfer matrix T linearized around its undeflected state is given by:

$$\begin{bmatrix} x_{act\,1} \\ x_{act\,2} \\ x_{act\,3} \\ x_{act\,4} \\ x_{act\,5} \\ x_{act\,6} \end{bmatrix} = \begin{bmatrix} -0.706 & -0.692 & 0.963 & 0.000710 & 0.000341 & 0.000736 \\ 0.706 & -0.692 & 0.963 & 0.000710 & -0.000341 & -0.000736 \\ -0.341 & 0.927 & 0.482 & 0.000173 & -0.000338 & 0.000769 \\ -0.936 & -0.370 & 1.323 & -0.000930 & -0.000926 & -0.000924 \\ 0.341 & 0.927 & 0.482 & 0.000173 & 0.000338 & -0.000769 \\ 0.936 & -0.370 & 1.323 & -0.000930 & 0.000926 & 0.000924 \end{bmatrix} \begin{bmatrix} x_{pl} \\ y_{pl} \\ z_{pl} \\ rx_{pl} \\ ry_{pl} \\ rz_{pl} \end{bmatrix} \tag{4.24}$$

The displacements of the actuators can now be related to the displacements of the platform. For example, the linearized actuator displacement for each comb-drive for an x_{pl} platform displacement, is shown in Figure 4.9. It is equal to the first column of T of equation 4.24.

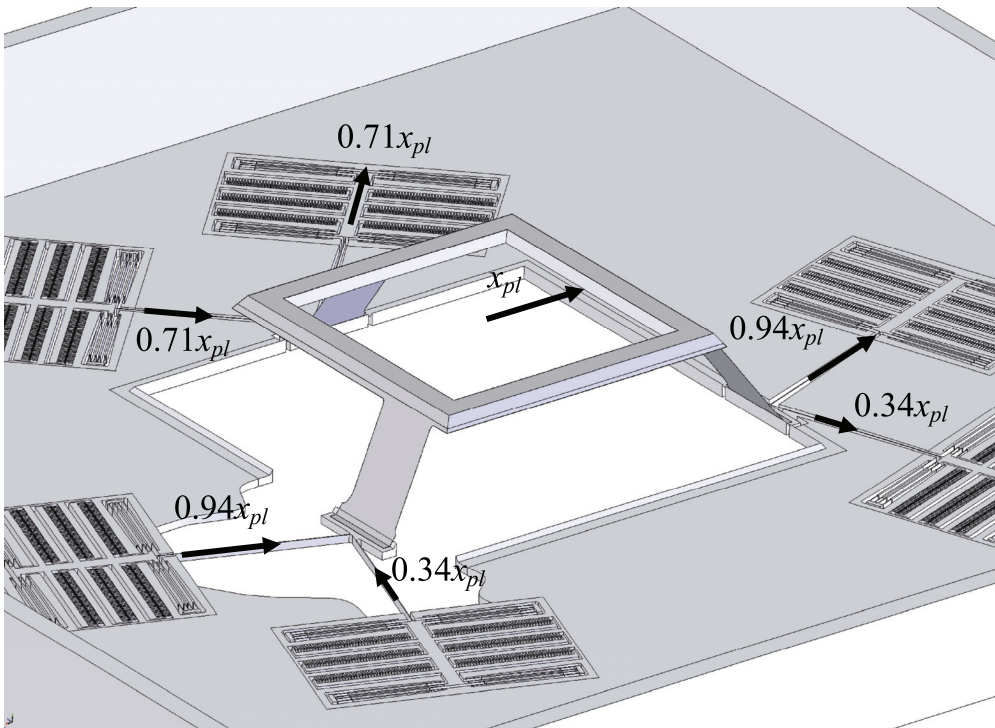

Figure 4.9: Example of an in-plane motion in the x-direction x_{pl} of the platform. The relative displacement of each of the actuators is given.

The stiffness matrix C_{act}^{pl} is given by:

$$C_{act}^{pl} = \begin{bmatrix} 41.2 & 0 & 0 & 0 & 0.0185 & 0.0003 \\ 0 & 40.7 & -21.1 & -0.00959 & 0 & 0 \\ 0 & -21.1 & 82.8 & -0.0103 & 0 & 0 \\ 0 & -0.00959 & -0.0103 & 0.0000412 & 0 & 0 \\ 0.0185 & 0 & 0 & 0 & 0.0000309 & 0.0000241 \\ 0.0003 & 0 & 0 & 0 & 0.0000241 & 0.0000560 \end{bmatrix} \quad (4.25)$$

The direct equation to determine the actuator forces that result in a platform displacement is given by:

$$\begin{bmatrix} F_{act1} \\ F_{act2} \\ F_{act3} \\ F_{act4} \\ F_{act5} \\ F_{act6} \end{bmatrix} = \begin{bmatrix} -10.70 & -10.24 & 14.77 & 0.01126 & 0.00607 & 0.01142 \\ 10.70 & -10.24 & 14.77 & 0.01126 & -0.00607 & -0.01142 \\ -4.39 & 12.31 & 6.83 & 0.00268 & -0.00525 & 0.01038 \\ -12.35 & -5.02 & 18.07 & -0.01306 & -0.01255 & -0.01256 \\ 4.39 & 12.31 & 6.83 & 0.00268 & 0.00525 & -0.01038 \\ 12.35 & -5.02 & 18.07 & -0.01306 & 0.01255 & 0.01256 \end{bmatrix} \begin{bmatrix} x_{pl} \\ y_{pl} \\ z_{pl} \\ rx_{pl} \\ ry_{pl} \\ rz_{pl} \end{bmatrix} \quad (4.26)$$

The linearized geometric transfer and actuation stiffness matrix can be used to determine the necessary actuator forces and strokes. However, first the errors made by linearizing around the undeflected state will be derived.

4.5.4 Errors due to the use of a first-order model

To calculate the actuator force and stroke for relatively small displacements of parallel kinematic manipulators, often a constant geometrical linear transfer function, in this case T, and a constant stiffness matrix, in this case C_{act}, are used (equation 4.24 and 4.26). Depending on the amount of relative displacement, errors due to linearization will be made. The question is: how large are these errors? In the next section, the difference between the platform position obtained by a linearized and a non-linear model will be determined. For a certain platform displacement $\underline{X}_{pl}$ the actuator forces $\underline{F}_{act}$ are calculated based on T and C_{act} using equation 4.26. These actuator forces are then used in SPACAR to determine displacements $\underline{X}_{pl-NL}$ in a non-linearized manner. The positional error of the platform due to the use of a constant T and C_{act} can then be calculated:

$$\underline{e}_{pl} = \begin{bmatrix} e_{pl\,x} \\ e_{pl\,y} \\ e_{pl\,z} \\ e_{pl\,rx} \\ e_{pl\,ry} \\ e_{pl\,rz} \end{bmatrix} = \left| \underline{X}_{pl} - \underline{X}_{pl-NL} \right| \tag{4.27}$$

The total errors are calculated as follows:

$$\begin{aligned} e_{pl\,trl} &= \sqrt{{e_{pl\,x}}^2 + {e_{pl\,y}}^2 + {e_{pl\,z}}^2} \\ e_{pl\,rot} &= \sqrt{{e_{pl\,rx}}^2 + {e_{pl\,ry}}^2 + {e_{pl\,rz}}^2} \end{aligned} \tag{4.28}$$

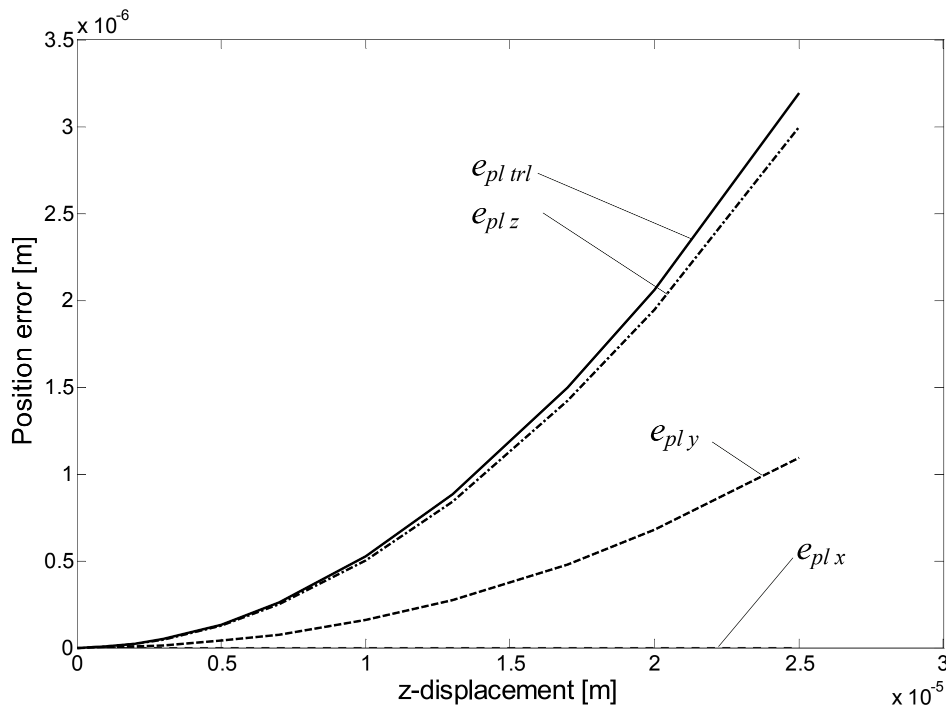

Figure 4.10: The translational position errors of the platform due to the use of a constant geometrical transfer function and stiffness matrix when displacing the platform in the z-direction.

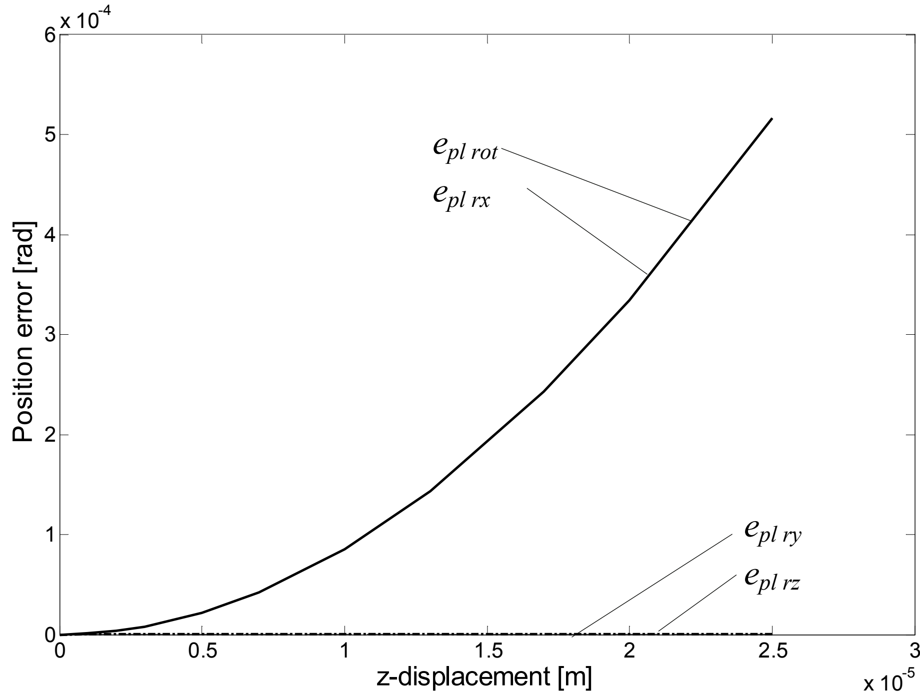

Figure 4.11: The rotational position errors of the platform due to the use of a constant geometrical transfer function and stiffness matrix when displacing the platform in the z-direction.

The position errors $\underline{e}_{pl}$ have been calculated for platform displacement in the *z*-direction (Figure 4.8). In the *z*-direction, the non-linearity between actuator and platform displacement is stronger than in the *x*- and *y*-direction, because the slanted leaf-springs are deflected when the platform is displaced in *z*-direction. Figure 4.10 shows these translational position errors. Because of the mirror symmetry along the *y*-axis, as shown in Figure 4.4, slanted leaf-spring 8 and 9 compensate for each other's errors. Therefore, there is no error in the *x*-direction. Figure 4.11 shows the rotational errors. In this case, because of the mirror symmetry along the *y*-axis, there is no error in the *ry*- and *rz*-direction.

The errors presented in this section are due to linearization. In reality both C_{act} and T are depending on the platform position. For a 25 μm displaced platform in the *z*-direction, C_{act} and T have been calculated, and compared to the matrices for the undeflected state. The change of the diagonal elements of C_{act} is up to 1.1%, while the change of the diagonal elements of T is up to 54%. Therefore, the geometric change due to displacement accounts mainly for the errors shown in Figure 4.10 and 4.11.

CONCLUSIONS

- The relationship between actuator force, stroke and platform displacement can only be examined for relatively small displacements, using a linear approximation of the geometrical transfer and a constant stiffness matrix.
- Mainly the geometric change due to displacement accounts for the errors made when linearizing.
- Feed-forward position control based on a constant T and C_{act} leads to positional errors of up to 3.2 μm at 25 μm displacement. If the total positional platform error should not exceed 10 nm (specification section 1.6) and feed-forward position control based on a constant T and C_{act} is used, the maximum platform displacement should then remain less than 1.4 μm.

4.5.5 Actuation force and stroke

An estimation of the actuation force and stroke can be made based on the geometrical transfer function matrix T and stiffness matrix C_{act} using equations 4.24 and 4.26. Although more accurate calculations can be made using SPACAR, these estimations are accurate enough for dimensioning the actuators sufficiently. To reach the specification listed in Table 1.2, i.e. 10 μm strokes in all directions and small correctional rotations at the same time, the actuators need displacements of about 50 μm in two directions. This actuator stroke is rather large. Therefore, in a first design of the manipulator the displacements of the comb-drives are limited to reduce risk. The input platform displacements are therefore tuned in such a way that the maximum actuator displacements are about 20 μm in two directions.

Several combinations of platform displacements are investigated. In Table 4.2 the displacements and forces of each of the actuators is calculated for a 2-way comb-drive configuration. Therefore, the displacements of the platform and actuators, and also the actuator forces listed, can have positive or negative signs. The "individual platform displacements" of Table 4.2 represent the six situations where a displacement in a single *x, y, z, rx, ry* or *rz* direction is made. In the "combined platform displacements" the largest displacement and force combination of one of the actuators is derived by combining platform displacements.

It is interesting to investigate which of the flexures contributes most to the force necessary to actuate. Depending on which actuator is examined and in which direction the platform is displaced, the folded flexures consume 80.0 to 100.0% of the actuator force. Translations in the *x*- or *y*- direction lead to even larger percentages. This confirms that the relative drive-stiffness (the stiffness of the

manipulator experienced by the actuators without the folded flexures, divided by the stiffness of the folded flexure, as explained in section 2.4.2) is very low, being less than 0.24. This is partly a consequence of the necessity to have a high *z*-stiffness of the platform and the large force leverage by the Si-leaf-springs from the platform to the folded flexures. Moreover, the space limits the length of the folded flexures.

			Individual platform displacements						Combined platform displacements						
Platform displ.	x_{pl}	µm	20	0	0	0	0	0	-4	4	-4	-4	4	4	
	y_{pl}	µm	0	20	0	0	0	0	-4	-4	4	-4	4	-4	
	z_{pl}	µm	0	0	15	0	0	0	4	4	4	4	4	4	
	rx_{pl}	°	0	0	0	1.2	0	0	0.2	0.2	0.2	-0.2	0.2	-0.2	
	ry_{pl}	°	0	0	0	0	1.2	0	0.2	-0.2	-0.2	-0.2	0.2	0.2	
	rz_{pl}	°	0	0	0	0	0	1.2	0.2	-0.2	0.2	-0.2	-0.2	0.2	
															max
Actuator displ.	$x_{act\,1}$	µm	-14	-14	14	15	7	15	***16***	3	8	3	-1	5	***16***
	$x_{act\,2}$	µm	14	-14	14	15	-7	-15	3	***16***	-1	5	8	3	***16***
	$x_{act\,3}$	µm	-7	***19***	7	4	-7	16	2	-4	12	-3	1	-2	***19***
	$x_{act\,4}$	µm	-19	7	20	-20	-19	-19	1	6	4	***20***	-3	0	***20***
	$x_{act\,5}$	µm	9	***19***	7	4	7	-16	-4	2	1	-2	12	-3	***19***
	$x_{act\,6}$	µm	19	7	20	-20	19	19	6	1	3	0	4	***20***	***20***
															max
Actuator force	$F_{act\,1}$	µN	-214	-205	222	236	127	239	***243***	36	119	43	-4.1	79	***243***
	$F_{act\,2}$	µN	214	-205	222	236	-127	-239	36	***243***	-4	79	119	43	***243***
	$F_{act\,3}$	µN	-88	***246***	103	56.1	-110	217	23	-48	158	-32	13.8	-31	***246***
	$F_{act\,4}$	µN	-247	-100	271	-274	-263	-263	8	85	56	***275***	-43	0.9	***275***
	$F_{act\,5}$	µN	88	***246***	103	56.1	110	-217	-48	23	14	-31	158	-32	***246***
	$F_{act\,6}$	µN	247	-100	271	-274	263	263	85	8	-43	0.9	56	***275***	***275***

Table 4.2: Individual actuator displacements and forces for several combinations of platform displacements (based on a constant geometrical transfer function and stiffness matrix). The actuators can be displaced in two directions. Therefore, the displacements of the platform and actuators and also the actuator forces listed can have positive or negative signs.

CONCLUSIONS

- The "individual platform displacements" are about 5 times larger than the "combined platform displacements", with the same actuator strokes.
- In parallel kinematic manipulators, the combinations of movements in different directions at the same time add up to relatively large actuator displacements (and forces in the case of a compliant mechanism). In this case, +/- 50 μm actuator strokes are necessary to result in combined +/- 10 μm strokes of the platform.
- Rotations of the platform result in large actuator displacements because of the relatively large size of the platform.
- For MEMS the calculated forces are rather large.
- In comparison to slanted and Si-leaf-springs, the folded flexures are relatively stiff in the actuation direction.
- The folded flexures are mainly responsible for the actuation force of the comb-drive actuators.

DIMENSIONING THE COMB-DRIVES

In the first clean room design the 2-way comb-drive actuators have been changed into one-directional comb-drives, because 2-way comb-drives introduce extra risk. The most demanding actuator, which needs to deliver 275 μN and a stroke of 20.2 μm, will be discussed. Based on the stroke the finger length should be about 28 μm. The electrostatic force in the x_{act}-direction is described by Legtenberg [81]:

$$F_{comb\,x} = \frac{\varepsilon\, n\, h_{si}\, U^2}{g_f} \tag{4.29}$$

where ε is the dielectric permittivity, n is the number of finger pairs, h_{si} is the height of the comb fingers, g_f is the gap spacing between the fingers and U is the voltage between the stationary and the movable part of the comb. With n = 240 and g_f = 3 μm the voltage necessary to create 275 μN, U = 105 V. The voltage can be decreased by decreasing the leaf-spring thickness and finger gap to 2 μm. In that case, the voltage would be U = 47 V. For reasons of robustness, however, the first integrated design is based on 3 μm gap technology. Lateral comb-drives tend to become unstable at large voltages and large finger overlaps. The transverse, or gap closing, force increase with displacement in the transverse direction is calculated according to Legtenberg [81]:

$$\frac{\partial F_e}{\partial g_f} = -\frac{\varepsilon \, n \, h_{si} \, l_{ov} \, U^2}{g_f^{\,3}} = -729 \frac{N}{m} \tag{4.30}$$

with l_{ov} = 24 μm being the maximum overlap of the fingers. Equation 4.30 shows a negative stiffness, meaning the force is oriented in the same direction as the displacement. The force also increases rapidly when the gap changes. The mechanical (positive) stiffness of the folded flexures should more than compensate for this negative stiffness, resulting in a stable situation.

The mechanical stiffness can be calculated using Figure 2.12. When displacing the folded flexure 20 μm in the actuation direction, only 5.8% of the initial stiffness in the *x*-direction, as shown in Figure 2.10, remains. The overlap of the comb fingers is about 24 μm at 20 μm displacement. In this instance, the voltage at the transition from stable to unstable (often called pull-in voltage) is 480 V (see section C.3.1). This is 4.6 times the voltage needed for actuation, so the situation is stable. In a second design the leaf-spring thickness and finger gap are 2 μm. The pull-in voltage would be 151 V, which is 3.2 times the necessary voltage. Therefore, the comb-drives will not experience pull-in at the requested voltages for actuation.

4.5.6 Platform stiffness blocked and unblocked

In this section two stiffness matrices, $C_{pl,unbl}$ and $C_{pl,bl}$, which couple the forces loaded onto the platform to the displacements of the platform, will be derived. $C_{pl,bl}$, is a 6x6 stiffness matrix to model the 6 DOFs stiffness of the platform for the situation that the actuators are blocked by the clamping mechanisms. $C_{pl,unbl}$, is a 6x6 stiffness matrix to model the 6 DOFs stiffness of the platform for the unblocked actuator situation.

The unblocked stiffness of the platform couples the forces loaded onto the platform to the displacements of the platform, if there are no other external forces loaded on the manipulator, and at an initially undeflected manipulator state. In this case only certain parts of equation 4.12 are of interest:

$$\begin{bmatrix} \underline{X}_{act} \\ \underline{X}_{pl} \\ \underline{X}_{r} \end{bmatrix} = \begin{bmatrix} \cdot & S_{12} & \cdot \\ \cdot & S_{22} & \cdot \\ \cdot & S_{23}^{\;T} & \cdot \end{bmatrix} \cdot \begin{bmatrix} \underline{0} \\ \underline{F}_{pl} \\ \underline{0} \end{bmatrix} \tag{4.31}$$

then:

$$\underline{F}_{pl} = C_{pl,unbl} \cdot \underline{X}_{pl} = S_{22}^{-1} \cdot \underline{X}_{pl} \qquad \Leftarrow \underline{F}_{act} = \underline{0}\,; \underline{F}_{r} = \underline{0} \tag{4.32}$$

Although the stiffness matrix C_{act}^{pl}, used to couple the actuator forces to the platform displacement, is located at the same place as $C_{pl,unbl}$, it is fundamentally different. This can be seen by comparing equation 4.16 and 4.32. This is similar to the 2 DOFs model of Figure 4.7, where c_{pl} (equation 4.4) is unequal to c_{act}^{pl} (equation 4.20).

The values of $C_{pl,unbl}$ are derived numerically from SPACAR and are linearized around the undeflected state. Equations 4.32 and 4.33 give the equation for the unblocked manipulator:

$$C_{pl,unbl} = \begin{bmatrix} 24.9 & 0 & 0 & 0 & 0.00171 & -0.00912 \\ 0 & 31.7 & -8.4 & 0.00864 & 0 & 0 \\ 0 & -8.4 & 29.1 & -0.00400 & 0 & 0 \\ 0 & 0.00864 & -0.00400 & 0.0000188 & 0 & 0 \\ 0.00171 & 0 & 0 & 0 & 0.0000133 & 0.0000140 \\ -0.00912 & 0 & 0 & 0 & 0.0000140 & 0.0000500 \end{bmatrix} \tag{4.33}$$

Comparing $C_{pl,unbl}$ and C_{act}^{pl} it is clear that the diagonal terms c_{33}, c_{44} and c_{55} of $C_{pl,unbl}$ are about 2.5 times lower than the terms of C_{act}^{pl}. The loss of stiffness of $C_{pl,unbl}$ is mainly due to the finite stiffness in *z*-direction. This can also be seen as the finite stiffness of c_2 of the 2 DOFs model of Figure 4.7. This is because the loading of Si-leaf-springs and folded flexures of the manipulator in the *z*-direction, in the situation used to calculate C_{act}^{pl}, is much less. If the height of the Si-leaf-springs and folded flexures was not restricted due to fabrication limitations, the *z*-stiffness would be much higher. The result in the 2 DOFs model would be, $c_2 >> c_1$ and therefore $c_{pl} \approx c_{act}^{pl}$. In case of the manipulator a good design would imply $C_{pl,unbl} \approx C_{act}^{pl}$ and each of the diagonal terms of $C_{pl,bl} >> C_{pl,unbl}$.

The blocked stiffness of the platform couples the forces loaded onto the platform to the displacements of the platform, if the external forces $\underline{F}_r = \underline{0}$, and the actuator position is locked by a stiff mechanism. In the model the forces on the actuator nodes $\underline{F}_{act}$ are such that $\underline{X}_{act} = \underline{0}$. In this case only certain parts of equation 4.12 are of interest:

$$\begin{bmatrix} \underline{0} \\ \underline{X}_{pl} \\ \underline{X}_r \end{bmatrix} = \begin{bmatrix} S_{11} & S_{12} & \cdot \\ S_{12}^{\ T} & S_{22} & \cdot \\ S_{13}^{\ T} & S_{23}^{\ T} & \cdot \end{bmatrix} \cdot \begin{bmatrix} \underline{F}_{act} \\ \underline{F}_{pl} \\ \underline{0} \end{bmatrix} \tag{4.34}$$

then:

$$\underline{F}_{pl} = C_{pl,bl} \cdot \underline{X}_{pl} = \left(- S_{12}^{\ T} S_{12}^{\ -1} S_{12} + S_{22}\right)^{-1} \cdot \underline{X}_{pl} \qquad \Leftarrow \underline{X}_{act} = \underline{0}\,;\, \underline{F}_r = \underline{0} \tag{4.35}$$

The values of $C_{pl,bl}$ are derived numerically from SPACAR and are linearized around the undeflected state. Equations 4.35 and 4.36 give the equation for the blocked manipulator.

$$\begin{bmatrix} F_{x,pl} \\ F_{y,pl} \\ F_{z,pl} \\ M_{x,pl} \\ M_{y,pl} \\ M_{z,pl} \end{bmatrix} = \begin{bmatrix} 822 & 0 & 0 & 0 & -0.372 & -0.773 \\ 0 & 1433 & -88.5 & 0.722 & 0 & 0 \\ 0 & -88.5 & 48.8 & -0.045 & 0 & 0 \\ 0 & 0.722 & -0.045 & 0.000392 & 0 & 0 \\ -0.372 & 0 & 0 & 0 & 0.000204 & 0.000471 \\ -0.773 & 0 & 0 & 0 & 0.000471 & 0.002493 \end{bmatrix} \begin{bmatrix} x_{pl} \\ y_{pl} \\ z_{pl} \\ rx_{pl} \\ ry_{pl} \\ rz_{pl} \end{bmatrix} \tag{4.36}$$

The z-stiffness is the lowest stiffness. Usually the z-stiffness is defined as $(\partial z/\partial F_z)^{-1}$, the inverse of element s_{33} of the compliance matrix. This is the experienced stiffness when a sole input force F_z is loaded onto the platform. The F_z force will not solely result in a z-displacement. In this case $(\partial z/\partial F_z)^{-1}$ = 43.3 N/m, while the pure z-displacement stiffness $\partial F_z/\partial z$ = 48.8 N/m. This is analogous to the 2 DOFs model comparing equation 4.1 and 4.2:

$$\left(s_{22}\right)^{-1} = \left(\frac{1}{c_1 \tan(\alpha)} + \frac{1}{c_2}\right)^{-1} = 240 \neq c_{22} = c_2 = 600 \tag{4.37}$$

The effectiveness of the clamping mechanism can be examined by comparing $C_{pl,bl}$ with $C_{pl,unbl}$. The stiffness increase in the z-direction in a blocked manipulator situation as opposed to an unblocked one is only 1.7 times. This is because the out-of-plane bending of the Si-leaf-springs is mainly responsible for the low stiffness in both cases. Therefore, clamping does not increase the stiffness in the z-direction much. The largest stiffness increase by blocking is in the rz-direction, i.e. 50 times.

The low stiffness of the platform in the *z*-direction means that small external forces cause quite a large position uncertainty. If, for an application such as micro assembly, the position uncertainty needs to be less than 1 μm (which is still quite inaccurate), the maximum external disturbance force should be less than 50 μN in this case, which is very small.

CONCLUSIONS:

- The difference in stiffness between a blocked and unblocked manipulator is not that great (unfortunately).
- The stiffness increase in the *z*-direction by blocking is lowest, i.e. only 68 %.
- The largest stiffness increase by blocking is in the *rz*-direction, i.e. 50 times.
- The absolute stiffness, especially in the *z*-direction, is relatively small.

4.5.7 Modal analysis

The coupling of the sample to the TEM column (Figure 1.3) should be very stable. Disturbances like acoustic noise or vibrations from a vacuum pump nearby cause the column to vibrate. High vibration mode frequencies of the manipulator make the resulting position error between the column and the sample small. Therefore, the first vibration mode frequency should be at least 1 kHz, as shown in the specifications of Table 1.2.

Although the stiffness of the manipulator, especially in the *z*-direction, is not very high, the suspended mass has become very low due to miniaturization. Therefore, the first vibration mode frequencies can still be high (>1kHz). Theoretically a good compliant mechanism design for a 6 DOFs manipulator should result in exactly 6 low frequency vibration modes with the actuators unblocked. These exactly 6 low frequency vibration modes are a result of the combination of compliance in the actuation direction and stiffness in all of the other directions. Blocking the actuators must therefore result in high vibration mode frequencies for all modes.

SPACAR was used to calculate the lowest vibration mode frequencies and the accompanying vibration modes. A distinction was made between the blocked and unblocked manipulator. Figures 4.12 and 4.13 show the first vibration modes, respectively, for a blocked and unblocked situation. The platform in the SPACAR is modeled as a rigid cross instead of a ring. The folded flexures, which are each replaced by six trusses, are not shown. The black wire frame represents the

undeformed state. The manipulator was modeled 100 times larger to gain precision in calculations. Therefore, the *x*-, *y*- and *z*-axis are 100 times larger. The resulting frequencies from SPACAR were scaled back by multiplying them by 100 (see also paragraph 2.2 for scaling rules).

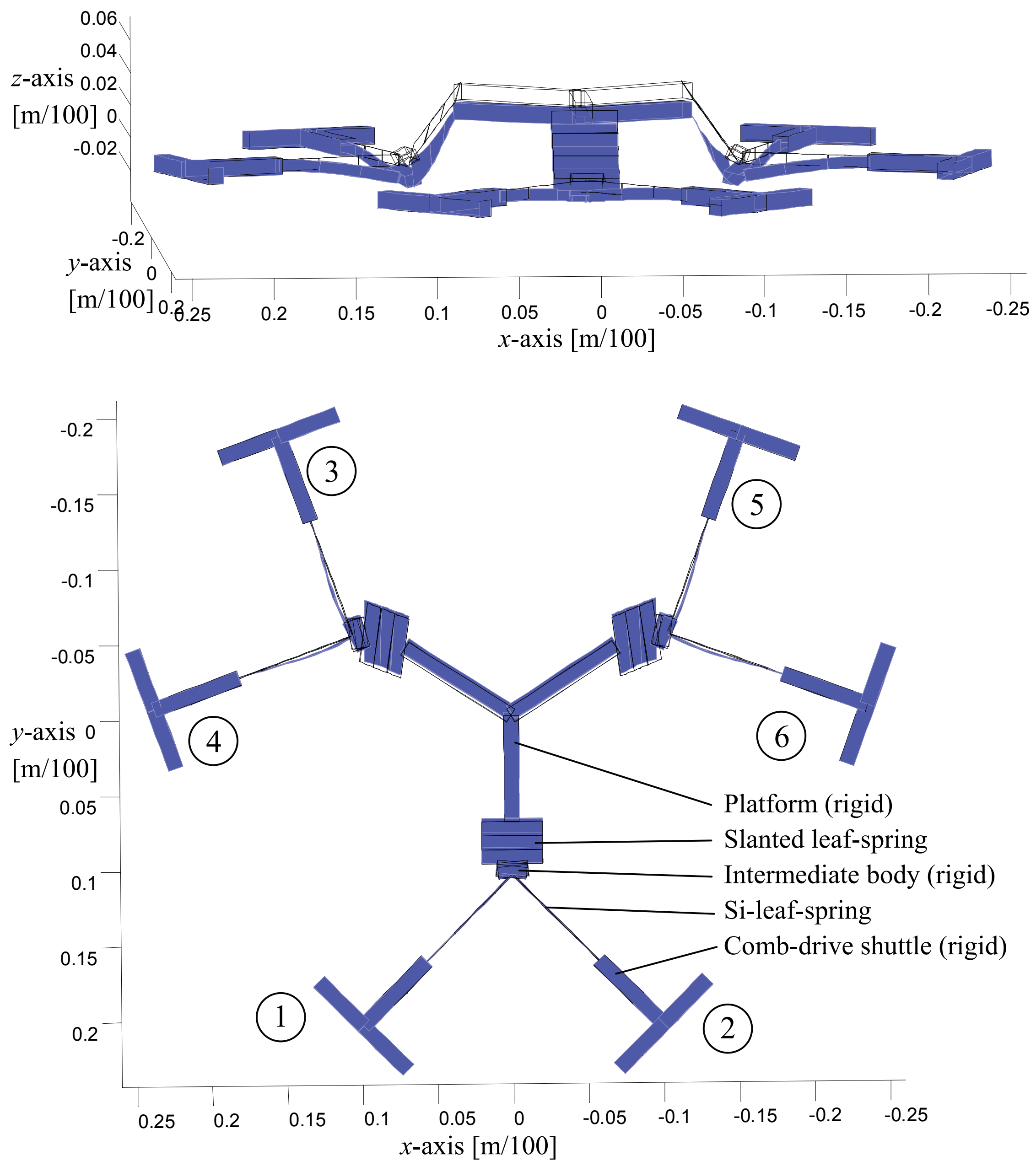

Figure 4.12: The first vibration mode with blocked actuators at 3.78 kHz. The platform mainly moves in the z-direction. The actuators do not move.

Figure 4.12 shows that the first vibration mode with blocked actuators at 3.78 kHz is a motion mainly in the *z*-direction. If a pure motion in the *z*-direction (*z*-stiffness is 49 N/m) is considered with only the platform mass moving being 65 μg, a frequency of 4.4 kHz would have resulted. The reason for the difference in frequency is that the real moving mass will be somewhat higher and the motion is not purely in the *z*-direction. Figure 4.12 also shows that the vibration mode is mainly caused by the out-of-plane bending of the Si-leaf-springs.

The second (4.1 kHz) and third (4.4 kHz) vibration mode show a mode which is also mainly caused by the out-of-plane bending of the Si-leaf-springs. However, the fourth vibration mode, with a much higher frequency of 18.2 kHz, is not caused by out-of-plane bending of the Si-leaf-springs. Therefore, if the out-of-plane bending stiffness of the Si-leaf-springs could be increased, the first three vibration mode frequencies would be increased considerably.

The leaf-springs are modeled by beams in SPACAR. A beam in SPACAR has a maximum of 6 independent deformation modes. In the model used for modal analysis, all the 162 deformation modes of all 27 beam elements have been taken into account. However, omitting the longitudinal compliance of all beams changes the first vibration mode frequency by only 0.025%. Therefore, the model can be reduced to 135 deformation modes of the beam elements, disregarding the longitudinal compliance of the leaf-springs.

Figure 4.13 shows the first vibration mode with unblocked actuators. The platform mainly moves in an *–ry*- and *x*-direction. The slanted leaf-springs 8 and 9 deflect in their compliant bending direction. Actuators 1 and 2 experience the largest displacements and move in anti-phase. Actuators 3, 4, 5 and 6 do not move considerably. This mode results from the asymmetry of the three slanted leaf-springs.

One would expect the first 6 vibration modes to be relatively low frequent, and to be mainly deformation modes in the compliant directions with a lot of actuator displacement. However, the blocked manipulator vibration mode frequencies are not much higher than the unblocked ones. Therefore, the first 6 vibration mode frequencies are not significantly lower than the rest of the vibration mode frequencies.

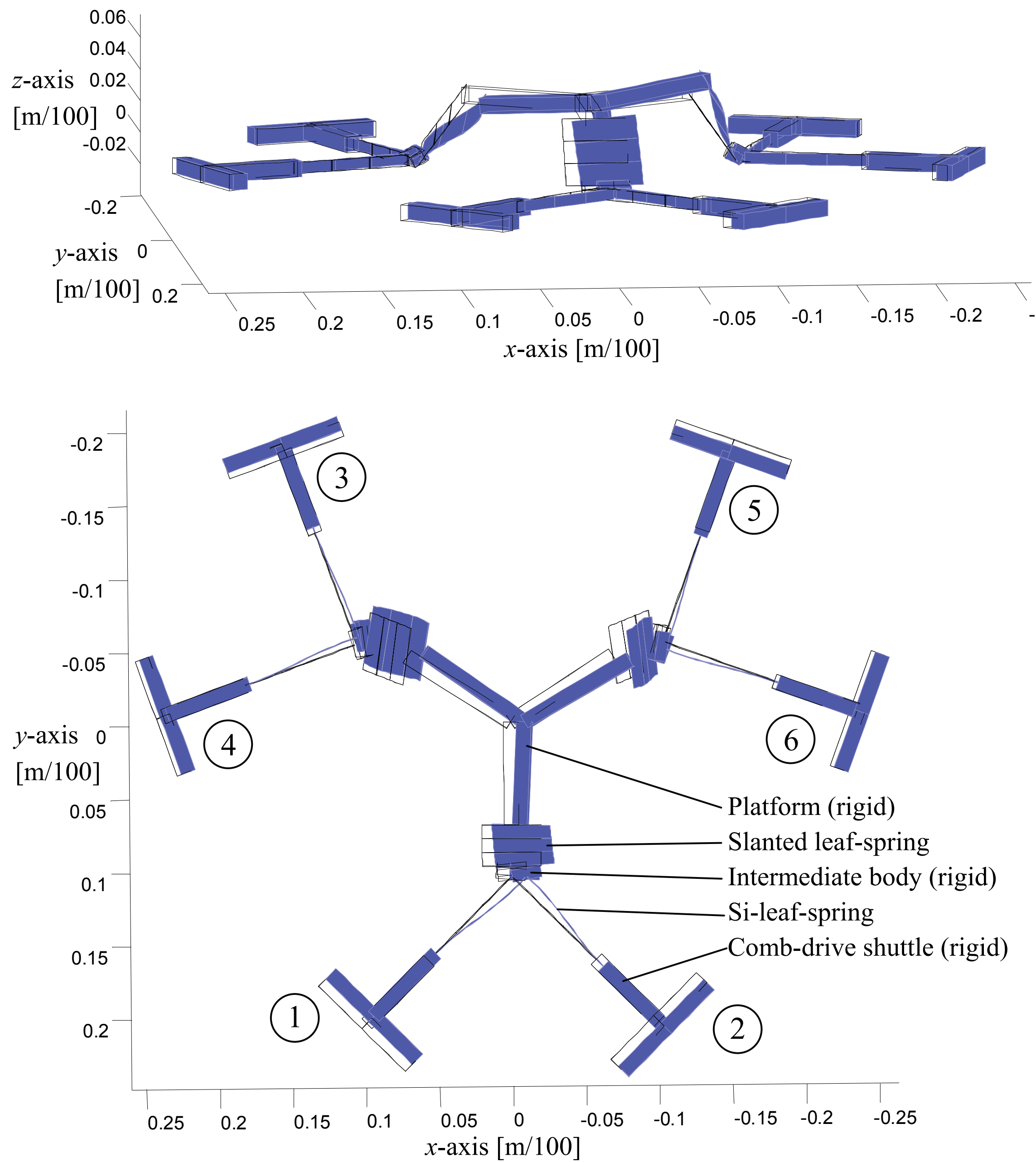

Figure 4.13: The first vibration mode with unblocked actuators at 2.55 kHz. The platform mainly moves in an –ry- and x-direction. Mainly actuators 1 and 2 displace in this vibration mode.

CONCLUSIONS:

- All vibration mode frequencies are well above the 1 kHz specification (Table 1.2).
- The first vibration modes of the unblocked manipulator are combinations of actuator movements (as expected).
- With blocked actuators the first three modes are caused by a low *z*-stiffness of the Si-leaf-spring. The bending stiffness of the Si-leaf-springs in the stiff direction (out-of-plane) is not enough compared to the compliant in-plane direction. This is caused by the limited height (35 μm) to thickness (3 μm) ratio of the Si-leaf-springs.
- The earlier mentioned *z*-stiffness remains low with the actuators blocked. Therefore, the increase of the first vibration mode frequency by blocking is only 48%.
- Because of limited design freedom a compromise had to be made between the preferably compliant and thus low frequency unblocked actuation modes and the preferably high frequent blocked actuator modes. This is essentially a trade-off between the necessary actuator force for displacing the platform and the first vibration mode frequency.

4.5.8 Vibration mode frequency shift due to platform displacement

The stiffness of leaf-springs changes when deflected, as explained in section 2.4. Therefore, the vibration mode frequencies of the platform are expected to change when the platform is deflected as well. SPACAR was used to investigate this frequency shift due to a displacement in the pure *x*, *y* and *z*-translations (Figure 4.14) and in the pure *rx*, *ry* and *rz*-rotation (Figures 4.15). In all cases, the actuators are blocked after initial displacement.

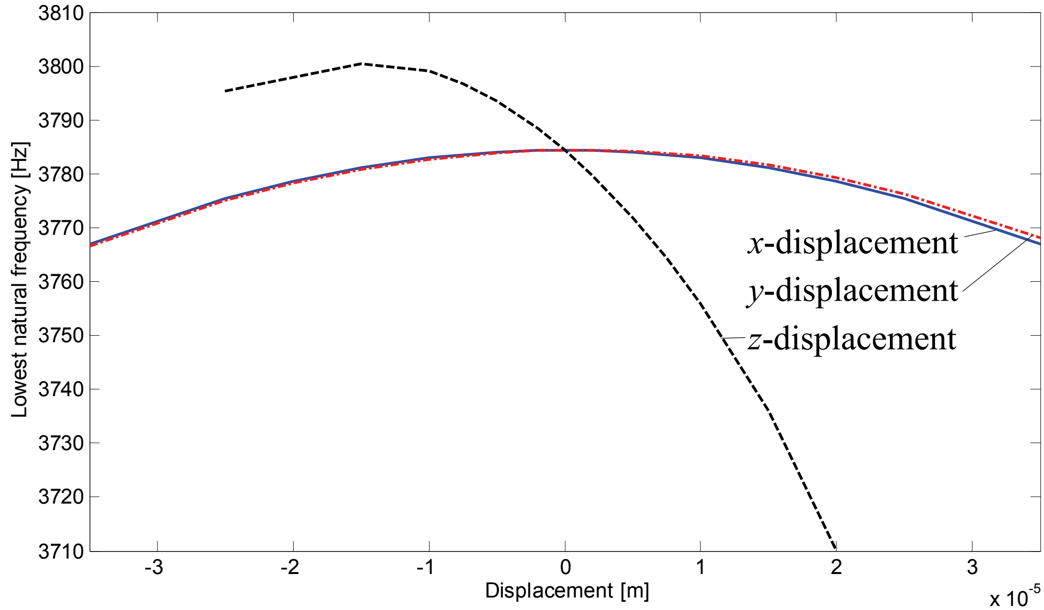

Figure 4.14: The first vibration mode change with blocked actuators due to platform displacement in the x-, y-, and z-direction.

The first vibration mode frequency with blocked actuators is a mode which mainly bends the Si-leaf-springs in the *z*-direction. The frequency shift of the mode is largest for a displacement in the *z*-direction. This shift is caused by the relatively large change in longitudinal stiffness of the slanted leaf-springs when deflected. In the *x*- and *y*-directions the slanted leaf-springs are not deflected. In-wafer-plane deflection of the Si-leaf-springs does not cause a large stiffness change in the *z*-direction, as is explained in section 2.4.1. However, the frequency shift due to platform translation is relatively small.

Figure 4.15 shows the vibration mode frequency change due to rotation. Rotation in the pure *rx*- and *ry*-direction results in the largest vibration mode frequency shift. The reason is that rotation in these directions requires the slanted leaf-springs to deflect, which causes a relatively strong stiffness decrease. However, the frequency shift due to rotation is relatively small.

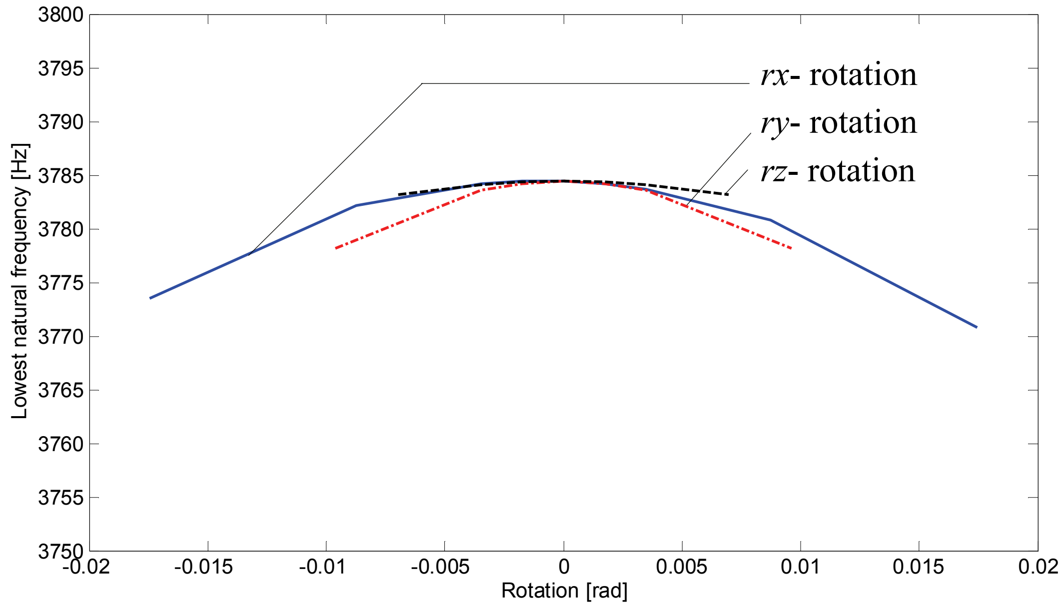

Figure 4.15: The first vibration mode frequency change with blocked actuators due to platform rotation in the rx-, ry-, and rz-direction.

CONCLUSIONS

- Although there is a frequency shift due to displacement and rotation, it is not significant.
- When comparing the vibration mode frequency shift due to displacements, displacing in the *z*-direction causes the largest frequency shift.

4.5.9 Robustness: Elastic stability and stress

There are several failure phenomena with regard to the parallel kinematic manipulator. Buckling is a mechanism where an external force causes the mechanism to become elastically unstable due to compressive stresses. The actual compressive stresses at failure are smaller than the ultimate compressive stresses that the material is capable of withstanding. Therefore, failure due to too high stress levels is another phenomenon. A distinction needs to be made between the stress resulting from internal forces due to deformation mainly in compliant directions, and stress resulting from external forces causing mainly tensile/compressive and or shear stress (in good designs). The two types of stress have different causes and are therefore treated separately.

ELASTIC STABILITY

With the actuators blocked in the undisplaced state, a force is loaded on the center of the platform. SPACAR has a mode for calculating the force causing elastic instability in a certain direction. This force is loaded on the platform from different directions to find the least buckling force. The least force was found exactly in the x-direction being 0.21 mN. In the y- and z-direction the buckling force is 0.41 mN and 0.91mN, respectively. The lowest buckling force is caused by the buckling of slanted leaf-spring 7 (Figure 4.4). It is possible to increase the thickness of the slanted leaf-springs in order to increase the buckling load.

STRESS FROM EXTERNAL FORCES

A force loaded onto the platform in the x-direction equal to the buckling load would result in a maximum stress of $11.6 \cdot 10^6$ N/m^2 in the slanted leaf-springs (SiRN). The maximum stress in Si-leaf-springs (SCS) is lower , i.e. $8.8 \cdot 10^5$ N/m^2. These stresses are low compared to the yield stresses of $14 \cdot 10^9$ N/m^2 of SiRN and $7.0 \cdot 10^9$ N/m^2 of SCS (Table 2.1), respectively, and therefore will not result in failure.

STRESS FROM INTERNAL FORCES

At a theoretical z-displacement of the platform of 25 μm the highest stress found in the folded flexures (SCS) is $180 \cdot 10^6$ N/m^2. The highest stress in the slanted leaf-springs (SiRN) is $120 \cdot 10^6$ N/m^2 and in the Si-leaf-springs (SCS) it is $70 \cdot 10^6$ N/m^2. These stresses are low compared to the yield stress, and therefore will not result in failure.

PRACTICAL CONSIDERATIONS REGARDING STRESS

Some design considerations have to be taken into account when designing compliant mechanisms. To prevent stress concentrations the connection of the Si-leaf-springs to the intermediate body is rounded with a 10 μm radius, as shown in Figure 4.16. The slanted leaf-spring has an additional support at the back of the intermediate body. The small overlap makes sure that, even though there will be mask layout and etching uncertainty, the slanted leaf-spring will conduct stiffness as shown in Figure 3.15b in the tensile and shear direction.

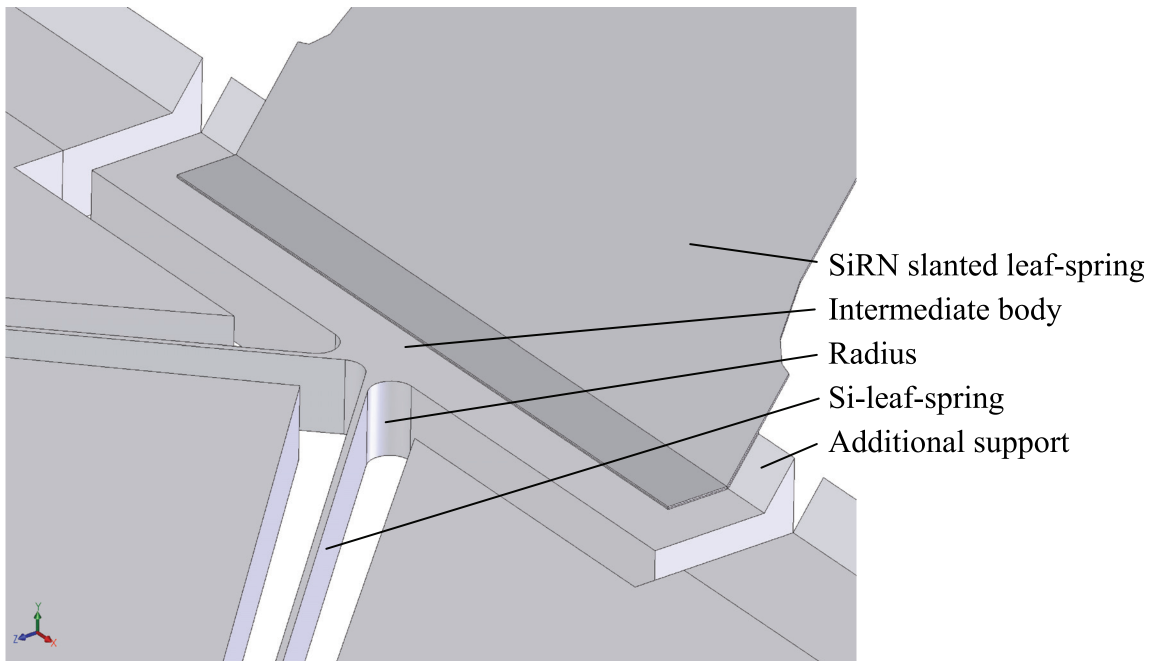

Figure 4.16: Detail of the connection of the SiRN leaf-spring and the Si-leaf-springs to the intermediate body.

CONCLUSIONS

- The stress by internal forces due to deflection is low. In general, this is the case if relatively low force actuators (comb-drives) are used in a compliant mechanism.
- The buckling load is the lowest in the x-direction, i.e. 0.21 mN.
- Stress caused by internal or external causes is not the failure mechanism for the manipulator, buckling is. This is the consequence of the long slender leaf-springs necessary to make the mechanism compliant enough for the low force actuators to result in the required strokes.

4.5.10 Thermal Stability

There are several sources causing thermal noise in the manipulator: the electron beam, sources attached to the TEM column, and thermo-mechanical noise. Thermo-mechanical noise is caused by the jiggles and jitters of matter having a finite temperature. It is equivalent to thermal fluctuations and causes motions of all DOFs of a system. At the micron scale the stiffness of a system can become so small that the small force fluctuation causes significant movement of the system. With respect to the possible heating by actuation, no significant heating is caused by the electrostatic comb-drive actuators.

LOW FREQUENCY THERMAL BEHAVIOR: DRIFT

Due to the interaction of the electrons with the sample, electrons lose about 0.02 % of their energy [106]. The electron beam with a current of 1 nA and 100 keV in the STEM mode heats the sample with 20 nW. The temperature difference between the surroundings and the sample on the platform can be roughly calculated using a simple electrical circuit as shown in figure 4.17. Q is the heat flow from the electron beam. The main energy exchange is due to conduction. C's and R's are the thermal capacitances and resistances, which can be calculated using equations 4.38 and 4.39. In Table 4.3 the definitions of the symbols are given and the numerical values of the thermal resistors and capacitances are derived.

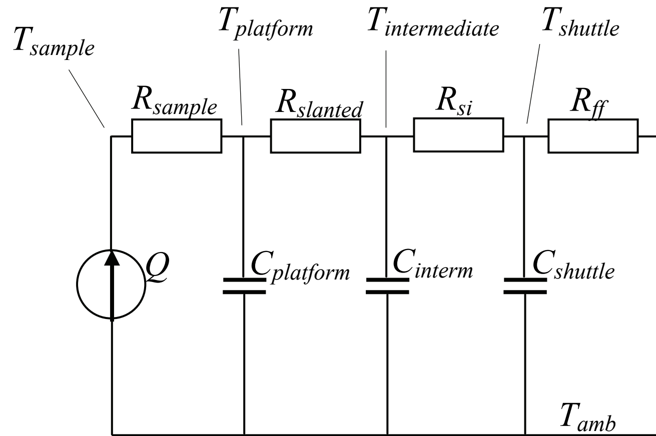

Figure 4.17: Analog electrical circuit of the thermal heat flow from sample to stationary SCS of the manipulator.

$$R = \frac{L}{A\,\lambda} \tag{4.38}$$

where L and A are the length and the cross-sectional area of a prismatic conductor. λ is the thermal conductance.

$$C = c_p\, V\, \rho \tag{4.39}$$

where c_p is the specific heat capacity, V is the volume and ρ is the specific mass.

	n	L	A	λ	R	
		m	m^2	W m^{-1} K^{-1}	K W^{-1}	
Sample [1]	1	2.00E-05	1.00E-12	157	1.3E+05	R_{sample}
3x Slanted leaf spring	3	4.03E-04	2.10E-10	19	3.4E+04	$R_{slanted}$
6x Si-leaf-spring	6	8.00E-04	1.05E-10	157	8.1E+03	R_{si}
24x Folded flexures [2]	24	4.60E-04	1.90E-10	157	6.4E+02	R_{ff}
		V	ρ	c_p	C	
		m^3	kg m^{-3}	J kg^{-1} K^{-1}	J K^{-1}	
Platform	1	2.8E-11	2300	700	4.6E-05	$C_{platform}$
3x Intermediated body	3	4.9E-13	2300	700	2.4E-06	$C_{intermediate}$
6x Shuttle	6	1.2E-12	2300	700	1.2E-05	$C_{shuttle}$

[1] Semiconductor Si sample

[2] Effective area of the reinforced leaf-springs

Table 4.3: Calculation of the thermal capacitances and thermal resistors.

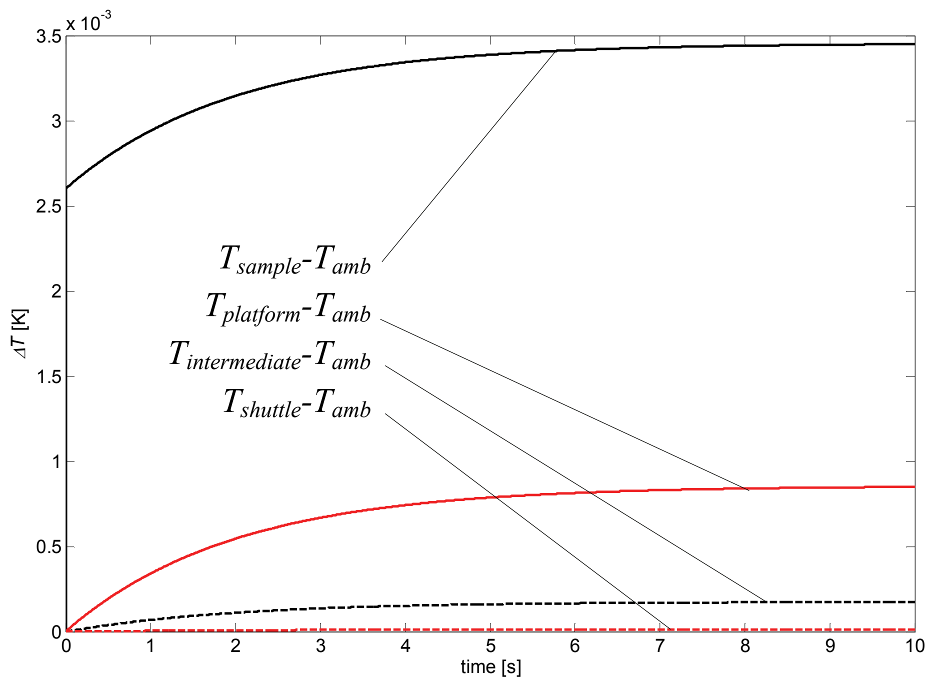

Figure 4.18: Temperature rise as a function of time at a step input of the E-beam heat source.

In a steady state of heat flow the maximum temperature difference between the sample and the platform will be 2.5 mK. The temperature difference between the platform and the surroundings will be 0.85 mK. The largest position change of the manipulator would arise due to the temperature increase of the slanted leaf-springs. The average temperature increase in the slanted leaf-springs is 0.42 mK. The thermal expansion coefficient of SiRN (Table 2.1), in combination with the length of the slanted leaf-springs, leads to an extension of 0.54 pm of the slanted leaf-springs. The corresponding z-displacement of the platform is 0.66 pm, which is

insignificant. The largest time constant of the electrical circuit shown in Figure 4.17 is 1.9 s. However, this time constant is small, which results in a fast adjustment of the sample and manipulator temperature to the TEM column temperature if, for example, a sample with manipulator is loaded into the TEM.

THERMO-MECHANICAL NOISE

Everything with a finite temperature jiggles and jitters around constantly. Therefore, temperature is principally causing motion. We can only speak of the temperature of a system if the velocities of the molecules in the system are distributed like the Maxwell distribution [85]. “H-theorem” says that no matter what the beginning condition of any system with a very large number of molecules is, after some time the velocities of the molecules within the system will attain the Maxwell distribution. The Maxwell distribution is the condition for equilibrium. Although a system might be in thermal equilibrium, the velocities of the molecules assume a huge range of values, but are not arbitrarily distributed. This thermal agitation of particles causes white noise and is called thermo-mechanical noise.

The equipartitian theorem [51] states that each degree of freedom which is quadratic in the Hamiltonian (such as energy storage in a spring, mass or capacitance) gets the mean energy:

$$< E > = 0.5\, c < x^2 > = 0.5\, k_B\, T \tag{4.40}$$

where $<E>$ is the mean energy, k_B is the Boltzmann constant, T is the absolute temperature, c is the spring constant related to the first vibration mode frequency and $<x^2>$ is the variance of the position. For a blocked actuator system, a spring constant equivalent to the highest inverse compliance (the z-direction) is taken, i.e. 43.3 N/m (section 4.5.6). At 293 K, $\sqrt{< x^2 >}$ becomes 9.7 pm. Therefore, the thermo-mechanical noise has no significant influence on the positional stability of the platform. The corresponding stiffness for 1 nm thermal-noise position uncertainty at 293 K is 4 mN/m, which is a very low stiffness.

CONCLUSIONS

- The largest temperature rise due to E-beam heating occurs in the sample itself, and is 3.5 mK.
- Temperature increase of the manipulator due to the E-beam leads to insignificant displacements of 0.66 pm.
- Time constants are small, i.e. <2s.

- Thermo-mechanical noise is not an issue.

4.6 Conclusions and recommendations

CONCLUSIONS

- A MEMS 6 DOFs manipulator design using 5 mask steps is presented.
- Individual platform displacements of x, y = 20 μm, z = 15 μm, rotations of 1.2° are possible.
- The overall dimensions are 6.2 x 6.2 mm.
- The first vibration mode frequencies are well above 1 kHz.
- The vibration mode frequency change due to platform displacement is insignificant.
- Actuation voltages up to 105 V are necessary in the current design.
- Stress caused by internal or external causes is not the failure mechanism for the manipulator, buckling is. This is the consequence of the long slender leaf-springs necessary to make the mechanism compliant enough for the low force actuators to result in the required strokes.
- The buckling force of the platform is quite small, even for a micro device, i.e. 0.21mN in the x-direction.
- The stiffness of the platform, especially in the z-direction, is small.
- The stiffness and first vibration mode frequency difference between blocked and unblocked actuators is not very large.
- The positional stability of the sample is not jeopardized by thermal disturbances as can be expected in a TEM.

- ***The total design is a synthesis of the fabrication process design and an exact kinematic constraint design.***

- ***The exact kinematic constraint design is a necessity to obtain both a high actuation compliance and high vibration mode frequencies.***

RECOMMENDATIONS

Depending on the application, the performance can be improved in several respects:

To downsize the actuators or to use lower voltages (downsizing the actuators makes it possible to downsize the total manipulator):

- Use comb-drive suspensions with a higher actuation compliance. Use 2 folded flexures per shuttle instead of 4. The leaf-spring length can then be increased as well (see Figure 2.13 for example).
- Use pre-curved leaf-springs for short stroke one-way actuators (section 2.5).
- Use more advanced designs for long stroke actuators (section 2.5).

To downsize the platform:

- Use thinned wafers, so that the <100> compensation structure width is smaller.
- Advanced wafer crystal alignment techniques might make the use of combined <100> and <110> compensation structures possible [4]. This would reduce the width of the compensation structure.

To increase the manipulator stiffness with blocked actuators:

- Increase the out-of-plane stiffness of the Si-leaf-springs. The Si-leaf-spring can be made thicker without compromising the actuation compliance too much.

To make the manipulator more robust:

- Thicken the slanted leaf-springs from 0.7 μm to 1.2 μm, which is the largest possible SiRN thickness at the moment. The actuation compliance will not change considerably
- Use thinned wafers, so that the slanted leaf-springs are shorter.

Chapter 5

DESIGN, FABRICATION AND TESTING OF A CLAMPING MECHANISM

In this chapter a design is presented for a relatively large force (0.5 mN) high precision MEMS clamping mechanism. The clamp is part of a MEMS TEM sample manipulator, which needs to be fixed unpowered once positioned. The elastic deformation of the clamp flexure has been optimized so as not to influence the TEM sample manipulator position during clamping. The device area of the total mechanism has been further optimized by finding a balance between the area necessary for sufficient flexure compliance and the actuator area necessary for sufficient actuation force and stroke. The process used for fabrication offers great design freedom, resulting in a compact design. Measurements show that the clamping mechanism is able to fix, hold and release a test actuator.

5.1 Introduction

Cross-talk between the electron-beam of the TEM and electric or magnetic fields from the actuators of the manipulator leads to undesired deflection of the E-beam and the manipulator. Therefore, the manipulator should be stably fixed without a magnetic or electric field in the TEM chamber. A mechanical clamp with a locking device is researched for that purpose. Clamping also prevents the low frequency vibration modes in the actuation direction of the manipulator, resulting from compliant actuator mechanisms, as is shown in chapter 4. Each of the six actuators of the 6 DOFs manipulator (chapter 4) will be equipped with a clamping mechanism.

Several grippers and clamps have been reported. Millet [96] describes a large stroke polysilicon gripper actuated by 16 scratch drives. Kota [77] demonstrates the existence of several grippers with distributed compliance. Bøggild [10] describes nanotweezers with gaps smaller than 330 nm. Skidmore [120] reports on several types of grippers used in the SEM environment. The clamp presented here is different from the reported ones, because it generates a relatively large clamp force and is able to maintain it without external power.

SPECIFICATIONS

There are several specific requirements for the clamping mechanism. The friction force to clamping force relationship of two DRIE surfaces in contact with each other is uncertain. Therefore, an adjustable clamp force is necessary in the first designs to test the necessary clamp force for fixing the manipulator. The manipulator actuators are able to deliver a force of 275 μN, as is calculated in section 4.5.4. At an estimated friction coefficient of 0.5 for silicon on silicon in air, the clamp hold force should be at least 275 μN. However, because of the uncertain friction coefficient the maximum clamp force of 500 μN with 100 μN adjustment steps is required. A smooth clamp force build-up is necessary to leave the position of the manipulator unaffected. The influence of clamping on the position of the manipulator actuator should be less than several nm. The required stiffness with which the clamping mechanism blocks one of the actuators of the 6 DOFs manipulator can be calculated: a maximum force of 275 μN (section 4.5.5) is loaded on the clamping mechanism. This is the force due to the elastic deformation of the compliant mechanism of the manipulator. This force is relayed from the manipulator actuator to the clamping mechanism when the manipulator actuator is switched off. If the deflection needs to be lower than 1 nm, the stiffness should be larger than 2.8 10^5 N/m. There will be six clamping mechanisms in the six DOFs manipulator. Therefore, the device area of the clamping mechanism should not exceed about 1.5 x 1.5 mm^2. The process should be compatible with the parallel kinematic manipulator process presented in chapter 4, Figure 4.3. In the total manipulator design the clamping mechanisms are etched in the 35-40 μm device plate in which the manipulator comb-drives are also etched (Figure 3.16).

The clamping mechanism specifications are:

- Adjustable clamp force up to 500 μN and a force resolution of 100 μN.
- Clamp force should build up smoothly.

- Position disturbance of the manipulator during clamping < 1 nm.
- Stiffness at which a manipulator actuator is blocked should be > $2.8\ 10^5$ N/m.
- Clamp force maintainable without an electrical voltage.
- Area of the clamping mechanism limited to 1.5 x 1.5 mm.
- Process compatible with the manipulator fabrication process as presented in section 4.2.

5.2 Conceptual design of the Clamping Mechanism

The comb-drives of the six DOFs manipulator have to be fixed in the actuation direction by clamping mechanisms (Figure 3.16). Therefore an extra leaf-spring, the stage-tail, is attached to each manipulator comb-drive. The six clamping mechanisms clamp the six stage-tails, and thereby fix the six DOFs of the manipulator.

In general, fabrication of two separate bodies by etching, like a clamping jaw and stage-tail, necessitates a gap (>2 μm) between them. In the macro world one would probably design a clamping system which is pre-tensioned in such a way that a passive clamp force blocks the stage-tail. Activating an actuator would then release the stage-tail. In MEMS, pre-tension can be obtained by using an extra actuator. One actuator will be used for generating pre-tension, and will be locked once the pre-tension is sufficient. A second actuator will be used for unlocking the stage-tail. However, because the clamp force needs to be adjustable, and to be built up gradually, two relatively large adjustable actuators are necessary. Another option is to use the stress generated in deposited films to generate a pre-tension. The stress is caused by temperature gradients in a film, and the difference between the expansion coefficients of the various materials used in the process. However, the stress and therefore the pre-tension is difficult to control. It would be interesting to research laser adjustment of silicon to generate an adjustable amount of pre-tension. However, this requires specialized research at this moment. The presented concept in this chapter consists of one small actuator and one large one. A relatively large comb-drive actuator generates an adjustable clamping force. A relatively small parallel plate actuator, used as an on-off switch, only locks the large actuator. The presented concept has a passive locked and unlocked position.

Linear comb-drives in general store a lot of strain energy in their suspension (Figures 2.9 and 2.10) in relation to the size of the flexure. This is because the leaf-springs have to bend in two directions. A first design has been based on a linear comb-drive actuator as can be found in JMM [13]. A rotational comb-drive tends to store less energy in its suspension during actuation because the bending only takes place in one direction. Therefore, the clamping mechanism concept will be based on a rotational comb-drive [14].

Figure 5.1 shows a schematic model of the compliant mechanism design of the clamp presented later. In the model, the leaf-springs are replaced by 1D stiffnesses and joints. The operation of the total clamp mechanism starts by closing the parallel plate actuator (Figure 5.1b). The pin moves down and the clamp comb shuttles are free to move. The clamp comb-drive actuator can now be activated. During the first part of the rotation (1.64°) of the jaw, the gap between the stage-tail and the jaws has to be closed (Figure 5.1c). The stage-tail is a leaf-spring that is attached to one of the actuators of the TEM manipulator, as shown in Figure 5.3. The comb-drive energy is stored in springs A, B, C, D and reinforcement spring F. The function of reinforcement F is to support the relatively large suspended mass in the out-of-plane wafer direction. When the jaws touch the stage-tail and the clamp comb-drive actuator force is increased, strain energy is mainly stored in springs C, D and reinforcement F (Figure 5.1d). At the same time, the clamp force starts building up. Once a desirable clamp force is obtained, the parallel plate actuators can be switched off, lowering the pins in the rack (Figure 5.1e). The clamp comb-drive can now be switched off (Figure 5.1f). There will be some backlash due to the movement of the pins in the rack until a stop is reached. Stiffnesses C and D ensure that only a small portion of the clamp force will be lost. However, they come at the cost of a larger clamp actuator stroke.

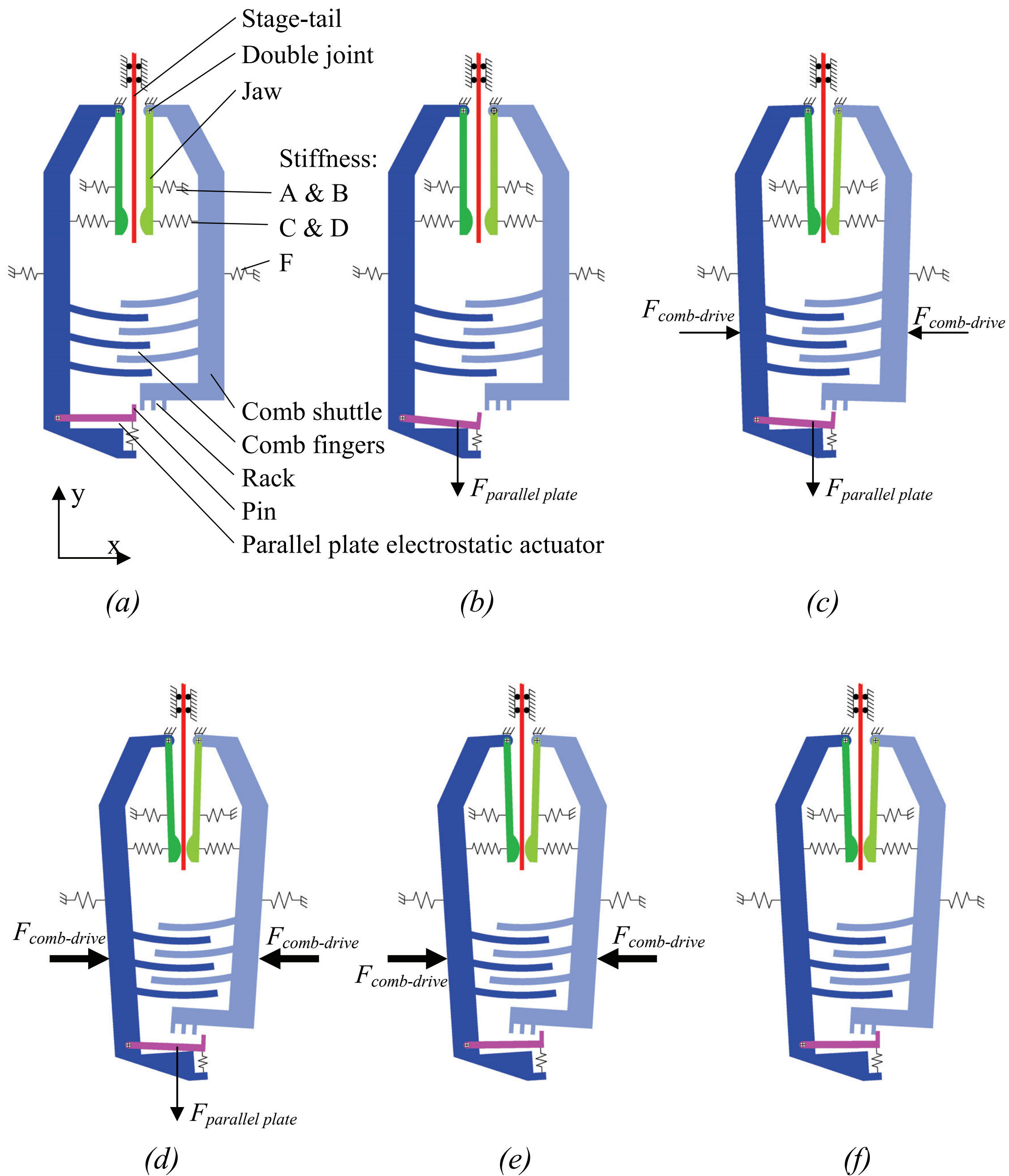

Figure 5.1: Model of the operation of the clamping mechanism. The model uses rigid bodies, joints and 1D springs to represent stiffness. a) The initial position as fabricated. b) The parallel plate electrostatic actuator is activated. c) The rotational comb-drive is activated. The jaws just touch the stage-tail. d) The comb-drive voltage is increased causing a clamping force of the jaws on the stage-tail. e) The parallel plate actuator is switched off. f) The comb-drive actuator is gradually switched off. The pin locks in the rack.

5.3 Clamp mechanism design

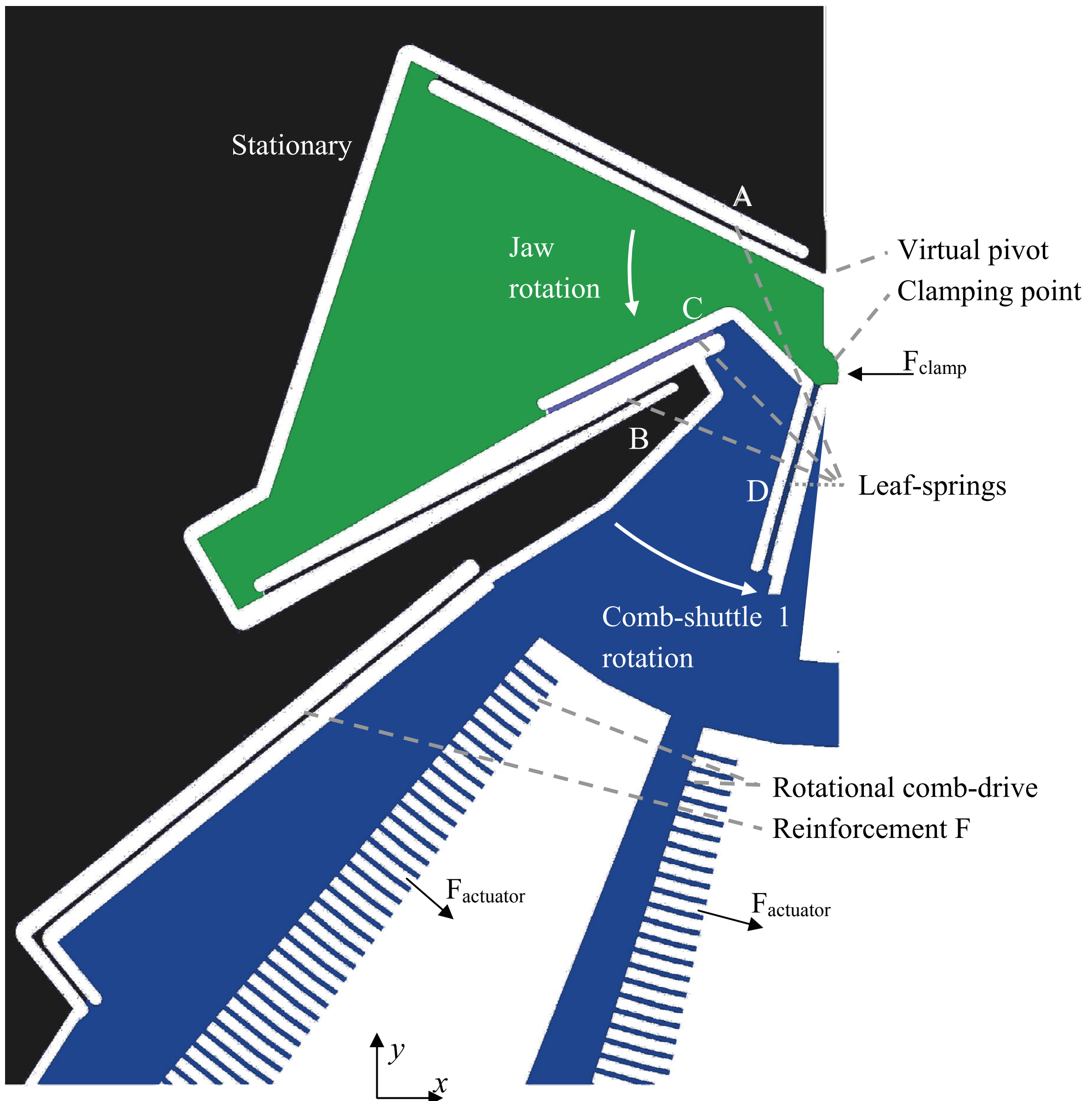

Figure 5.2: Half the clamping mechanism. The black body is stationary.

The jaw is suspended by leaf-springs A and B, as shown in Figure 5.2. In general, leaf-springs are very stiff in the longitudinal direction while being compliant in the lateral (bending) direction. When the two leaf-springs A and B deform together, the jaw will rotate around a virtual pivot (Figure 5.2). The virtual pivot is the intersecting axis of leaf-springs A and B. This virtual pivot is the center of rotation represented by the joints of the model shown in Figure 5.1. The rotational comb generates force at a larger radius than the clamp force. Therefore, the comb-drive force is amplified. Leaf-springs C and D intersect at the same virtual pivot as leaf-springs A and B. For relatively small deflections, the rotational comb-drive will

rotate around the common virtual pivot. Leaf-springs A, B, C and D are located close to the virtual pivot to minimize strain energy storage. Reinforcement F is a folded leaf-spring flexure, supporting the comb shuttle in out-of-plane direction, without constraining the other DOFs.

Because of the large clamp forces, and therefore the risk of buckling, the relatively long and slender leaf-springs A and B are tensile loaded during clamping. Leaf-springs A, B, C and D are initially pre-curved, so that at the maximum overlap of the comb-fingers the deformation causes them to be straight. The electrostatic pull-in force is greatest exactly at the point of maximum finger overlap, which is at a large voltage. However, the straightened leaf-spring's longitudinal stiffness is largest at the same time, effectively counteracting the pull-in risk. The two jaws are collectively actuated by one comb-drive. One large comb-drive actuator consumes less space than two separate ones. The stage-tail is compliant in the x-direction (Figure 5.3) to obtain an equal distribution of the clamp force in the jaws, and leaves the x-position of the manipulator unaffected by clamping.

To minimize the manipulator position deterioration due to the clamping force, several measures have been taken. First, the virtual pivot is located at the surface of the stage-tail. Therefore, nearly pure motion in the x-direction of the jaw at the clamping surface results, leaving the manipulator position unaffected. Second, the clamping force results in a tensile elongation of leaf-springs A and B. The leaf-spring tensile stiffnesses are tuned so that the clamp force will result almost solely in an x-displacement of the clamping area of the jaw. The residual y-displacement due to the abovementioned effect is tuned so that it is less than 1 nm (section 5.4). The Hertzian contact deformation due to clamping of the stage-tail results in an elongation of the tail of 0.19 nm in the y-direction, which is considered to be insignificant. Consequently, by clamping, the position of the stage will only be affected on a sub-nanometer scale.

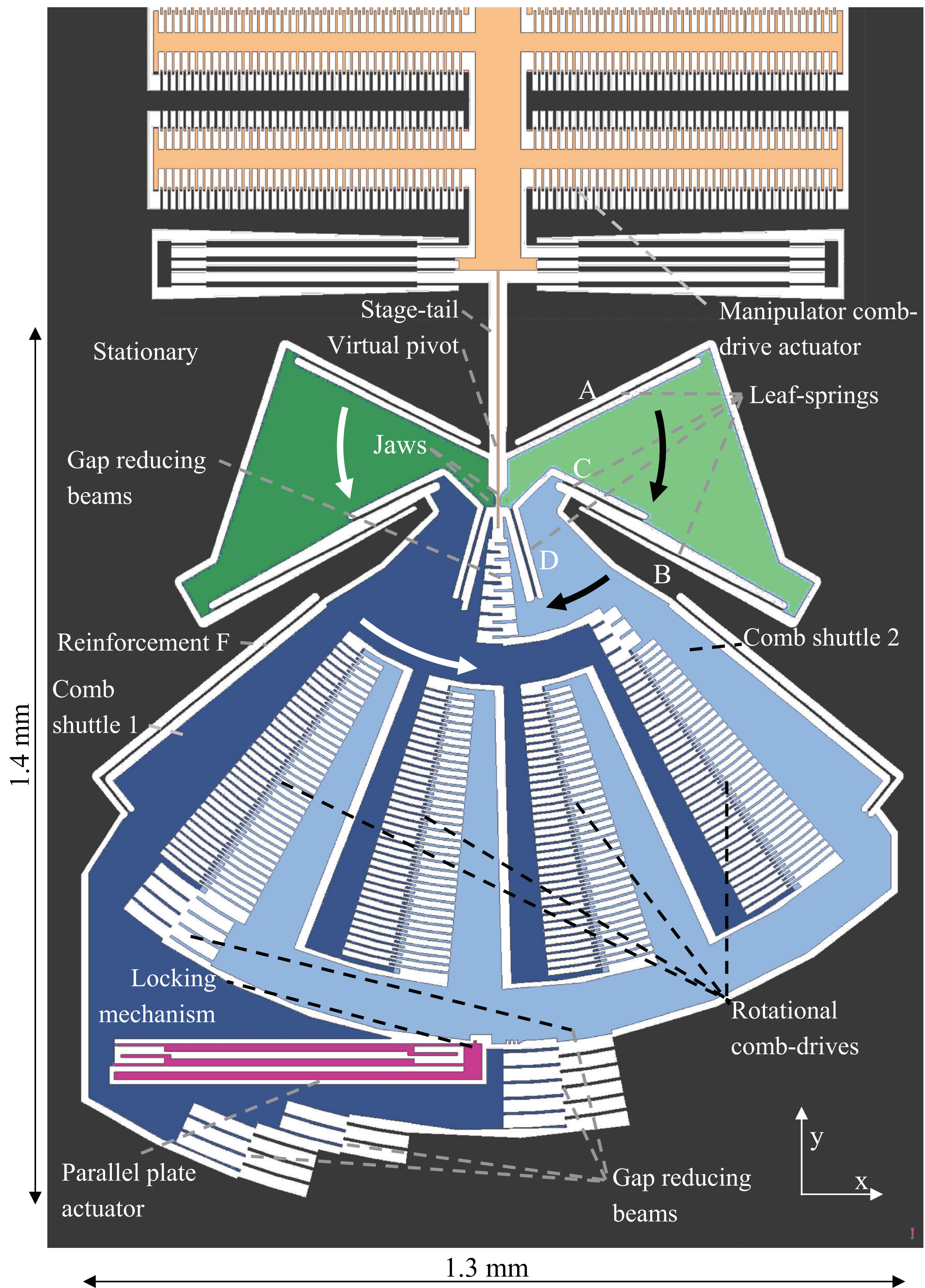

Figure 5.3: Top view of the total clamping mechanism with part of the manipulator comb-drive actuator.

The mechanism consists of several actuators. One actuator, the rotational comb-drive, is used to create a controllable clamp force (Figure 5.3). The mirror symmetric design of the two rotational combs that interact results in mostly similar geometric displacements with respect to the *y*-direction. This is beneficial to the alignment of the combs fingers. The second actuator, the parallel plate actuator, is much smaller and locks the position of the first actuator. The combination of a small locking mechanism and a larger controllable clamp offers a relatively small clamping device. The applied clamp comb-drive has 144 comb-finger pairs and delivers a torque of 52nNm which is an average force of 97μN at 80V in the middle of the rotational comb-drive. The longest comb-fingers are 93 μm long and 3 μm wide. According to Elata [44] this finger geometry does not cause the compliance of the fingers themselves to pull in at 80V.

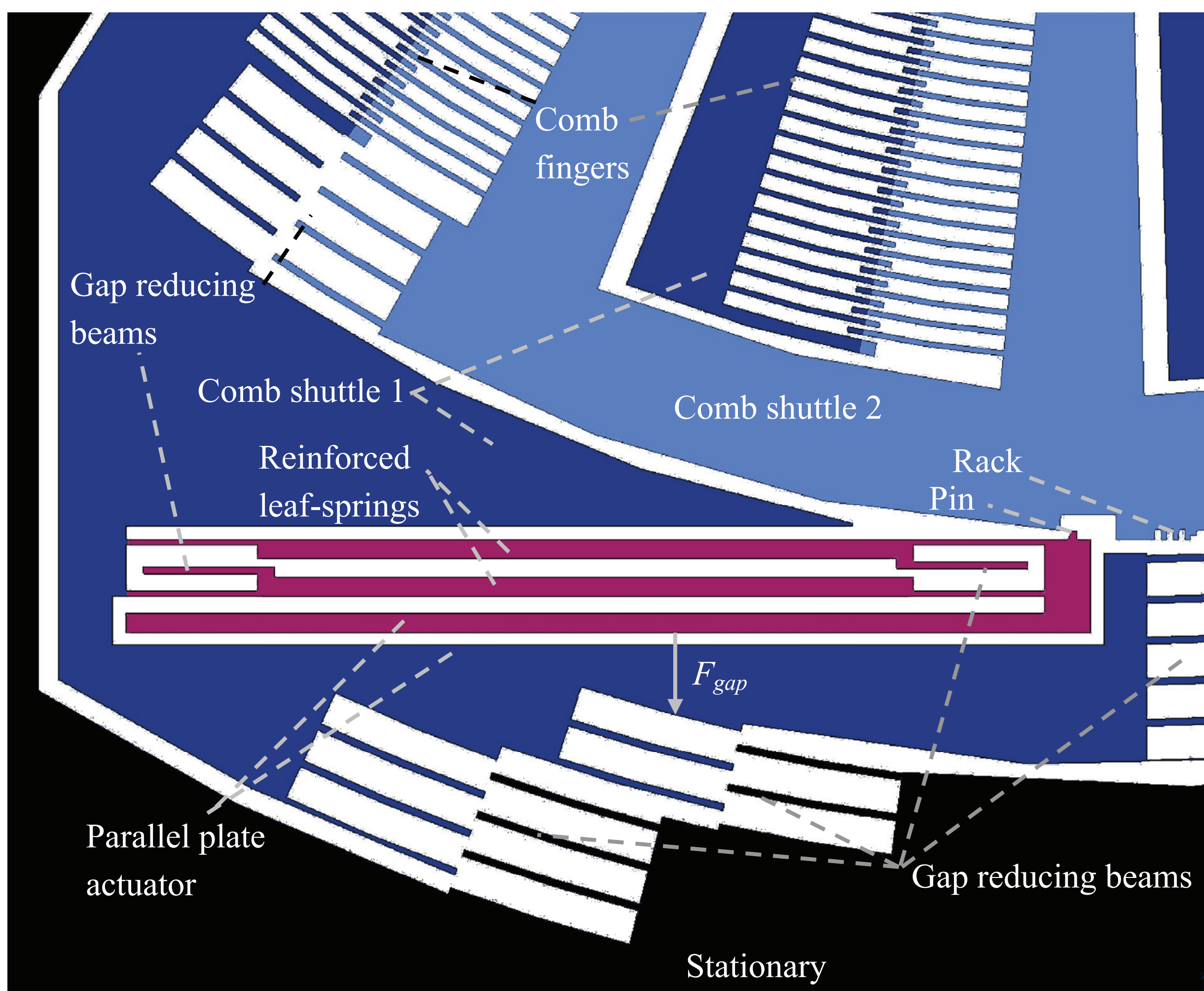

Figure 5.4: Fixation mechanism of the clamping mechanism.

Because of its short stroke and large force, a gap closing actuator is used for the pin locking mechanism (Figure 5.4). The basic operation of the actuator can be seen in Appendix C, Figure C.4. At 60V the pull-in voltage is reached and the comb-drive is free to move. The shear stress in the locking pin is small, $1.5\ 10^6$ N/m^2. Reinforced leaf-springs suspend the pin and increase the buckling load. Because of low contact pressure the wear of the pin and rack will be small. The locking mechanism is located far from the virtual pivot to decrease rotational backlash at the pivot. Backlash is due to the movement of the pins in the rack until a stop is reached.

Steps of 100μN hold force are determined by the stiffness of leaf-spring C, D and reinforcement F in combination with the locking resolution. Making the leaf-springs too compliant will require extra stroke and actuator energy for the comb-drive. Making leaf-springs too stiff leads to unacceptable loss of clamp force when locking.

CONCLUSION:

- A combination of a comb-drive actuator and an on-off switching parallel plate actuator leads to a clamping concept with an adjustable clamping force level and relatively small area, capable of maintaining the clamp force without a voltage.
- Rotation around the virtual pivot is the only compliant DOF in the exact kinematic constraint design, making the device relatively small with respect to the generated force, while still being robust.
- A rotational comb-drive suspension stores a minimal amount of strain energy.
- The comb-drive force is amplified.
- Leaf-springs A, B, C and D are initially pre-curved for pull-in risk reduction.
- The tensile stiffnesses of leaf-springs A, B, C and D are tuned so the clamp force will result almost solely in an *x*-displacement of the clamping area of the jaw.
- Leaf-springs A and B are tensile loaded to avoid buckling.
- The symmetric design of the two combs interacting results in mostly similar geometric displacements of the comb-shuttles.

5.4 Modeling the clamping mechanism

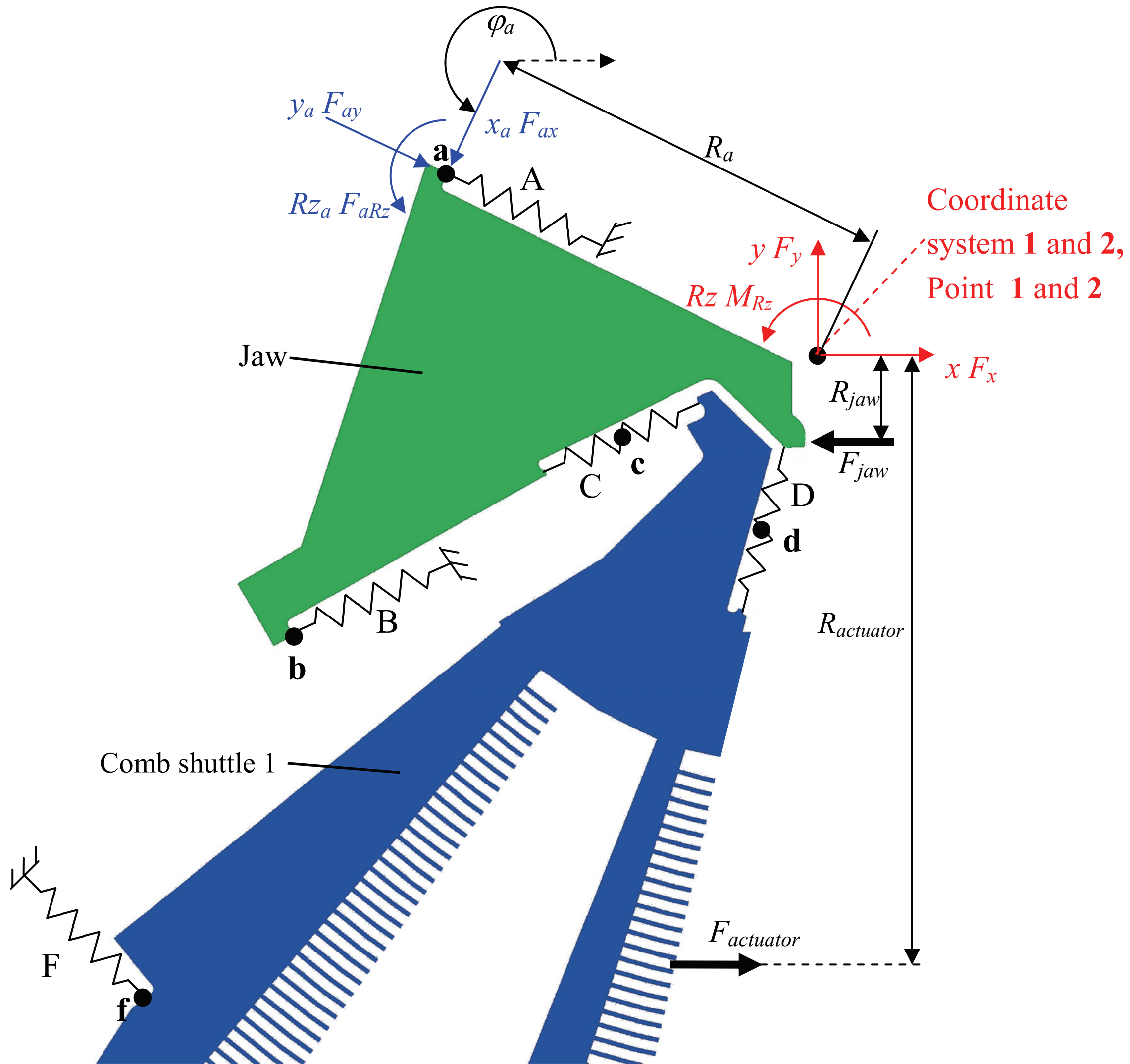

Figure 5.5: Model of half the clamping mechanism. In the drawing the leaf-springs and reinforcement F are replaced by springs, which each represent a 3 x 3 stiffness matrix. Coordinate system 1 represents the displacements of the 'jaw', while coordinate system 2 represents the displacements of 'comb-shuttle 1'. In the model used, the coordinate systems coincide.

A planar linear static equilibrium model as shown in Figure 5.5 has been set up for determining the strain energy storage and stress in the elastic elements, the displacements of the rigid bodies and the stiffnesses. This linear analysis is valid only for relatively small displacements.

Goal of the model:

- Determine actuator force and stroke.
- Optimize dimensions of leaf-springs A and B and their angle φ for minimizing the displacement of the stage-tail in the y-direction during clamping.
- Optimize the occupied area. This area is a combination of the dimensions of the leaf-springs and the actuator. Long leaf-springs, occupying a large area, lead to small strain energy storage which requires a small actuator. Short leaf-springs require a large actuator force to deflect. The optimum can be found somewhere in the middle.
- Tune leaf-springs C and D for a 0.1 mN clamp force resolution.
- Determine the buckling force.
- Determine the stress in the flexures.

The model depicted in Figure 5.5 regards half the clamping mechanism. It consists of 2 rigid bodies: the 'jaw' and the 'comb-shuttle 1'. There are 5 elastic elements: leaf-springs A, B, C, D and the reinforcement F. Coordinate system **1** gives the displacements of point **1** of the rigid body 'jaw', and is located, for ease of calculation, at the virtual pivot. In general, it could be located anywhere. It is the point at which equilibrium is examined. Coordinate system **a** gives the displacements of point **a** of the rigid body 'jaw', and is located at one end of leaf-spring **A** (Figure 5.5). A displacement of point **1** in coordinate system **1**, given by displacement matrix $\underline{X}_1$, leads to displacement matrix $\underline{X}_a$ of point **a** in coordinate system **a**:

$$\underline{X}_a = T_{1a}\underline{X}_1 \tag{5.1}$$

where T_{1a} is the transformation matrix representing the linear geometric transfer of displacements $\underline{X}_1$ of point **1** to displacements of point **a,** $\underline{X}_a$ in coordinate system **a**. In this case:

$$\begin{bmatrix} x_a \\ y_a \\ Rz_a \end{bmatrix} = \begin{bmatrix} \cos(\varphi_a) & \sin(\varphi_a) & R_a \\ -\sin(\varphi_a) & \cos(\varphi_a) & 0 \\ 0 & 0 & 1 \end{bmatrix} \begin{bmatrix} x_1 \\ y_1 \\ Rz_1 \end{bmatrix} \tag{5.2}$$

with R_a the distance and φ_a the angle between the coordinate systems, as is shown in Figure 5.5. The stiffness matrix C_a represents the stiffness of leaf-spring **A** in point **a** in coordinate system **a**. Multiplying the displacement of $\underline{X}_a$ by stiffness matrix C_a, results in the force matrix $\underline{F}_{ax1}$ in point **a**, in coordinate system **a**:

$$\underline{F}_{ax1} = C_a T_{1a} \underline{X}_1 \tag{5.3}$$

In this case:

$$\underline{F}_{ax1} = \begin{bmatrix} F_{ax1\,x} \\ F_{ax1\,y} \\ M_{ax1\,Rz} \end{bmatrix} = \begin{bmatrix} \frac{12\, E_{ya} I_a}{L_a^3} & 0 & \frac{-6\, E_{ya} I_a}{L_a^2} \\ 0 & \frac{E_{ya} A_a}{L_a} & 0 \\ \frac{-6\, E_{ya} I_a}{L_a^2} & 0 & \frac{4 E_{ya} I_a}{L_a} \end{bmatrix} T_{1a} \underline{X}_1 \tag{5.4}$$

where E_{ya} is the Young's modulus in the y_a direction, as is shown in Figure 5.5, I_a is area moment of inertia, A_a is the cross sectional area and L_a is the length of the leaf-spring. This force matrix is converted to a force matrix at point **1**, expressed in coordinate system **1** of the 'jaw':

$$\underline{F}_{1ax1} = \begin{bmatrix} F_{1ax1\,x} \\ F_{1ax1\,y} \\ M_{1ax1\,Rz} \end{bmatrix} = T_{1a}^{\ T} C_a T_{1a} \underline{X}_1 \tag{5.5}$$

In a similar way, the force matrices $\underline{F}_{1bx1}$ and $\underline{F}_{1cx1}$ caused by the stiffnesses of leaf-springs C and D and the displacement of point **1** can be determined. Displacements of point **2** of the rigid body 'comb shuttle 1' are expressed in coordinate system **2**, which is located at the virtual pivot (for convenient calculation purposes). In this design, coordinate systems **1** and **2** coincide. A displacement of point **2** also leads to forces on point **1**. The force matrix $\underline{F}_{cx2}$ in point **c** due to displacement of point **2** is:

$$\underline{F}_{cx2} = C_c T_{2c} \underline{X}_2 \tag{5.6}$$

where T_{2c} is the transfer matrix representing the linear geometric transfer between the displacements of point **2** on 'comb shuttle 1' and the displacements of point **c**. In this case $T_{1c} = T_{2c}$, but in general this is not true. Force matrix $\underline{F}_{cx2}$ is converted to force matrix $\underline{F}_{1cx2}$ at point **1** of the 'jaw' induced by displacement of point **2** of the 'comb shuttle 1':

$$\underline{F}_{1cx2} = T_{1c}{}^{T} C_c T_{2c} \underline{X}_2 \tag{5.7}$$

In a similar way, the force matrix $\underline{F}_{1dx2}$ resulting from stiffness D can be calculated. Combining the forces on point **1** leads to the equilibrium equation. Free body analysis results in:

$$\begin{aligned} &T_{1a}{}^{T} C_a T_{1a} \underline{X}_1 + T_{1b}{}^{T} C_b T_{1b} \underline{X}_1 + T_{1c}{}^{T} C_c T_{1c} \underline{X}_1 + T_{1d}{}^{T} C_d T_{1d} \underline{X}_1 \\ &\quad - T_{1c}{}^{T} C_c T_{2c} \underline{X}_2 - T_{1d}{}^{T} C_d T_{2d} \underline{X}_2 = \underline{F}_1 \end{aligned} \tag{5.8}$$

where $\underline{F}_1$ is the external force matrix acting on the 'jaw' at point **1**. In a similar way, the equilibrium at point **2** can be determined:

$$\begin{aligned} &T_{2c}{}^{T} C_c T_{2c} \underline{X}_2 + T_{2d}{}^{T} C_d T_{2d} \underline{X}_2 + T_{2f}{}^{T} C_f T_{2f} \underline{X}_2 \\ &\quad - T_{2c}{}^{T} C_c T_{1c} \underline{X}_1 - T_{2d}{}^{T} C_d T_{1d} \underline{X}_1 = \underline{F}_2 \end{aligned} \tag{5.9}$$

The external forces acting on the system are the jaw force, F_{jaw}, and the comb-drive actuator force, $F_{actuator}$:

$$\underline{F}_1 = \begin{bmatrix} F_{jaw} \\ 0 \\ F_{jaw} \cdot R_{jaw} \end{bmatrix}; \quad \underline{F}_2 = \begin{bmatrix} F_{actuator} \\ 0 \\ F_{actuator} \cdot R_{actuator} \end{bmatrix} \tag{5.10}$$

where R_{jaw} is the distance from the 'jaw' to the virtual pivot, and $R_{actuator}$ is the distance from the middle of the comb-drive actuator to the virtual pivot (Figure 5.5). The displacements of the 'jaw' and 'comb-shuttle 1' as a function of the jaw force and the comb-drive force can be calculated given a certain geometry.

DIMENSIONING THE LEAF-SPRINGS

Leaf-springs A and B are optimized by tuning angles φ_a and φ_b and the lengths L_a and L_b in such a way that the displacement in the y-direction during clamping is less than 1 nm. The total device area is optimized by tuning the length of the leaf-springs in relation to the necessary comb-drive area. The compliance of leaf-springs C and D is tuned so that a clamp resolution of 0.1 mN results. The resulting leaf-spring dimensions are given in Table 5.1. The reinforcement F is chosen to be as long and thin as possible, to store the least amount of energy during deflection. In several implemented design variations on the actual wafer, the reinforcement F is left out to test if it is necessary for robustness.

	Dimensions: length x height x thickness [μm^3]	Angle with origin φ [°]	Distance of associated stiffness matrix to origin R [μm]
Leaf-spring A	315 x 35 x 3	245	347
Leaf-spring B	355 x 35 x 3	300	503
Leaf-spring C	150 x 35 x 3.6	295	175
Leaf-spring D	150 x 35 x 3.6	346	155

Table 5.1: Geometry of the leaf-springs of the clamping mechanism.

MOTION OF THE JAWS AND COMB-SHUTTLES

In the first 1.64° rotation of the 'jaw', when the 'jaw' does not touch the stage-tail, the comb-drive energy is stored in leaf-springs A, B, C, D and reinforcement F. At 1.64° rotation of the 'jaw' and 1.87° rotation of the 'comb-shuttle 1', the 'jaw' touches the stage-tail. Due to the bending compliance of leaf-springs C and D, jaw force will be built up from 0 to 0.5 mN by rotation of 'comb-shuttle 1' from 1.87° to 2.36° by the comb-drive actuator.

Based on geometry, disregarding elastic energy storage, the force transmission ratio between the actuator force and the clamp force would be 1:7.7. Using the model it can be shown that the actual force transmission ratio is 5.2, denoting the significance of modeling the elastic energy. 33% of the comb-drive force and 79% of the stroke is necessary for closing the 2 μm gap between the stage-tail and the 'jaw'. This minimum gap dimension is necessary for etching, and is determined by the DRIE process.

STIFFNESS OF THE JAWS IN MANIPULATOR ACTUATOR MOTION DIRECTION

The stiffness at which the jaws clamp the stage-tail of the manipulator in the actuation direction is equal to the stiffness in the x-direction of the two 'jaws' at the virtual pivot. This stiffness is 4.1 10^4 N/m, which is quite large for a small device. It is caused by the large tensile stiffness of leaf-springs A and B. However, loading the two 'jaws' with the maximum force of the compliant mechanism of the manipulator (which is equal to the maximum manipulator comb-drive force of 275 μN) results in 6.7 nm 'jaw' displacement. Therefore, when the manipulator actuator is switched off and the jaws take over, the manipulator actuator displaces a maximum of 6.7 nm due to the compliant mechanism force. This displacement is too much for the TEM sample manipulator application. Therefore, the manipulator has to be controlled in the TEM application by means of feed-forward position control.

STRESS IN THE LEAF-SPRINGS

With the rotation and the displacement of the leaf-springs known, the bending moment, the shear force and the tensile or compressive force in each of the leaf-springs are known. However, the tensile and compressive stress due to clamping is small compared to the bending stress. The highest stress occurs in leaf-spring C. The 13 mRad rotation and 4.37 μm lateral displacement due to bending cause a bending stress of 405 10^6 N/m^2. With a Young's modulus in the φ_c direction of 150 10^9 N/m^2 this means that the maximum strain is 0.27%, which is acceptable for single crystal silicon.

BUCKLING OF THE LEAF-SPRINGS

Leaf-spring A and B are designed in such a way that they are tensile loaded. Leaf-spring A is loaded by 25μN, which would be 26% of the buckling load if leaf-spring A would be loaded compressively. Therefore, it is a safe choice to design leaf-spring A (and B) so that it is loaded tensile. Leaf-springs C and D are loaded compressively, with leaf-spring D loaded the heaviest by 131 μN, which is 3.1% of the buckling load.

The calculations show that most of the specifications mentioned in section 5.1 are satisfied.

5.5 Process design

The clamp is a planar mechanism which needs to be integrated in the parallel kinematic manipulator. Therefore, the fabrication process needs to be compatible with the parallel kinematic manipulator fabrication process. Several MEMS-based process recipes exist for fabrication of planar mechanisms. In ***Surface micro machining***, a structural layer is deposited on a sacrificial layer, as shown by Legtenberg [81]. The deposited layer is, however, limited to 5 – 10 μm in thickness. The ***Twin process*** as described by Sarajlic [112] is a bulk micro machining process resulting in a 35 μm thick structural layer. A drawback is the limited bandwidth of the gaps and trenches, as a result of the isotropic under etch, which limits design freedom. ***Silicon on insulator*** technology offers great design freedom, but is incompatible with the parallel kinematic manipulator process. The ***backside release*** process as demonstrated by Sarajlic [112] offers a 35 μm thick structural layer, offers reasonable design freedom (trenches 3-20μm) and is compatible with the parallel kinematic manipulator process.

The process implemented is a three mask process based on the backside release process demonstrated by Sarajlic [112]. The full process document is shown in Appendix H. The first mask is a layout of the insulation of the electrical wiring. In MEMS, however, this insulation is also a structural mechanical connection. The process is usually referred to as trench isolation [141]. In a P^+ doped (for conductivity) <100> double-sided polished Si wafer trenches of 2 μm wide and 40 μm deep are etched by Standard Bosch, Deep Reactive Ion Etching (DRIE) Step 1, Figure 5.6a. The Bosch process uses passivation of the side walls by deposition of fluor-carbon. A dry oxidation step removes the passivation so a good bond between the SiRN and Si can be made. By Low Pressure Chemical Vapor Deposition (LPCVD) of Silicon rich Nitride (SiRN) the trenches will be filled. The deposition of SiRN is largest at the top of the trench. Filling the straight walled trench in one step results in a small depth weld of SiRN at the top of the trench. Therefore, the trenches are filled in two steps with an etch step in between. First the trenches are filled up to 75% by SiRN, step 2 Figure 5.6a. By selective etching of SiRN the top restriction is removed from the trench, step 3. It is important to use a very selective recipe, at the Adix 100DE for example. Otherwise the trenches will stick out of the silicon and will be difficult to cover in resist later on. Figure 5.8 shows the consequences of resist with bad step coverage. Figure 5.7 shows optical microscope pictures of the trench filling process. A second layer of SiRN is deposited to fill the

trenches and provide a 4-6 μm long connection at the top of the trench, step 4. The electrical insulation by SiRN has been buried in the wafer. The planar SiRN at the bottom side is structured to function as a KOH mask. KOH etches silicon anisotropically.

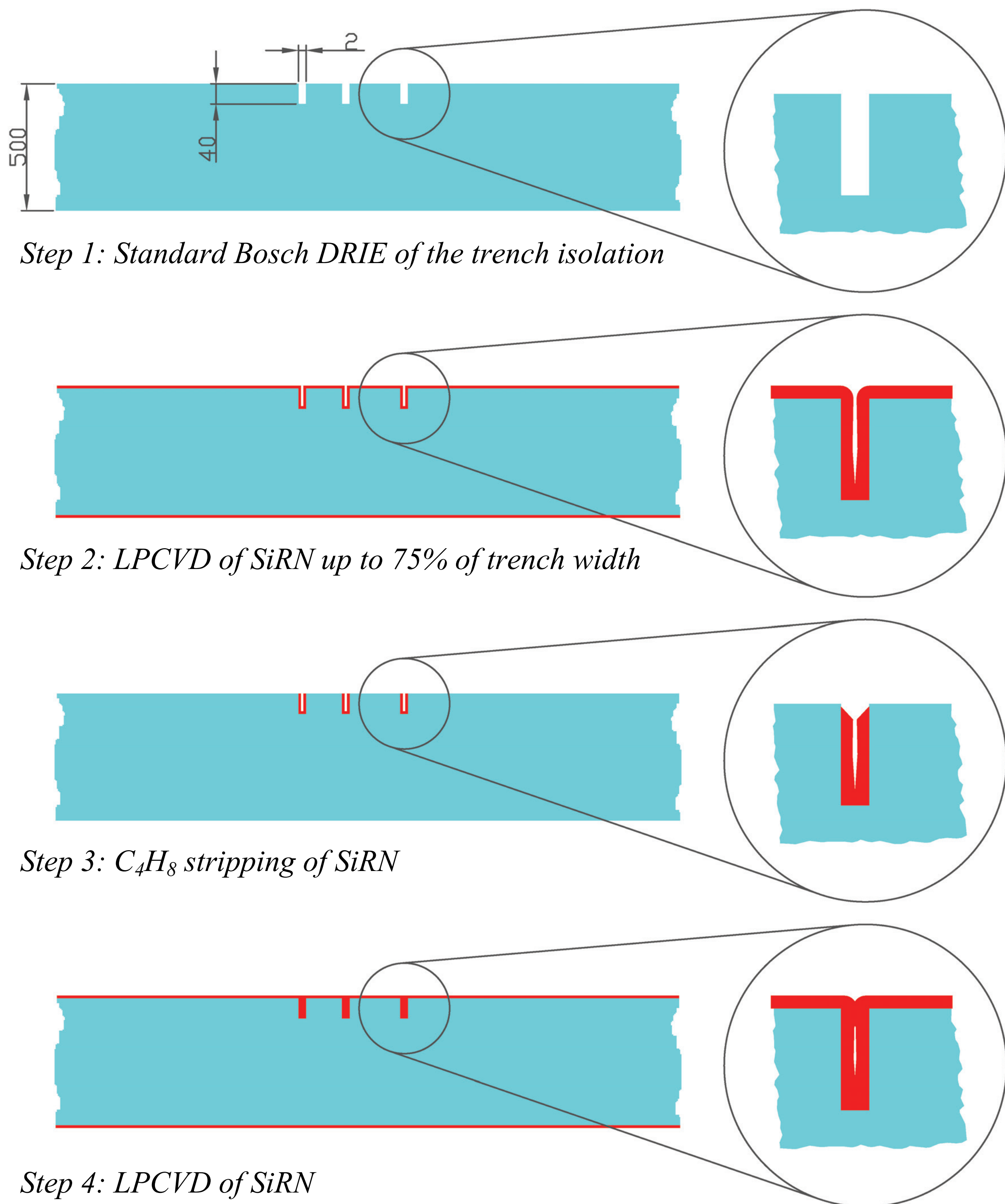

Figure 5.6a: The clamp fabrication process

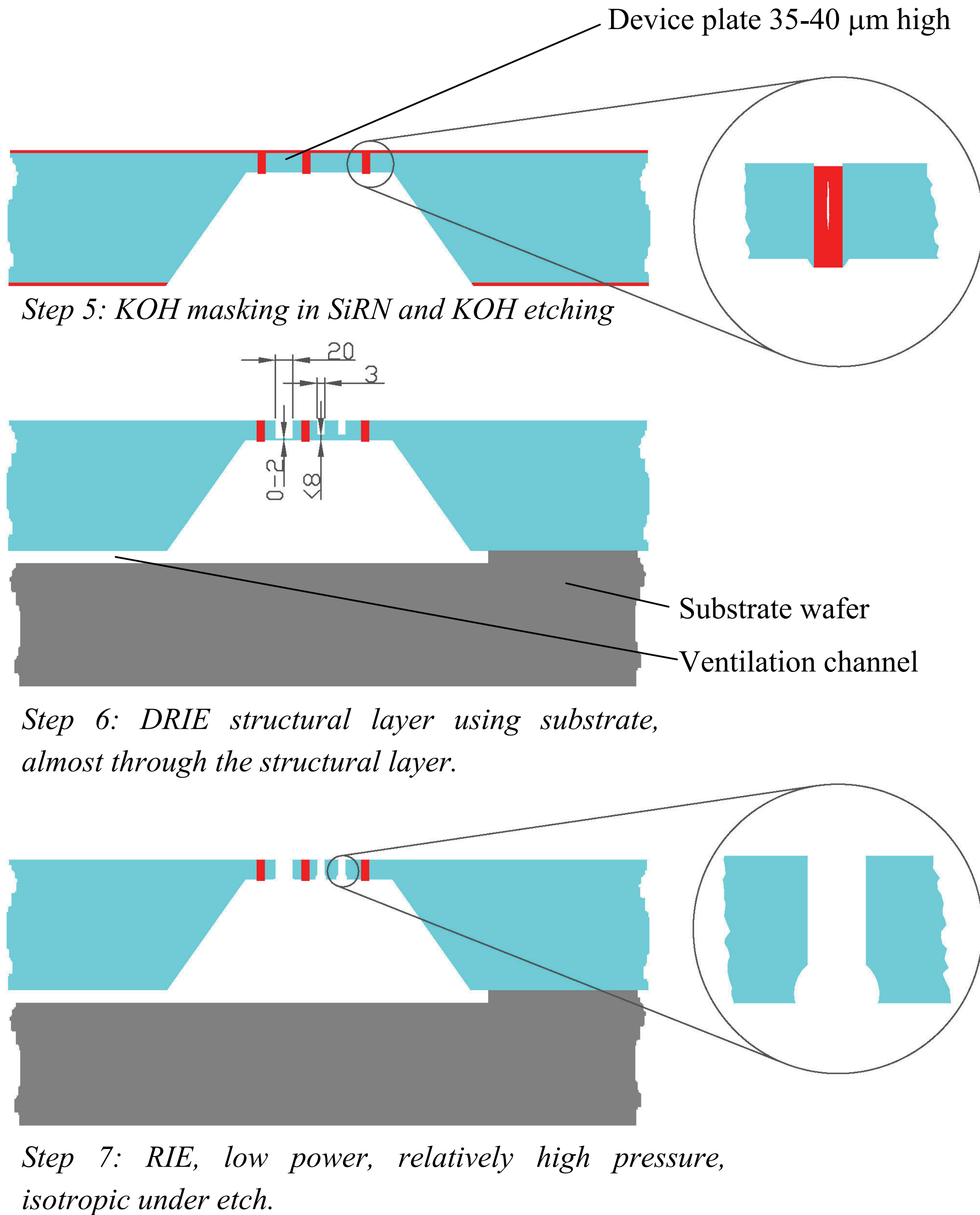

Figure 5.6b: The clamp fabrication process.

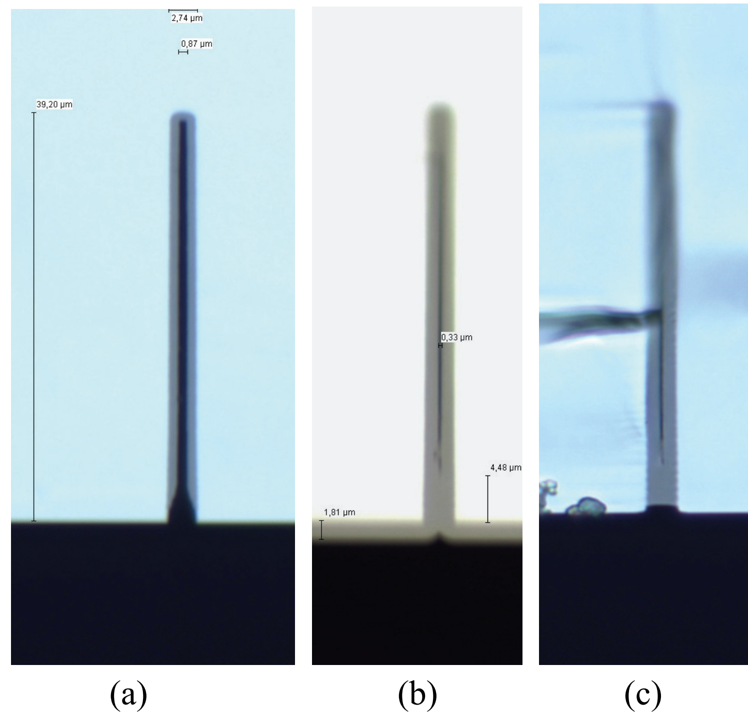

Figure 5.7: The trench isolation process. a) The first layer of SiRN has been selectively etched. b) The second layer provides a 4-6 µm long connection of SiRN. c) After removal of the planar SiRN a strong connection remains.

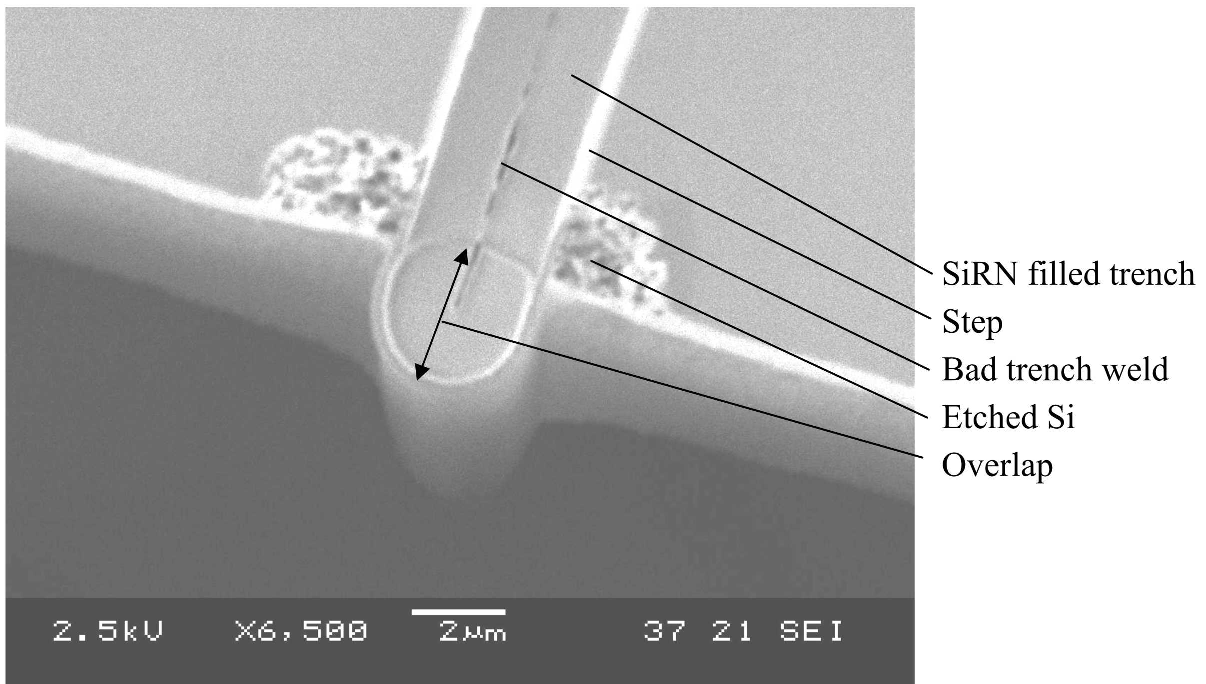

Figure 5.8: Close-up of a SiRN trench isolation. The overlap of the SiRN in the trench is 4 µm on the mask. It compensates for mask misalignment and non-vertical DRIE of the side walls. A bad weld due to non-selective SiRN stripping is visible at the top. The step coverage of the resist next to the SiRN is partly etched away, which is why the Si itself has been etched.

In the <111> direction, KOH etches about 1000 times slower than in the other directions. The <111> crystal plane makes a 54.74° with the <100> plane, step 6 Figure 5.6b. A wafer consists of one silicon crystal and the crystal orientation is well-known within one degree. Therefore, KOH bulk etching from the backside of 3 mm devices has a front-to-backside uncertainty of less than 50 µm and is an easy process. The KOH etching is stopped when the trench isolation of the device layer is visible from the backside. The 40 µm thick device layer is still stiff and strong enough for the next mask step if the devices do not exceed about 8 x 8 mm. Through the use of a Bosch etching recipe, wide trenches etch faster than narrow ones. This Aspect Ratio Dependent Etching (ARDE) is demonstrated in the gaps of a comb-drive in Figure 5.9. An Aspect Ratio Compensated Etching (ARCE) Bosch-based recipe is used to minimize this effect, step 6 Figure 5.6b. The mechanical structure is etched in the device layer. A small trench depth remains between the wide and narrow trenches. It is important to keep this difference small (<6 µm), because the next step, the isotropic RIE, is not capable of etching deeply through the silicon. Therefore, the trench width is limited to between 3 and 20 µm in the clamp design. It is also important not to etch through the wafer too much in step 6, Figure 5.6b, because of overheating of the suspended devices as shown in Figure 5.10. The heat conduction through the thin leaf-springs is poor while the large suspended structures accumulate heat. A possible solution to overheating is to decrease the area of the suspended structure as shown in Figure 5.11. During (D)RIE in the Adix 100SE a carrier has been used because possible holes in the device layer formed during etching cause leakage of the He-backside cooling. The carrier wafer has channels to ventilate the entrapped air in the KOH pits between the carrier and the device wafer. The carrier wafer is bonded to the device wafer using vacuum compatible Fomlin oil. The isotropic RIE etching also etches the sidewall passivation of the trenches. The best results were found without using an extra passivation. Extra passivation requires an extra DRIE to open up the passivation at the bottom of the trenches, causing the risk of overheating again. The standard passivation of the Bosch process was found to last for about 10 min. of isotropic etching, which is long enough for the isotropic etching to etch through the wafer in step 7. The isotropic etching is a slow, low chemical reactant, low heat producing plasma recipe. In the last step, the passivation and resist are removed by a barrel etcher. Figures 5.12, 5.13 and 5.14 are SEM pictures of the clamping device made by applying the abovementioned process.

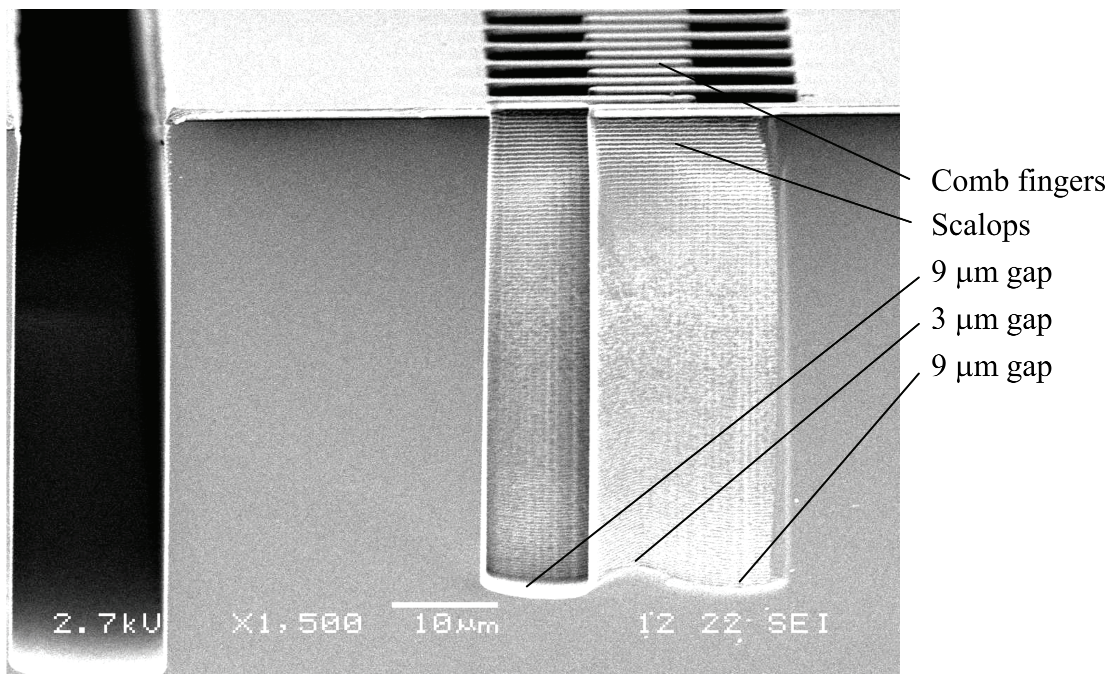

Figure 5.9: A cross-section through the comb-drives. The aspect ratio dependent etching is visible.

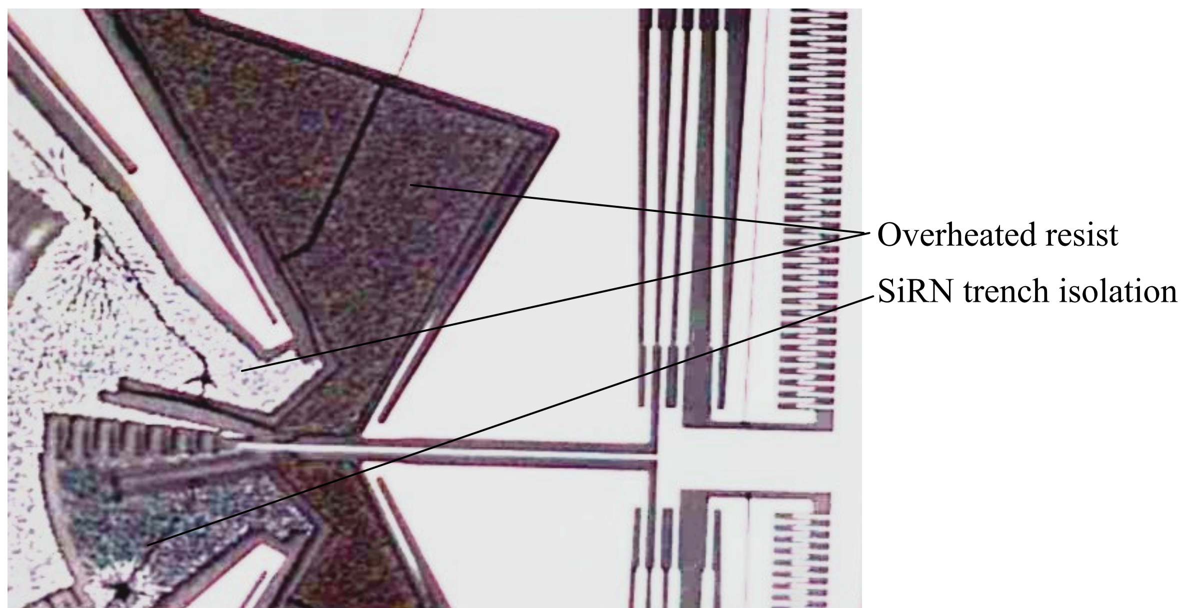

Figure 5.10: Overheated resist due to DRIE. The resist of the suspended structures has been overheated during DRIE as a result of poor heat conduction through the thin leaf-springs and large heat-accumulating suspended structures.

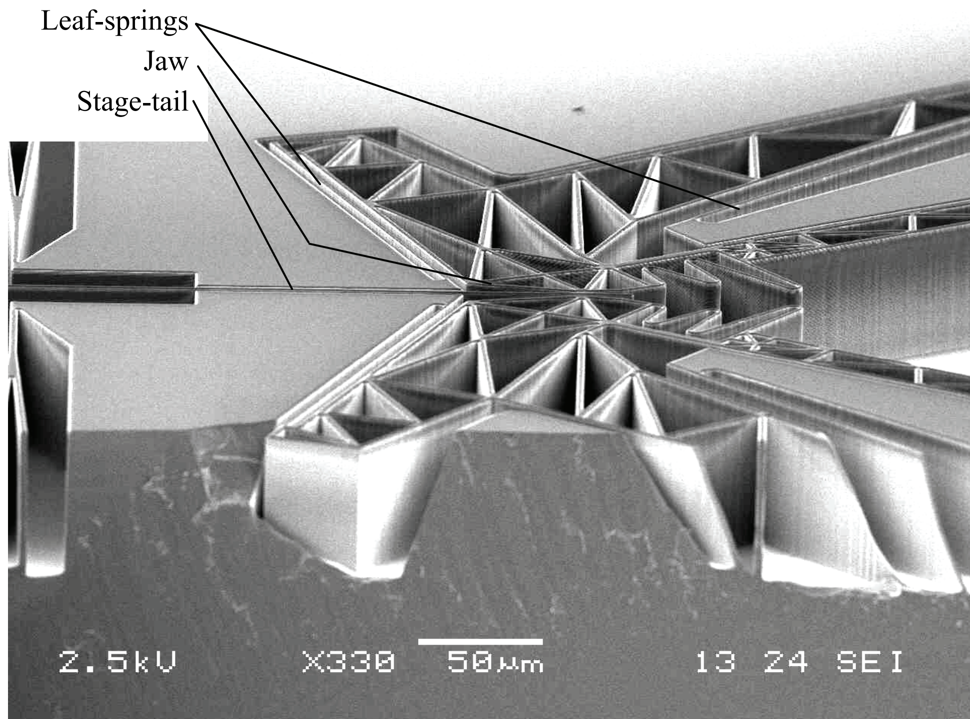

Figure 5.11: Open triangular suspended structure. A possible solution to overheating of suspended structures during DRIE is to decrease the area of the suspended structure. The ion bombardment during DRIE causes most of the heating. The bombardment is proportional to the area, so it helps to reduce the area by building up the suspended structure out of triangles.

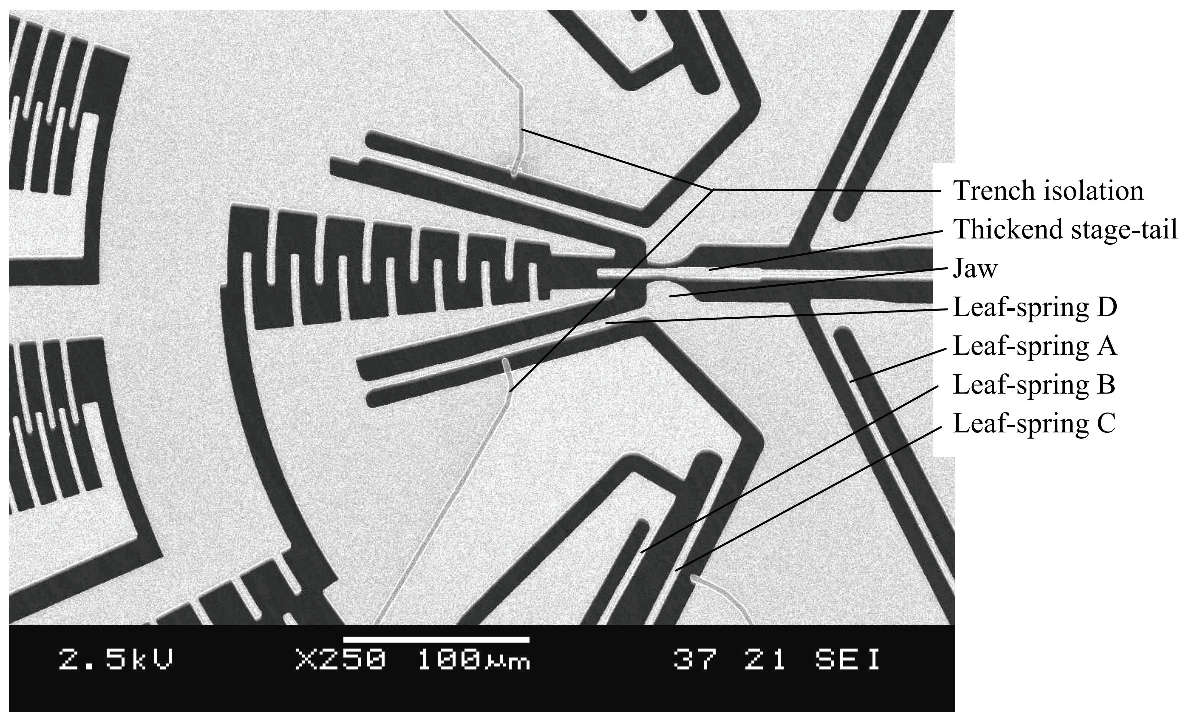

Figure 5.12: Detail of a thickened stage-tail. In this case, misalignment of the trench isolation is visible. However, the device is still operational.

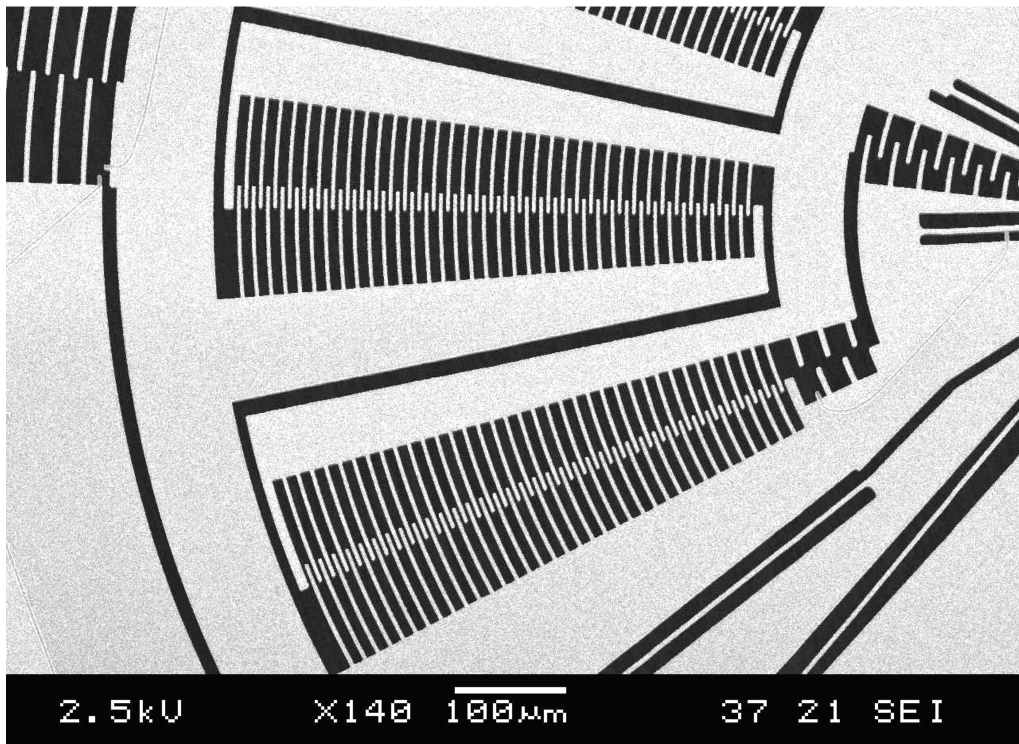

Figure 5.13: Detail of the rotational comb-drives.

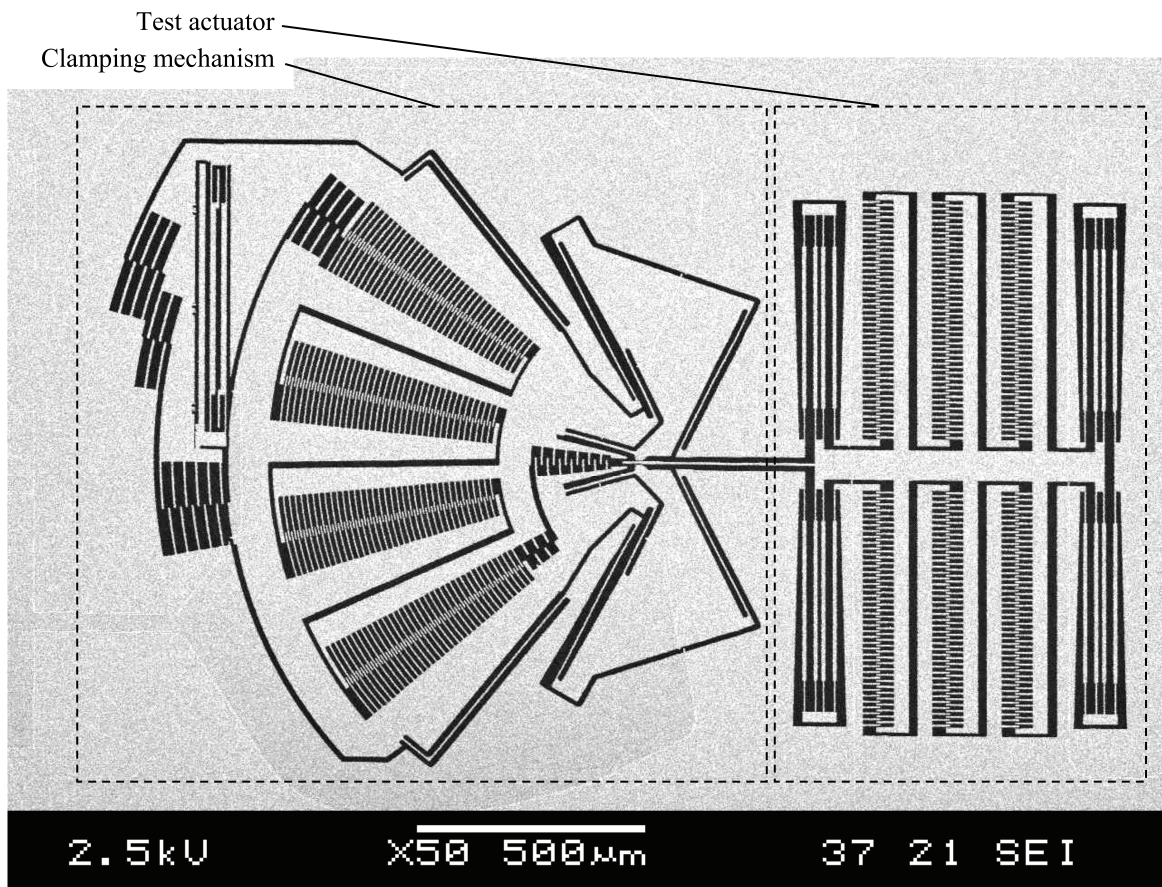

Figure 5.14: Overview of the clamping mechanism and test actuator.

5.6 Measurement results

Several clamping mechanisms have been briefly characterized. The functioning of the test actuator, the clamp comb-drive actuator and the locking system have been tested. A test actuator, as is shown in Figure 5.14, replaced the manipulator comb-drive actuator in the fabricated clamping mechanisms.

PRINCIPLE OF OPERATION

The test actuator can be used to measure the blocking force. The blocking force is equal to the maximum test actuator force. Using an optical microscope camera, the images shown in Figure 5.15 have been made. Figure 5.15a shows the initial (as fabricated) situation of the manipulator comb-drive. The stage-tail is translated in between the jaws (Figure 5.15b, see also the magnified box) by applying up to 60V to the test actuator. Figure 5.15c shows the initial (as fabricated) situation of the locking mechanism. In Figure 5.15d the parallel plate actuator is activated. At 55V the gap of the parallel plates was closed (this was calculated to be 60V). In Figure 5.15e the rotational comb-drive is activated. The pin of the parallel plate actuator can be lowered into the rack by switching off the parallel plate actuator (Figure 5.15f). Subsequently, the clamp comb-drive can be switched off. Finally, the test actuator can be switched off.

Tests on various clamp mechanisms showed that the test actuator can be effectively clamped and locked without any voltage left on the device. However, although the Hertzian contact stress is very low, stiction of the pin to the rack resulted in material transport, or in permanent locking. Often the pin no longer locked after 1 to 10 cycles. The pins of other tested devices sometimes locked permanently, blocking the entire device. Therefore, a larger pin and rack as well as locking actuator were needed. Stiction can then be prevented by rounding the pin and rack, like the jaws clamping the stage-tail.

THICKENED STAGE-TAIL

The first manufactured clamping mechanisms had straight stage-tails, which proved to be difficult to clamp. This is because, due to DRIE, the gap between the jaw and the stage-tail had become too large to generate sufficient clamping force. Therefore, the next generation clamping mechanisms, as shown in Figure 5.12, were equipped with a thickened stage-tail. However, the stage-tail was not thickened over its entire length, because in that case the gap for etching would have been reduced too much. As a consequence the thickened part is not in between the jaws in the initial situation. The stage-tail has been partially thickened by 1 μm on both sides.

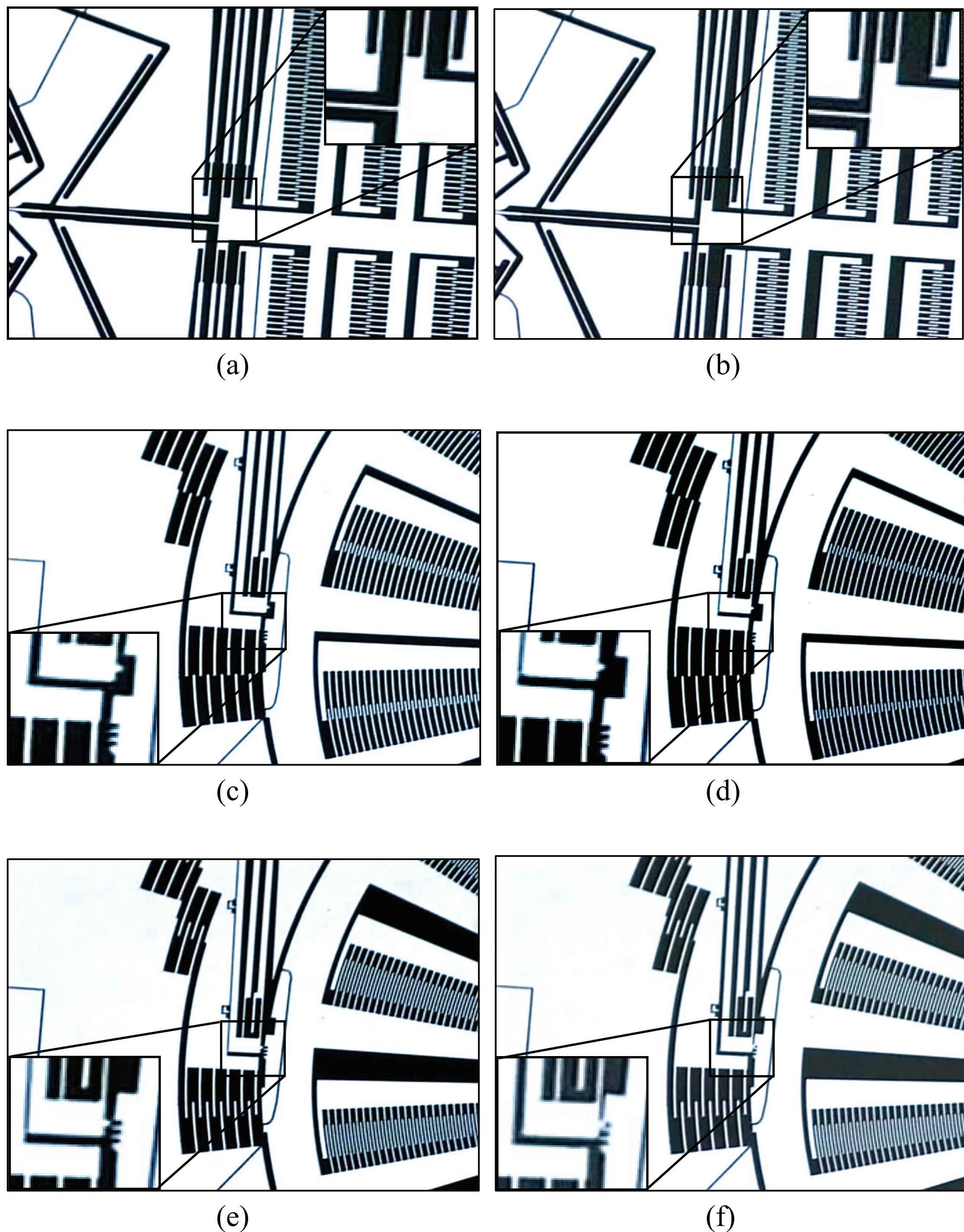

Figure 5.15: The operational clamping mechanism. Note that the gaps are black and the material is white. a) The initial fabricated situation of the manipulator comb-drive. b) The manipulator comb-drive is actuated. c) The initial fabricated situation of the clamping mechanism. d) The parallel plate actuator is activated. e) The rotational comb-drive is activated. f) The parallel plate actuator is switched off, locking the pin in the rack.

MEASURED BLOCKING FORCE

The test actuator voltage was varied between 0V and 60V. The corresponding maximum blocking force was 97 μN. Measurements on several clamp comb-drive actuators showed that a voltage of between 45V and 53V was necessary to generate the 97 μN blocking force. Although the clamp comb-drives of several tested devices could withstand 120V, the test actuator voltage could not be increased enough in the test set-up. With the same friction coefficient between the jaw and the stage tail and the clamp actuator driven at 120V, the blocking force would be 1.4 mN. However, this was not measured.

FIRST VIBRATION MODE FREQUENCY MEASUREMENTS OF THE TEST ACTUATOR

The first vibration mode frequency of the test actuator was determined by a Polytec laservibrometer. This frequency was then examined in more detail by in-plane camera detection, also on a Polytec machine. The result is shown in Figure 5.16. The first vibration mode shows a shuttle motion in the compliant actuation direction. The measured first vibration mode frequency of the test actuator was 3735 Hz. The phase lag changes 100° from 3700 to 3800 Hz, which indicates a Q-value of 31. The squeeze film damping of the air in between the combs causes the relatively low Q-value. The stiffness in the compliant actuation direction of the four folded flexures suspending the test actuator comb-drive shuttle can be derived accurately, because the mass of the shuttle is known quite well. The effective mass is calculated by SolidWorks, and is 1.49 10^{-8} kg. The combination of the first mode vibration frequency and the effective mass results in an actuation stiffness of 8.20 N/m. Due to DRIE the dimensions of the mask and the dimensions of the fabricated device are different. The actuation stiffness of the folded flexures should have resulted in a stiffness of 9.66 N/m, based on the dimensions of the folded flexures on the mask. In this calculation the compliance of the reinforced middle part of the leaf-springs and the anisotropic Young's modulus of the SCS are taken into account. Therefore, the difference in actuation stiffness is caused by the geometric differences of the leaf-springs. The effective thickness of the leaf-springs derived from the first mode vibration frequency is 2.84 μm. On the mask the leaf-spring thickness is 3.00 μm. Consequently, DRIE reduced the thickness of the leaf-springs by 0.16 μm.

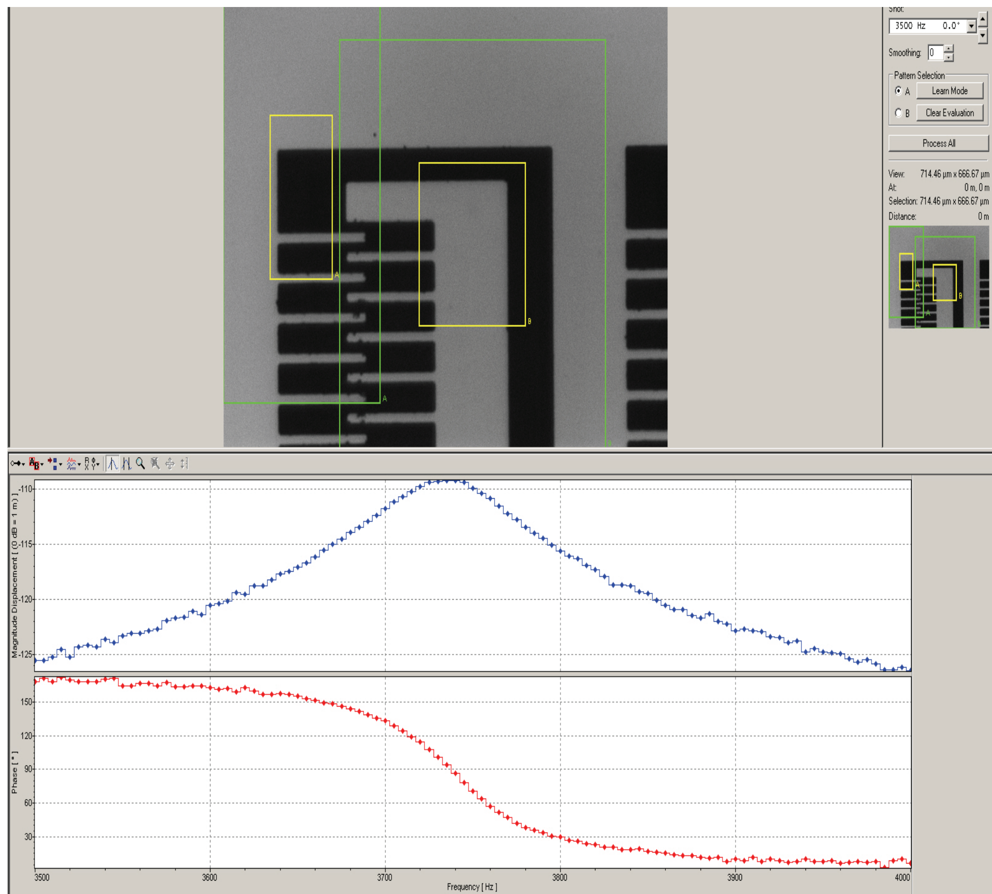

Figure 5.16: Results from an in-plane camera measurement on a Polytec system. The first vibration mode frequency measured on the test comb-drive is 3735 Hz. The phase lag changes 100° from 3700 to 3800 Hz which indicates a Q-value of 31. The squeeze film damping of the air in between the combs causes the relatively low Q-value.

First and second vibration mode frequency measurements of the clamping mechanism

In a manner similar to the test actuator vibration mode frequency measurement, the first and second vibration mode frequencies of the clamp mechanism have been measured. One half of the clamping mechanism can be interpreted as a system containing 2 masses and 2 springs, as shown in Figure 5.17. Only the in-plane (of the wafer) motion is observed. The clamping mechanism's leaf-springs A and B, as shown in Figure 5.3, can be interpreted as 1 spring with a rotational compliance around the virtual pivot. Together, they connect the jaw to the surroundings. The jaw is one mass. The clamping mechanism's leaf-springs C and D can be interpreted as another spring with a rotational compliance around the virtual pivot. Together, they connect the comb shuttle to the jaw. The comb shuttle is another mass.

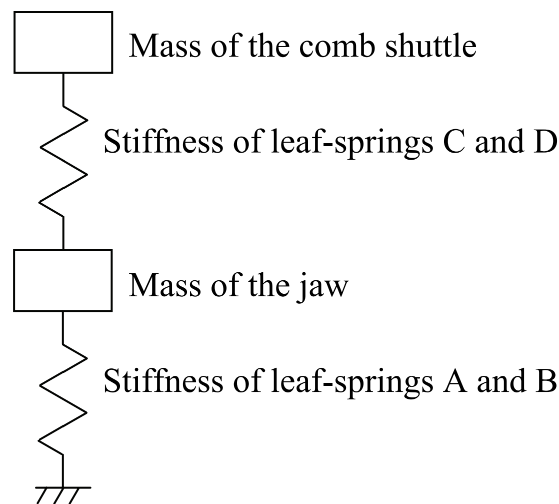

Figure 5.17: Basic in-plane dynamic model. 2 masses and 2 springs represent one half of the clamping mechanism.

The first vibration mode frequency of the jaw and comb-shuttle 1 (Figure 5.3) is 830 Hz, and the first vibration mode frequency of the jaw and comb-shuttle 2 is 965 Hz. The difference in frequency is caused by the fact that comb shuttle 1 is heavier than comb shuttle 2, because it contains the locking mechanism. This results in a lower vibration mode frequency. In SolidWorks the moment of inertia of the jaws and comb shuttles has been derived around the virtual pivot axis. The rotational stiffnesses, taking into account the anisotropic behavior of silicon, based on the dimensions on the mask, are known using the model described in section 5.4. The two masses and the measured first vibration mode frequency have been used to determine the leaf-spring thickness decrease due to DRIE with respect to the thickness on the mask. The leaf-springs connecting to comb shuttle 1 are effectively 0.227 µm thinner. The leaf-springs connecting to comb shuttle 2 are 0.195 µm thinner. The second vibration mode frequencies of the system have been calculated to be much larger than the first. They are just above 13 kHz for both shuttles.

DETERMINING THE FRICTION COEFFICIENT

Theoretically, it is possible to derive a friction coefficient from the measurements. With the stiffnesses of the leaf-springs and gaps of the system known, the clamp force and test actuator force are calculable. However, the sensitivity of the friction coefficient (f_w) for the gap (g) between the jaws and the stage-tail is calculated to be $\partial f_w/\partial g \approx 1.7/\mu m$. Since the gap is known only up to several tenths of a micrometer,

friction coefficient calculations have a large uncertainty. The sensitivity for gap variations is mainly caused by the amplification of the jaw displacement by the comb displacement. To obtain accurate results regarding the friction coefficient, the angles of the jaws and the position of the test actuator need to be monitored statically and accurately during clamping. To test the influence of the gap in the mask design, gaps of 1.5, 2.0 and 2.5 μm were manufactured. Clamps with the smallest gap were not released (trenches were not etched through the device plate shown in Figure 5.6b) during DRIE. Clamps with the largest gap required a too large comb-drive force and displacement, and therefore did not sufficiently clamp the stage-tail.

POSITION DISTURBANCE OF THE STAGE-TAIL

During clamping, it is difficult to measure the position disturbance of the stage-tail and test actuator in the y-direction (Figure 5.3) or the position disturbance of the platform in the complete design. It should be measured statically and with a measurement uncertainty of less than a nm. A specialized measurement device attached to the test actuator would be required. Another option would be to use the TEM to determine the test actuator position disturbance during clamping.

MEASUREMENT RESULTS:

- The rotational comb-drive design with virtual pivots is well designed for the function. Most devices survived voltages of 120V.
- A relatively large mass is suspended robustly even without reinforcement F. These clamp mechanisms were robust with regard to manufacturing.
- Depending on the gap between the stage-tail and the jaws, 45V to 120V are necessary to clamp the stage-tail sufficiently.
- The locking mechanism, fixing the clamping mechanism without power, worked in several cases.
- The pin and rack need to be larger to be robust. A larger locking actuator is necessary.
- On average, the effective thickness of the leaf-springs was reduced by 0.194 μm as compared to the dimensions on the mask.
- The design is sensitive for gap variations between the jaws and the stage-tail.
- The position disturbance of the stage-tail and test actuator during clamping is difficult to measure.

5.7 Conclusions and recommendations

CONCLUSIONS

- A clamp mechanism based on a process compatible with the manipulator process has been designed, fabricated and briefly characterized.
- The exact kinematic constraint design with low strain energy storage results in a relatively large maximum clamp force of 0.5 mN for a MEMS device of 1.4 x 1.3 mm. (97 μN was measured in the measurement set-up).
- The device has proven to be robust for manufacturing even with the relatively large suspended masses and without extra reinforcement.
- Although the clamp force varies depending on the allowable voltage and the gap dimension between the stage-tail and the jaws, in general it is strong enough to clamp a test actuator. Voltages necessary for clamping were measured to be between 45V and 120V.
- The locking mechanism worked in several instances, making the clamp force maintainable without an electrical voltage.
- On average, the effective thickness for lateral stiffness of the leaf-springs was reduced by 0.194 μm as compared to the dimensions on the mask.
- It proved difficult to measure the friction coefficient because of its large sensitivity for gap variations.
- Position disturbance of the manipulator during clamping is calculated to be less than 1 nm. However, it could not be verified.
- The stiffness at which the manipulator actuator is blocked is not large enough to maintain the manipulator position within 1 nm when the manipulator actuators are switched off. A feed-forward control strategy is necessary.

RECOMMENDATIONS

- The design is sensitive for gap variations between the jaws and the stage-tail. This sensitivity can be decreased by decreasing the amplification factor of displacement from actuator to jaw by 20-30%. A somewhat larger actuator will then be necessary, however.
- The pin and rack need to be larger to provide a rounding off to prevent stiction. Therefore, a larger fixing actuator will be necessary.
- The effective thickness for lateral stiffness of the leaf-springs was reduced by 0.194 μm on average as compared to the dimensions on the mask. This knowledge can be used for tuning the design by compensating for the leaf-spring thickness in a next design. This would result in:
    - Better optimized dimensions of leaf-springs A and B and their angle φ for minimizing the displacement of the stage-tail in the y-direction during clamping.
    - A better optimized 'foot-print' area. This area is a combination of the dimensions of the leaf-springs and the actuator. Long leaf-springs lead to small strain energy storage, which requires a small actuator. Short leaf-springs require a large actuator force to deflect.
    - Better tuning of leaf-springs C and D for a 0.1 mN clamp force resolution.
- For testing purposes: increase the stroke of the test actuator and make the stage tail in steps with several thicknesses. The gaps between the jaws and the stage tail can then be varied within one device, resulting in the necessary measurement information for determining the friction coefficient more accurately, for example.
- For testing purposes: increase the maximum force of the test actuator up to 1 mN, by increasing the test actuator voltage to 120 V and increasing the number of finger pairs to 615 (instead of the current 246).

Chapter 6

CONCLUSIONS

In this chapter the overall conclusions of this research will be presented, combined with the strong and weak points of MEMS-based precision manipulation. More specific conclusions and recommendations have been given in the individual chapters: exact kinematic constraint design in MEMS, the behavior of deflected MEMS leaf-springs and straight guiding mechanisms are treated in section 2.6, concepts for MEMS-based 6 DOFs manipulation in section 3.8, fabrication and modeling of the 6 DOFs manipulator in section 4.6, and the clamping mechanism in section 5.7.

6.1 Research objective

The goal of this research is twofold:

1. Design and manufacture a 6 DOFs manipulator with nanometer resolution positioning in MEMS technology (section 6.1.1).

2. Derive principle solutions for the synthesis of exact kinematic constraint design and MEMS fabrication technology for multi DOFs precision manipulation in the micro domain (section 6.1.2).

6.1.1 Designing and manufacturing a 6 DOFs manipulator

The synthesis of design principles and fabrication has resulted in a design study of a 5 mask process for a 6 DOFs MEMS-based manipulator capable of satisfying the specifications (section 1.6). However, the clean room fabrication of the total manipulator required more time than available during the project.

For 6 DOFs motion of the manipulator, the necessary combination of in- and out-of-plane motion in MEMS is rather new. A motion converting mechanism using only one type of actuator is chosen in favor of a combination of in- and out-of-plane actuators. Six electrostatic comb-drives are used for actuation. The manipulator is a parallel kinematic mechanism.

The specifications for a precision manipulator require high frequency vibration modes (with blocked actuators) combined with compliant actuation modes. The compliant actuation modes are necessary to generate sufficient displacement by the low force MEMS actuators. Therefore the design principles, exact kinematic constraint design in particular, have been applied as much as possible. However, trade-offs had to be made between what is required from an exact kinematic constraint design point of view and what is feasible with the available fabrication processes. Therefore, to determine flexure and actuator dimensions, the used flexure mechanisms have been modeled, taking into account geometric non-linearities.

Several fabrication steps of the manipulator design have been tested. A 3 mask step fabrication process of the clamping mechanism based on the 5 mask step process of the 6 DOFs manipulator served as a test case for the fabrication. The clamping mechanism has been designed, fabricated and characterized. The clamping mechanism is able to create a relatively large clamping force of at least 97 μN and maintain it unpowered, fixing the 6 DOFs manipulator once positioned. The elastic deformation of the clamping mechanism flexures during clamping has been optimized so as not to influence the position of the TEM sample manipulator. The device area of the total mechanism has been further optimized by balancing the area necessary for sufficient flexure compliance and the actuator area necessary for sufficient actuation force and stroke.

The following can be concluded regarding the presented 6 DOFs design:

- Because of limited design freedom a compromise had to be made between the preferably compliant and thus low frequency unblocked actuation modes and the preferably high frequency blocked actuator modes. This is essentially a trade-off between the necessary actuator force for displacing the platform and the frequency of the first vibration mode. For example: due to fabrication limitations, the bending stiffness of the (DRIE SCS) Si-leaf-springs in the intended stiff out-of-wafer-plane direction is relatively low compared to the stiffness in the intended compliant in-wafer-plane direction. The reason is that the minimum thickness of the Si-leaf-springs of 2-3 μm requires a length of 500-800 μm to result in adequate actuation compliance. As a consequence, the combination of a limited height (35 μm) and a length of 500-800 μm does not result in a high out-of-plane stiffness.
- The difference between the first vibration mode frequency of the blocked manipulator and an unblocked manipulator is small. This is primarily because of the limited thickness to height ratio of 1:20 of the DRIE SCS leaf-springs.
- In parallel kinematic manipulators, the combinations of movements in different directions at the same time add up to relatively large actuator displacements (and forces in the case of a compliant mechanism). In this case +/- 50 μm actuator strokes are necessary to result in combined +/- 10 μm platform strokes.
- The overall dimensions of 6.2 x 6.2 x 0.5 mm^3 are not that small.
- The first vibration mode frequency at 3.7 kHz with blocked actuators is well above the 1 kHz specification.
- The change of the first vibration mode frequency due to platform displacement is small.
- Stress is not the failure mechanism for the manipulator, buckling is. This is the consequence of the long slender leaf-springs necessary to make the mechanism compliant enough for the low force actuators to result in the required strokes.
- The absolute stiffness of the platform, especially in the z-direction, has a small value, i.e. 43.3 N/m.
- The positional stability of the sample is not jeopardized by disturbances, as can be expected in a TEM.
- Feed-forward position control based on a linear relationship between actuator force and platform position leads to relatively large positional errors of more than 15% of the displacement.
- The stiffness of the folded flexures of the comb-drive suspensions are 80 - 100 % responsible for the actuation forces necessary to actuate the platform.

6.1.2 Principle solutions for MEMS-based kinematic constraint design

Finding a synthesis of exact kinematic constraint design and the fabrication process possibilities requires knowledge of where and how much exact kinematic constraint design can be compromised in favor of better manufacturability. To calculate the implications of compromising exact kinematic constraint design, modeling is required that takes geometrical non-linearities into account. Currently, the following fabrication limitations in particular restrict MEMS design freedom:

- DRIE limits leaf-spring dimensions: thickness > 2 μm, height < 20 x thickness.
- Limited overall size to feature accuracy (<10^4 for DRIE)
- Combining in-plane with out-of-plane leaf-springs requires a combination of process techniques that usually becomes complicated.

There are several solutions to deal with the restricted fabrication possibilities, but they often compromise exact kinematic constraint design:

- Creating absolute stiffness can require an over-constraint design.
- An over-constraint design is often needed to create extra strength for robustness.
- A symmetric design often compromises exact kinematic constraint design:
  1. More convenient vibration mode shapes.
  2. Better thermodynamics.
  3. Deformation as a result of stress can be compensated for.

In MEMS, the compliant actuation direction (the *y*-direction in Figures 2.9, 2.10 and 2.11) of a flexure mechanism is often not constrained by a stiff drive system, like a spindle or a controlled linear motor. The relatively low drive-stiffness, see section 2.4.2, has the following implications:

- The longitudinal stiffness (c_x in Figures 2.9, 2.10 and 2.11) of the parallel leaf-spring guidance or folded flexure designs that are often used, decreases rapidly with the deflection.
- Reinforcing leaf-springs of a folded flexure or a parallel leaf-spring guidance usually has more negative than positive effects.

Constraining the displacement of the intermediate body in a 1 to 2 ratio with respect to the shuttle of a folded flexure increases the longitudinal stiffness at deflection considerably. Two improved folded flexure designs incorporating this 1 to 2 lever are proposed for large deflections, as shown in section 2.5.4.

6.2 The strong and weak points of MEMS-based micro manipulators

MEMS for micro manipulators have the following technological strong points:

- First vibration mode frequencies are generally very high.
- Very pure base material (silicon), enabling thin elastic elements.
- Silicon has low internal damping, enabling large Q-factors and very deterministic behavior.
- High thermal stability because of the combination of a monolithic system, good conduction coefficient (SCS), low expansion coefficient (SCS) and small overall size for small expansion and small time constants.
- Overall size of a device can be small.

From a technological point of view, MEMS micro manipulators have limited potential in applications where the requirements are close to the following:

- Actuator force larger than 5 mN [112].
- Displacement larger than 100 μm [112].
- Absolute stiffness greater than 100 Nm^{-1} (section 4.5.6).
- Robustness for external forces larger than 100 μN (4.5.9).
- Resolution of 5 nm of a measurement system [79].
- Strong separation between compliant actuation modes and stiff suspension modes (4.5.6).

When it comes to finances, the main strong point of MEMS is often also its weak point:

The financial strong point of MEMS is the integration of mechanics, actuators, sensors and electronics in one technology. This integration has the potential to produce low-cost systems when mass produced.

The main financial weak point of MEMS, however, has to do with the investment in time and money that is required for research and development:

1. The integration of technologies requires a strong multi-disciplinary design strategy because trade-offs need to be made. Therefore, the design trajectory is relatively long and specialized people are necessary.
2. The manufacturing in a clean room environment is costly and (lead) time consuming. Even testing part of a process becomes costly quickly.
3. Risk accumulates with each added process step in an integrated monolithic clean room design. The risk associated with each process step is relatively high. This is because of the following reason: although each process step might have been proven separately, stacking a process step on top of previous ones influences the results of the past process steps. Past process steps also influence the process steps that will follow. Therefore each process design, although based on previous ones, seems relatively new.

Therefore, when designing new MEMS-based systems, especially for small volumes, it is wise to use proven processes and designs as a starting point. Small manufacturing volumes bear the full burden of the research and development expenses, regardless of how “enabling” the technology may be [93]. The key element of cost-effective competitiveness for MEMS is mass fabrication, diluting the overall impact of fixed costs as well as the costs of research and development.

APPENDIX A

ADDITIONAL BACKGROUND ON THE TEM

A.1 Introduction to electron microscopy

The maximum spatial resolution that one can image by optical microscopy is limited by the wavelength of the photons that are being used to probe the sample. In the early days the resolution was limited by the wavelength of 400-700 nm. Currently, achieving a magnification of up to 100 times with a resolution of up to 0.2 micrometers is not uncommon. Using smaller wavelengths - like ultraviolet light - soon causes problems with absorption. X-rays with wavelengths of less than 10 nanometers exhibit a lack of interaction, both when it comes to focusing and actually interacting with the sample.

Electrons have both wave and particle properties (as theorized by Louis-Victor de Broglie). The wave-like properties mean that a beam of electrons can, under some circumstances, be made to behave like a beam of radiation. Electrons have a wavelength in the order of a few picometers, depending on their energy (momentum). This wavelength is much smaller than that of visible light, yet electrons can still interact with the sample due to their electrical charge. It provides a resolution far better than is possible with light microscopes, with the added benefit of improved depth of field.

A.2 TEM

The TEM is a microscope which uses an imaging technique whereby a beam of electrons is used to project a magnified image of a sample onto a fluorescent screen, or via imaging by a CCD camera. Although electrons with enough energy can be detected with a CCD camera, usually an indirect method is applied whereby the image of the fluorescent screen is projected onto the CCD. The TEM is used in both materials science/metallurgy and the biological sciences and is able to image at sub-angstrom resolution.

A TEM consists of a long column which is isolated from floor vibrations. The column features an electron gun, a number of electromagnetic lenses, the sample manipulator, a diaphragm, a fluorescent screen and a camera system (see Figure 1.1). The electrons in a TEM are generated by thermionic discharge in the same manner as the cathode in a cathode ray tube, or by field emission. They are then accelerated by an electric field and focused by electromagnetic condenser lenses onto a sample. The sample is situated in the objective lens, where the electrons travel parallel to the column. The projector lenses project and magnify the image on a screen. A major advantage of these electromagnetic lenses is that the focal length can be changed without moving parts. It makes mechanical lens adjustments superfluous. However, like optical lenses, these lenses exhibit aberrations. To minimize aberrations, the gap between the lens pole pieces focusing the electron beam onto the sample (see Figure 1.2) needs to be minimized. As a result, little space for a sample manipulator is left.

An additional class of TEMs is the electron cryomicroscope, which includes a sample stage that is cooled by liquid nitrogen or liquid helium. The technique is used for biological samples, typically, that need cooling to withstand the vacuum. The sample is first embedded in vitreous ice or fixated using negative staining. Staining is the use of an electron dense material around, but not on top of, the specimen to improve the contrast.

A.3 TEM applications

For biological samples, the maximum sample thickness is roughly 1 micrometer. Typical biological applications include tomographic reconstructions of small cells or thin sections of larger cells and 3D reconstructions of individual molecules via Single Particle Reconstruction. Tomography involves the generation of a three-dimensional reconstruction with help of slices or sections through a three-dimensional object obtained with the TEM.

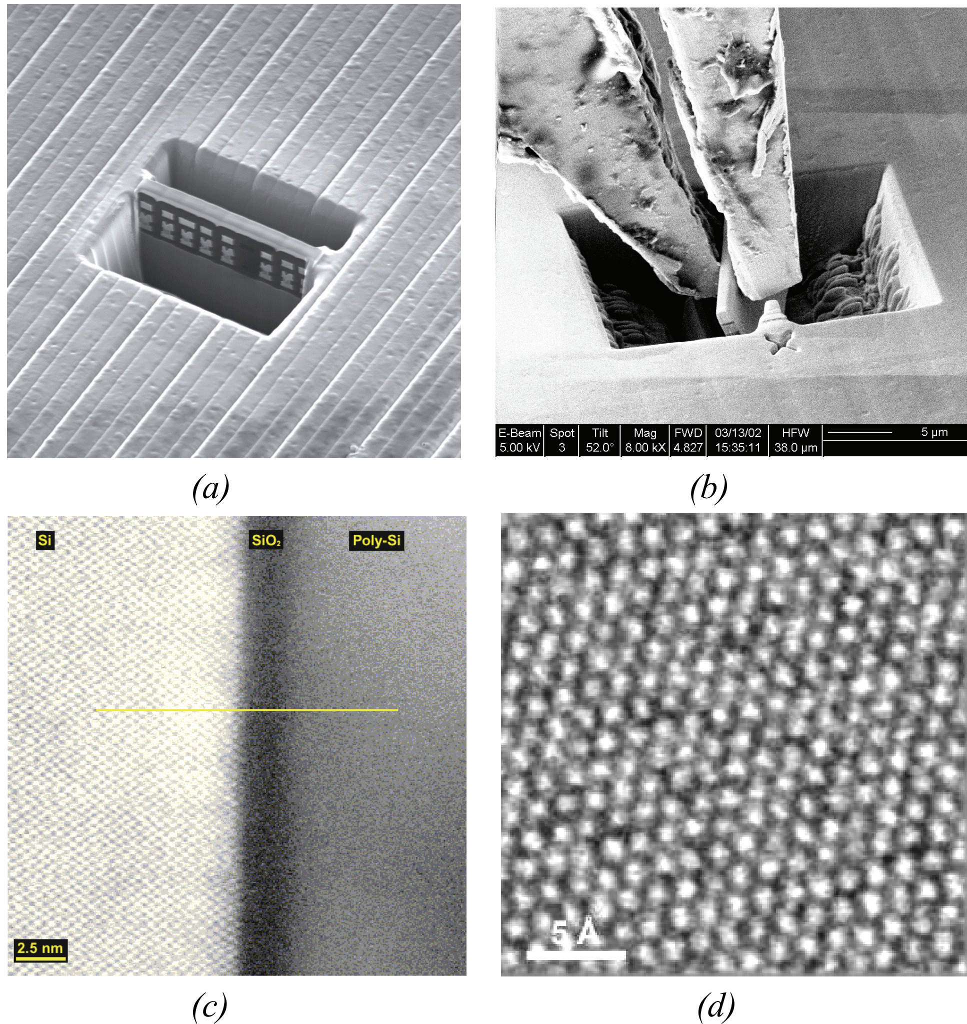

Figure A.1: a) SEM picture of a semiconductor sample in a wafer, milled by a Focused Ion Beam (FIB)(Courtesy of FEI). b) SEM picture of a semiconductor sample picked by a gripper (Courtesy of Philips Applied Technologies). c) TEM high resolution image of an interface between SCS and poly Si. The periodic atomic structure is clearly visible in the SCS, in contrast to the poly Si. d) A close-up TEM picture of the SCS (Courtesy of FEI).

In materials science/metallurgy the samples tend to be naturally resistant to a vacuum, but must be prepared as a thin foil or etched in such a way that some portion of the sample is thin enough for the beam to penetrate. Generally the thickness of a sample is less than 300 nm. Preparation techniques to obtain an electron transparent region include ion beam milling and wedge polishing. The focused ion beam (FIB) is a relatively new technique to prepare thin samples for TEM examination from larger samples. Because the FIB can be used to micro-machine samples very precisely, it is possible to mill very thin membranes from a specific area of a sample, such as a semiconductor or metal (Figures A.1a and A.1b).

The TEM has the ability to determine the positions of atoms within materials. Figures A.1c and A.1d show two high resolution images, with the atomic structure clearly visible, of semiconductor materials typically used in material research.

There are a number of drawbacks to the TEM technique. Many materials require extensive sample preparation to produce a sample thin enough to be electron transparent, which makes TEM analysis a relatively time consuming process with a low throughput of samples. The structure of the sample may be changed during the preparation process as well. The field of view is relatively small also, making it possibile that the region analyzed may not be characteristic for the whole sample. The electron beam may damage the sample, particularly in the case of biological materials.

APPENDIX B

CONCEPT FOR LOADING A SAMPLE IN A TEM

A semiconductor sample can be milled out of a wafer by a FIB in a dual beam SEM / FIB system (see Figure A.1a). By ”welding” using a gas (tungsten) the FIB joins the sample to a rod, which can be micro manipulated. Another option is to use a micro manipulated gripper (see Figure A.1b), which can be used to pick up the sample. The MEMS stage is meant to be mounted in the tilt stage. The combination of the MEMS-stage and tilt stage is loaded in the dual beam system. The sample is manipulated to the center of the MEMS-stage. The FIB joins the sample to the MEMS stage by “welding”. The FIB decouples the rod from the sample or, in the case of a gripper, the gripper releases the sample. The tilt and MEMS stage with the sample are loaded into the TEM via a load-lock in one of the side entries (see Figure 1.2). A relatively simple manipulator with a repeatability of tenths of a millimeter positions the tilt stage frame on the lower pole-piece. Three balls in the three V-grooves might be used, for example. The repeatability of positioning spheres in a V-groove is generally in the micron domain, which means the sample is positioned at micron repeatability in the TEM. The stroke of the MEMS manipulator is large enough to compensate for this uncertainty.

APPENDIX C

MEMS-BASED ACTUATORS FOR PRECISION MANIPULATION

In this appendix, analyses of the four actuation principles that are currently most relevant for MEMS-based precision manipulation - piezoelectric, thermal, electrostatic and magnetic actuators - are summarized. The scaling of the actuators, a commonly accepted analytic way of expressing the physical implications when the dimensions change, will be explained briefly. However, scaling does not take into account the physical and practical limitations when designing actuators. Therefore, in this appendix, a numerical evaluation based on designs including the physical and practical limitations of the abovementioned actuator principles will be presented.

C.1 Introduction

When scaling down to micro dimensions, the ranking of the actuation principles of drive systems changes. The goal of this appendix is to compare the four actuation principles that are currently most relevant for MEMS-based precision manipulation: piezoelectric, thermal, electrostatic and magnetic actuators. In the literature, many comparisons between micro-actuator types based on physical formulas can be found [6, 86, 126]. Although scaling is a generalized way of explaining physical implications when dimensions change, other important aspects need to be regarded as well:

- Physical and practical limitations: maximum tolerable temperature, current density, electrical field, remanent flux density of a magnet, aspect ratio of etching, feature size of the mask, maximum thickness of a deposited magnet or coil.
- Extra space required to generate an electrostatic or electromagnetic field: the space of a comb-drives mechanical structure, a coil or a permanent magnet required to generate a field.

Scaling, for example, shows the rate of performance change of a certain actuator type when dimensions change. However, the performance of one type of actuator cannot be compared to another based on scaling alone, because it does not reveal anything about the absolute level of performance.

The practical and physical limitations and the space required to generate a field influence the performance of the actuators and need to be taken into account if a ranking needs to be made. Therefore, a numerical theoretical analysis of the four most relevant actuation principles for MEMS-based precision manipulation is presented in this appendix [16]. The electromagnetic and electrostatic actuators are based on designs, because a large construction volume is required to generate fields. Piezo and thermal actuators use active material as a structure and therefore depend much less on a specific design and to a much greater degree on material properties. An effort is made to choose all designs so that, with current knowledge, the maximum work per unit volume (Work density) is achieved. It must be stated, however, that this comparison based on designs is less generic than a comparison by scaling factors, and that it will change over time.

Many actuator types have been reported in the literature. As is explained in section 3.2.6, in MEMS it currently is difficult to obtain accurate feedback for position control. Therefore, in precision manipulation systems it is a great advantage, if not a necessity, to use actuators with a high repeatability. Although interesting, several other micro actuator principles like (magnetic) shape memory alloy [73], thermo-pneumatic [89], fluid activated [108] and electrochemical actuators [97] do not have the required deterministic behavior and/or lack speed, force or stroke. Therefore, they are not investigated in this research. Steppers can be considered to be built up out of the principles presented and will therefore not be regarded separately.

To calculate the work density, the volume of an actuator has to be determined. In this research, the volume of the actuator does not include the volume of transmissions like benders or other stroke amplification mechanisms [77]. Depending on the design and the amplification requirement of the application an amplification mechanism stores an extra amount of strain energy. Including the amplification mechanism volume in the work density calculation will result in a work density which is application specific, and therefore less universal.

The load of the actuators in general can consist of several different types of contributions like inertial force, damping force, compliance force and friction force. In precision manipulation of MEMS, but often also in the more general design principles (see section 2.3) also, the use of compliant mechanisms is almost a necessity. A fully compliant mechanism lacks friction. Moreover, in manipulation in MEMS the inertial forces are low due to a combination of low accelerations and masses. Additionally, the damping force is low due to the low speeds for MEMS precision manipulation, especially in relation to relatively large compliant forces. Therefore, in this research the work generated is based solely on a compliance load, because the strain energy is often the main energy storing mechanism. The compliance for each individual design is tuned to an optimal compliance so that for each actuator the maximum work output is obtained. The work of the actuators presented here is based on one cycle of their full stroke.

The work density per second, the power density, might seem a more general performance indicator for actuators as it indicates how often per time period work from a certain actuator volume can be delivered. However, for non-commutating or stepping actuators and relatively slow positioning compliant systems the work density is more important. Since some actuator types have a relevant speed limitation, the characteristic time constant or maximum speed will be derived. Also, the dissipation of the actuator itself is regarded.

In this appendix the relationships between work, volume, dissipation and characteristic time constant are compared for the four actuation principles that are most relevant for MEMS-based precision manipulation.

C.2 Electro-magnetic actuators

There are several types of electro-magnetic actuators:

- Lorentz actuator
- Reluctance motor
- Induction motor
- (Giant) Magnetostriction

On one hand there are the actuators that rely on a coil to generate a variable magnetic field: the reluctance motor, the motor based on magnetostriction and the induction motor. On the other hand there is the Lorentz actuator, which uses a stationary magnetic field. In Appendix D, it is shown that a stationary magnetic field on a small scale can best be created by a permanent magnet, as it leads to the highest magnetic flux density. For the reluctance and induction actuators, the low flux density leads to low work density. Magnetostrictive actuators could in theory have a large work density. However, these giant magnetostrictions are limited to cryogenic temperatures. Although the strain (elongation per unit length, for example) is comparable to the strain of PZT piezo, a large volume is needed to create the magnetic field. Although magnetostriction seems to be an interesting actuation principle, more research is necessary, especially with regard to the micro domain. The Lorentz actuator using a permanent magnet, because of the stationary magnetic field, seems to have the best work density on a small scale.

C.2.1 Lorentz actuator

A Lorentz actuator is a combination of a current flowing through a current conductor and a magnetic field resulting in a mechanical force between the conductor and the field generator. A typical example of a Lorentz actuator is the voice coil of a loudspeaker. Lorentz actuators display a direct proportional coupling between the force and the current in a constant magnetic field.

Design and Fabrication concept

A design for a Lorentz actuator is presented, which should be manufacturable with MEMS techniques, thus without the assembly of a magnet or coil. The fabrication concept is only briefly explained to show its feasibility.

Figures C.1 and C.2 show an example of a micro Lorentz actuator. A sputtered aluminum coil is deposited on a standard silicon substrate. A sacrificial layer, such as oxide, is used to create a gap between the coil and the magnet. A magnetron sputter deposited permanent magnet [83] is suspended above the coil. Several researchers have demonstrated high permeability magnetic films. According to Lemke [82], Nd-Fe-B films prepared under optimal conditions can result in $Br = 0.4$ T, with B_r the remanent flux density. Commercially available Nd-Fe-B magnets generally have a larger Br, but Nd-Fe-B is difficult to deposit with the desired properties. A stronger remanent flux density of 0.88 T by a composition of SmCo has been obtained by Levy et al. [83]. The magnet can be made with a thickness of up to about 10 μm. The guidance of the magnet is not taken into account and is therefore not shown. The magnet is magnetized in the z-direction. The current in the coil passes the magnetic field in the x-direction, which will result in a force on the magnet in the y-direction. The force and movement combination of the magnet in the y-direction delivers mechanical work. Due to the high current density necessary to obtain a high work density, the coil creates a considerable amount of heat. The coil is therefore attached stationary to the substrate so that heat is conducted to the surroundings. The relatively large cross-sectional area of the coil wire requires large electrical connections to the coil. Therefore it is also convenient to keep the coil stationary and the magnet suspended.

The use of soft magnetic material like iron for guiding the magnetic flux, is not regarded because it complicates the fabrication of a micro Lorentz actuator. It also adds mass to the suspended magnet which is unfavorable for high bandwidth purposes. Although a design with two magnets magnetized in opposite direction would result in better use of the coil, it requires that the magnets are assembled. Since the magnet needs to be magnetized in-situ, only one magnetization direction can be used and, as a consequence, only one magnet is used.

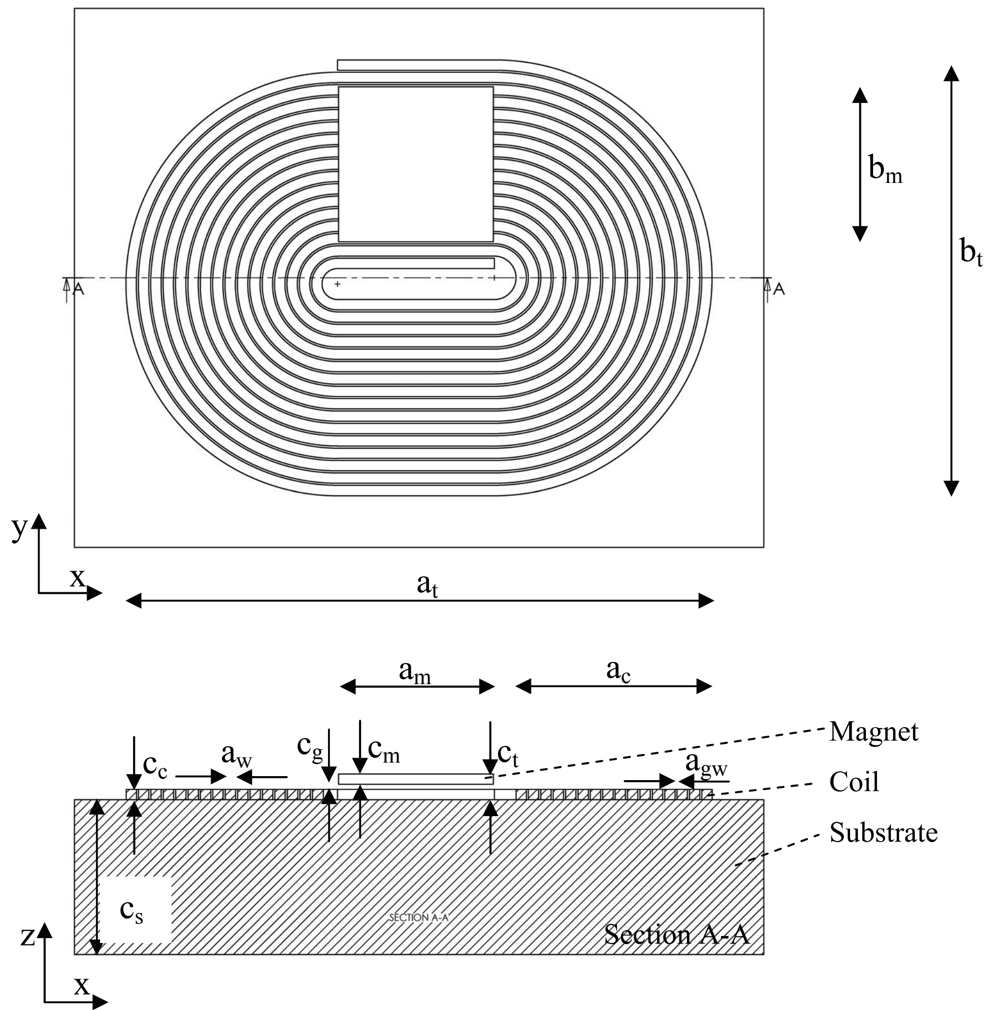

Figure C.1: 2D view of a micro Lorentz actuator with a suspended SmCo permanent magnet above a metal coil attached to a substrate.

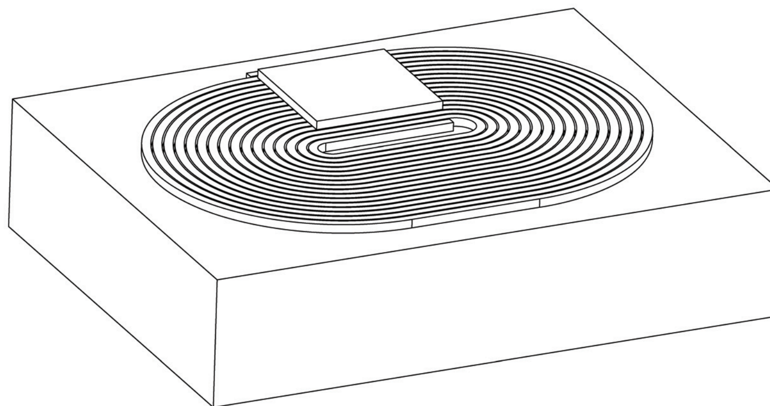

Figure C.2: 3D view of a micro Lorentz actuator with a suspended SmCo permanent magnet above a metal coil attached to a substrate.

ANALYTIC MODEL OF THE LORENTZ ACTUATOR

In the micro domain the current density can be high, because the heat generated due to resistivity in relation to the heat transport is low. The current density is not limited by the temperature rise of the coil, as in macro scale Lorentz actuators, but by electromigration as shown in Appendix E. The current density J scales as:

$$J \sim r^0 \tag{C.1}$$

where r represents the scaling factor as explained in the section on scaling in paragraph 2.2. The dissipation becomes:

$$P_d = \rho_e \, J^2 \, V_c \sim r^3 \tag{C.2}$$

where ρ_e is the specific electrical resistance and V_c is the coil volume. The scaling of the average flux density in the coil, B_{avg} , of a permanent magnet driven circuit scales better than a coil driven circuit for the micro domain (appendix D):

$$B_{avg} \sim r^0 \tag{C.3}$$

The flux density of a system containing a permanent magnet doesn't scale. Another advantage is that it dissipates less energy than a coil driven circuit. The Lorentz force created is:

$$F = V_{cm} \, J \, B_{avg} \sim r^3 \tag{C.4}$$

where V_{cm} is the coil volume opposing the magnet and F is the Lorentz force generated. The motor constant k_m is the ratio of force F to current I_e:

$$k_m = \frac{F}{I_e} = \frac{F}{J a_w c_c} \sim r^1 \tag{C.5}$$

Dimensions a_w and c_c are illustrated in Figure C.1. The motor constant scales linearly. The motor constant is also the ratio of the electromotive force to velocity v. The electromotive force scales as:

$$EMF = k \, v \sim r^2 \tag{C.6}$$

Therefore, the electromotive force voltage is low for micro Lorentz actuators. The deliverable work by the Lorentz actuator is the sum of work in two directions:

$$W = \int_{-0.5s}^{0.5s} F dy = F\ s \sim r^4 \tag{C.7}$$

where W is the work generated and s is the total stroke. A flat spiral air coil has an estimated inductance of [137]:

$$L = \frac{(0.5b_t)^2 N^2}{(b_t + 2.8c_w)10^5} \sim r^1 \tag{C.8}$$

where N is the number of turns of the coil winding. The electrical resistance of the coil R_c scales as:

$$R_c = \frac{\rho_e\, l_w}{a_w c_c} \sim r^{-1} \tag{C.9}$$

where l_w is the length of the winding. The scaling of the electrical time constant becomes:

$$\tau = \frac{L}{R_c} = \frac{a_w c_c (0.5b_t)^2 N^2}{\rho_e l_w (b_t + 2.8c_c)10^5} \sim r^2 \tag{C.10}$$

NUMERICAL EVALUATION

The performance of the design shown in Figure C.1 will be calculated numerically, taking into account its physical and practical restrictions. The scaling of the MEMS-based Lorentz actuator will be verified.

Parameter	Symbol	Unit	Smallest MEMS design	Largest MEMS design
Magnet width	a_m	µm	15	150
Magnet depth	b_m	µm	15	150
Magnet height	c_m	µm	1	10
Gap height	c_g	µm	0.5	5
Winding width	a_w	µm	3	8
Coil height	c_c	µm	3	30
Substrate height	c_s	µm	500	500
Gap between windings	a_{gw}	µm	2	3
Number coil turns	N	-	5	23
Total width	a_t	µm	70	707
Total depth	b_t	µm	55	557
Total height	c_t	µm	4.5	45
Total volume	V_t	m^3	$1.7\ 10^{-14}$	$1.8\ 10^{-11}$

Table C.1: Dimensions of the smallest and largest MEMS-based Lorentz actuator design shown in Figure C.1.

Bancel [5] has derived analytic formulas to calculate the spatial field created by one parallelepiped magnet. The interaction force is numerically calculated after multiplication by the electrical current. To calculate the work, the stroke is considered to be equal to the coil width (a_c) minus the magnet width (b_m). A model which makes use of the formulas of Bancel has been set up, implemented and verified by J. Compter (Philips Applied Technologies). The design presented in Figure C.1 has been modeled for various dimensions to cover the range from a relatively small design to a relatively large design. The smallest and largest design parameters are listed in Table C.1. Calculations based on these design parameters resulted in the values given in Table C.2. At a certain magnet thickness, the coil

height and the number of windings are optimized for a maximum work density. They can also be optimized for dissipation. The work delivered by the actuator is based on the deformation of an elastic mechanism. The load of the elastic mechanism delivers a force on the actuator proportional to the displacement. The compliance of the load is chosen so that the maximum load force is equal to the maximum actuator force exactly at the maximum displacement of the actuator.

Parameter	**Symbol**	**Unit**	**Analytic scaling factor**	**Smallest MEMS design**	**Largest MEMS design**
Current density	J	A/m^2	0	10^9	10^9
Current	I_e	A	2	$9.0\ 10^{-3}$	0.24
Voltage	U	V	1	0.017	0.78
Dissipated power	P_d	W	3	$1.5\ 10^{-4}$	0.187
Remanent flux density	B_r	T	0	0.88	0.88
Average flux density	B_{avg}	T	0	0.040	0.040
Time constant	τ	s	2	$1.4\ 10^{-9}$	$2.0\ 10^{-7}$
Motor constant	k	N/A	1	$6.0\ 10^{-6}$	$2.3\ 10^{-4}$
Force	F	N	3	$2.7\ 10^{-8}$	$2.7\ 10^{-5}$
Total stroke	s	μm	1	10	103
Work	W	J	4	$2.7\ 10^{-13}$	$2.8\ 10^{-9}$
Work density	W/V_t	J/m^3	1	15.7	158
Mech. Power	P	W	2	-	-

Table C.2: Analytically derived scaling factors compared to the performance of the smallest and largest MEMS-based Lorentz actuator design shown in Figure C.1 and the dimensions listed in Table C.1.

Comparing the small and large actuator design, the winding width a_w and gap a_{gw} between the windings have not been scaled linearly. Fabrication implications have resulted in the dimensions listed in Table C.1. These dimensions do not scale exactly. Therefore, the scaling of current, voltage, time constant and the motor constant of the design do not scale exactly according to the analytic scaling rules given in Table C.2. The stroke of the actuators has been tuned to scale linearly. The dissipated power, average flux density, force, work and work density scale almost

exactly according to the analytic rules. In fact, the work can be estimated within 2% for the given design by using the following rule:

$$W = \xi \cdot V_t^{4/3} \sim r^4 \quad | \quad 1.7 \cdot 10^{-14} \leq V_t \leq 1.8 \cdot 10^{-11}$$
$$\xi \approx 5.8 \cdot 10^5 \text{ N/m}^3 \tag{C.11}$$

To determine ξ, a design was necessary. Based on scaling rules alone the work could not have been determined. Based on the design features listed in Table C.2, Figures C.8 and C.9 were created.

C.2.2 Conclusion regarding Electromagnetic actuators

Electromagnetic actuators using a permanent magnet to develop a field produce a larger work density than actuators using a coil on a small scale. Therefore, MEMS-based Lorentz actuator designs with a permanent magnetic field are presented. The permanent magnet is sputter deposited. However, the stability of the magnetic properties is not trivial. The Lorentz actuator combines a relatively small force with a large displacement. The dissipation is large. The dissipated power, average flux density, force, work and work density of the proposed small and large MEMS-based Lorentz actuator designs (Figure C.1) scale according to the analytic scaling rules. However, based on scaling alone, the absolute performance cannot be determined. Electron migration, for example, limits the current density. Static force delivery requires constant energy input. In addition, the range of the actuator volume and corresponding performance indicators is dependent on the design and the fabrication techniques used with the inherent limitations. For the presented design the work can be estimated within 2% based on a certain actuator volume according to equation C.11.

In practical applications, a relatively large assembled external magnet is often used. This is the case in the Robert-Bosch yaw rate sensor, for example [90]. The combination of a small wafer thickness, which is the gap in yoke of the magnet circuit, and the large flux density of a relatively large assembled magnet can result in successful systems. This type of system is especially convenient for distributed magnetic actuators (or sensors).

C.3 Electrostatic actuation

Several types of electrostatic actuators exist:

- (Lateral) comb-drive actuator
- Parallel plate, gap closing or transverse comb-drive actuator
- Electrostatic induction actuators

Comb-drive actuators, both lateral and transverse, can be made with common DRIE technology. A lateral comb-drive actuator is shown in Figure C.3. It moves in the *x*-direction. A transverse comb-drive moves in the direction perpendicular to the comb fingers, as shown in Figure C.5. Electrostatic induction motors are a relatively new development as shown, for example, by Livermore [88]. This actuation principle shows potential, at least theoretically, with regard to output power-density. However, the technology is still too young to draw conclusions.

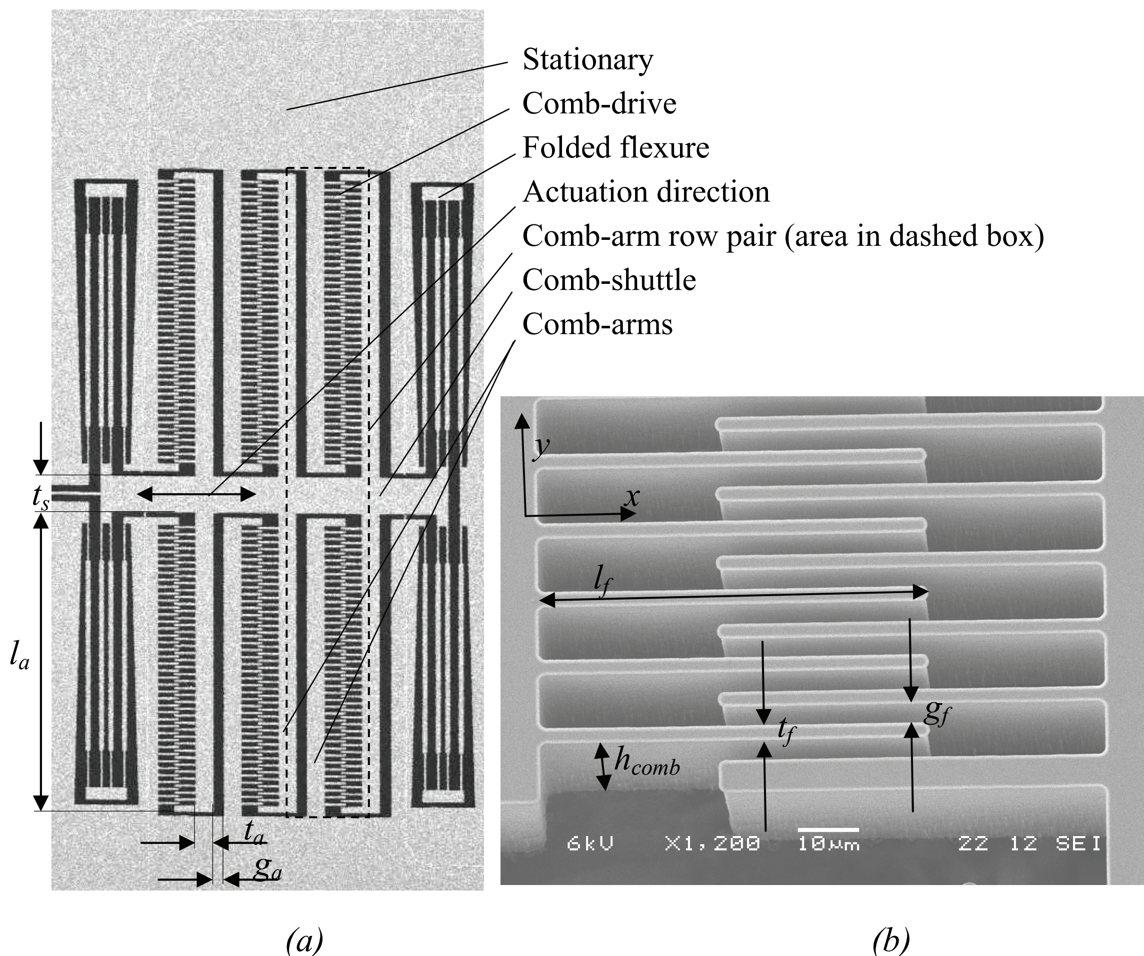

(a) *(b)*

Figure C.3: SEM pictures of (lateral) comb-drive actuators. a) Overview, showing the folded flexure suspension. b) Detail of the comb fingers (Sarajlic).

C.3.1 Comb-drive actuator (lateral)

Comb-drives are linear motors that utilize electrostatic forces that act between two conductor combs. In a lateral comb-drive actuator (Figure C.3) the fingers are typically arranged in such a way that they can slide past one another until each finger occupies the slot in the opposite comb. One comb is fixed and the other one is connected to a suspension with compliance in the longitudinal direction of the fingers. Applying a voltage difference between the comb structures will result in a movement by electrostatic forces in the finger direction.

DESIGN AND FABRICATION

The designs presented in this section are based on Deep Reactive Ion Etching (DRIE) fabrication technology. High aspect ratio (1:20) comb-drives are usually made by DRIE. This technology results in vertical trenches of which the side walls can have a good flatness (for MEMS). The smallest gap is about 2 μm, resulting in a maximum height of 40 μm for the fingers. Parts of the wafer are electrically isolated from other parts in a planar direction either by vertical trench isolation as shown by Sarajlic [112, 114] or by Silicon on Insulator technology (SOI).

In Figure C.3, trench isolation was used. Trench isolation starts by etching a trench that is slightly deeper than the comb structure using DRIE. This trench is refilled by an insulator such as silicon rich nitride (SiRN), reconnecting the part mechanically. The combs are made by DRIE. The movable structures have to be released on the bottom side which can be done by isotropic etching on the bottom side as shown by Sarajlic [112], or by locally thinning a wafer by back-etching [112] or using a silicon on insulator (SOI) wafer.

ANALYTIC MODELING OF THE LATERAL COMB-DRIVE

The lateral electrostatic force in the x-direction, as shown in Figure C.3, is described by Legtenberg [81]:

$$F_x = \frac{\varepsilon\, n\, h_{comb}\, U^2}{g_f} = \varepsilon\, n\, AR\, {g_f}^2 {E_e}^2 \sim r^2 \qquad \text{(C.12)}$$

where n is the number of finger pairs, ε is the dielectric constant, h_{comb} is the height of the comb fingers, g_f is the gap spacing between the fingers, U is the voltage between the stationary and movable part of the comb, E_e is the field in the gap and AR is the maximum aspect ratio of the etching machine. For gaps smaller than about 5 μm the electric field is restricted to 75 V/μm, as described by Wallash

[133], so $E_e \sim r^0$. Furthermore, $AR \sim r^0$ and $n \sim r^0$ results in F_y scaling as r^2. The current equipment in MESA[+], Adix 100SE and the mask writer require $AR \leq 20$ and $g_f \geq 2$ μm. The maximum energy that a comb-drive transfers to an elastic suspension becomes:

$$W = 0.5 F_x s = \frac{\varepsilon\, n\, h_{comb}\, U^2\, s}{2 g_f} = \frac{\varepsilon\, n\, AR\, g_f^{\,2} E_e^{\,2}\, s}{2} \sim r^3 \tag{C.13}$$

The work density of the comb-drive can be calculated if the volume of the comb-drive is known. The total comb-drive volume V_t can be estimated by adding the volume of the fingers and the electric energy field V_f, the arms of the fingers V_a, the shuttle V_s and the space between the comb-arms V_{ga}:

$$V_t = V_f + V_a + V_s + V_{ga} \tag{C.14}$$

The suspension is not taken into account, just as in the volume calculation of the electromagnetic actuator. In the next section, the thickness of the comb-arms and the necessary gap between the comb-arms will be calculated. When these two variables are known, the volume of the comb-drive can be determined.

THICKNESS OF THE COMB-ARMS

The thickness of the comb arms, t_a, can be estimated based on the tolerable change of the gap between the fingers. If this gap changes too much, side pull-in will restrict the comb-drive force. A calculation is given below.

Pull-in can be explained as follows: In an electrostatic actuator mechanical forces guide a shuttle (rotor or translator). Electrostatic forces displace the shuttle in the actuation direction. However, there are also electrostatic forces perpendicular to the actuation direction. If the voltage of the electrostatic lateral comb-drive actuator is increased too much, the electrostatic forces perpendicular to the actuation direction become larger than the mechanical forces providing the guidance. At that point the mechanical guidance fails and the system becomes unstable. This is called pull-in. If the voltage of the electrostatic parallel plate or transverse comb-drive actuator is increased too much, the electrostatic forces in the actuation direction become larger than the mechanical counteracting forces. The shuttle position in the actuation direction has become unstable.

The number of fingers attached to one arm is:

$$n = \frac{l_a}{2g_f + 2t_f} \tag{C.15}$$

with l_a, g_f and t_f shown in Figure C.3. Using equation C.15, the comb-drive force F_x in the x-direction can be transferred into a distributed force along a comb-arm, q_{comb}:

$$q_{comb} = \frac{F_x}{l_a} = \frac{\varepsilon\ h_{comb}\ g_f E_e^{\ 2}}{2(g_f + t_f)} \tag{C.16}$$

The distributed force q_{comb} deforms the single sided fixed comb-arm according to Young [139]:

$$\varphi_a = \frac{q_{comb}\ l_a^{\ 3}}{6E_y I} = \frac{2q_{comb}\ l_a^{\ 3}}{E_y\ h_{comb}\ t_a^{\ 3}} \tag{C.17}$$

where φ_a is the maximum rotation of the arm, E_y is the Young's modulus, I is the area moment of inertia and t_a is the thickness of the comb arms. This rotation causes the comb-fingers to approach each other by a maximum of e_f. This approach should be restricted because it causes side pull-in of the comb-drive.

$$e_f = \varphi_a\ l_f \tag{C.18}$$

where l_f is the finger length. Combining equations C.12, C.16, C.17 and C.18 results in the thickness of the comb-arms:

$$t_a = \sqrt[3]{\frac{\varepsilon\ g_f\ E_e^{\ 2} l_a^{\ 3} l_f}{e_f E_y (g_f + t_f)}} \tag{C.19}$$

In the design presented in Figure C.3a, E_e = 75 V/μm, l_a = 500 μm, l_f = 36 μm and e_f = 30 nm results in t_a = 30 μm.

GAP BETWEEN THE COMB-ARMS

The gap between the comb-arms should be large enough so that the influence of the parallel plate attraction force, given by Legtenberg [81], between the arms depicted in Figure C.3a is sufficiently lower than the comb-drive force. The parallel plate attraction force is distributed along the comb-arm:

$$q_{pp} = \frac{\varepsilon \, h_{comb} \, U^2}{2{g_a}^2} \tag{C.20}$$

Variable ζ links the distributed force of the parallel plates to the distributed comb-drive force. $\zeta << 1$:

$$q_{pp} = \zeta \, q_{comb} \tag{C.21}$$

Combining equations C.16, C.20 and C.21 results in:

$$g_a = \sqrt{\frac{{g_f}^2 + g_f \, t_f}{\zeta}} \tag{C.22}$$

For the design shown in Figure C.3, $g_f = 3$ μm, $\zeta = 0.05$ results in $g_a = 20$ μm.

TOTAL VOLUME OF A COMB-DRIVE ACTUATOR

In this section the volume of one comb-arm row pair as shown in Figure C.3a will be determined. The volume of the fingers and electric energy field V_f is:

$$V_f \approx 4 l_f l_a h_{comb} \tag{C.23}$$

The initial overlap of the comb-fingers, usually >6 μm, is disregarded because relatively long comb-fingers (>50 μm) will be used for calculation. Long fingers result in a large work density, as will be shown later. The volume of the arms of the fingers V_a:

$$V_a = 2 l_a t_a h_{comb} \tag{C.24}$$

To accurately determine the minimum thickness of the shuttle, a FEM calculation is necessary. In this calculation the shuttle in-plane thickness is set at twice the comb-arm thickness. The volume of the shuttle V_s becomes:

$$V_s = 2t_a h_{comb}\left(2l_f + 2l_a + g_a\right) \tag{C.25}$$

The volume of the space between the comb-arms V_{ga}:

$$V_{ga} = 2l_a g_a h_{comb} \tag{C.26}$$

The number of fingers in one comb-arm row pair is:

$$n = \frac{l_a}{g_f + t_f} \tag{C.27}$$

The work density of one comb-arm row pair is equal to the work density of a comb-drive:

$$\frac{W}{V_t} = \frac{\varepsilon\, l_a\, l_f\, g_f\, E_e^{\,2}}{4\left(g_f + t_f\right)\left(2t_a + 2l_f + g_a\right)\left(l_a + t_a\right)} \tag{C.28}$$

where a value for l_f is chosen that is equal to stroke s. For gaps smaller than about 4-5 μm the electric field is restricted to 75 V/μm, as described by Wallash [133]. The finger length is restricted by finger pull-in. According to Elata [44] the minimum finger thickness for a certain finger geometry and electrical field is:

$$t_f > \sqrt[3]{\frac{1.94\,\varepsilon\, E_e^{\,2} l_f^{\,4}}{g_f\, E_y}} \tag{C.29}$$

In addition, the shuttle suspension guiding stiffness should be high enough to overcome shuttle pull-in. The design depicted in Figure C.3 has been dimensioned based on $\zeta = 0.05$, $e_f = 30$ nm, $E_e = 75$ V/mm, $t_f > 2$μm, 2 μm ≤ g_f ≤ 4 μm and $l_a =$ 500 μm. The finger dimensions are selected so that they are just at the point of pull-in. For the length of the comb-arms a reasonable value of 500 μm is chosen. A smaller value would result in a larger work density according to equation C.28. However, this is because boundary effects such as extra thick fingers and extra

space at the end of a comb-row are not taken into account in the equation. Several designs have been optimized, three of which are presented in Table C.3. Designs 1 and 2 are based on a smallest feature size of the mask of 2 and 4 µm, respectively. Design 3 uses a combination of small gaps and thick fingers. Designs 2 and 3 require a high voltage.

Parameter	**Symbol**	**Unit**	**Design 1**	**Design 2**	**Design 3**
Comb height	h_{comb}	µm	40	40	40
Voltage	U	V	150	300	300
Electrical field	E_e	V/µm	75	75	75
Finger gap	g_f	µm	2.0	4.0	4.0
Fing.pairs in comb-arm row pair	n	-	125	63	83
Length of fingers	l_f	µm	69	139	83
Thickness of fingers	t_f	µm	2.0	4.0	2.0
Length of arms	l_a	µm	500	500	500
Transverse / lateral force	ζ	-	0.05	0.05	0.05
Gap of the arms	g_a	µm	13	25	22
Finger approach by arm rotation	e_f	nm	30	30	30
Thickness of arms	t_a	µm	37	47	43
Total volume	V_t	m^3	9.7 10^{-12}	17 10^{-12}	12 10^{-12}
Force	F	µN	497	498	664
Stroke	s	µm	69	139	83
Work	W	J	17 10^{-9}	35 10^{-9}	27 10^{-9}
Work density	W / V_t (ξ)	J / m^3	1.8 10^3	2.0 10^3	2.3 10^3
Efficiency	η	-	0.072	0.080	0.093

Table C.3: Three optimized designs of lateral comb-drive actuators

At a constant electrical field the force is maximized by maximizing the product $n\ g_f$ in one comb-arm row (design 3, Table C.3). The work density is maximized in combination with a long finger length. The work density obtained can purely be compared to the energy density in the space between the fingers, the theoretical maximum energy density:

$$\frac{W}{V_t} \approx \eta\ 0.5\ \varepsilon\ E_e^{\ 2} \ \mid\ 0.072 \le \eta \le 0.093 \qquad \text{(C.30)}$$

The work of design 3 can be estimated based on the actuator volume for 1 to 500 finger pairs, according to the rule set by equation C.31. In Figure C.8 the work versus volume is plotted.

$$W = \xi \cdot V_t \sim r^3 \quad | \quad 1.5 \cdot 10^{-13} \leq V_t \leq 7.2 \cdot 10^{-11}$$
$$\xi \approx 2300 \text{ N/m}^3 \qquad \text{(C.31)}$$

THE ELECTRICAL TIME CONSTANT AND DISSIPATION

The electrical time constant of a comb-drive is extremely high because the electrical resistance is small. In systems containing a unilateral force comb-drive (so that an electrostatic force can be made only in one direction) and an elastic energy storage element, the time constant is determined by the first vibration mode frequency. In section 5.6 the first vibration mode frequency of a translational and a rotational comb-drive is calculated and measured.

Statically there is almost no dissipation if the insulation is good. Dynamically, however, the energy of the charge in the comb is lost when the charge in the capacitance is decreased. The energy is dissipated in the amplifier, so self heating of the actuator is not an issue.

C.3.2 Transverse comb-drive actuator

DESIGN AND FABRICATION

A parallel plate actuator is an actuator that decreases the gap between two parallel plates when a voltage is applied. Because capacitance is dependent on the gap, the capacitance is increased at the same time. Figure C.4 shows an example which is used in the clamp mechanism presented in chapter 5. The gap, g_f, can be decreased by charging one of the plates. The design of Figure C.4 is used for switching, not for precision manipulation. Figure 5.15 shows SEM pictures of the activated parallel plate actuator. The actuator is also sometimes referred to as a gap closing actuator. If more than 1 parallel plate pair is used the design looks like a comb-drive, but then with transverse movement (Figure C.5).

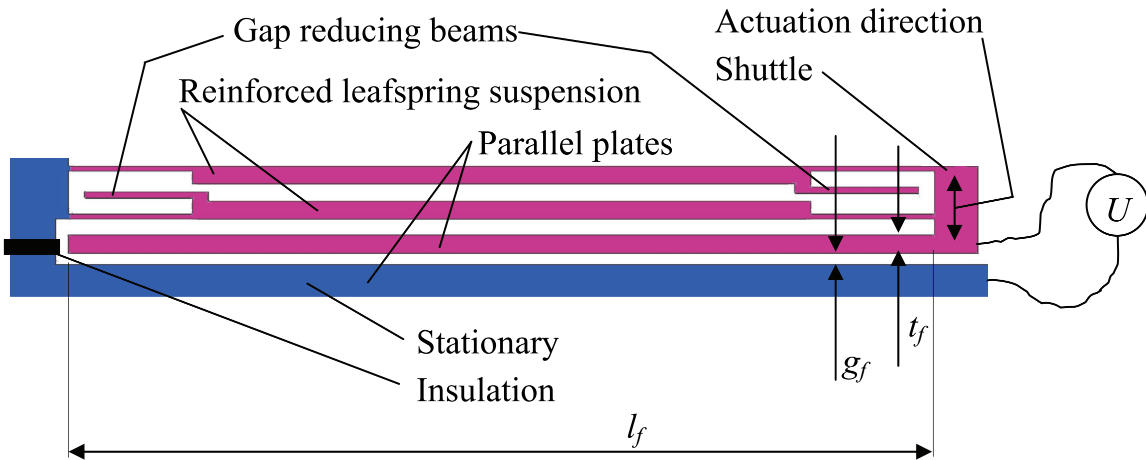

Figure C.4: Electrostatic parallel plate actuator with parallel reinforced leaf-spring suspension designed for DRIE technology, which requires gap reducing beams. This design is implemented in the clamp mechanism (chapter5).

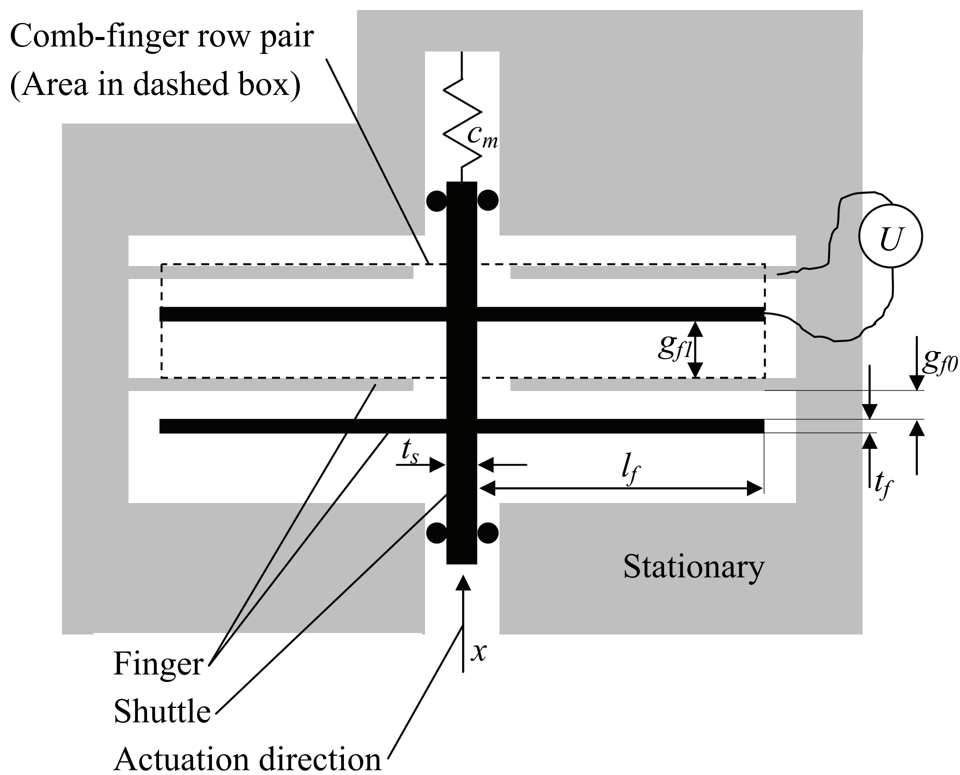

Figure C.5: Schematic representation of a transverse comb-drive actuator.

Transverse comb-drive actuators can be fabricated with DRIE technology [114], in which case the movement is in-plane with regard to the wafer. Tas [125] shows several transverse comb-drives in surface micro machining technology. Out-of-plane gap closing actuators are made in surface micro machining technology as shown by Sarajlic [112]. The designs discussed in this section are based on DRIE fabrication technology.

ANALYTIC MODEL OF THE TRANSVERSE COMB-DRIVE ACTUATOR

Transverse comb-drive actuators suspended by a compliant mechanism have a stable and an unstable part of their stroke of operation. For precision manipulation, the stable part will be evaluated in this section. For latching or switching purposes, the unstable part of the stroke can be used. If the full displacement of the parallel plate actuator can be utilized, because there is some kind of control system, the work density will be larger. However, for a control system such as this, fast and sub-micron repeatability sensors in MEMS are necessary. At the moment these sensors are not available, and therefore the full displacement can not be used.

In this section a transverse comb-drive will be evaluated, because often the force of a single parallel plate actuator is insufficient for manipulation. In addition, the volume of a transverse comb-drive can be estimated more accurately because for a single parallel plate actuator the size of the surroundings play a much bigger role. For precision manipulation a transverse comb-drive actuator will be evaluated in this section.

TRANSITION FROM STABLE TO UNSTABLE POINT OF OPERATION

The transition from the stable to unstable point of operation for the transverse comb-drive will be derived. The gap closing electrical force F_e is given by Legtenberg [81]:

$$F_e = \frac{\varepsilon\, n\, A\, U^2}{2}\left(\frac{1}{\left(g_{f0}-x\right)^2} - \frac{1}{\left(g_{f1}+x\right)^2}\right) \tag{C.32}$$

where ε is the dielectric constant, A is the area of the opposing flat plates, g_{f0} and g_{f1} are the initial distances between the plates (Figure C.5), x is the displacement of the shuttle and U is the voltage between the plates. In equilibrium the electrical gap closing force is counteracting the force of a compliant mechanism suspension F_m with stiffness c_m:

$$F_m = c_m\, x \tag{C.33}$$

where c_m is the stiffness of the parallel plate suspension. For stability, the change of mechanical force with respect to the distance between the plates should be larger than or equal to the change of gap closing force. The transition from the stable to unstable state occurs when:

$$F_e = -F_m \wedge \frac{\partial F_e}{\partial x} = -\frac{\partial F_m}{\partial x} \tag{C.34}$$

The results of numerically solving equation C.34 are presented in Table C.4:

g_{f1} / g_{f0}	x_{pi} / g_{f0}	κ
∞	0.333	0.544
10	0.332	0.545
5	0.329	0.549
3	0.322	0.556
2	0.307	0.569
1.5	0.282	0.589
1.3	0.259	0.606
1.2	0.239	0.620

Table C.4: Relative displacement x_{pi} / g_{f0} at the transition from a stable to an unstable state of a transverse comb-drive and the corresponding dimensionless voltage factor κ (equation C.35).

The relative displacement x_{pi} / g_{f0} at the transition from a stable to an unstable state is irrespective of the stiffness c_m. The corresponding voltage at the transition from the stable to unstable state is given by:

$$U_{pi} = \kappa \sqrt{\frac{c_m \, g_{f0}^{\;3}}{\varepsilon \, n \, A}} \tag{C.35}$$

The energy delivered to the elastic mechanism at the transition from the stable to unstable state is:

$$W = \int_{x=0}^{x_{pi}} F_m dx = \frac{c_m x_{pi}^{\;2}}{2} \sim r^3 \tag{C.36}$$

WORK DENSITY

For the work density of the transverse comb drive, the volume of one comb-finger row pair V_t (Figure C.5) will be calculated. This volume can be estimated by adding the volume of the fingers V_f, the volume of the gaps between the parallel plates V_g and the volume of the shuttle V_s:

$$V_t = V_f + V_g + V_s \tag{C.37}$$

The suspension is not taken into account, just like in the electromagnetic and lateral comb-drive actuator volume calculation. In the next section the thickness of the fingers will be calculated.

The finger thickness t_f depends on the amount of deflection f that is tolerable. For stepper or latching mechanisms the fingers or plates may be designed for deflecting. However, for precision manipulation the deflection should remain small compared to the initial gap: $f << g_{f0}$. The deflection f for a single-sided fixed finger loaded by a distributed force F_e / l_f at equilibrium is given by Young [139]:

$$f = \frac{F_e \, l_f^{\,3}}{8E_y I} = \frac{3c_m \, x_{pi} l_f^{\,3}}{2E_y \, h_{comb} \, t_f^{\,3}} \tag{C.38}$$

A variable λ is introduced to describe the relationship between the maximum stable working displacement of the actuator and the deflection:

$$f = \lambda \, x_{pi} \tag{C.39}$$

This results in:

$$t_f = \sqrt[3]{\frac{3c_m \, l_f^{\,3}}{2\lambda \, E_y \, h_{comb}}} \tag{C.40}$$

The volume of the fingers in one comb-finger row pair becomes:

$$V_f = 4 t_f l_f h_{comb} \tag{C.41}$$

The volume of the gaps is:

$$V_g = 2(g_{f0} + g_{f1}) l_f h_{comb} \tag{C.42}$$

To accurately determine the minimum thickness of the shuttle, a FEM calculation is necessary. In this calculation the shuttle thickness is set at twice the comb-finger thickness. The volume of the shuttle V_s becomes:

$$V_s = 2t_f h_{comb} (g_{f0} + g_{f1} + 2t_f) \tag{C.43}$$

With the total volume and work known, the work density can be calculated based on a design. Two designs that are optimized for work density are presented in Table C.5. One design is based on small gaps. The second design is based on the largest gap, which allows a field of 75 V/μm according to Wallash [133]. Both designs are calculated based on 2 finger pairs, but both can be scaled to up to approximately 500 finger pairs if necessary. The work density does not change. With $\lambda = 0.05$, $t_f =$ 2.0 μm and $E_e = 75$ V/μm, g_{f1} / g_{f0} has been optimized to be 2. It results in: 32 μm < l_f < 43 μm and 104 V < U < 338 V (Table C.5). The design with the large gap has a 49 % larger work density.

The work density is given by:

$$\frac{W}{V_t} \approx \eta \, 0.5 \, \varepsilon \, E_e^{\,2} \;\; | \;\; 0.023 \le \eta \le 0.035 \tag{C.44}$$

In fact, the work of design 2 can be estimated based on the actuator volume according to equation C.45. It is plotted in Figure C.8.

$$\begin{aligned} & W = \xi \cdot V_t \sim r^3 \quad | \quad 8.9 \cdot 10^{-14} \le V_t \le 2.1 \cdot 10^{-11} \\ & \xi \approx 866 \text{ N/m}^3 \end{aligned} \tag{C.45}$$

Parameter	Symbol	Unit	Design 1	Design 2
Height	h_{comb}	μm	40	40
Gap 1	g_{f0}	μm	2.0	6.5
Gap 2	g_{f1}	μm	4.0	13
finger pairs	n	-	2	2
Finger length	l_f	μm	32	43
Finger thickness	t_f	μm	2.0	2.0
Relative deflection of fingers	λ	-	0.05	0.05
Stiffness	c_m	N/m	94.4	39.0
Displacement at pull-in	x_{pi}	μm	0.61	2.00
Voltage at pull-in	U	V	104	338
Force at pull-in	F_e	μN	57.9	77.8
Work	W	J	$17.8\ 10^{-12}$	$77.6\ 10^{-12}$
Volume	V_t	m^3	$30.7\ 10^{-15}$	$89.7\ 10^{-15}$
Work density	$W/V_t\ (\xi)$	J/m^3	580	866
Efficiency	η	-	0.0233	0.0348

Table C.5: Two optimized designs of transverse comb-drive actuators.

TIME CONSTANT AND DISSIPATION

Just as in the case of the lateral comb-drive the electrical time constant is extremely high, as is the mechanical time constant. The dissipation in the actuator is negligible.

C.3.3 Conclusion regarding electrostatic actuation

The energy density of lateral and transverse comb-drives depends greatly on the electrical field. If the mechanical structure is designed in such a way that pull-in of the shuttle or fingers is overcome, the work density is restricted by electrical breakdown, which limits the maximum field. This is a physical limit. The smallest gap size used in the comb-drive actuators is determined by DRIE technology. However, the gap size does not influence the work density much if the allowable voltage is not limited. Decreasing the gap size leads to small drive voltages. Lateral comb-drive electrostatic actuators combine moderate force and displacement. However, large voltages are needed for significant force. Transverse comb-drive actuators show a smaller work-density than lateral comb-drive actuators if only the passively stable part of the stroke is used.

C.4 Piezo actuators

DESIGN AND FABRICATION

Piezoelectric actuation can provide large work density. ZnO was researched quite extensively in the 1980s because of the theoretical large coupling coefficient. The coupling coefficient describes the ability of a piezoelectric material to transform electrical energy into mechanical energy and vice versa. However, it was proven difficult to reach a high electrical resistance, high breakdown voltage and low dielectric losses [39].

AlN, which is non-ferroelectric, results in low losses making AlN films especially suitable for sub-nanometer displacements at GHz high frequency vibration mode applications. Dubois [68, 69] presents an overview of several thin film methods of depositing AlN. Single crystal films have the highest d_{33} but are not regarded. The piezoelectric coefficient d_{33} couples the electrical field in the 3-direction to the mechanical strain in the 3-direction, in which the 3-direction is the direction perpendicular to the electrodes. Similarly, the piezoelectric coefficient d_{31} couples the electrical field in the 3-direction to the mechanical strain in the 1-direction, in which the 1-direction is the longitudinal direction of the beam shown in Figure C.6. The thin film properties vary depending on the deposition technique.

Lead Zirconate Titanate (PZT) possesses a much larger piezoelectric coefficient than AlN and ZnO, making larger work densities possible. Various techniques exist to deposit PZT. Sakata et al [111] show that a thin film PZT piezoelectro actuation layer can be made up to 5 μm thick by magnetron sputtering with a large d_{31} coefficient of 100 pC/N. Gardeniers [52] uses a sol-gel technique which results in a thin film layer of up to 300 nm thick with a d_{31} of 160 pC/N. Thicker layers can be made by gas jet deposition and screen printing as has been shown by [118]. PZT, however, is difficult to integrate into MEMS devices. The lead concentration is difficult to control. In the sol-gel technique the volume of the gel can shrink up to 30% of the initial volume upon crystallization at 600 ˚C, during which process about 10% of the lead is evaporated. To overcome the lead concentration difficulties, bonding a PZT wafer containing actuators to a Si wafer containing sensors and mechanisms could be interesting. As PZT is ferroelectric, it needs to be poled by a strong external electric field to orient the crystals. Trolier-McKinstry et al [127] present a nice overview of several thin film piezo ceramics. With respect to work density and losses the relevant material properties found in the literature are summarized in Table C.6.

	Unit	PZT (film)	PZT (bulk PI PIC 151)	AlN (film)	ZnO (film)
Source		[12],[52], [111],[128], [143]	[101]	[39], [69], [109]	[21], [55]
Piezo electric coefficient (d_{33})	10^{-12} m/V	108…140	500	1.6…3.54	12.4
Piezo electric coefficient (d_{31})	10^{-12} m/V	-29…-160	-210	-1.1...-1.9	-4.1
Stiffness coefficient (c_{11})	10^9 Nm^{-2}	130..150	150	394	211
Max field (E_3)	10^6 Vm^{-1}	20-40	10	80	
Coupling coefficient (k_{31})	%	72	38	31	48
Work density $d_{31}{}^2E_3{}^2c_{11}/8$	1000 Nm	5.5..770	83	0.38..1.1	

Table C.6: Material properties of the three most relevant piezo materials.

Often, bimorph benders are used in systems containing piezo actuators. The bimorph stores a lot of energy, and it is actually a mechanism to increase the stroke at the cost of a reduced force output. The theoretical maximum work density is obtained by disregarding stroke amplifiers. Therefore, the maximum work output for an elastic load is calculated by regarding the longitudinal work (work delivered in Δl direction in Figure C.6) delivered to a compliant load. The compliance of the load is optimized for maximum work density, as will be explained.

MODEL OF A LONGITUDINAL PIEZO ACTUATOR

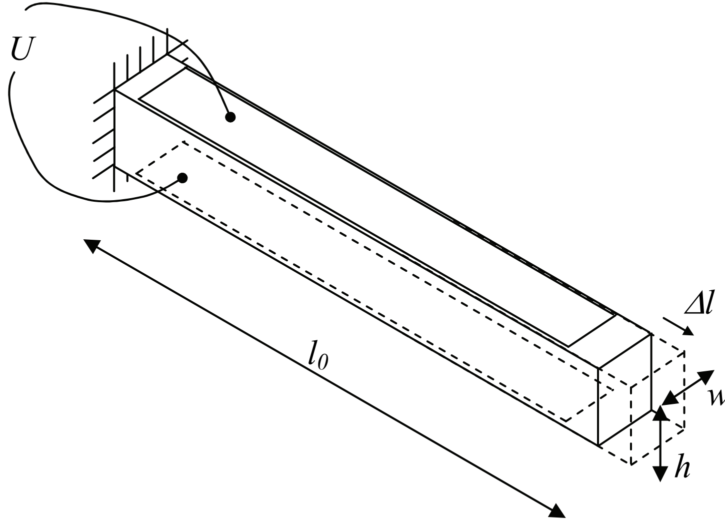

Figure C.6: A field in the height direction of the beam creates an elongation of the beam in the longitudinal direction.

The free displacement or maximum displacement (without a load force) the piezoelectric beam shown in Figure C.6 is capable of, is related to the d_{31} coefficient:

$$\Delta l_{\max} = d_{31} E_{3,\max} l_0 \tag{C.46}$$

where $E_{3,max}$ is the maximum electrical field between the electrodes. The blocking force the piezo can deliver to a load or maximum force is created by constraining the displacement:

$$F_{\max} = c_{piezo}\, \Delta l_{\max} = d_{31} E_{3,\max} c_{11} A \tag{C.47}$$

where c_{piezo} is the stiffness of the piezo, which is:

$$c_{piezo} = \frac{c_{11} A}{l_0} \tag{C.48}$$

and:

$$A = h \cdot w \tag{C.49}$$

where c_{11} is the ratio of longitudinal stress to longitudinal strain. The force F_{piezo} which the piezo can deliver to an external load at a certain displacement Δl can be calculated by:

$$F_{piezo} = F_{\max} - \frac{\Delta l}{\Delta l_{\max}} F_{\max} \tag{C.50}$$

This force is in equilibrium with the load force:

$$F_{piezo} = c_{load}\ \Delta l \tag{C.51}$$

where c_{load} is the stiffness of the load. Using equations C.50 and C.51, the displacement can be written as:

$$\Delta l = \frac{F_{\max} \Delta l_{\max}}{\Delta l_{\max}\ c_{load} + F_{\max}} \tag{C.52}$$

The work delivered by the piezo to the elastic load is:

$$W = \frac{c_{load}}{2} \left(\frac{F_{\max} \Delta l_{\max}}{\Delta l_{\max}\ c_{load} + F_{\max}} \right)^2 \tag{C.53}$$

The optimum load stiffness for maximum work is found when:

$$\frac{dW}{dc_{load}} = 0 \ \Rightarrow\ c_{load} = \frac{F_{\max}}{\Delta l_{\max}} = c_{piezo} \tag{C.54}$$

The maximum work becomes:

$$W = \frac{F_{\max} \Delta l_{\max}}{8} \tag{C.55}$$

The maximum work density becomes:

$$\frac{W}{V} = \frac{{d_{31}}^2 {E_{3,\max}}^2 c_{11}}{8} \tag{C.56}$$

The work density is calculated for PZT and AlN and based on average material property values as given in Table C.6. For PZT, c_{11} = 150 10^9 N/m^2, d_{31} = 100 10^{-12} and $E_{3,max}$ = 40 V/µm result in a work density W/V of 3.0 10^5 J/m^3. For AlN, c_{11} = 320 10^9 N/m^2, d_{31} = 1.6 10^{-12} and $E_{3,max}$ = 80 V/µm result in a work density W/V of 6.6 10^2 J/m^3. With the beam dimensions varying from 0.1 x 2 x 50 µm^3 to 2 x 40 x 1000 µm^3 (h x w x l_o), the lines plotted in Figure C.8 are obtained. A 0.3 µm "thick" PZT layer generates the same work as a 40 µm thick lateral comb-drive with the same device area.

Because of the small displacement, a displacement leverage mechanism is usually necessary. Bimorphs can be created relatively easily by depositing the piezoelectric material on a substrate which acts as an elastic bender. The displacement of bimorphs is calculated by Gardeniers et al. [52]. The work density of bimorphs, however, is much lower than that of an extender depending on the thickness and Young's modulus of the layers. The input energy is mainly stored as a stress-strain combination in the bimorph.

CONCLUSION REGARDING PIEZOELECTRIC ACTUATORS

PZT piezoelectric actuators exhibit a very large work density. However, because of the small displacement and fabrication technology, benders are often implemented which decrease the work density. The integration in MEMS technology remains difficult. Bonding a PZT wafer containing actuators to a Si wafer containing sensors and mechanisms could be interesting. For high frequency applications PZT piezo actuators might display significant self-heating. AlN piezoelectric actuators are interesting for GHz high frequency vibration modes and small displacement applications like resonators. However, the work density of AlN piezo actuators in general is small.

C.5 Thermal actuators

OVERVIEW OF SEVERAL THERMAL ACTUATOR DESIGNS

One can distinguish between several basic types of thermal actuators: *longitudinal expanders* are shown by Paalvast [98], *bent-beam* actuators are shown by Que et al [105] and Chu et al [27], *hot-cold-leg* actuators are shown by Deladi [34], Chen et al [25], Huang et al [59] and Kolesar et al [75], *bimorph* cantilevers are calculated in a handy force-deflection-frequency design chart by Vaganov et al [131], and *joint-actuators* are shown by Ebefors et al [42]. Although theoretically many materials can be used for expansion, silicon is often used. Ebefors [42], however, shows polyimide joint actuators. The practical heating upper limit for polysilicon is 600-800˚C, beyond which self-annealing may cause irreversible changes. Although heat in general introduces positional drift it is interesting to point out that on the micro scale nanometer stability is less troublesome to reach (with respect to thermal expansion). For example, a 400 µm long silicon beam needs a homogenous temperature increase of 1 K to expand 1.0 nm, while macro precision machines nm's drift are caused by mK's. Que et al [105] claim that no cross-talk was observed between closely spaced heated microstructures.

A brief overview of the work densities found in the literature is presented in Table C.7. The calculated work density varies greatly, however. Therefore, a calculation of the work density, time constant and dissipation will follow.

Literature	Blocking force	Free displacement	Max elastic work	Work density	Temp. increase	Material	Type
	µN	µm	J	J/m³	K		
Que	8300	5.0	$5.19\ 10^{-9}$	$1.26\ 10^{5}$	750	Si	bent-beam
Chu	10600	72.5	$9.61\ 10^{-8}$	$1.48\ 10^{4}$	600	Si	bent-beam
Paalvast	8320	0.039	$4.05\ 10^{-11}$	$5.78\ 10^{3}$	450	SCS	beam
Vaganov	1800	50.0	$1.13\ 10^{-8}$	$5.63\ 10^{3}$	100	Al/Si	bimorph
Chen	17.0	9.0	$1.91\ 10^{-11}$	$1.44\ 10^{3}$	1390	poly Si	hot-cold leg
Deladi	12.0	15.0	$2.25\ 10^{-11}$	$8.45\ 10^{2}$	max	poly Si	hot-cold leg
Kolesar	8.1	10.0	$1.01\ 10^{-11}$	$5.15\ 10^{2}$		poly Si	hot-cold leg

Table C.7: Brief overview of the literature on thermal actuators. The reported displacement and force combination result in greatly varying work density.

ANALYTIC MODEL OF A THERMAL ACTUATOR

Usually a leverage mechanism is used to increase the displacement of a thermal actuator. These mechanisms store energy. In the following elaboration the consequences of a leverage mechanism for the output energy, energy density and the characteristic time-constant will not be considered. The maximum energy density and the smallest time constant are derived.

An estimation of the force, displacement and work of a thermal actuator can be made based on the Young's modulus, the expansion coefficient, solid conduction, and the temperature difference with the ambient. Radiation, convection and conduction by air are neglected. Paalvast [98] shows that for silicon at average temperature differences of 600K for long slender beams this assumption has a mismatch of only 3% for steady state situations with respect to finite element models. The properties of the material are assumed to be constant. Small silicon thermal actuators up to several microns high can be made by surface micro machining. Larger beams can be made by DRIE.

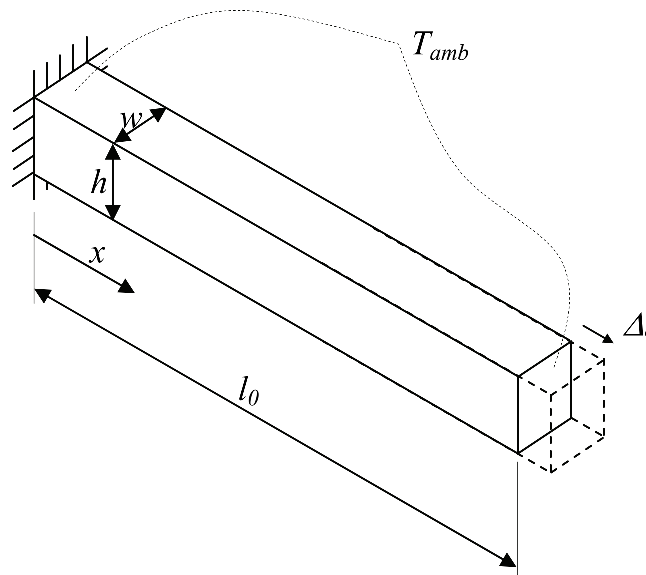

Figure C.7: Elongation of a prismatic beam due to heating

A current flowing through a prismatic beam in combination with the specific resistance of the beam creates the heat source. A beam is heated by constant heat input P_d, which is uniformly distributed along the beam if the specific resistance is constant. The calculations are based on the assumption that the temperature at both

ends of the beam is close to ambient. According to Paalvast [98] the temperature T at a certain point $0 \leq x \leq l_0$ is :

$$T(x) = -\frac{P_d\ x^2}{2\lambda\ A\, l_0} + \frac{P_d\ x}{2\lambda\ A} + T_{amb} \tag{C.57}$$

where λ is the thermal conductivity and $A = w\ h$. The maximum temperature difference is:

$$\Delta T_{\max} = T\left(\frac{l_0}{2}\right) - T_{amb} = \frac{P_d l_0}{8\lambda\ A} \tag{C.58}$$

The average temperature difference with the surroundings is:

$$\Delta T_{avg} = \frac{1}{l_0}\int_0^{l_0} (T(x) - T_{amb})dx = \frac{P_d l_0}{12\ \lambda\ A} \tag{C.59}$$

The dissipated power therefore scales: $P_d \sim r^1$. The free displacement Δl_{max} of the beam without load becomes:

$$\Delta l_{\max} = l_0\ \alpha\ \Delta T_{avg} = \frac{\alpha\ l_0^{\ 2}\ P_d}{12\ \lambda\ A} \tag{C.60}$$

where α is the thermal expansion coefficient. The blocking force F_{bl} at zero extension is equal to the free displacement multiplied by the beam stiffness:

$$F_{bl} = \frac{E_y A}{l_0}\Delta l_{\max} = \frac{\alpha\ E\ l_0\ P_d}{12\ \lambda} \tag{C.61}$$

where E is the Young's modulus. The maximum work that can be obtained from the thermal actuator with an elastic load requires a stiffness of the load as calculated at the piezo actuator, using equation C.54:

$$c = \frac{F_{bl}}{\Delta l_{\max}} \tag{C.62}$$

The maximum work becomes:

$$W = \frac{c\left(\frac{\Delta l_{\max}}{2}\right)^2}{2} = \frac{F_{bl}\ \Delta l_{\max}}{8} = \frac{1}{1152}\frac{\alpha^2\ E_y}{\lambda^2}\frac{l_0^{\ 3}}{A}P_d^{\ 2} \qquad \text{(C.63)}$$

The amount of elastic work can also be expressed in terms of the maximum temperature difference:

$$W = \frac{V}{18}\alpha^2 E_y\ \Delta T_{\max}^{\ \ 2} \sim r^3 \qquad \text{(C.64)}$$

where V is the volume of the heated material. For several materials the theoretical work density factor $\alpha^2\ E_y\ \Delta T_{max}$ is given in Table C.8. For precision actuation the amount of heat brought into the system potentially disturbs the accuracy. Therefore, the work / dissipated power is important:

$$\frac{W}{P_d} = \frac{l_0^{\ 2}}{144}\frac{\alpha^2 E_y\ \Delta T_{\max}}{\lambda} \qquad \text{(C.65)}$$

For several materials $\alpha^2\ E_y\ \Delta T_{max}\ /\ \lambda$ is given in Table C.8. The transient behavior can be modeled by a distributed capacitance and a distributed resistance and is derived by Paalvast [98]. It is accurate within 10% of a finite element model also modeled by Paalvast:

$$\tau = \frac{l_0^{\ 2}}{\pi^2}\frac{C_p\ \rho}{\lambda} \sim r^2 \qquad \text{(C.66)}$$

where C_p is the specific heat capacity. The time constant is dominated by the reciprocal of the thermal diffusivity a:

$$a = \frac{\lambda}{C_p\ \rho} \qquad \text{(C.67)}$$

The thermal diffusivity a is given in Table C.8 for several materials. In general, materials with a large expansion coefficient, a large Young’s modulus and a high tolerable temperature in particular are advantageous to work density. The time-constant and dissipated power are a trade-off between the length of the beam and

the thermal conduction coefficient. Several materials have been ranked based on work density in Table C.8. More material considerations can be found in Jonsmann et al [69].

For polysilicon and polyimide, the two most often used expander materials, beams have been dimensioned to characterize the performance. The polysilicon beam dimensions were varied from 0.5 x 2 x 50 μm^3 to 10 x 40 x 1000 μm^3 (h x w x l_o) at a maximum temperature difference of 600°C. The polyimide beam dimensions were varied from 1 x 2 x 70 μm^3 to 20 x 40 x 1400 μm^3 (h x w x l_o), at a maximum temperature difference of 150°C. The characteristics have been plotted in Figures C.8, C.9 and C.10.

Symbol	E_y	α	Cp	ρ	λ	ΔT	$E\,\alpha^2\,\Delta T\,\lambda^{-1}$	$E\,\alpha^2\,\Delta T^2$	$C_p\,\rho\,\lambda^{-1}$
Unit	N m^{-2}	K^{-1}	J kg^{-1} K^{-1}	kg m^{-3}	W m^{-1} K^{-1}	K	s m^{-2}	J	s m^{-2}
	x10^9	x10^{-6}					$\sim W\,P_d^{-1}$	$\sim W\,V^{-1}$	$\sim\tau$
Mercury*	25	182	140	13500	8.4	300	3.0 10^4	7.5 10^7	2.3 10^5
PolyImide	2.5	55.0	2000	1420	0.16	250	1.2 10^4	4.7 10^5	1.8 10^7
Manganese	191	23.0	477	7400	7.81	600	7.8 10^3	3.6 10^7	4.5 10^5
Zink	93	29.7	390	7140	116	300	2.1 10^2	7.4 10^6	2.4 10^4
Nickel	196	12.7	460	8890	92	600	2.1 10^2	1.1 10^7	4.4 10^4
SiliconNitride	3.23	2.8	700	3100	19	600	8.0 10^1	9.1 10^5	1.1 10^5
Aluminum	70	23.2	899	2700	237	500	7.9 10^1	9.4 10^6	1.0 10^4
Copper	124	16.8	390	8960	390	600	5.4 10^1	1.3 10^7	9.0 10^3
SiliconOxide	73	0.55	1000	2300	1.4	600	9.5	7.9 10^3	1.6 10^6
Chroom	25	7.0	450	7190	87	600	8.4	4.4 10^5	3.7 10^4
Silicon	160	2.6	700	2400	157	600	4.1	3.9 10^5	1.1 10^4

Table C.8: Material properties ranked by work density at a similar temperature change. For mercury, the Bulk modulus instead of the Young's modulus is used.

It must be pointed out that liquids like mercury and paraffin potentially perform well. Carlen et al [20] demonstrates two designs, both capped by parylene, containing paraffin as expansion material.

CONCLUSION REGARDING THERMAL ACTUATORS

Polyimide thermal actuators are attractive because of their moderate work density and heat generation, if slow speed is not important. Silicon thermal actuators possess a larger work density, if high temperatures are tolerable. They are much faster than polyimide thermal actuators, but also dissipate much more. This dissipation is present at static force delivery also. For precision manipulation, thermal actuators are difficult to use because of the inherent lack of position stability they cause.

C.6 Steppers

In MEMS, stepper actuators are shown based on piezo, electrostatic and thermal actuators. The steppers convert a small actuator displacement into a large displacement, often generating a large force as well. Sarajlic [113] demonstrates a shuffle motor which has a maximum achieved travel range of ± 70 μm and a maximum output force of 1.7 mN at 55 V. The motor was operated for 5 days at a stepping frequency of 80 kHz and traveled a cumulative distance of more than 1500 m in 34×10^9 steps without observable deterioration in performance. Ebefors et al [42] fabricated and tested a micro-robotic conveyance system, comprising polyimide joint actuators using electrical heating. The chip dimensions are 15 x 5 mm^2, the maximum payload was 35 mN, velocities were tested up to 12 mm/s and 2×10^8 cycles were tested. Pai et al [99] describe an electrothermal vibromotor intended for optical bench applications. The slide can travel up to 10.2 mm/s with a 12 V square wave signal at 10.5 kHz. Livermore et al [88] show the possibility of an electrostatic induction motor generating several watts by calculation, and achieved a generation of 20 mW mechanical power at a rotational speed of 55,000 rpm. Piezo materials can be used for stepper engines also. Ruffieux [109] presents an AlN stepper.

C.7 Conclusion regarding actuation principles for MEMS

The four most relevant actuation principles for MEMS-based precision manipulation designs - piezoelectric, thermal, electrostatic and magnetic actuators - have been analyzed. The scaling factors for three important performance indicators for precision manipulation in MEMS have been derived and are presented in Table C.9. With respect to the scaling of the work output, not much can be concluded. The fact that the work density of electromagnetic actuators scales faster than others presented does not imply that it performs worse than the others. Because of a rapidly decreasing time constant, thermal actuators are interesting at small dimensions. The dissipated power of electromagnetic actuators increases rapidly with size.

Parameter	Electro-magnetic	Electro-static	Piezo	Thermal
Work	**4**	**3**	**3**	**3**
Dissipated power	**3**	-	-	**1**
Time constant	**2**	-	-	**2**

Table C.9: Comparison of analytically derived scaling factors of the four most common MEMS-based actuator types.

New in this research is that the actuators have been evaluated in more detail by presenting actuator designs. By using designs, physical and practical limitations have been taken into account. The volume necessary to create the total actuator has been estimated. This is important because, with regard to the electrostatic and electromagnetic actuator, this volume is much larger than the volume containing the field. The designs have been used to calculate the work density (Figure C.8), the dissipation (Figure C.9) and the time constant (Figure C.10).

Based on work density a ranking of the actuators can be made. However, many drawbacks and complications need to be taken into account. The largest work density is demonstrated by ***PZT piezoelectric actuators***. A 0.3 µm "thick" PZT layer generates the same work as a 40 µm thick lateral comb-drive with the same device area. PZT, however, is difficult to integrate in MEMS devices. The small stroke usually requires a stroke amplification mechanism storing the majority of the input energy. ***AlN piezoelectric actuators*** are useful for small displacement, large force applications only. Because of the small dissipation they are specifically suitable for applications requiring low self-heating for high frequency applications. In thermal actuator design an inherent paradox is represented by the amount of heat conduction. Large heat conduction leads to small time constants and much dissipation, small heat conduction lead to large time constants and little dissipation. The dissipation is present at static force delivery also. ***Polyimide thermal actuators*** are attractive because of the moderate work density at moderate temperature differences, if slow speed is not important. ***Si thermal actuators*** possibly possess a larger work density if large temperature differences are tolerable. They are much faster than polyimide thermal actuators, but also dissipate much more. Thermal actuators are not ideal for precision manipulation because of the inherent lack of

position stability. ***Electromagnetic actuators*** with a permanent magnet incorporated in a surface micro machining process lack sufficient work density. Electromagnetic actuators for MEMS appliances are interesting if an assembled external macro magnet is used. The total volume, however, is large in that case. ***Transverse comb-drive electrostatic actuators*** are particularly good for latching, because the force builds up enormously when the gap between two parallel plates is closed. However, they are surpassed by comb-drive actuators when it comes to fine positioning. ***Lateral comb-drive electrostatic actuators*** combine moderate force and displacement. The fabrication by DRIE technology is becoming more and more standard. However, large voltages are needed for significant force. Overall, there is no obvious winning actuator principle. Depending on the various demands, a trade-off needs to be made.

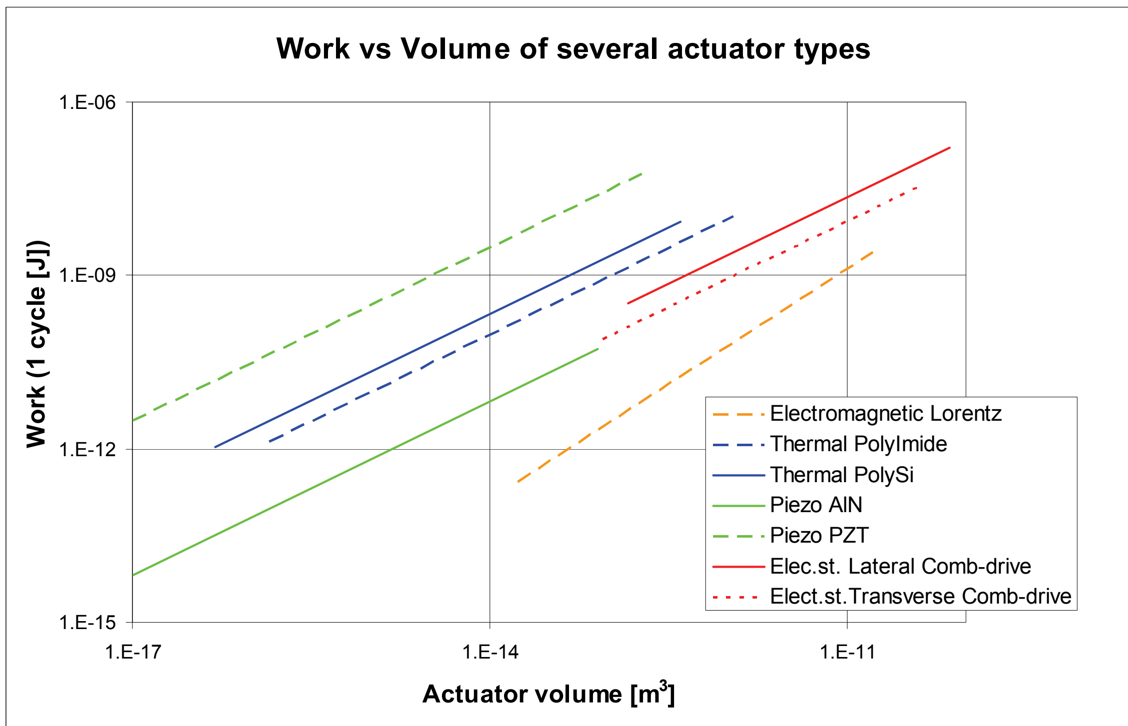

Figure C.8: Work versus Volume of several MEMS-based actuator types.

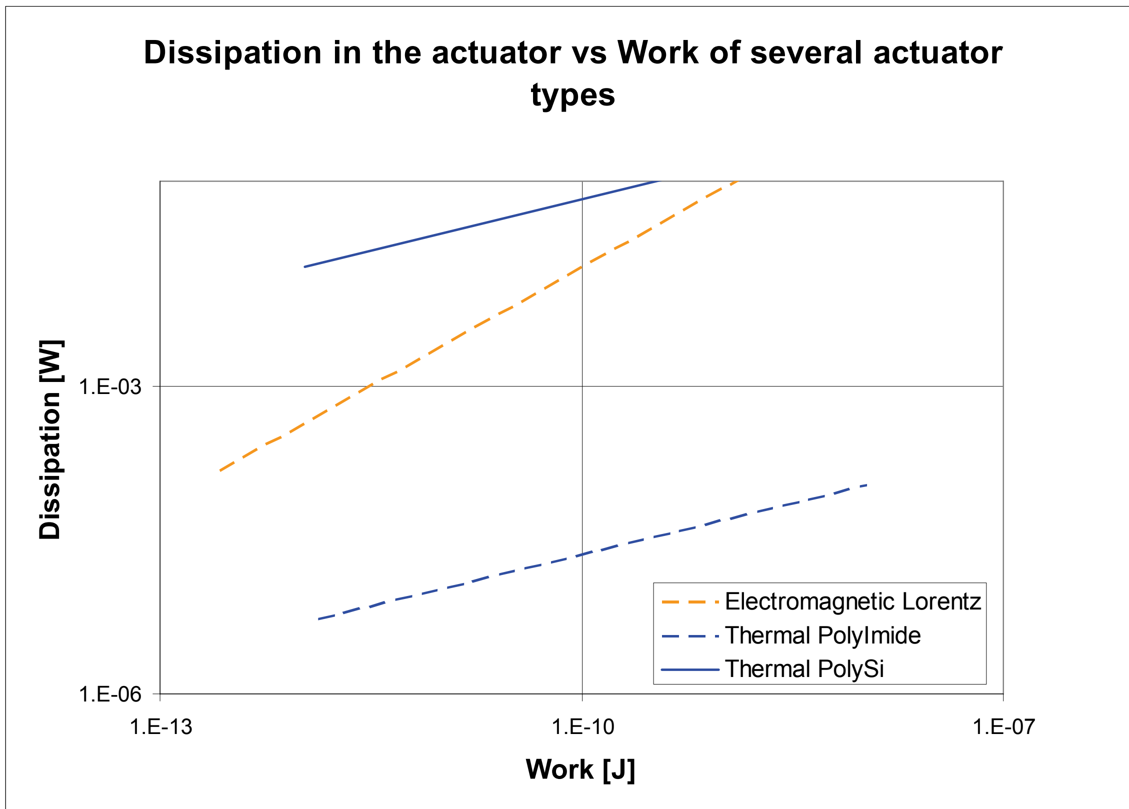

Figure C.9: The dissipation in the actuator of several MEMS-based actuator types.

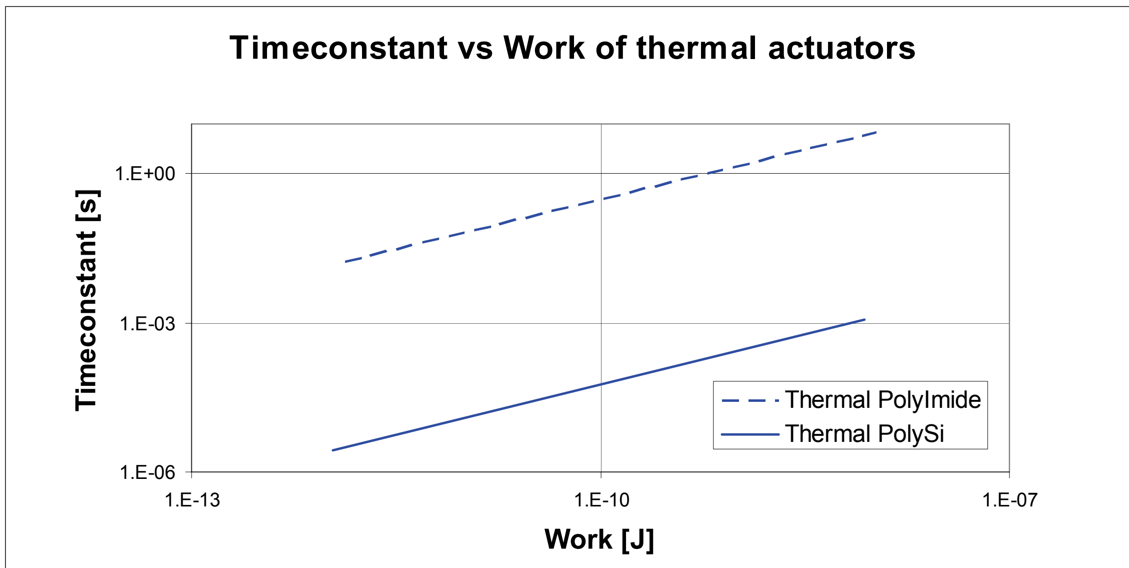

Figure C.10: The time constant of thermal MEMS-based actuators.

OUTLOOK

At present, fabricated MEMS actuators show relatively low work output. There are several options to increase the work output of MEMS-based actuators in the future. However, the ***electrostatic comb-drive*** design is difficult to improve much by design or by fabrication technology. Decreasing the mask feature size, for example, does not help to improve the work density. Increasing the aspect ratio of etching improves the comb-drive actuator (slightly) by making higher structures possible. Although this does not increase the work density, the work obtained from a certain (usually large) suspended device area becomes larger. Furthermore, the comb-drive as presented in this thesis, is designed close to several physical limits. Therefore, not much improvement can be expected in the future. Although not taken into account in this research, the suspension, especially for large strokes, can be improved (see section 2.5.4). The only electrostatic based actuator principle that shows large work density is the electrostatic stepper. ***Thermal actuators*** are difficult to improve. The designs are optimized and the material properties can not be significantly improved. The trade-off between the time constant and the dissipation can be improved by controlling the heat conduction. This requires a heat flux path that can be controlled, whether in contact or not, with the heated medium. Although this is possible, it complicates the design considerably. ***PZT piezo actuators*** are difficult to integrate in MEMS devices. If the fabrication technology of PZT is improved, the actuator work in MEMS will be greatly increased. Improving the ***electromagnetic actuator*** design by using improved fabrication technology does not lead to significantly more work density.

In conclusion, the demand for higher work density actuators requires new actuation principles, or electrostatic steppers, which can be manufactured in a straightforward way, or PZT piezo actuators whose fabrication technology shows improved compatibility.

APPENDIX D

SCALING OF FLUX DENSITY

The flux density of a magnetic circuit created by a coil is derived and compared to the flux density created by a permanent magnet. Based on scaling factors, a conclusion will be presented regarding a magnetic circuit in the micro domain.

MAGNETIC CIRCUIT CREATED BY A COIL

Any time-varying electric field generates a circulating magnetic field according to Maxwell:

$$\oint_{C_m} \underline{H} \cdot \underline{\tau}_m dC_m = \oiint_{A_m} \underline{J} \cdot \underline{n}_m dA_m + \frac{d}{dt} \oiint_{A_m} \underline{D} \cdot \underline{n}_m dA_m \qquad \text{(D.1)}$$

where:

Symbol	Unit	Description
H	Am^{-1}	Magnetic field strength
C_m	m	Contour
J	Am^{-2}	Current density
A_m	m^2	Cross-sectional area
D	Asm^{-2}	Electrical displacement
τ_m	-	Unity tangent
n_m	-	Unity normal

The electrical displacement $\underline{D}$ and the flux leakage are neglected. Assume $\underline{H}$ is in the same direction as unity tangent $\underline{\tau}_m$.

$$B = \mu H \qquad \text{(D.2)}$$

$$B\ A = \phi_C \qquad \text{(D.3)}$$

results in Hopkinson's law:

$$\phi_C \oint_{C_m} \frac{dC_m}{\mu A} = Ni \tag{D.4}$$

where:

Symbol	Unit	Description
B	T	Flux density
μ	TmA^{-1}	Permeability
ϕ_c	Tm^2	Flux
N	-	Number of windings
i	A	Current
A	m^2	Cross-sectional area

If the contour can be divided into k discrete segments:

$$\oint \underline{H} d\underline{l} = \sum_{j=1}^{k} Hl_j = Ni \tag{D.5}$$

A magnetic field is source free according to Maxwell:

$$\oiint_A \underline{B} \cdot \underline{n} da = \sum_{j=1}^{k} A_j B_j = 0 \tag{D.6}$$

If one assumes that the cross-sectional area A is constant in the magnetic circuit, there is no flux leakage and the circuit consists of a finite number k elements of length l_j and permeability μ_j, the flux density B_{coil} becomes:

$$B_{coil} = \frac{Ni}{\sum_{j=1}^{k} \frac{l_j}{\mu_j}} = \frac{N\ J\ A}{\sum_{j=1}^{k} \frac{l_j}{\mu_j}} \sim r_J\ r^1 \tag{D.7}$$

where r is a scaling factor as explained in the section on scaling in paragraph 2.2. $N{\cdot}A \sim r^2$, and r_J is the scaling factor of J. The flux density B_{coil}, of a magnetic circuit created by a coil thus depends on the scaling of the current density J.

MAGNETIC CIRCUIT CREATED BY A PERMANENT MAGNET

For a system with a permanent magnet, without a current conducting coil the flux density equation D.5 becomes:

$$\oint \underline{H} d\underline{l} = 0 \tag{D.8}$$

$$H_m l_m + \sum_{j=1}^{k} H_j l_j = 0 \tag{D.9}$$

where H_m is the magnetic field strength in the magnet and l_m is the length of the magnet. Equation D.6 becomes:

$$A_m B_m - \sum_{j=1}^{k} A_j B_j = 0 \tag{D.10}$$

where B_m is the flux density in the magnet. The load-line equation of the circuit becomes:

$$B_m = -\mu_0 \frac{\sum_{j=1}^{k} A_j l_j}{A_m l_m} H_m \tag{D.11}$$

To find the operating point of the magnet in the circuit, the demagnetization curve of the magnet has to be in equilibrium with the load line:

$$B_m = \mu_0 H_m + B_r \tag{D.12}$$

where B_r is the remanent flux density of the magnet, which does not scale. If the cross-sectional area is constant, the flux density in the gap is:

$$B_{PM} = \frac{l_m}{\sum_{j=1}^{k} l_j + l_m} B_r \sim r^0 \tag{D.13}$$

The magnetic flux density created by a circuit containing a permanent magnet scales by r^0. When comparing equation D.7 with equation D.13, it depends on the scaling of the current density if a coil driven or a permanent magnet driven circuit is advantageous in the micro domain. In the macro world the heat flow is dominated by convection, natural or forced, leading to $J \sim r^{-0.5}$. In the micro world the heat

flow is often dominated by conduction. The current density is then limited by electromigration, leading to $J \sim r^0$, as the temperature rise due to heat flow is relatively small and usually not limiting the current density. Depending on the design, it is possible that in a transition area going from micro to macro sizes the heat flow is dominated by conduction and is also limited by the temperature rise due to conductive heat flow. Electronmigration will not limit the current density then. In that case $J \sim r^{-1}$. However, in all cases the scaling of the flux density of a magnet driven circuit is advantageous in the micro domain. Conversely, the scaling of the flux density of a coil driven system is advantageous in the macro domain. The transition from coil to magnet depends on the design and the fabrication techniques.

APPENDIX E

THERMAL CONDUCTION IN A MEMS LORENTZ ACTUATOR

For the accurate modeling of the heat flow by conduction and the resulting temperature rise in the coil shown in Figure C.1, a 3D finite element analysis is required. However, the goal of this appendix is merely to show that the heat flow on a micro scale for a design like the one presented in Figure C.1 is governed by conduction. In the following calculation, the temperature rise displayed by the coil will be assumed to be negligible for now and therefore electromigration limits the current density. At the end of the appendix this assumption will be checked. A rough steady-state 1D model which overestimates the coil temperature due to heat generation will suffice for these purposes.

The aluminum coil shown in Figure C.1 is stationary and directly attached to the silicon substrate wafer. The coil of the Lorentz actuator is heated by the current it conducts. The generated heat is assumed to be uniformly distributed across the coil. The temperature variation in the coil is assumed to be 1 dimensional, only in the z-direction. The resistive heating of the coil is represented by the heat q in Figure E.1. T_c is the temperature at the top of the coil, T_i is the temperature at the interface of the coil and substrate, and T_{amb} is the ambient temperature. The heat is assumed to flow from the top of the coil down to the interface and further down to the bottom of the substrate. Heat distribution to the sides of the substrate is neglected. This is an overestimation of the thermal resistance, and therefore the temperature rise is also overestimated. The bottom of the substrate is assumed to have the ambient temperature. All material properties are assumed to be constant.

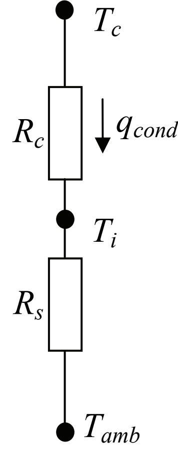

Figure E.1: 1-dimensional thermal conduction model for evaluating the temperature rise of the coil of a Lorentz actuator.

The total heat put into the coil is:

$$P_d = \rho_e J^2 V_c \tag{E.1}$$

where P_d is the dissipated power, ρ_e is the specific electrical resistance of the coil, J is the current density and V_c is the total coil volume. The thermal coil resistance for the model presented in Figure E.1can be written as:

$$R_c = \frac{c_c}{\lambda_c A_c} \tag{E.2}$$

where R_c is the thermal resistance of the coil, c_c is the height of the coil as shown in Figure C.1, λ_c is the thermal conductance, and A_c is the coil area perpendicular to the heat flow. The thermal resistance of the substrate can be written as:

$$R_s = \frac{c_s}{\lambda_s A_s} \tag{E.3}$$

The steady state temperature resulting from heat transport by conduction is found by the equation $q_{cond} = P_d$.The coil temperature is then given by:

$$T_c = q_{cond}\left(R_c + R_s\right) + T_{amb} \tag{E.4}$$

In Table E.1, the dimension and material properties of the coil and substrate are listed. The current density of the coil is set at 10^9 A/m^2, which is the electron

migration limit for micron sized aluminum current conductors as given by Sirinvasan [123]. The temperature rise is numerically calculated for the smallest and largest MEMS-based Lorentz actuator design shown in Figure C.1.

		small MEMS actuator	large MEMS actuator
c_c	m	3.00E-06	3.00E-05
A_c	m^2	3.40E-09	1.31E-07
V_c	m^3	1.02E-14	3.93E-12
c_s	m	5.00E-04	5.00E-04
A_s	m^2	3.40E-09	1.31E-07
ρ_c	Ω m	2.70E-08	2.70E-08
λ_c	W/(m k)	2.37E+02	2.37E+02
λ_s	W/(m k)	1.57E+02	1.57E+02
J	A/m^2	1.00E+09	1.00E+09
conduction			
q_{cond}	W	2.75E-04	1.06E-01
R_c	K/W	3.72E+00	9.66E-01
R_s	K/W	9.37E+02	2.43E+01
T_c-T_{amb}	K	2.59E-01	2.68E+00
convection			
h_c	$W/(m^2K)$	1.15E+01	1.31E+01
q_{conv}	W	1.01E-08	4.60E-06

Table E.1: Temperature rise in a small and large MEMS-based Lorentz actuator design.

Since the heat conduction through the aluminum coil and silicon substrate is good, the generated heat does not cause a significant rise in temperature. Therefore, the current density is limited by electromigration and not by the temperature rise caused by heat conduction.

With the calculated temperature difference it is possible to check if the heat flow by convection is much smaller than by conduction. CTT [31] derived formulas based on average measurement results mentioned in the literature. The convection coefficient can be estimated for the top side of a horizontal plate for laminar flow by:

$$h_c = 1.41\left(\frac{T_c - T_{amb}}{\sqrt{A_c}}\right)^{0.25} \tag{E.5}$$

where $\sqrt{A_c}$ is a characteristic dimension of the heated horizontal surface. The convection coefficient is calculated for the two differently dimensioned designs given in Table E.1. Based on this convection coefficient the heat flow by convection is calculated:

$$q_{conv} = \left(T_c - T_{amb}\right) h_c \; A_c \tag{E.6}$$

In Table E.1, the heat flow by convection is calculated for the given temperature difference. The assumption is that the convection does not influence the total heat flow. The heat flow by convection is at least 4 orders of magnitude smaller than the heat flow by conduction. Therefore, heat flow is governed by conduction.

CONCLUSIONS

- Heat flow is governed by conduction
- Electromigration limits the current density

These conclusions might not hold true for coils suspended by a compliant mechanism. In that case, the long and slender beams become a restriction for the heat to flow through and therefore the temperature might rise much more depending on the design.

APPENDIX F

MULTIBODY SYSTEMS MODELED BY FINITE ELEMENTS

Multibody systems with deformable bodies may well be modeled by finite elements. This nonlinear finite element approach was initiated in the 1970s by Besseling [7] and has been developed further by, amongst others, Van der Werff [135, 136], Jonker [65, 66, 68], Géradin and Cardona [53, 19], Meijaard [94] and Schwab [117]. The distinguishing point in this finite element approach is the specification of independent deformation of the finite elements, the so-called generalized deformations. These are the algebraic equivalent of the continuous field description of deformations. Rigid body motions are displacements for which the generalized deformations are zero. If the specification of the generalized deformations remains valid for arbitrary large translations and rotations, then flexible multibody systems can also be analyzed by setting the generalized deformation associated with rigid elements at zero. The deformation equations are the constraint equations which express the rigidity of the elements. Deformable bodies are handled by allowing non-zero deformations and specifying constitutive equations for the generalized stress, which are the duals of the generalized deformations. The formulation accounts for geometric nonlinear effects of flexible elements due to axial and transverse modal displacements. The method is applicable for flexible multibody systems as well as for flexible structures in which the system members experience only relatively small displacement motions and elastic deformations with respect to an equilibrium position. With the use of a rather limited number of elements types it is possible to model a wide class of flexible multibody systems. Typical elements are beam, truss and hinge elements. The computer program SPACAR [67] is based on the abovementioned finite element theory for multi-degree of freedom mechanisms. Recently a linearized state-space formulation [68] for flexible multibody systems is developed in which an arbitrary combination of positions, velocities, accelerations and forces can be taken as input variables and as output variables.

SPACAR is able to model relatively large deflection behavior of leaf-springs with a small number of elements quickly and accurately. For the calculations made in this thesis, 3 beam elements proved sufficiently accurate to model 1 leaf-spring.

APPENDIX G

PROCESS DOCUMENT OF THE MANIPULATOR

Step	Process		Comment
1			Fabrication of device wafers
2	**Substrate selection - Silicon <100> DSP** (#subs012)	TST/Boudewijn de Jong (2811) Supplier: Orientation: <100> Diameter: 100mm Thickness: 500µm +/- 10µm Polished: Double side Resistivity: 0.0015-0.019Ωcm Type: p	12 DSP wafers + xx OSP dummy wafers thickness measurement
3	**Wafer thickness measurement** (#char012)	CR112B-1 / LEE-Tool01	500 um
4	**Lithography - Priming (Gamma 60)** (#lith003)	CR117B / Gamma 60 HexaMethylDiSilazane (HMDS)	Manual priming (gas) needed, info Huib
5	**Lithography - Coating Olin907-17 (Gamma 60)** (#lith008)	CR117B / Gamma 60 Olin 907-17 • Program: ???	t4-4k.txt
6	**Lithography - Alignment & Exposure Olin 907-17 (EV)** (#lith021)	CR117B / EVG 20 Electronic Vision Group 20 Mask Aligner • Hg-lamp: 12 mW/cm^2 • Exposure Time: 4sec	Check mask, measure line width for horizontal and vertical trenches. For difference contact Meint mask: trenches, time 3. 2- 3.5 secs

7	**Lithography - Development Olin Resist** (#lith011)	CR112B / Wet-Bench 11 Developer: OPD4262 Hotplate 120°C (CR112B or CR117B) • After Exposure Bake (120°C): 60sec Development: • Time: 30sec in Beaker 1 • Time: 15-30sec in Beaker 2 • Quick Dump Rinse <0.1µS • Spin drying	30+25...30 secs
8	**Optical microscopic inspection - Lithography** (#char001)	CR112B / Nikon Microscope	Measure trench width. (2 microns)
9	**Plasma etching of Si BOSCH-ADIX** (# ID etch056)	CR125c/Adixen SE See for profile downloads on the mishomepage **Parameters** / **Etch** / **Deposition** Gas / SF6 / C4F8 Flow sccm / 300 / 150 Time sec / 7 / 2 Priority / 2 / 1 APC % / 25 / 25 ICP Watt / 1800 / 1800 CCP Watt [LF] / 80 / 80 Pulsed (LF) ms. / 10on/90off / 10on/90 off He mBar / 10 / 10 SH mm / 200 / 200 Electrode temp.°C. / 10 / 10 Er Olin907 / 25-50 nm/min Er silicon / 3-5 µm/min	Apply first test run check etch depth and directional profile. Detpth = 40 microns.
10	**Optical microscopic inspection - Lithography** (#char001)	CR112B / Nikon Microscope	Measure depth, width and check profile (dummy wafer)
11	**Stripping of polymers in HNO_3 multipurpose** (#lith014)	CR116B / Wet-Bench 2 HNO_3 (100%) Selectipur: MERCK 100453 • Beaker 1: HNO_3 (100%) 20min • Quick Dump Rinse <0.1µS • Spin drying	stripping time > 20 min
12	**Optical microscopic inspection** (#char002)	CR112B / Nikon Microscope CR117B / Olympus Microscope CR102B / Olympus Microscope	check wafers on Pr residue.

13	**Cleaning Standard** (#clean003)	CR112B / Wet-Bench 3-2 HNO_3 (100%) Selectipur: MERCK 100453 HNO_3 (69%) VLSI: MERCK 116445 • Beaker 1: fumic HNO_3 (100%), 5min • Beaker 2: fumic HNO_3 (100%), 5min • Quick Dump Rinse <0.1µS • Beaker 3: boiling (95°C) HNO_3 (69%), 10min • Quick Dump Rinse <0.1µS • Spin drying	
14	**Dry Oxidation (DOX) at 800°C of Silicon** (#depo026)	CR112B / Furnace B3 Standby temperature: 800°C • Program: DOX-800 • Temp.: 800°C • Gas: O_2 • Flow: 4l/min	30 min FC-removal
15	**Etching HF (50%) LPCVD SiN or Thermal oxide** (#etch029)	CR112B / Wet-Bench 3-3 HF (50%) VLSI: MERCK 100373.2500 • Quick Dump Rinse <0.1µS • Spin drying Etchrate SiRN = 5nm/min Etchrate SiO_2 = 1 µm/min	Important for good mechanical connection between silicon and nitride. strip time = 2 minutes,
16	**Optical microscopic inspection** (#char002)	CR112B / Nikon Microscope CR117B / Olympus Microscope CR102B / Olympus Microscope	Measure trench width again. Widthdetermines Nitride deposition time in step 160 and 190
17	**Cleaning Standard** (#clean003)	CR112B / Wet-Bench 3-2 HNO_3 (100%) Selectipur: MERCK 100453 HNO_3 (69%) VLSI: MERCK 116445 • Beaker 1: fumic HNO_3 (100%), 5min • Beaker 2: fumic HNO_3 (100%), 5min • Quick Dump Rinse <0.1µS • Beaker 3: boiling (95°C) HNO_3 (69%), 10min • Quick Dump Rinse <0.1µS • Spin drying	
18	**Etching HF (1%) Native Oxide** (#etch027)	CR112B / Wet-Bench 3-3 HF (1%) VLSI: MERCK 112629.500 • Etch time: >1min • Quick Dump Rinse <0.1µS • Spin drying	2min, removal of native oxide

19	**LPCVD SiRN - low stress** (#depo002)	CR125C / Tempress LPCVD/HC Tube: G2 SiH_2Cl_2 flow: 70sccm NH_3 flow: 18sccm temperature: 850°C pressure: 200mTorr • program: SiRN deposition rate: 7.3 nm/min N_f: 2.14	Thickness: 0.8 micron SiRN; 2:15 hr. Cleave dummy, inspect cross-section and make picture
20	**Plasma etching of Quartz - SF_6 (Plasma Therm)** (#etch019)	CR102A / Plasma Therm SLR 770 Parameters are valid for 100mm wafer Use quartz cover plates for long runs (>>30min) to avoid resputtering of ALOx particles **Parameters** — **Value** SF_6 [sccm] — 30 Ar [sccm] — 60 He-backside cooling [sccm] — 9 He-backside cooling [Torr] — 6 ICP [W] — 1200 CCP [W] — 18 V_{DC} [V] — 114 p [mTorr] — 5 Temp. Chiller [°C] — 25 Temp. LN_2 [°C] — 20 **Material** — **Etch [nm/min]** Fused silica (use Cr or Ni as mask material) — ? Olin907 using LN_2=20°C — >330 Silicon Rich Nitride (SiRN) — 240 Poly-Silicon 590°C — >750 Mono-Crystal-Silicon 10Ωcm — ? SiO_2 (PECVD/TEOS) — 200-210	strip 90 % of front + backside nitride layer
21	**Plasma etching SiN (Etske)** (#etch004)	CR102A / Elektrotech PF310/340 Dirty chamber Styros electrode • Electrode temp.: 10°C • CHF_3 flow: 25sccm • O_2 flow: 5sccm • pressure: 10mTorr • power: 75W Etchrate SiN = 50nm/min (for V_{DC}=-460V) Etchrate Olin resist = 95nm/min If DC-Bias < 375V apply chamber clean (#etch003)	Strip front and backside(first backside), an overetch is needed to create a good mechanical connection at the top of the trench.

22	**Cleaning Standard** (#clean003)	CR112B / Wet-Bench 3-2 HNO_3 (100%) Selectipur: MERCK 100453 HNO_3 (69%) VLSI: MERCK 116445 • Beaker 1: fumic HNO_3 (100%), 5min • Beaker 2: fumic HNO_3 (100%), 5min • Quick Dump Rinse <0.1µS • Beaker 3: boiling (95°C) HNO_3 (69%), 10min • Quick Dump Rinse <0.1µS • Spin drying	
23	**Dry Oxidation (DOX) at 800°C of Silicon** (#depo026)	CR112B / Furnace B3 Standby temperature: 800°C • Program: DOX-800 • Temp.: 800°C • Gas: O_2 • Flow: 4l/min	removal of FC, needed for good connection between nitride layers
24	**Etching HF (1%) Native Oxide** (#etch027)	CR112B / Wet-Bench 3-3 HF (1%) VLSI: MERCK 112629.500 • Etch time: >1min • Quick Dump Rinse <0.1µS • Spin drying	removal of native oxide !
25	**LPCVD SiRN - low stress** (#depo002)	CR125C / Tempress LPCVD/HC Tube: G2 SiH_2Cl_2 flow: 70sccm NH_3 flow: 18sccm temperature: 850°C pressure: 200mTorr • program: SiRN deposition rate: 7.3 nm/min N_f: 2.14	1.6 mu (depending on cross-section) +/- 3hr,
26	**Optical microscopic inspection - Lithography** (#char001)	CR112B / Nikon Microscope	use dummy to check nitride fill
27	**Cleaning Standard** (#clean003)	CR112B / Wet-Bench 3-2 HNO_3 (100%) Selectipur: MERCK 100453 HNO_3 (69%) VLSI: MERCK 116445 • Beaker 1: fumic HNO_3 (100%), 5min • Beaker 2: fumic HNO_3 (100%), 5min • Quick Dump Rinse <0.1µS • Beaker 3: boiling (95°C) HNO_3 (69%), 10min • Quick Dump Rinse <0.1µS • Spin drying	optional

<table>
<tr><td>28</td><td>Plasma etching of Quartz - SF_6 (Plasma Therm)
(#etch019)</td><td>CR102A / Plasma Therm SLR 770
Parameters are valid for 100mm wafer
Use quartz cover plates for long runs (>>30min) to avoid resputtering of ALOx particles

Parameters — Value
SF_6 [sccm] — 30
Ar [sccm] — 60
He-backside cooling [sccm] — 9
He-backside cooling [Torr] — 6
ICP [W] — 1200
CCP [W] — 18
V_{DC} [V] — 114
p [mTorr] — 5
Temp. Chiller [°C] — 25
Temp. LN_2 [°C] — 20

Material — Etch [nm/min]
Fused silica (use Cr or Ni as mask material) — ?
Olin907 using LN_2=20°C — >330
Silicon Rich Nitride (SiRN) — 240
Poly-Silicon 590°C — >750
Mono-Crystal-Silicon 10Ωcm — ?
SiO_2 (PECVD/TEOS) — 200-210</td><td>etch front + backside, 90 % of layer</td></tr>
<tr><td>29</td><td>Plasma etching SiN (Etske)
(#etch004)</td><td>CR102A / Elektrotech PF310/340
Dirty chamber
Styros electrode
• Electrode temp.: 10°C
• CHF_3 flow: 25sccm
• O_2 flow: 5sccm
• pressure: 10mTorr
• power: 75W
Etchrate SiN = 50nm/min (for V_{DC}=-460V)
Etchrate Olin resist = 95nm/min
If DC-Bias < 375V apply chamber clean (#etch003)</td><td>etch front + backside and stop on silicon</td></tr>
<tr><td>30</td><td>Cleaning Standard
(#clean003)</td><td>CR112B / Wet-Bench 3-2
HNO_3 (100%) Selectipur: MERCK 100453
HNO_3 (69%) VLSI: MERCK 116445
• Beaker 1: fumic HNO_3 (100%), 5min
• Beaker 2: fumic HNO_3 (100%), 5min
• Quick Dump Rinse <0.1µS
• Beaker 3: boiling (95°C) HNO_3 (69%), 10min
• Quick Dump Rinse <0.1µS
• Spin drying</td><td></td></tr>
</table>

31	**LPCVD SiRN - low stress** (#depo002)	CR125C / Tempress LPCVD/HC Tube: G2 SiH_2Cl_2 flow: 70sccm NH_3 flow: 18sccm temperature: 850°C pressure: 200mTorr • program: SiRN deposition rate: 7.3 nm/min N_f: 2.14	300 nm layer, mask for KOH
32	**Lithography - Priming (Gamma 60)** (#lith003)	CR117B / Gamma 60 HexaMethylDiSilazane (HMDS)	backside, use manual priming (gas), info Huib
33	**Lithography - Coating Olin907-17 (Gamma 60)** (#lith008)	CR117B / Gamma 60 Olin 907-17 • Program: ???	backside
34	**Lithography - Alignment & Exposure Olin 907-17 (EV)** (#lith021)	CR117B / EVG 20 Electronic Vision Group 20 Mask Aligner • Hg-lamp: 12 mW/cm ^{2} • Exposure Time: 4sec	mask: backside KOH etching, use programm first mask load , split-up batch??
35			Is Vangbo procedure needed (Y/N) Ask Erwin
36	**Lithography - Development Olin Resist** (#lith011)	CR112B / Wet-Bench 11 Developer: OPD4262 Hotplate 120°C (CR112B or CR117B) • After Exposure Bake (120°C): 60sec Development: • Time: 30sec in Beaker 1 • Time: 15-30sec in Beaker 2 • Quick Dump Rinse <0.1µS • Spin drying	
37	**Lithography - Postbake standard** (#lith009)	CR112B / Hotplate 120°C • Time: 30min	
38	**Plasma etching SiN (Etske)** (#etch004)	CR102A / Elektrotech PF310/340 Dirty chamber Styros electrode • Electrode temp.: 10°C • CHF_3 flow: 25sccm • O_2 flow: 5sccm • pressure: 10mTorr • power: 75W Etchrate SiN = 50nm/min (for V_{DC}=-460V) Etchrate Olin resist = 95nm/min If DC-Bias < 375V apply chamber clean (#etch003)	During nitride etch the edge of the wafer should be proctected by kapton foil (orange). The the wafer is than less fragile after KOH.

39	**Stripping of polymers in HNO_3 multipurpose** (#lith014)	CR116B / Wet-Bench 2 HNO_3 (100%) Selectipur: MERCK 100453 • Beaker 1: HNO_3 (100%) 20min • Quick Dump Rinse <0.1µS • Spin drying	Check if resist is stripped
40	**Cleaning Standard** (#clean003)	CR112B / Wet-Bench 3-2 HNO_3 (100%) Selectipur: MERCK 100453 HNO_3 (69%) VLSI: MERCK 116445 • Beaker 1: fumic HNO_3 (100%), 5min • Beaker 2: fumic HNO_3 (100%), 5min • Quick Dump Rinse <0.1µS • Beaker 3: boiling (95°C) HNO_3 (69%), 10min • Quick Dump Rinse <0.1µS • Spin drying	
41	**Etching HF (1%) Native Oxide** (#etch027)	CR112B / Wet-Bench 3-3 HF (1%) VLSI: MERCK 112629.500 • Etch time: >1min • Quick Dump Rinse <0.1µS • Spin drying	
42	**Etching of Silicon by KOH - standard** (#etch038)	CR102B / KOH KOH: MERCK 105019.500 KOH:DI = (1:3) 25wt% KOH: 500g KOH pellets in 1500ml DI water • Temp.: 75°C • Stirrer • Quick Dump Rinse <0.1µS • Spin drying Etchrates: Si <100> = 1µm/min Si <111> = 12.5nm/min SiO_2 (thermal) = 180nm/hr SiRN < 0.6nm/hr	Membrane thickness: ca. 40 microns Trench depth ca.40 microns KOH depth ca, 460 micron. time based on <100> beam structures. Check membrane surface where iso-structures appear.
43	**Cleaning RCA-2 ($HCL/H_2O_2/H_2O$)** (#clean007)	CR102A / Wet-Bench 9 HCL (32%) Selectipur: MERCK 100322.2500 H_2O_2 (31%) VLSI: MERCK 108552.2500 Only use the dedicated wafer carriers and glass rod! $HCL:H_2O_2:H_2O$ (1:1:5) vol% • add HCL to H_2O • add H_2O_2 when mixure at 70°C • temperature 70-80°C • cleaning time 10-15min • Quick Dump Rinse <0.1µS • Spin drying	

44	**Plasma etching SiN (Etske)** (#etch004)	CR102A / Elektrotech PF310/340 Dirty chamber Styros electrode • Electrode temp.: 10°C • CHF_3 flow: 25sccm • O_2 flow: 5sccm • pressure: 10mTorr • power: 75W Etchrate SiN = 50nm/min (for V_{DC}=-460V) Etchrate Olin resist = 95nm/min If DC-Bias < 375V apply chamber clean (#etch003)	strip SiRN on front- and backside
45	**Cleaning Standard** (#clean003)	CR112B / Wet-Bench 3-2 HNO_3 (100%) Selectipur: MERCK 100453 HNO_3 (69%) VLSI: MERCK 116445 • Beaker 1: fumic HNO_3 (100%), 5min • Beaker 2: fumic HNO_3 (100%), 5min • Quick Dump Rinse <0.1µS • Beaker 3: boiling (95°C) HNO_3 (69%), 10min • Quick Dump Rinse <0.1µS • Spin drying	
46	**LPCVD TEOS** (#depo004)	CR112B / Tempress LPCVD Tube: B4-TEOS Bubbler: 40.0°C Temperature: 700°C pressure: 400mTorr • program: TEOS02 deposition rate: 7-13 nm/min N_f: ??	thickness 1.5 micron, = buried mask for device on frontside and SiRN beam protection during thinning of table. add some dummy wafers for DRIE and litho process. Do test for step 680, removal Si and check if oxide is thick enough??
47	**Annealing at 900°C with N_2 for diffusion of B or P** (#anne003)	CR112B / Furnace B3 Standby temperature: 700°C • Program: ANN-900-N2 • Temp.: 900°C • Gas: N_2 • Flow: 1l/min • Ramp: 20°C/min	Outgassing of H2, time 30 min, to avoid cracking of oxide layer and damamge of nitride leaf!
48	**Lithography - Priming (Gamma 60)** (#lith003)	CR117B / Gamma 60 HexaMethylDiSilazane (HMDS)	use manual priming (gas) ask Huib
49	**Lithography - Coating Olin907-17 (Gamma 60)** (#lith008)	CR117B / Gamma 60 Olin 907-17 • Program: ???	t4-4k.txt
50	**Lithography - Alignment & Exposure Olin 907-17 (EV)** (#lith021)	CR117B / EVG 20 Electronic Vision Group 20 Mask Aligner • Hg-lamp: 12 mW/cm^2 • Exposure Time: 4sec	mask: device, check mask !! , time 3. 2- 3.5 secs

51	**Lithography - Development Olin Resist** (#lith011)	CR112B / Wet-Bench 11 Developer: OPD4262 Hotplate 120°C (CR112B or CR117B) • After Exposure Bake (120°C): 60sec Development: • Time: 30sec in Beaker 1 • Time: 15-30sec in Beaker 2 • Quick Dump Rinse <0.1µS • Spin drying	30+25...30 secs
52			Fabrication of substrate wafer with channel structure to avoid breaking of devices wafer during oxide etch in Adixen. See fabrication substrate carrier
53			Coat substrate wafer with fomlin oil. 4000 rpm. 20 sec. Put the device wafer direct after spinning on the substrate wafer. Move the device wafer a little to be sure if the wafers are connected!
54	**Plasma etching of SiO_2** (#etch057	CR 125c/Adixen AMS 100 DE **Parameters** — **Value** C_4F_8 [sccm] — 15 He [sccm] — 150 CH_4 [sccm] — 15 He-backside cooling — 10 ICP [watt] — 2800 CCP [Watt] — 350 p [mbar] — $8.5\ 10^{-3}$ Eelctrode temperature [°C] — 10 Substrate height [mm] — 120 Etch rate SiO2 [µm/min] — 0.470-0.530 Etch rate Olin 907 [µm/min] — ca. 0.05 Etch rate poly-Silicon (µm/min) Etch rate SiRN [µm/min] — ca. 0.1-0.3 variable!	use -20 degreess as substrate temperature to avoid burning of fotoresist
55			Remove the device wafer manually from substrate wafer and clean the wafers with IPA.

56	**Stripping of polymers in HNO_3 multipurpose** (#lith014)	CR116B / Wet-Bench 2 HNO_3 (100%) Selectipur: MERCK 100453 • Beaker 1: HNO_3 (100%) 20min • Quick Dump Rinse <0.1µS • Spin drying	
57	**Optical microscopic inspection - Lithography** (#char001)	CR112B / Nikon Microscope	check if PR is completely removed
58	**Cleaning Standard** (#clean003)	CR112B / Wet-Bench 3-2 HNO_3 (100%) Selectipur: MERCK 100453 HNO_3 (69%) VLSI: MERCK 116445 • Beaker 1: fumic HNO_3 (100%), 5min • Beaker 2: fumic HNO_3 (100%), 5min • Quick Dump Rinse <0.1µS • Beaker 3: boiling (95°C) HNO_3 (69%), 10min • Quick Dump Rinse <0.1µS • Spin drying	
59	**LPCVD SiRN - low stress** (#depo002)	CR125C / Tempress LPCVD/HC Tube: G2 SiH_2Cl_2 flow: 70sccm NH_3 flow: 18sccm temperature: 850°C pressure: 200mTorr • program: SiRN deposition rate: 7.3 nm/min N_f: 2.14	Thickness 0.7 um (tolerance: 0.65-0.75) micron), measure layer thickness.
60			Preparation and aligning of shadow mask
61	**Evaporation of Al (BAK600)** (#depo027)	CR106A / Balzers BAK600 • Crucible: 1 (Aluminium) • Voltage: kV • Emission current: A • Base pressure Density: 2.7 Depositionrate:	deposit a layer thickness 0.3 microns on backside
62			Etske can be used, process ? Or Adixen alla Henrie: SF6 cryo SirN (1:50), for adixen the carrier with fomlin is needed

63	**Plasma etching SiN (Etske)** (#etch004)	CR102A / Elektrotech PF310/340 Dirty chamber Styros electrode • Electrode temp.: 10°C • CHF_3 flow: 25sccm • O_2 flow: 5sccm • pressure: 10mTorr • power: 75W Etchrate SiN = 50nm/min (for V_{DC}=-460V) Etchrate Olin resist = 95nm/min If DC-Bias < 375V apply chamber clean (#etch003)	Etchrate nitride ca. 70 nm/min and for oxide 40 nm/min, overetch of 10 min gives 400 nm oxide removal, which leaves 1.1 micron Teos on backside
64	**Etching of Al Wet** (#etch035)	CR116B / Wet-Bench 2 Aluminium etch: MERCK 115435.2500 • Temp.: 55°C • Quick Dump Rinse <0.1µS • Spin drying Etchrates = 1µm/min	Strip Al om backside, Al layer is coated with AlF3, gives delay in etching process, temperature of solutiuon >55 degrees
65	**Optical microscopic inspection** (#char002)	CR112B / Nikon Microscope CR117B / Olympus Microscope CR102B / Olympus Microscope	check if all Al is stripped
66	**Cleaning Standard** (#clean003)	CR112B / Wet-Bench 3-2 HNO_3 (100%) Selectipur: MERCK 100453 HNO_3 (69%) VLSI: MERCK 116445 • Beaker 1: fumic HNO_3 (100%), 5min • Beaker 2: fumic HNO_3 (100%), 5min • Quick Dump Rinse <0.1µS • Beaker 3: boiling (95°C) HNO_3 (69%), 10min • Quick Dump Rinse <0.1µS • Spin drying	
67	**Plasma etching - chamber cleaning (Etske)** (#etch003)	CR102A / Elektrotech PF310/340 Select chamber for desired etch process Select electrode for desired etch process • Electrode temp.: 10°C or 25°C • O_2 flow: 20sccm • pressure: 50mTorr • power: 150W • DC-Bias: 780V Chamber is clean when plasma color is white	

<table>
<tr>
<td>68</td>
<td>Plasma etching SiN (Etske)
(#etch004)</td>
<td>CR102A / Elektrotech PF310/340
Dirty chamber
Styros electrode
• Electrode temp.: 10°C
• CHF_3 flow: 25sccm
• O_2 flow: 5sccm
• pressure: 10mTorr
• power: 75W
Etchrate SiN = 50nm/min (for V_{DC}=-460V)
Etchrate Olin resist = 95nm/min
If DC-Bias < 375V apply chamber clean (#etch003)</td>
<td>use interfero meter for end-point dectection. The nitride deposited on the vertical walls will stay there, which gives a reduction of the trench width of the comdrive structures! (next time modify mask)</td>
</tr>
<tr>
<td>69</td>
<td>Plasma etching of Si B-ARCE-1
(# ID etch066)</td>
<td>CR125c/Adixen SE
See for etch profile downloads on MIS homepage
<table>
<tr><td>Parameters</td><td>Etch</td><td>Deposition</td></tr>
<tr><td>Gas</td><td>SF6</td><td>C4F8</td></tr>
<tr><td>Flow sccm</td><td>400</td><td>300</td></tr>
<tr><td>Time sec</td><td>5</td><td>2</td></tr>
<tr><td>Priority</td><td>2</td><td>1</td></tr>
<tr><td>APC %</td><td>100</td><td>100</td></tr>
<tr><td>ICP Watt</td><td>1500</td><td>1500</td></tr>
<tr><td>CCP Watt [LF]</td><td>100</td><td>100</td></tr>
<tr><td>Pulsed (LF) ms.</td><td>10on/90off</td><td>10on/90 off</td></tr>
<tr><td>He mBar</td><td>10</td><td>10</td></tr>
<tr><td>SH mm</td><td>200</td><td>200</td></tr>
<tr><td>Electrode temp.°C.</td><td>-10</td><td>-10</td></tr>
<tr><td>Er Olin907 [nm/min]</td><td>???</td><td></td></tr>
<tr><td>Er silicon [µm/min]</td><td>1-5</td><td></td></tr>
</table></td>
<td>Etching of combdrive structures, 35-40 microns depth (less deep than trench depth)and stop on oxide?. Use substrate carrier with channels to proctect wafer</td>
</tr>
<tr>
<td>70</td>
<td>Optical microscopic inspection
(#char002)</td>
<td>CR112B / Nikon Microscope
CR117B / Olympus Microscope
CR102B / Olympus Microscope</td>
<td>Check etch result, overheating of freestanding structures may give extra underetch</td>
</tr>
<tr>
<td>71</td>
<td></td>
<td></td>
<td>Fabrication of shadow mask "two" by KOH, aligin mask on frontside by hand under microscope</td>
</tr>
</table>

72	**Plasma etching of Silicon** (#etch063)	CR 125c/Adixen AMS 100 SE Applications: Waferback etch with high selectivity for oxide layers **Parameters** — **Value** SF_6 [sccm] — 400 O_2 [sscm] — 50 He-backside cooling [mbar] — 10 ICP [watt] — 2500 LF source CCP [Watt] — 10 for 90% wafer thickness, last 10 % use a CCP setting of 0 Watt. Vdc [Volts] — 160 p [Pa] — 10 APC position % — 15 Electrode temperature [°C] — 10 Substrate height [mm] — 110 Etch rate SiO2 [µm/min] — good ! Etch rate Olin 907 [µm/min] — Low Etch rate -Silicon (µm/min) — 40 Etch rate SiRN [µm/min] — ?	Modify recipi,..Etch depth ca. 300 microns, use isotropic plasma, which has a very high selectivity for Sio2 (TEOS 1.5 um).Be care full with heating-up the freehanging silicon structure. Stop etching process too cooldown the wafer (few minutes).Alter
73			Removal of oxide by Vapor HF process(Ask Jason) Alternative: is BHF and freeze drying (many steps may damage structure)
74			Dannes gaat scoren
75			Fabrication of substrate carrier,
76	**Substrate selection - Silicon <100> OSP** (#subs001)	CR112B / Wafer Storage Cupboard Supplier: Orientation: <100> Diameter: 100mm Thickness: 525µm +/- 25µm Polished: Single side Resistivity: 5-10Ωcm Type: p	4
77	**Lithography - Priming (Gamma 60)** (#lith003)	CR117B / Gamma 60 HexaMethylDiSilazane (HMDS)	Manual priming (gas) needed, info Huib

<table>
<tr><td>78</td><td>Lithography - Coating Olin907-17 (Gamma 60)
(#lith008)</td><td>CR117B / Gamma 60
Olin 907-17
• Program: ???</td><td>t4-4k.txt</td></tr>
<tr><td>79</td><td>Lithography - Alignment & Exposure Olin 907-17 (EV)
(#lith021)</td><td>CR117B / EVG 20
Electronic Vision Group 20 Mask Aligner
• Hg-lamp: 12 mW/cm^2
• Exposure Time: 4sec</td><td></td></tr>
<tr><td>80</td><td>Lithography - Development Olin Resist
(#lith011)</td><td>CR112B / Wet-Bench 11
Developer: OPD4262
Hotplate 120°C (CR112B or CR117B)
• After Exposure Bake (120°C): 60sec
Development:
• Time: 30sec in Beaker 1
• Time: 15-30sec in Beaker 2
• Quick Dump Rinse <0.1µS
• Spin drying</td><td>30+25...30 secs</td></tr>
<tr><td>81</td><td>Optical microscopic inspection - Lithography
(#char001)</td><td>CR112B / Nikon Microscope</td><td></td></tr>
<tr><td>82</td><td>Plasma etching of Si BOSCH-ADIX
(# ID etch056)</td><td>CR125c/Adixen SE
See for profile downloads on the mishomepage
<table>
<tr><th>Parameters</th><th>Etch</th><th>Deposition</th></tr>
<tr><td>Gas</td><td>SF6</td><td>C4F8</td></tr>
<tr><td>Flow sccm</td><td>300</td><td>150</td></tr>
<tr><td>Time sec</td><td>7</td><td>2</td></tr>
<tr><td>Priority</td><td>2</td><td>1</td></tr>
<tr><td>APC %</td><td>25</td><td>25</td></tr>
<tr><td>ICP Watt</td><td>1800</td><td>1800</td></tr>
<tr><td>CCP Watt [LF]</td><td>80</td><td>80</td></tr>
<tr><td>Pulsed (LF) ms.</td><td>10on/90off</td><td>10on/90 off</td></tr>
<tr><td>He mBar</td><td>10</td><td>10</td></tr>
<tr><td>SH mm</td><td>200</td><td>200</td></tr>
<tr><td>Electrode temp.°C.</td><td>10</td><td>10</td></tr>
<tr><td>Er Olin907</td><td>25-50 nm/min</td><td></td></tr>
<tr><td>Er silicon</td><td>3-5 µm/min</td><td></td></tr>
</table></td><td>Depth = 150 microns.</td></tr>
<tr><td>83</td><td>Optical microscopic inspection - Lithography
(#char001)</td><td>CR112B / Nikon Microscope</td><td>Measure depth</td></tr>
<tr><td>84</td><td>Stripping of polymers in HNO_3 multipurpose
(#lith014)</td><td>CR116B / Wet-Bench 2
HNO_3 (100%) Selectipur: MERCK 100453
• Beaker 1: HNO_3 (100%) 20min
• Quick Dump Rinse <0.1µS
• Spin drying</td><td>stripping time > 20 min</td></tr>
</table>

85	**Optical microscopic inspection** (#char002)	CR112B / Nikon Microscope CR117B / Olympus Microscope CR102B / Olympus Microscope	check wafers on Pr residue.
86	**Cleaning Standard** (#clean003)	CR112B / Wet-Bench 3-2 HNO_3 (100%) Selectipur: MERCK 100453 HNO_3 (69%) VLSI: MERCK 116445 • Beaker 1: fumic HNO_3 (100%), 5min • Beaker 2: fumic HNO_3 (100%), 5min • Quick Dump Rinse <0.1µS • Beaker 3: boiling (95°C) HNO_3 (69%), 10min • Quick Dump Rinse <0.1µS • Spin drying	
87	**Dry Oxidation (DOX) at 800°C of Silicon** (#depo026)	CR112B / Furnace B3 Standby temperature: 800°C • Program: DOX-800 • Temp.: 800°C • Gas: O_2 • Flow: 4l/min	30 min FC-removal
88			Do test to be sure if channels are deep enough!
89			Preparation and aligning of shadow mask
90	**Substrate selection - Silicon <100> OSP** (#subs001)	CR112B / Wafer Storage Cupboard Supplier: Orientation: <100> Diameter: 100mm Thickness: 525µm +/- 25µm Polished: Single side Resistivity: 5-10Ωcm Type: p	4
91	**Cleaning Standard** (#clean003)	CR112B / Wet-Bench 3-2 HNO_3 (100%) Selectipur: MERCK 100453 HNO_3 (69%) VLSI: MERCK 116445 • Beaker 1: fumic HNO_3 (100%), 5min • Beaker 2: fumic HNO_3 (100%), 5min • Quick Dump Rinse <0.1µS • Beaker 3: boiling (95°C) HNO_3 (69%), 10min • Quick Dump Rinse <0.1µS • Spin drying	
92	**Wet Oxidation (WOX) at 1150°C of Silicon** (#depo014)	CR112B / Furnace B2 Standby temperature: 800°C Check water level of bubbler • Program: WOX-1150 • Temp.: 1150°C • Gas: $H_2O + N_2$ (Bubbler)	1 um

93	**Lithography - Priming (Gamma 60)** (#lith003)	CR117B / Gamma 60 HexaMethylDiSilazane (HMDS)	Manual priming (gas) needed, info Huib
94	**Lithography - Coating Olin907-17 (Gamma 60)** (#lith008)	CR117B / Gamma 60 Olin 907-17 • Program: ???	t4-4k.txt
95	**Lithography - Alignment & Exposure Olin 907-17 (EV)** (#lith021)	CR117B / EVG 20 Electronic Vision Group 20 Mask Aligner • Hg-lamp: 12 mW/cm ^{2} • Exposure Time: 4sec	mask for making step in Silicon
96	**Lithography - Development Olin Resist** (#lith011)	CR112B / Wet-Bench 11 Developer: OPD4262 Hotplate 120°C (CR112B or CR117B) • After Exposure Bake (120°C): 60sec Development: • Time: 30sec in Beaker 1 • Time: 15-30sec in Beaker 2 • Quick Dump Rinse <0.1µS • Spin drying	30+25...30 secs
97	**Optical microscopic inspection - Lithography** (#char001)	CR112B / Nikon Microscope	
98	**Lithography - Postbake standard** (#lith009)	CR112B / Hotplate 120°C • Time: 30min	
99	**Etching BHF (1:7) SiO_2** (#etch024)	CR112B / Wet-Bench 3-3 NH_4F/HF (1:7) VLSI: MERCK 101171.2500 • Quick Dump Rinse <0.1µS • Spin drying Etchrate thermal SiO_2 = 60-80nm/min Etchrate PECVD SiO_2 = 125/nm/min Etchrate TEOS SiO_2 = 180/nm/min	time ca. 14 min
100	**Optical microscopic inspection - Lithography** (#char001)	CR112B / Nikon Microscope	Measure depth
101	**Stripping of polymers in HNO_3 multipurpose** (#lith014)	CR116B / Wet-Bench 2 HNO_3 (100%) Selectipur: MERCK 100453 • Beaker 1: HNO_3 (100%) 20min • Quick Dump Rinse <0.1µS • Spin drying	stripping time > 20 min

102	**Cleaning Standard** (#clean003)	CR112B / Wet-Bench 3-2 HNO_3 (100%) Selectipur: MERCK 100453 HNO_3 (69%) VLSI: MERCK 116445 • Beaker 1: fumic HNO_3 (100%), 5min • Beaker 2: fumic HNO_3 (100%), 5min • Quick Dump Rinse <0.1µS • Beaker 3: boiling (95°C) HNO_3 (69%), 10min • Quick Dump Rinse <0.1µS • Spin drying	
103	**Lithography - Priming (Gamma 60)** (#lith003)	CR117B / Gamma 60 HexaMethylDiSilazane (HMDS)	
104	**Lithography - Coating Olin907-17 (Gamma 60)** (#lith008)	CR117B / Gamma 60 Olin 907-17 • Program: ???	
105	**Lithography - Alignment & Exposure Olin 907-17 (EV)** (#lith021)	CR117B / EVG 20 Electronic Vision Group 20 Mask Aligner • Hg-lamp: 12 mW/cm^2 • Exposure Time: 4sec	
106	**Lithography - Development Olin Resist** (#lith011)	CR112B / Wet-Bench 11 Developer: OPD4262 Hotplate 120°C (CR112B or CR117B) • After Exposure Bake (120°C): 60sec Development: • Time: 30sec in Beaker 1 • Time: 15-30sec in Beaker 2 • Quick Dump Rinse <0.1µS • Spin drying	
107	**Optical microscopic inspection - Lithography** (#char001)	CR112B / Nikon Microscope	

108	**Plasma etching of Si BOSCH-ADIX** (# ID etch056)	CR125c/Adixen SE See for profile downloads on the mishomepage **Parameters** / **Etch** / **Deposition** Gas / SF6 / C4F8 Flow sccm / 300 / 150 Time sec / 7 / 2 Priority / 2 / 1 APC % / 25 / 25 ICP Watt / 1800 / 1800 CCP Watt [LF] / 80 / 80 Pulsed (LF) ms. / 10on/90off / 10on/90 off He mBar / 10 / 10 SH mm / 200 / 200 Electrode temp.°C. / 10 / 10 Er Olin907 / 25-50 nm/min Er silicon / 3-5 µm/min	Apply first test run check etch depth and directional profile. Detpth = 40 microns.
109	**Optical microscopic inspection - Lithography** (#char001)	CR112B / Nikon Microscope	Measure depth, width and check profile (dummy wafer)
110	**Stripping of polymers in HNO_3 multipurpose** (#lith014)	CR116B / Wet-Bench 2 HNO_3 (100%) Selectipur: MERCK 100453 • Beaker 1: HNO_3 (100%) 20min • Quick Dump Rinse <0.1µS • Spin drying	stripping time > 20 min
111	**Optical microscopic inspection** (#char002)	CR112B / Nikon Microscope CR117B / Olympus Microscope CR102B / Olympus Microscope	check wafers on Pr residue.
112	**Cleaning Standard** (#clean003)	CR112B / Wet-Bench 3-2 HNO_3 (100%) Selectipur: MERCK 100453 HNO_3 (69%) VLSI: MERCK 116445 • Beaker 1: fumic HNO_3 (100%), 5min • Beaker 2: fumic HNO_3 (100%), 5min • Quick Dump Rinse <0.1µS • Beaker 3: boiling (95°C) HNO_3 (69%), 10min • Quick Dump Rinse <0.1µS • Spin drying	
113	**Dry Oxidation (DOX) at 800°C of Silicon** (#depo026)	CR112B / Furnace B3 Standby temperature: 800°C • Program: DOX-800 • Temp.: 800°C • Gas: O_2 • Flow: 4l/min	30 min FC-removal

114	**LPCVD SiRN - low stress** (#depo002)	CR125C / Tempress LPCVD/HC Tube: G2 SiH_2Cl_2 flow: 70sccm NH_3 flow: 18sccm temperature: 850°C pressure: 200mTorr • program: SiRN deposition rate: 7.3 nm/min N_f: 2.14	0.5 micron
115	**Lithography - Priming (Gamma 60)** (#lith003)	CR117B / Gamma 60 HexaMethylDiSilazane (HMDS)	
116	**Lithography - Coating Olin907-17 (Gamma 60)** (#lith008)	CR117B / Gamma 60 Olin 907-17 • Program: ???	
117	**Lithography - Alignment & Exposure Olin 907-17 (EV)** (#lith021)	CR117B / EVG 20 Electronic Vision Group 20 Mask Aligner • Hg-lamp: 12 mW/cm^2 • Exposure Time: 4sec	
118	**Lithography - Development Olin Resist** (#lith011)	CR112B / Wet-Bench 11 Developer: OPD4262 Hotplate 120°C (CR112B or CR117B) • After Exposure Bake (120°C): 60sec Development: • Time: 30sec in Beaker 1 • Time: 15-30sec in Beaker 2 • Quick Dump Rinse $<0.1\mu S$ • Spin drying	
119	**Optical microscopic inspection - Lithography** (#char001)	CR112B / Nikon Microscope	
120	**Plasma etching SiN (Etske)** (#etch004)	CR102A / Elektrotech PF310/340 Dirty chamber Styros electrode • Electrode temp.: 10°C • CHF_3 flow: 25sccm • O_2 flow: 5sccm • pressure: 10mTorr • power: 75W Etchrate SiN = 50nm/min (for V_{DC}=-460V) Etchrate Olin resist = 95nm/min If DC-Bias $<$ 375V apply chamber clean (#etch003)	

121	**Stripping of polymers in HNO_3 multipurpose** (#lith014)	CR116B / Wet-Bench 2 HNO_3 (100%) Selectipur: MERCK 100453 • Beaker 1: HNO_3 (100%) 20min • Quick Dump Rinse <0.1µS • Spin drying	
122	**Etching HF (1%) Native Oxide** (#etch027)	CR112B / Wet-Bench 3-3 HF (1%) VLSI: MERCK 112629.500 • Etch time: >1min • Quick Dump Rinse <0.1µS • Spin drying	1 min
123	**Etching of Silicon by KOH - standard** (#etch038)	CR102B / KOH KOH: MERCK 105019.500 KOH:DI = (1:3) 25wt% KOH: 500g KOH pellets in 1500ml DI water • Temp.: 75°C • Stirrer • Quick Dump Rinse <0.1µS • Spin drying Etchrates: Si <100> = 1µm/min Si <111> = 12.5nm/min SiO_2 (thermal) = 180nm/hr SiRN < 0.6nm/hr	stop on nitride, membrane thickness ca. 40 microns
124	**Cleaning RCA-2 ($HCL/H_2O_2/H_2O$)** (#clean007)	CR102A / Wet-Bench 9 HCL (32%) Selectipur: MERCK 100322.2500 H_2O_2 (31%) VLSI: MERCK 108552.2500 Only use the dedicated wafer carriers and glass rod! $HCL:H_2O_2:H_2O$ (1:1:5) vol% • add HCL to H_2O • add H_2O_2 when mixure at 70°C • temperature 70-80°C • cleaning time 10-15min • Quick Dump Rinse <0.1µS • Spin drying	
125	**Etching HF (50%) LPCVD SiN or Thermal oxide** (#etch029)	CR112B / Wet-Bench 3-3 HF (50%) VLSI: MERCK 100373.2500 • Quick Dump Rinse <0.1µS • Spin drying Etchrate SiRN = 5nm/min Etchrate SiO_2 = 1 µm/min	
126	**Wet Oxidation (WOX) at 1150°C of Silicon** (#depo014)	CR112B / Furnace B2 Standby temperature: 800°C Check water level of bubbler • Program: WOX-1150 • Temp.: 1150°C • Gas: $H_2O + N_2$ (Bubbler)	1 micron

127			fabrication of etchmask for release of leafspring
128	**Substrate selection - Silicon <100> OSP** (#subs001)	CR112B / Wafer Storage Cupboard Supplier: Orientation: <100> Diameter: 100mm Thickness: 525µm +/- 25µm Polished: Single side Resistivity: 5-10Ωcm Type: p	4
129	**Lithography - Priming (Gamma 60)** (#lith003)	CR117B / Gamma 60 HexaMethylDiSilazane (HMDS)	Backside Manual priming (gas) needed, info Huib
130	**Lithography - Coating Olin907-17 (Gamma 60)** (#lith008)	CR117B / Gamma 60 Olin 907-17 • Program: ???	t4-4k.txt
131	**Lithography - Alignment & Exposure Olin 907-17 (EV)** (#lith021)	CR117B / EVG 20 Electronic Vision Group 20 Mask Aligner • Hg-lamp: 12 mW/cm ^{2} • Exposure Time: 4sec	
132	**Lithography - Development Olin Resist** (#lith011)	CR112B / Wet-Bench 11 Developer: OPD4262 Hotplate 120°C (CR112B or CR117B) • After Exposure Bake (120°C): 60sec Development: • Time: 30sec in Beaker 1 • Time: 15-30sec in Beaker 2 • Quick Dump Rinse <0.1µS • Spin drying	30+25...30 secs
133	**Optical microscopic inspection - Lithography** (#char001)	CR112B / Nikon Microscope	

<table>
<tr><td>134</td><td>Plasma etching of Si BOSCH-ADIX
(# ID etch056)</td><td>CR125c/Adixen SE
See for profile downloads on the mishomepage
<table><tr><td>Parameters</td><td>Etch</td><td>Deposition</td></tr><tr><td>Gas</td><td>SF6</td><td>C4F8</td></tr><tr><td>Flow sccm</td><td>300</td><td>150</td></tr><tr><td>Time sec</td><td>7</td><td>2</td></tr><tr><td>Priority</td><td>2</td><td>1</td></tr><tr><td>APC %</td><td>25</td><td>25</td></tr><tr><td>ICP Watt</td><td>1800</td><td>1800</td></tr><tr><td>CCP Watt [LF]</td><td>80</td><td>80</td></tr><tr><td>Pulsed (LF) ms.</td><td>10on/90off</td><td>10on/90 off</td></tr><tr><td>He mBar</td><td>10</td><td>10</td></tr><tr><td>SH mm</td><td>200</td><td>200</td></tr><tr><td>Electrode temp.°C.</td><td>10</td><td>10</td></tr><tr><td>Er Olin907</td><td>25-50 nm/min</td><td></td></tr><tr><td>Er silicon</td><td>3-5 μm/min</td><td></td></tr></table></td><td>Depth = 20 microns.</td></tr>
<tr><td>135</td><td>Optical microscopic inspection - Lithography
(#char001)</td><td>CR112B / Nikon Microscope</td><td>Measure depth</td></tr>
<tr><td>136</td><td>Stripping of polymers in HNO_3 multipurpose
(#lith014)</td><td>CR116B / Wet-Bench 2
HNO_3 (100%) Selectipur: MERCK 100453
• Beaker 1: HNO_3 (100%) 20min
• Quick Dump Rinse <0.1μS
• Spin drying</td><td>stripping time > 20 min</td></tr>
<tr><td>137</td><td>Optical microscopic inspection
(#char002)</td><td>CR112B / Nikon Microscope
CR117B / Olympus Microscope
CR102B / Olympus Microscope</td><td>check wafers on Pr residue.</td></tr>
<tr><td>138</td><td>Cleaning Standard
(#clean003)</td><td>CR112B / Wet-Bench 3-2
HNO_3 (100%) Selectipur: MERCK 100453
HNO_3 (69%) VLSI: MERCK 116445
• Beaker 1: fumic HNO_3 (100%), 5min
• Beaker 2: fumic HNO_3 (100%), 5min
• Quick Dump Rinse <0.1μS
• Beaker 3: boiling (95°C) HNO_3 (69%), 10min
• Quick Dump Rinse <0.1μS
• Spin drying</td><td></td></tr>
<tr><td>139</td><td>LPCVD SiRN - low stress
(#depo002)</td><td>CR125C / Tempress LPCVD/HC
Tube: G2
SiH_2Cl_2 flow: 70sccm
NH_3 flow: 18sccm
temperature: 850°C
pressure: 200mTorr
• program: SiRN
deposition rate: 7.3 nm/min
N_f: 2.14</td><td>0.5 micron</td></tr>
</table>

140	**Lithography - Priming (Gamma 60)** (#lith003)	CR117B / Gamma 60 HexaMethylDiSilazane (HMDS)	
141	**Lithography - Coating Olin907-17 (Gamma 60)** (#lith008)	CR117B / Gamma 60 Olin 907-17 • Program: ???	
142	**Lithography - Alignment & Exposure Olin 907-17 (EV)** (#lith021)	CR117B / EVG 20 Electronic Vision Group 20 Mask Aligner • Hg-lamp: 12 mW/cm^2 • Exposure Time: 4sec	backside alignment
143	**Lithography - Development Olin Resist** (#lith011)	CR112B / Wet-Bench 11 Developer: OPD4262 Hotplate 120°C (CR112B or CR117B) • After Exposure Bake (120°C): 60sec Development: • Time: 30sec in Beaker 1 • Time: 15-30sec in Beaker 2 • Quick Dump Rinse <0.1µS • Spin drying	
144	**Optical microscopic inspection - Lithography** (#char001)	CR112B / Nikon Microscope	
145	**Plasma etching SiN (Etske)** (#etch004)	CR102A / Elektrotech PF310/340 Dirty chamber Styros electrode • Electrode temp.: 10°C • CHF_3 flow: 25sccm • O_2 flow: 5sccm • pressure: 10mTorr • power: 75W Etchrate SiN = 50nm/min (for V_{DC}=-460V) Etchrate Olin resist = 95nm/min If DC-Bias < 375V apply chamber clean (#etch003)	
146	**Stripping of polymers in HNO_3 multipurpose** (#lith014)	CR116B / Wet-Bench 2 HNO_3 (100%) Selectipur: MERCK 100453 • Beaker 1: HNO_3 (100%) 20min • Quick Dump Rinse <0.1µS • Spin drying	
147	**Etching HF (1%) Native Oxide** (#etch027)	CR112B / Wet-Bench 3-3 HF (1%) VLSI: MERCK 112629.500 • Etch time: >1min • Quick Dump Rinse <0.1µS • Spin drying	1 min

148	**Etching of Silicon by KOH - standard** (#etch038)	CR102B / KOH KOH: MERCK 105019.500 KOH:DI = (1:3) 25wt% KOH: 500g KOH pellets in 1500ml DI water • Temp.: 75°C • Stirrer • Quick Dump Rinse <0.1µS • Spin drying Etchrates: Si <100> = 1µm/min Si <111> = 12.5nm/min SiO_2 (thermal) = 180nm/hr SiRN < 0.6nm/hr	stop on nitride, membrane thickness ca. 40 microns
149	**Cleaning RCA-2 ($HCL/H_2O_2/H_2O$)** (#clean007)	CR102A / Wet-Bench 9 HCL (32%) Selectipur: MERCK 100322.2500 H_2O_2 (31%) VLSI: MERCK 108552.2500 Only use the dedicated wafer carriers and glass rod! $HCL:H_2O_2:H_2O$ (1:1:5) vol% • add HCL to H_2O • add H_2O_2 when mixure at 70°C • temperature 70-80°C • cleaning time 10-15min • Quick Dump Rinse <0.1µS • Spin drying	
150	**Etching HF (50%) LPCVD SiN or Thermal oxide** (#etch029)	CR112B / Wet-Bench 3-3 HF (50%) VLSI: MERCK 100373.2500 • Quick Dump Rinse <0.1µS • Spin drying Etchrate SiRN = 5nm/min Etchrate SiO_2 = 1 µm/min	
151	**Wet Oxidation (WOX) at 1150°C of Silicon** (#depo014)	CR112B / Furnace B2 Standby temperature: 800°C Check water level of bubbler • Program: WOX-1150 • Temp.: 1150°C • Gas: $H_2O + N_2$ (Bubbler)	1 micron

APPENDIX H

PROCESS DOCUMENT OF THE CLAMPING MECHANISM

Step	Process		Comment
1	**Substrate selection - Silicon <100> DSP** (#subs012)	TST/Boudewijn de Jong (2811) Supplier: Orientation: <100> Diameter: 100mm Thickness: 500µm +/- 10µm Polished: Double side Resistivity: 0.0015-0.019Ωcm Type: p	8 DSP wafers + 4 OSP dummy wafers thickness measurement
2	**Lithography - Priming (Gamma 60)** (#lith003)	CR117B / Gamma 60 HexaMethylDiSilazane (HMDS)	8 DSP
3	**Lithography - Coating Olin907-17 (Gamma 60)** (#lith008)	CR117B / Gamma 60 Olin 907-17 • Program: ???	t4-4k.txt
4	**Lithography - Alignment & Exposure Olin 907-17 (EV)** (#lith021)	CR117B / EVG 20 Electronic Vision Group 20 Mask Aligner • Hg-lamp: 12 mW/cm^{2} • Exposure Time: 4sec	mask: trenches, check mask !! , time 3. 2-3.5 secs
5	**Lithography - Development Olin Resist** (#lith011)	CR112B / Wet-Bench 11 Developer: OPD4262 Hotplate 120°C (CR112B or CR117B) • After Exposure Bake (120°C): 60sec Development: • Time: 30sec in Beaker 1 • Time: 15-30sec in Beaker 2 • Quick Dump Rinse <0.1µS • Spin drying	30+25...30 secs

6	**Optical microscopic inspection - Lithography** (#char001)	CR112B / Nikon Microscope	Measure trench width. Max. width is 2 microns
7	**Plasma etching of Si BOSCH-ADIX** (# ID etch056)	CR125c/Adixen SE See for profile downloads on the mishomepage **Parameters** / **Etch** / **Deposition** Gas / SF6 / C4F8 Flow sccm / 300 / 150 Time sec / 7 / 2 Priority / 2 / 1 APC % / 25 / 25 ICP Watt / 1800 / 1800 CCP Watt [LF] / 80 / 80 Pulsed (LF) ms. / 10on/90off / 10on/90 off He mBar / 10 / 10 SH mm / 200 / 200 Electrode temp.°C. / 10 / 10 Er Olin907 / 25-50 nm/min Er silicon / 3-5 µm/min	RIE-lag is minimised for B-Adix recipe, when a mask is used with a window spacing of 3 upto 20 micron for a depth 40 microns.
8	**Optical microscopic inspection - Lithography** (#char001)	CR112B / Nikon Microscope	Check depth, width and profile use dummy wafer
9	**Stripping of polymers in HNO_3 multipurpose** (#lith014)	CR116B / Wet-Bench 2 HNO_3 (100%) Selectipur: MERCK 100453 • Beaker 1: HNO_3 (100%) 20min • Quick Dump Rinse <0.1µS • Spin drying	
10	**Cleaning Standard** (#clean003)	CR112B / Wet-Bench 3-2 HNO_3 (100%) Selectipur: MERCK 100453 HNO_3 (69%) VLSI: MERCK 116445 • Beaker 1: fumic HNO_3 (100%), 5min • Beaker 2: fumic HNO_3 (100%), 5min • Quick Dump Rinse <0.1µS • Beaker 3: boiling (95°C) HNO_3 (69%), 10min • Quick Dump Rinse <0.1µS • Spin drying	
11	**Dry Oxidation (DOX) at 800°C of Silicon** (#depo026)	CR112B / Furnace B3 Standby temperature: 800°C • Program: DOX-800 • Temp.: 800°C • Gas: O_2 • Flow: 4l/min	30 min FC-removal

12	**Etching HF (1%) Native Oxide** (#etch027)	CR112B / Wet-Bench 3-3 HF (1%) VLSI: MERCK 112629.500 • Etch time: >1min • Quick Dump Rinse <0.1µS • Spin drying	50% HF was used instead of 1 %, time 2 min
13	**Cleaning Standard** (#clean003)	CR112B / Wet-Bench 3-2 HNO_3 (100%) Selectipur: MERCK 100453 HNO_3 (69%) VLSI: MERCK 116445 • Beaker 1: fumic HNO_3 (100%), 5min • Beaker 2: fumic HNO_3 (100%), 5min • Quick Dump Rinse <0.1µS • Beaker 3: boiling (95°C) HNO_3 (69%), 10min • Quick Dump Rinse <0.1µS • Spin drying	
14	**LPCVD SiRN - low stress** (#depo002)	CR125C / Tempress LPCVD/HC Tube: G2 SiH_2Cl_2 flow: 70sccm NH_3 flow: 18sccm temperature: 850°C pressure: 200mTorr • program: SiRN deposition rate: 7.3 nm/min N_f: 2.14	1 micron SiRN (Bob's method "nitride-las"), 2:15 hr. deposit, dummy cleave, inspect cross-section
15	**Plasma etching of SiO_2** (#etch057	CR 125c/Adixen AMS 100 DE **Parameters** — **Value** C_4F_8 [sccm] — 15 He [sccm] — 150 CH_4 [sccm] — 15 He-backside cooling — 10 ICP [watt] — 2800 CCP [Watt] — 350 p [mbar] — $8.5\ 10^{-3}$ Eelctrode temperature [°C] — 10 Substrate height [mm] — 120 Etch rate SiO2 [µm/min] — 0.470-0.530 Etch rate Olin 907 [µm/min] — ca. 0.05 Etch rate poly-Silicon (µm/min) — Etch rate SiRN [µm/min] — ca. 0.1-0.3 variable!	A proces with a low etch rate for silicon is needed; to remove nitride at the top of trench without creating nitride "ears". Alternative process: etch#019+ etch# 004

16	**Cleaning Standard** (#clean003)	CR112B / Wet-Bench 3-2 HNO_3 (100%) Selectipur: MERCK 100453 HNO_3 (69%) VLSI: MERCK 116445 • Beaker 1: fumic HNO_3 (100%), 5min • Beaker 2: fumic HNO_3 (100%), 5min • Quick Dump Rinse <0.1μS • Beaker 3: boiling (95°C) HNO_3 (69%), 10min • Quick Dump Rinse <0.1μS • Spin drying	
17	**Dry Oxidation (DOX) at 800°C of Silicon** (#depo026)	CR112B / Furnace B3 Standby temperature: 800°C • Program: DOX-800 • Temp.: 800°C • Gas: O_2 • Flow: 4l/min	
18	**Etching HF (1%) Native Oxide** (#etch027)	CR112B / Wet-Bench 3-3 HF (1%) VLSI: MERCK 112629.500 • Etch time: >1min • Quick Dump Rinse <0.1μS • Spin drying	
19	**LPCVD SiRN - low stress** (#depo002)	CR125C / Tempress LPCVD/HC Tube: G2 SiH_2Cl_2 flow: 70sccm NH_3 flow: 18sccm temperature: 850°C pressure: 200mTorr • program: SiRN deposition rate: 7.3 nm/min N_f: 2.14	1.5 mu (depending on cross-section) +/- 3hr.
20	**Optical microscopic inspection - Lithography** (#char001)	CR112B / Nikon Microscope	use dummy to check fill
21	**Cleaning Standard** (#clean003)	CR112B / Wet-Bench 3-2 HNO_3 (100%) Selectipur: MERCK 100453 HNO_3 (69%) VLSI: MERCK 116445 • Beaker 1: fumic HNO_3 (100%), 5min • Beaker 2: fumic HNO_3 (100%), 5min • Quick Dump Rinse <0.1μS • Beaker 3: boiling (95°C) HNO_3 (69%), 10min • Quick Dump Rinse <0.1μS • Spin drying	optional
22	**Lithography - Priming (Gamma 60)** (#lith003)	CR117B / Gamma 60 HexaMethylDiSilazane (HMDS)	back-side, all DSP wafers, program 4k4.txt

23	**Lithography - Coating Olin907-17 (Gamma 60)** (#lith008)	CR117B / Gamma 60 Olin 907-17 • Program: ???	
24	**Lithography - Alignment & Exposure Olin 907-17 (EV)** (#lith021)	CR117B / EVG 20 Electronic Vision Group 20 Mask Aligner • Hg-lamp: 12 mW/cm ^{2} • Exposure Time: 4sec	mask: backside KOH etching
25	**Lithography - Development Olin Resist** (#lith011)	CR112B / Wet-Bench 11 Developer: OPD4262 Hotplate 120°C (CR112B or CR117B) • After Exposure Bake (120°C): 60sec Development: • Time: 30sec in Beaker 1 • Time: 15-30sec in Beaker 2 • Quick Dump Rinse <0.1µS • Spin drying	
26	**Lithography - Postbake standard** (#lith009)	CR112B / Hotplate 120°C • Time: 30min	postbake necessary????
27	**Plasma etching of SiO_2** (#etch057	CR 125c/Adixen AMS 100 DE **Parameters** — **Value** C_4F_8 [sccm] — 15 He [sccm] — 150 CH_4 [sccm] — 15 He-backside cooling — 10 ICP [watt] — 2800 CCP [Watt] — 350 p [mbar] — 8.5 10^{-3} Eelctrode temperature [°C] — 10 Substrate height [mm] — 120 Etch rate SiO2 [µm/min] — 0.470-0.530 Etch rate Olin 907 [µm/min] — ca. 0.05 Etch rate poly-Silicon (µm/min) — Etch rate SiRN [µm/min] — ca. 0.1-0.3 variable!	etch backside, Alternative process: etch#019+ etch# 004; protect the edge of the wafer with a ring of kapton foil

28	**Stripping of Olin PR by oxygen plasma** (#lith017)	CR102A / Tepla 300E Barrel Etcher (2.45 GHz) Multipurpose sytem • O_2 flow: 200sccm (50%) • Power: 500W • Pressure: 1.2 mbar • Time: 10 min for 1-3 wafers, 400 nm/min • Time: 20 min for 4-10 wafers • End point detection by visual inspection of the plasma color. • Blue color means still photoresist on the wafer, purple means clean.	20 min depending on SiRN etch time or recipe 01
29	**Cleaning Standard** (#clean003)	CR112B / Wet-Bench 3-2 HNO_3 (100%) Selectipur: MERCK 100453 HNO_3 (69%) VLSI: MERCK 116445 • Beaker 1: fumic HNO_3 (100%), 5min • Beaker 2: fumic HNO_3 (100%), 5min • Quick Dump Rinse <0.1µS • Beaker 3: boiling (95°C) HNO_3 (69%), 10min • Quick Dump Rinse <0.1µS • Spin drying	
30	**Etching HF (1%) Native Oxide** (#etch027)	CR112B / Wet-Bench 3-3 HF (1%) VLSI: MERCK 112629.500 • Etch time: >1min • Quick Dump Rinse <0.1µS • Spin drying	
31	**Etching of Silicon by KOH - standard** (#etch038)	CR102B / KOH KOH: MERCK 105019.500 KOH:DI = (1:3) 25wt% KOH: 500g KOH pellets in 1500ml DI water • Temp.: 75°C • Stirrer • Quick Dump Rinse <0.1µS • Spin drying Etchrates: Si <100> = 1µm/min Si <111> = 12.5nm/min SiO_2 (thermal) = 180nm/hr SiRN < 0.6nm/hr	etch depth: waferthickness (500) - 38 = 462 um

<table>
<tr>
<td>32</td>
<td>Cleaning RCA-2 ($HCL/H_2O_2/H_2O$)
(#clean007)</td>
<td>CR102A / Wet-Bench 9
HCL (32%) Selectipur: MERCK 100322.2500
H_2O_2 (31%) VLSI: MERCK 108552.2500
Only use the dedicated wafer carriers and glass rod!
$HCL:H_2O_2:H_2O$ (1:1:5) vol%
• add HCL to H_2O
• add H_2O_2 when mixure at 70°C
• temperature 70-80°C
• cleaning time 10-15min
• Quick Dump Rinse <0.1µS
• Spin drying</td>
<td></td>
</tr>
<tr>
<td>33</td>
<td>Plasma etching of SiO_2
(#etch057</td>
<td>CR 125c/Adixen AMS 100 DE

<table>
<tr><th>Parameters</th><th>Value</th></tr>
<tr><td>C_4F_8 [sccm]</td><td>15</td></tr>
<tr><td>He [sccm]</td><td>150</td></tr>
<tr><td>CH_4 [sccm]</td><td>15</td></tr>
<tr><td>He-backside cooling</td><td>10</td></tr>
<tr><td>ICP [watt]</td><td>2800</td></tr>
<tr><td>CCP [Watt]</td><td>350</td></tr>
<tr><td>p [mbar]</td><td>$8.5\ 10^{-3}$</td></tr>
<tr><td>Eelctrode temperature [°C]</td><td>10</td></tr>
<tr><td>Substrate height [mm]</td><td>120</td></tr>
<tr><td>Etch rate SiO2 [µm/min]</td><td>0.470-0.530</td></tr>
<tr><td>Etch rate Olin 907 [µm/min]</td><td>ca. 0.05</td></tr>
<tr><td>Etch rate poly-Silicon (µm/min)</td><td></td></tr>
<tr><td>Etch rate SiRN [µm/min]</td><td>ca. 0.1-0.3 variable!</td></tr>
</table>
</td>
<td>Frontside;Use a proces with a low etch rate for silicon, to avoid nitrirde "ears" first backside SiRN strip (plus overetch (inspect topside by sight) Alternative process: etch#019+ etch# 004</td>
</tr>
<tr>
<td>34</td>
<td>Lithography - Priming (liquid)
(#lith001)</td>
<td>CR112B / Suss Micro Tech Spinner (Delta 20)
Hotplate 120 °C
HexaMethylDiSilazane (HMDS)
• Dehydration bake (120°C): 5min
• Spinning acceleration: 4000rpm/s
• Spinning speed: 4000rpm
• Spinning time: 20s</td>
<td>Frontside, all DSP wafers</td>
</tr>
<tr>
<td>35</td>
<td>Lithography - Coating Olin907-17
(#lith005)</td>
<td>CR112B / Suss Micro Tech Spinner (Delta 20)
Hotplate 95 °C
Olin 907-17
• Spinning acceleration: 4000rpm/s
• Spinning speed: 4000rpm
• Spinning time: 20s
• Prebake (95°C): 90s</td>
<td></td>
</tr>
</table>

<table>
<tr><td>36</td><td>Lithography - Alignment & Exposure Olin 907-17 (EV)
(#lith021)</td><td>CR117B / EVG 20
Electronic Vision Group 20 Mask Aligner
• Hg-lamp: 12 mW/cm^2
• Exposure Time: 4sec</td><td>mask device layout, 3.2 - 3.5s, support 3pt ????</td></tr>
<tr><td>37</td><td>Lithography - Development Olin Resist
(#lith011)</td><td>CR112B / Wet-Bench 11
Developer: OPD4262
Hotplate 120°C (CR112B or CR117B)
• After Exposure Bake (120°C): 60sec
Development:
• Time: 30sec in Beaker 1
• Time: 15-30sec in Beaker 2
• Quick Dump Rinse <0.1µS
• Spin drying</td><td></td></tr>
<tr><td>38</td><td>Optical microscopic inspection - Lithography
(#char001)</td><td>CR112B / Nikon Microscope</td><td></td></tr>
<tr><td>39</td><td>Plasma etching of Si BOSCH-ADIX
(# ID etch056)</td><td>CR125c/Adixen SE
See for profile downloads on the mishomepage
<table>
<tr><th>Parameters</th><th>Etch</th><th>Deposition</th></tr>
<tr><td>Gas</td><td>SF6</td><td>C4F8</td></tr>
<tr><td>Flow sccm</td><td>300</td><td>150</td></tr>
<tr><td>Time sec</td><td>7</td><td>2</td></tr>
<tr><td>Priority</td><td>2</td><td>1</td></tr>
<tr><td>APC %</td><td>25</td><td>25</td></tr>
<tr><td>ICP Watt</td><td>1800</td><td>1800</td></tr>
<tr><td>CCP Watt [LF]</td><td>80</td><td>80</td></tr>
<tr><td>Pulsed (LF) ms.</td><td>10on/90off</td><td>10on/90 off</td></tr>
<tr><td>He mBar</td><td>10</td><td>10</td></tr>
<tr><td>SH mm</td><td>200</td><td>200</td></tr>
<tr><td>Electrode temp.°C.</td><td>10</td><td>10</td></tr>
<tr><td>Er Olin907</td><td>25-50 nm/min</td><td></td></tr>
<tr><td>Er silicon</td><td>3-5 µm/min</td><td></td></tr>
</table></td><td>front-side: etch depth 95 % of height of nitride plug = 38 micron. Use vent-substrate wafer with fomlin. End with SF6 cycle to achieve a good release, step 38</td></tr>
</table>

40	Plasma etching of Si Low power release (# ID etch068)	CR125c/Adixen SE Application: release of actuator structure Parameters Etch Gas SF6 Flow sccm 15 Time sec X Priority - APC % 100 ICP Watt 200 CCP Watt [LF] 0 Pulsed (LF) ms. off He mBar 10 SH mm 200 Electrode temp.°C. 20 Er Olin907 xx nm/min Er silicon 0,35µm/min	Apply after each minute of etching a cooldown step (= temp 60sec), total etch time in order of 8min. (FC passivation of B-adix is suitable to withstand 16 min of low power release).
41	**Stripping of Olin PR by oxygen plasma** (#lith017)	CR102A / Tepla 300E Barrel Etcher (2.45 GHz) Multipurpose sytem • O_2 flow: 200sccm (50%) • Power: 500W • Pressure: 1.2 mbar • Time: 10 min for 1-3 wafers, 400 nm/min • Time: 20 min for 4-10 wafers • End point detection by visual inspection of the plasma color. • Blue color means still photoresist on the wafer, purple means clean.	recipe 01 , 30 min 800 Watt O2
42	**Optical microscopic inspection** (#char002)	CR112B / Nikon Microscope CR117B / Olympus Microscope CR102B / Olympus Microscope	Yield: close to 100 %, for a few devices we observed between the fingers a very thin silicon residue.

REFERENCES

1 G. Akoun, J. Yonnet, '3D analytical calculation of the forces exerted between two cuboidal magnets', IEEE transactions on magnetics 34 (September 1984) NO. 5.

2 American society for precision engineering, http://www.aspe.net/index.html.

3 D.P. Arnold, S. Das, F. Cros, I. Zana, M.G. Allen, and J.H. Lang, Magnetic induction machines integrated into bulk-micromachined silicon, Journal of MEMS, vol. 15, no. 2, pp. 406–414, 2006.

4 M. Bao, C. Burrer, J. Esteve, J. Bausells, S. Marco, Etching front control of <110> strips for corner compensation, Sensors and Actuators A, 37-38, (1993), pp. 727-732.

5 F. Bancel and G. Lemarquand, 'Three-Dimensional analytical Optimization of Permanent Magnets Alternated Structure', IEEE Transactions of Magnetics 34 (January 1998) NO. 1.

6 N. Belov, et al., Comparison of Thermo-Mechanical Actuators with other Types of Actuators, Eurosensors XIII, The 13th European Conference on Solid-State Transducers, September 1999.

7 J.F. Besseling, The complete analogy between the matrix equations and continuous field equations of structural analysis, int. symposium on analogue and digital techniques applied to aeronautics, Bruxelles, 1964, pp. 223-242.

8 D.L. Blanding, Exact Constraint: Machine design using kinematic principles, ISBN 0-7918-0085-7, 1999.

9 C. Body, G. Reyne, G. Meunier, Modelling of magnetostrictive thin films, application to a micromembrane, J. Phys. III France 7, 1997, pp. 67-85.

10 P. Bøggild, T. Hansen, C. Tanasa, F. Grey, Fabrication and actuation of customized nanotweezers with a 25 nm gap, Nanotechnology 12 (2001) 331–335 PII: S0957-4484(01)22628-2.

11 T. Bourouina, E. Lebrasseur, G. Reyne, H. Fujita, T. Masuzawa, A. Ludwig, E. Quandt, H. Muro, T. Oki, A. Asaoka, A Novel Optical Scanner with Integrated Two-Dimensional Magnetostrictive Actuation and Two-Dimensional Piezoresistive Detection, The 11th International Conference on Solid-State Sensors and Actuators, Munich, Germany, June 10 – 14, 2001.

12 M. Brissauld, S. Ledren, P. Gonnard, Modelling of a cantilever non-symmetric piezoelectric bimorph, Journal of Micromechanics and Microengineering, 13, 2003, pp. 832-844.

13 D.M. Brouwer, B.R. de Jong, H.M.J.R. Soemers, J. van Dijk, Sub-nanometer stable precision MEMS clamping mechanism maintaining clamp force unpowered for TEM application, Journal of Micromechanics and Microengineering, 16, 2006, pp.7-12.

14 D.M. Brouwer, B.R. de Jong, M. J. de Boer, H.M.J.R. Soemers, Rotational precision MEMS-based Clamping Mechanism for stable fixation of Elastic Mechanisms, ASPE, Monterey, California, USA, 2006, pp. 275-278.

15 D.M. Brouwer, B.R. De Jong, and H.M.J.R. Soemers, Design and modelling of a precision 6 degrees-of-freedom MEMS-based parallel kinematic TEM sample manipulator, in ASPE, Monterey, California, USA, p. Session VIII, 2006, pp.115-118.

16 D.M. Brouwer, B.R. de Jong, H.M.J.R. Soemers, G.J.M. Krijnen, Numerical evaluation of piezo, thermo, electro-magnetic and electro-static MEMS actuators based on designs, EUSPEN Conference, Baden bei Wien, Oostenrijk, mei 2006, pp. 172-175.

17 G.J. Burger, E.J.T. Smulders, J.W. Berenschot, T.S.J. Lammerink, J.H.J. Fluitman, S. Imai, High-resolution shadow mask patterning in deep holes and its application to an electrical wafer feed-through, Sensors and Actuators A 54_1996.669–673.

18 J.T. Butler, V.M. Bright, W.D. Cowan, Average power control and positioning of polysilicon thermal actuators, Sensor and Actuators (A), Vol. 72, 1999, pp. 88-97.

19 A. Cardona, M. Géradin, D.B. Doan, Rigid and flexible joint modeling in multibody dynamics using finite-elements, Computer mthods in applied mechanics and engineering 89, 1991, pp.395-418.

20 E.T. Carlen, C.H. Mastrangelo, Simple, high actuation power, thermally activated paraffin microactuator, Transducers conference, Sendai, Japan, June 7-10, 1999.

21 G. Carlotti, G. Socino, A. Petri, E. Verona, Proceedings 1987 IEEE Ultrasonic Symposium, 1987, pp. 295.

22 H.-C. Chang, J.M.-L. Tsai, H.-C. Tsai, and W. Fang, A novel 3-DOF micromanipulator, in ASME IMECE, Washington D.C., U.S.A., pp. 1–6, 2003.

23 K.H. Chau, et al., An integrated force-balanced capacitive accelerometer for low-G applications, Proc. 8th Int. Conf. on Solid State Sensors and Actuators, Stockholm, Sweden, June 25-29, 1995, pp.593-596ss.

24 S.-C. Chen and M.L. Culpepper, Design of a six-axis micro-scale nanopositioner μ–HexFlex, Precision Engineering, vol. 30, pp. 314–324, 2006.

25 R.S. Chen, C. Kung, G.B. Lee, Analysis of the optimal dimension on the electrothermal microactuator, J. Micromech. Microeng. 12 2002 pp. 291-296.

26 W.-J. Cheng and D. L. DeVoe, Linear micromotors and spatial micromechanisms based on UVLIGA, IEEE MEMS'05, Miami Beach, Florida, USA, pp. 399–402, 2005.

27 L.L. Chu, Y.B. Gianchandani, A micromachined 2D positioner with electrothermal actuation and sub-nanometer capacitive sensing, J. Micromech. Microeng. 13, 2003, pp. 279-285.

28 H.-Y. Chu, S.-W. Lee, and W. Fang, Design and fabrication of multi-degrees-of-freedom single crystal silicon movable platforms on SOI wafer, in IEEE MEMS, Seoul, Korea, pp. 737–740, 2005.

29 J. Corbett, P. C. McKeown, G. N. Peggs, and R. Whatmore, Nanotechnology: International Developments and Emerging Products, Annals of the CIRP, vol. 49, no. 2, pp. 523–545, 2000.

30 F. Cros, H. Koser, M.G. Allen, and J.H. Lang, Magnetic induction micromachine–Part II: Fabrication and testing, Journal of MEMS, vol. 15, no. 2, pp. 427–439, 2006.

31 CTT internal Philips, Lecture notes on Heat Transport.

32 M. L. Culpepper and G. Anderson, Design of a low-cost nano-manipulator which utilizes a monolithic spatial compliant mechanism, Journal of Precision Engineering, vol. 28, pp. 469–482, 2004.

33 D. J. Dagel, W. D. Cowan, O. B. Spahn, G. D. Grossetete, A. J. Gri ˜ ne, M. J. Shaw, P. J. Resnich, and B. Jokiel Jr, Large-stroke MEMS deformable mirrors for adaptive optics, Journal of MEMS, vol. 15, no. 3, pp. 572–583, 2006.

34 S. Deladi, MEMS generated and AFM-based surface modification, Ph.D Thesis, University of Twente, the Netherlands, 2005.

35 S. Deladi, G. Krijnen, and M.C. Elwenspoek, Parallel-beam/lever electrothermal out-of-plane actuator, in DTIP, Cannes-Mandelieu, France, 2003.

36 S. Deladi, M.J. De Boer, G. Krijnen, and D. Ros´en, Innovative process development for a new micro-tribosensor using surface micromachnining, JMM, vol. 13, pp. S17–S22, 2003.

37 J.A. Deijnen, Modelling leaf-springs in MEMS, M.Sc thesis WA 1043, mechanical engineering, technical design sciences, University of Twente, the Netherlands, 2006.

38 Van Drieënhuizen et al, Force balanced accelerometer with mG resolution, fabricated using silicon fusion bonding and deep reactive ion etching, Proc. 1997 int. conf. on solid-state sensors and actuators, Chicago, Il, June 16-19, 1997, Vol. 2, pp. 1229-1230.

39 M.A. Dubois, P. Muralt, Properties of aluminum nitride thin films for piezoelectric transducers and microwave filter applications, Applied physics letters, vol 74, nb 20 pp. 3032-3034, 1999.

40 M.A. Dubois, P. Muralt, Stress and piezoelectric properties of aluminum nitride thin films deposited onto metal electrodes by pulsed direct current reactive sputtering, Journal of Applied Physics, Vol. 89, No. 11, 2001.

41 T. Eberfors, E. Kälvesten, G. Stemme, Dynamic actuation of polyimide V-grooves joints by electrical heating, Eurosensors XI, Warsaw, Poland, 1997.

42 T. Eberfors, J.U. Mattsson, E. Kälvesten, G. Stemme, A robust micor conveyer realized by arrayed polyimid joint actuators, Journal of Micromechanics and Microengineering, 10, 2000, pp. 337-349.

43 J. van Eijk, On the design of plate-spring mechanisms, Ph.D. Thesis, Delft, The Netherlands, 1985.

44 D. Elata, V. Leus, How slender can comb-drive fingers be, J. Micromech. Microeng., 15, 2005, 1055-1059.

45 M. Elwenspoek, R. Wiegerink, Mechanical Microsensors, Springer, ISBN 3540675825, 2001.

46 G. Engdahl, Handbook of giant Magnetostrictive Materials, ISBN 0-12-238640-X, 2000

47 C.J. Evans, Precsion Engineering: An evolutionary view, Cranfield Press, Cranfield England, 1989.

48 L. Fan, C. W. Wu, K. D. Choquette, and M. H. Crawford, Self-assembled microactuated xyz stages for optical scanning and alignment, in Transducers ’97, Chicago, USA, pp. 319–322, 1997.

49 L.G. Fréchette, S.A. Jacobson, K.S. Breuer, F.F. Ehrich, R. Ghodssi, R. Khanna, C.W. Wong, X. Zhang, M.A. Schmidt, and A.H. Epstein, High-speed microfabricated silicon turbomachinery and fluid film bearings, Journal of MEMS, vol. 14, no. 1, pp. 141–152, 2005.

50 A. Friedberger, R.S. Muller, Improved surface-micromachined hinges for fold-out structures, Journal of microelectromechanical systems, vol. 7, no. 3, September 1998

51 T.B. Gabrielson, Mechanical-thermal noise in micromachined acoustic and vibrationsensors, IEEE Transactions on Electron Devices, Vol. 40, no. 5, pp. 903-090, 1993.

52 J.G.E. Gardeniers, A.G.B.J. Verholen, N.R. Tas, M. Elwenspoek, Direct measurement of piezo properties of sol-gel PZT films, Journal of the Korean Physical Society, Vol. 32, February 1998, pp. S1573-S1577.

53 M. Géradin, A. Cardona, Flexible multibody dynamics: A finite element approach, Wiley, Chichester, 2001.

54 J. C. Greenwood, C. J. Welham, Silicon Micromachined Resonator with a Q Greater than 350,000, Eurosensors XIII, September 12-15, 1999, The Hague, the Netherlands

55 J.G. Gualtieri, J.A. Kosinski, A. Ballato, Transactions UFFC, 41, 53, 1994.

56 L.C. Hale, Principles and Techniques for Designing Precision Machines, Ph.D thesis, Lawrence Livermore National Laboratory, Feb. 1999.

57 V.A. Henneken, M. Tichem, P.M. Sarro, In-Package MEMS-based thermal actuators for micro-assembly, 16th MME MicroMechanics Europe Workshop, Sep. 2005, Gothenburg, Sweden.

58 V. Henneken, Design of a MEMS XY microstage for nanometer applications in a transmission electron microscope, Master's thesis, Delft University of Technology, The Netherlands, 2002.

59 Q.A. Huang, N.K.S. Lee, A simple approach to characterizing the driving force of polysilicon laterally driven thermal actuators, Sensors and actuators, 80, 2000, pp. 267-272.

60 W.S. Janna, Engineering heat transfer, ISBN 027800051, 1988, p. 529.

61 B.J. Jokiel, G.L. Benavides, L.F. Bieg, and J.J. Allen, Planar and Spatial Three-Degree-of-Freedom Micro-Stages in Silicon MEMS, Proceedings of ASPE annual meeting 2001, vol. 25, pp. 32–35, 2001.

62 R.V. Jones, Instruments and experiences, papers on measurement and instrument design, ISBN 0 471 91763 X, 1988

63 B.R. de Jong, A Six Degrees of Freedom MEMS Manipulator, Ph.D Thesis, University of Twente, Enschede, the Netherlands, 2006, ISBN 90-365-2413-X.

64 B.R. De Jong, D.M. Brouwer, H.V. Jansen, M.J. De Boer, T.G. Lammertink, S. Stramigioli, and G. J. M. Krijnen, A planar 3 DOF sample manipulator for nano-scale characterization, in MEMS, Istanbul, Turkey, pp. 750–753, 2006.

65 J.B. Jonker, A finite element dynamic analysis of flexible spatial mechanisms and manipulators, Ph.D. Thesis, Delft, 1988.

66 J.B. Jonker, A finite element dynamic analysis of flexible spatial mechanisms and manipulators, Comp. Methods Appl. Mech. Eng.,76, pp. 17-40, 1989

67 J.B. Jonker, J.P. Meijaard, SPACAR-computer program for dynamic analysis of flexible spatial mechanisms and manipulators, in Multi-body Systems Handbook, W.Schielen(ed.), Springer-Verlag, Berlin, 1990, pp. 123-143.

68 J.B. Jonker, J.van Dijk and R.G.K.M. Aarts, An extended input-output representation for control synthesis in multibody system representation for control synthesis in multibody system dynamics, Multibody Dynamics 2007, Eccomas Thematic Conference, Milano, Italy, 25-28 June 2007.

69 J. Jonsmann, S. Bouwstra, Material considerations for Topology optimized thermal microactuators, Eurosensors XIV, Copenhagen, Denmark, 2000.

70 I.W. Jung, U. Krishnamoorthy, and O. Solgaard, High fill-factor two-axis gimbaled tip-tilt-piston micromirror array actuated by self-aligned vertical electrostatic combdrives, Journal of MEMS, vol. 15, no. 3, pp. 563–571, 2006.

71 P.F. van Kessel, et al., A MEMS-based projection display, Integrated sensors, Microactuators & Microsystems, pp. 1887-1704, Proc. of the IEEE, Vol. 86, No. 8, Aug. 1998.

72 M.H. Kiang, O. Solgaard, K.Y. Lau, R. Muller, Electrostatic combdrive-actuated micromirros for laser-beam scanning and positioning, Journal of microelectromechanical systems, vol 7, no 1, March 1998.

73 M. Kohl, D. Dittmann, E. Quandt and B. Winzek, Thin film shape memory microvalves with adjustable operation temperature, Sensors and Actuators A, 83 (2000), pp. 214-219.

74 M. Kohl1, D. Brugger and B. Krevet, Ferromagnetic shapememory actuator for large 2D optical scanning, MEMS 2006, pp. 794-797.

75 E.S. Kolesar et al, Single- and double-hot arm asymmetrical polysilicon surface micromachined electrothermal microactuators applied to realize a microengine, Thin solid films 420-421, 2002, pp. 530-538.

76 M.P. Koster, Constructieprincipes voor het nauwkeurig bewegen en positioneren, Twente University Press, ISBN 903651455x.

77 S. Kota, J. Hetrick, Z. Li, S. Rodgers, T. Krygowski, Synthesizing High-Performance Compliant Stroke Amplification Systems for MEMS, Proc. of the IEEE Thirteenth Annual International Conference on Micro Electro Mechanical Systems, Miyazaki, Japan, Jan 23-27, 2000, pp. 164-169.

78 M. Kruizinga, Design of a sub nm stable rotation stage for application in a TEM, Master’s thesis, University of Twente, the Netherlands, May 2005.

79 A.A. Kuijpers, Micromachined Capacitive Long-Range Displacement Sensor for Nano-Positioning of Microactuator Systems, Ph.D. Thesis, University of Twente, Enschede, the Netherlands, 2004, ISBN90-365-2119-X.

80 S. Kwon, V. Milanovi´c, and L. P. Lee, Vertical combdrive based 2-D gimbaled micromirrors with large static rotation by backside island isolation, IEEE Journal of Selected Topics in Quantum Electronics, vol. 10, no. 3, pp. 498–504, 2004.

81 R. Legtenberg, Electrostatic actuators fabricated by surface micromachining techniques, Ph.D thesis, University of Twente, Enschede, the Netherlands, 1996, p. 139.

82 H. Lemke, T. Long, T. Göddenheinrich, et al, Micro patterning of thin Nd-Fe-B Films, Journal of Magnetism and Magnetic Materials, Vol. 148, 1995, pp. 426-432.

83 M. Levy, R.M. Osgood, H. Hegde, F.J. Cadieu, R. Wolfe, V.J. Fratello, Integrated optical isolators with sputter deposited thin-film magnets, IEEE Photonics technology letters, Vol. 8, No. 7, July 1996, pp. 903-905.

84 Xinxin Li, Takahito Ono, Yuelin Wang, Masayoshi Esashi, Ultrathin single-crystalline-silicon cantilever resonators: Fabrication technology and significant specimen size effect on Young’s modulus, applied physics letters volume 83, number 15 13 October 2003.

85 E M Lifshitz, L D Landau, Statistical Physics (Course of Theoretical Physics, Volume 5), ISBN 0750633727.

86 C. Liu, Y. Bar-Cohen, Scaling Laws of Microactuators and Potential Applications of Electroactive Polymers in MEMS, Proceedings of SPIE, 6th Annual International Symposium on Smart Structures and Materials, 1999.

87 C. Liu, T. Tsao, G-B. Lee, J. Leu, Y. Yi, Y-C. Tai, C-M. Ho, Out-of-plane magnetic actuators with electroplated permalloy for fluid dynamics control, Sensor and actuators 78, pp. 190-197, 1999.

88 C. Livermore, A. Forte, T. Lyszczarz, S. D. Umans and J.H. Lang, “A High-Power MEMS Electric Induction Motor,” in Proc. Solid-State Sensor, Actuator and

Microsystems, Workshop, pp.251–254, Hilton Head Island, South, Carolina, 2002-6.

89 Antonio Luque, José M. Quero, Cyrille Hibert, Philippe Flückiger and Alfonso M. Gañán-Clavo, Integrable silicon microfluidic valve with pneumatic actuation, Sensors and Actuators A, 118 (2005), pp. 144-151.

90 M. Lutz et al., A precision yaw rate sensor in silicon micromachining, proc. 1997 Int. Conf. on Solid-State sensors and actuators, Chicago, Il, June 16-19, 1997, Vol. 2, pp. 847-850.

91 C.H. Mastrangelo, Thermal applications of microbridges, Ph.D. dissertation, U.C. Berkley, 1991.

92 M.J. Madou, Fundamentals of Microfabrication, ISBN 0-8493-9451-1, 1997.

93 N. Maluf, An introduction to microelectromechanical systems engineering, Artech house, 2000, ISBN 0-89006-581-0.

94 J.P. Meijaard, Direct determination of periodic solutions of the dynamical equations of flexible mechanisms and manipulators, Int. journal for numerical methods in engineering 32, 1991, pp. 1691-1710.

95 V. Milanović, "Multilevel Beam SOI-MEMS Fabrication and Applications," J. MEMS, vol. 13, no. 1, pp. 19–30, 2004.

96 O. Millet, et al, Micro gripper driven by SDAs coupled to an amplification mechanism, Transducers, 12th int. conf. on solid state sens., act. & microsys., Boston, June, 8-12, 2003.

97 C. Neagu, H. Jansen, H. Gardeniers and M. Elwenspoek, The electrolysis of water an actuation principle for MEMS with a big opportunity, Actuator 1998, Bremen, Germany.

98 S.L. Paalvast, Design of MEMS thermal actuators for improved tracking performance in hard disk drives, Master Thesis. Faculty of Design, April 2003, Delft, The Netherlands.

99 M. Pai, N.C. Tien, Low voltage electrothermal vibromotor for silicon optical bench applications, Sensor and actuators 83, 2000, pp. 237-243.

100 K.E. Peterson, Silicon as a mechanical material, Proceedings of IEEE, Vol70, No.5 pp.420-457, May 1982.

101 PI Ceramic, http//www.piceramic.com.

102 K.S.J. Pister, M.W. Judy, S.R. Burgett, and R.S. Rearing, Microfabricated hinges, Sensors and Actuators A, vol. 33, pp. 249–256, 1992.

103 W.O. Pril, Development of high precision mechanical probes for coordinate measurement machines, Ph.D. thesis, 2002, Eindhoven, ISBN 90-386-2654-1.

104 E. Quandt, A.E. Clark, Giant magnetostrictive materials and properties, Actuator 1998, Bremen, Germany.

105 L. Que, J.-S. Park, Y.B. Gianchandani, Bent-bem electro-thermal actuators –part I: Single beam and cascaded devices, journal of microelectromechanical systems, VOL 10, NO 2, June 2001. pp. 247-254.

106 L. Reimer, Transmission electron microscopy, physics of image formation and microanalysis, Springer Verlag, Berlin, Germany 1993, ISBN 3-540-56849-2.

107 Roger Grace Associates / Nexus: http://www.rgrace.com/Papers/killerapps.html.

108 N. Roxhed, B. Samel, L. Nordquist, P. Griss and G. Stemme, Compact, seamless integration of active dosing and actuation with microneedles for transdermal drug delivery, MEMS 2006, pp. 414-417.

109 D. Ruffieux, M.A. Dubois, N.F. de Rooij, An AlN piezoelectric microarray actuator, MEMS 2000.

110 R. Saini, Z. Jandric, M. Nolan, and S.A.M. Mentink, Microassembled MEMS minisem with carbon nanotube emitter, in IEEE MEMS, Istanbul, Turkey, pp. 918–921, 2006.

111 M. Sakata, S. Wakabayashi, H. Goto, H. Totani, M. Takeuchi, T. Yada, Sputtered high d31 coefficient PZT thin film for micro actuators, Micro Electro Mechanical Systems, 1996, MEMS apos; 96, Proceedings. apos; An Investigation of Micro Structures, Sensors, Actuators, Machines and Systemsapos;. IEEE, The Ninth Annual International Workshop onVolume , Issue , 11-15 Feb 1996, pp.263 – 266.

112 E. Sarajlic, Electrostatic microactuators fabricated by vertical trench isolation, Ph.D thesis, University of Twente, Enschede, The Netherlands, 2005.

113 E. Sarajlic, E. Berenschot, H. Fujita, G. Krijnen, and M. Elwenspoek, Bidirectional electrostatic linear shuffle motor with two degrees of freedom, in IEEE MEMS'05, Miami Beach, Florida, USA, pp. 391–394, 2005.

114 E. Sarajlic, M. J. De Boer, H. V. Jansen, N. Arnal, M. Puech, G. Krijnen, and M. Elwenspoek, Bulk micromachining technology for fabrication of two-level MEMS in standard silicon substrate, in Transducers'05, vol. 2, Seoul, Korea, pp. 1404–1405, 2005.

115 N. Sarkar, C. Baur, E. Stach, Z. Jandric, R. Stallcup, M. Ellis, G. Skidmore, J. Liu, and G. K. Fedder, Modular MEMS experimental platform for transmission electron microscopy, in IEEE MEMS, Istanbul, Turkey, pp. 146–149, 2006.

116 P. Schellekens, N. Rosielle, H. Vermeulen, M. Vermeulen, S. Wetzels, W. Pril, Design for precision: current status and trends, Cirp. annals, Vol. 47/2/1998, pp.557-586.

117 A.L. Schwab, Dynamics of flexible multibody systems, Ph.D. thesis, Delft, April 2002.

118 U. Simu, S. Johansson, Fabrication of monolithic piezoelectric drive units for a miniature robot, Joural of Micromechanics and Microengineering, 12, 2002, pp. 582-589.

119 J. Singh, T. Gan, A. Agarwal, Mohanraj, and L. Saxon, 3D free space thermally actuated micromirror device, Sensors and Actuators A, vol. 123-124, pp. 468–475, 2005.

120 G. Skidmore, M. Ellis, A. Geisberger, K. Tsui, K. Tuck, R. Saini, T. Udeshi, M. Nolan, R. Stallcup, and J. Von Ehr II, Assembly technology across multiple length

scales from the microscale to the nano-scale, MEMS 2004, Jan. 25-29, pp. 588-592, Maastricht, the Netherlands

121 A.H. Slocum, Precision Machine Design, Prentice Hall, Englewood Cliffs, New Jersey, 1992.

122 S.T. Smith, D.G. Chetwynd, Foundations of Ultra-Precision Mechanism Design, Developments in Nanotechnology, Vol 2,ISBN 2-88449-001-9, 1992.

123 R. Srinivasan, Microfabricated reactors for partial oxidation reactors, Ph.D-thesis, Massachusetts Institute of Technology (MIT), Boston (MA), USA 1998.

124 W.C. Tang, T.C. Nguyen and R.T. Howe, Laterally driven polysilicon resonant microstructures, Sensors and Actuators, 20, 1989, pp. 25-32.

125 N.R. Tas, Electrostatic Micro Walkers. PhD thesis, University of Twente, Enschede, The Netherlands, 2000, ISBN 90-36514355.

126 E. Thielicke, E. Obermeier, Microactuators and their technologies, Mechatronics 10, 2000.

127 S. Trolier-McKinstry, P. Muralt, Thin film Piezoelectronics for MEMS, Journal of Electroceramics, 12, 7-17, 2004.

128 Tsubouchi, et al, IEEE Ultrasonic Symposium, 1981, p. 375.

129 K. Tsui, A.A. Geisberger, M. Ellis, and G.D. Skidmore, Micromachined end-effector and techniques for direct MEMS assembly, JMM, vol. 14, pp. 542–549, 2004.

130 Y.-C. Tung and K. Kurabayashi, A Single-Layer PDMS-on-Silicon Hybrid Microactuator With Multi-Axis Out-of-Plane Motion Capabilities-Part II: Fabrication and Characterization, J. MEMS, vol. 14, no. 3, pp. 558–566, 2005.

131 V. Vaganov, N. Belov, S. in't Hout, S. Terry, Large force and deflection thermo-mechanical actuators, Eurosensors 13, Sept. 12-15, 1999 The Hague, The Netherlands

132 P. Vettiger, G. Cross, M. Despont, U. Drechsler, U. Dürig, B. Gotsmann, W. Häberle, M. A. Lantz, H. E. Rothuizen, R. Stutz, and G. K. Binnig, The "Millipede"–Nanotechnology Entering Data Storage, IEEE Transactions on Nanotechnology, vol. 1, no. 1, pp. 39–55, 2002.

133 A. Wallash et al, Electrical breakdown and ESD phenomena for devices with nanometer-to-micron gap, SPIE, Jan 2003.

134 J.A. Walraven, B. Jokiel, Failure analysis of a multi-degree-of-freedom spatial microstage, proceedings of SPIE Vol. 4980, 2003, pp. 97-105.

135 K. van der Werff, Kinematic and dynamic analysis of mechanisms, A finite element approach, Ph.D thesis, Delft, 1977.

136 K. van der Werff, J.B. Jonker, 'Dynamics of flexible mechanisms' in computer aided analysis and optimization of mechanical system dynamics, Springer Verlag, Berlin, 1984, pp. 381-400

137 Wikipedia, the free encyclopedia: www.wikipedia.org.

138 H. van der Wulp, Piezo-driven stages for nanopositioning with extreme stability, Ph.D. thesis, Delft, the Netherlands, 1997, ISBN 90-407-1491-6.

139 W.C. Young, Roark's formulas for stress and strain, ISBN 0-07-72541-1.

140 De-Yuan Zhang, Takahito Onob, Masayoshi Esashi, Piezoactuator-integrated monolithic microstage with six degrees of freedom, Sensors and Actuators 122 (2005), pp. 301–306.

141 G Yan, Y Zhu, Z Wang, R Zhang, Z Chen, X Liu and Y. Wang, Integrated bulk-micromachined gyroscope using deep trench isolation technology, Int. Conf. on Micro Electro Mechanical Systems MEMS 2004, Maastricht, The Netherlands, pp. 605-608.

142 R. Yeh, E.J.J. Kruglick, and K.S.J. Pister, Surface-micromachined components for articulated microrobots, Journal of MEMS, vol. 5, no. 1, pp. 10–16, 1996.

143 W. Zhu, K. Yao, Z. Zhang, Design fabrication of a novel piezoelectric multilayer actuator by thick film screen printing technology, Sensors and actuators 86, 2000, pp. 149-153.

ABSTRACT

In the future, the precision manipulation of small objects will become more and more important for appliances such as data storage, micro assembly, sample manipulation in microscopes, cell manipulation, and manipulation of beam paths by micro mirrors. At the same time, there is a drive towards miniaturized systems. Therefore, Micro ElectroMechanical Systems (MEMS), a fabrication technique enabling micron sized features, has been researched for precision manipulation. MEMS devices comprise micro sensors, actuators, mechanisms, optics and fluidic systems. They have the ability to integrate several functions in a small package. MEMS can be commercially attractive by providing cost reduction or enabling new functionality with respect to macro systems. Combining design principles, a mature design philosophy for creating precision machines, and MEMS fabrication, a technology for miniaturization, could lead to micro systems with deterministic behavior and accurate positioning capability. However, in MEMS design trade-offs need to be made between fabrication complexity and design principle requirements. Therefore, the goal of this research has been twofold:

1. Design and manufacture a 6 Degrees-of-Freedom (DOFs) MEMS-based manipulator with nanometer resolution positioning.

2. Derive principle solutions for the synthesis of exact kinematic constraint design and MEMS fabrication technology for multi DOFs precision manipulation in the micro domain.

The Transmission Electron Microscope (TEM) sample manipulator has been used as a suitable carrier for the project. Design principles which are relevant to MEMS in particular, such as exact kinematic constraint design, and using compliant mechanisms to avoid backlash, play, friction, wear and hysteresis, have been studied. Special attention has been given to leaf-spring stiffness reduction due to large deflections. This was essential because deflections of compliant mechanisms in MEMS are relatively large and often feature leaf-springs as elastic elements. Designs have been presented for improved straight guiding with respect to the

traditional folded flexure. This is important for the performance of electrostatic comb-drive actuators.

For the 6 DOFs motion of the manipulator, the necessary combination of in- and out-of-plane motion of the wafer in MEMS is rather new. A motion converting mechanism using only one type of actuator has been chosen in favor of a combination of in- and out-of-plane actuators. Six electrostatic comb-drives have been used for actuation. The manipulator is a parallel kinematic mechanism. Based on these system design choices, three concepts have been presented and evaluated. Each concept includes a fabrication process in conjunction with an exact kinematic constraint design.

The specifications for a precision manipulator require high frequency vibration modes combined with compliant actuation modes. The compliant actuation modes are necessary to generate sufficient displacement of +/- 10 μm by the low force MEMS actuators. Therefore, the design principles, especially exact kinematic constraint design, have been applied as much as possible. However, trade-offs had to be made between what is required from an exact kinematic constraint design point of view and what is feasible with the available fabrication processes. Therefore, to determine flexure dimensions, the used flexure mechanisms have been modeled taking into account geometric non-linearities. Although the design incorporates relatively long and slender leaf-springs, the first vibration mode frequency is 3.8 kHz (with blocked actuators). However, the clean room fabrication of the total manipulator required more time than available during the project. Therefore, only several fabrication steps of the manipulator design have been tested.

A 3 mask step fabrication process of the clamping mechanism based on the 5 mask step process of the 6 DOFs manipulator served as a test case for the fabrication. A clamping mechanism with a locking device enhances the passive stability of the manipulator by unpowered clamping of the manipulator actuators once the manipulator has reached its targeted position. The cross-talk between the electron-beam of the TEM and electric fields from the actuators of the manipulator is also decreased. Additionally, by using a clamping mechanism, the manipulator can be switched between compliant actuation modes for positioning, and high frequency vibration modes during imaging. The precision MEMS-based clamping mechanism for a relatively large force (0.5 mN) was developed, fabricated and characterized. The elastic deformation of the clamp flexures was optimized so as not to influence the position of the TEM sample manipulator. The device area of the total

mechanism was further optimized by balancing the area necessary for sufficient flexure compliance in the actuation direction and the actuator area necessary for sufficient actuation force and stroke. Measurements showed that the clamping mechanism is able to fix a test actuator, hold it without power, and release it.

SAMENVATTING

In de toekomst wordt het nauwkeurig manipuleren van kleine objecten steeds belangrijker voor toepassingen als dataopslag, microassemblage, manipulatie van preparaten in microscopen, cel manipulatie en optische weg manipulatie. Tegelijkertijd is er een trend gaande naar steeds kleinere systemen. Om deze redenen richt dit onderzoek zich op nauwkeurige manipulatie door gebruik te maken van Micro-ElektroMechanische Systemen (MEMS): een technologie waarmee microstructuren gefabriceerd kunnen worden. MEMS-technologie maakt het mogelijk om microsensoren, actuatoren, mechanismen, optica en fluidische systemen te bouwen. Een belangrijke eigenschap van MEMS is de integratie van functies in een kleine module. Daarnaast kan MEMS in vergelijking tot macrosystemen de kosten reduceren en meer functionaliteit bieden. Het combineren van constructieprincipes, een beproefde ontwerpmethodiek om precisiemachines te bouwen, en MEMS, een fabricagetechnologie voor het verkrijgen van microstucturen, kan leiden tot microsystemen met deterministisch gedrag en verbeterde positionerings eigenschappen. Echter, in MEMS-technologie dienen ontwerpcompromissen gemaakt te worden tussen fabricagecomplexiteit en de fundamentele constructieprincipes. Daarom is het doel van dit onderzoek tweeledig:

1. ontwerp en fabriceer een zes vrijheidsgraden op MEMS-gebaseerde manipulator om met nanometerresolutie te kunnen positioneren.

2. principiële oplossingen dienen afgeleid te worden voor de synthese tussen statisch bepaald construeren en MEMS fabricagetechnologie voor het positioneren in meerdere vrijheidsgraden in het microdomein.

De Transmissie Elektronen Microscoop (TEM) preparaatmanipulator is gebruikt als toepassing in dit project. Constructieprincipes die in het bijzonder relevant zijn voor MEMS, zoals statisch bepaald construeren en het gebruik van elastische mechanismen om speling, wrijving, slijtage en hysterese te vermijden, zijn onderzocht. Speciale aandacht is geschonken aan de reductie van de stijfheid van bladveren ten gevolge van relatief grote verplaatsingen. Dit is essentieel omdat in

MEMS vaak elastische mechanismen toegepast worden, in het bijzonder bladveer constructies met relatief grote verplaatsingen. Ontwerpen zijn gepresenteerd voor verbeterde rechtgeleiding ten opzichte van de traditioneel veel toegepaste ‘folded flexure’. Dit is belangrijk om de prestaties van elektrostatische kamactuatoren te verbeteren.

Om zes graden van vrijheid van de manipulator te realiseren is het nodig om zowel in- als uit-het-vlak te kunnen bewegen van de wafer, wat voor MEMS vrij nieuw is. Er is gekozen om een bewegings converterend mechanisme toe te passen dat slechts één type actuator nodig heeft in plaats van een combinatie van in- en uit-het- vlak actuatoren voor het bewegen in zes vrijheidsgraden. Er zijn zes elektrostatische kamactuatoren toegepast. De manipulator is een parallel kinematisch mechanisme. Op basis van deze systeemkeuzes zijn er drie concepten gepresenteerd en geëvalueerd. Ieder concept bevat een fabricage proces in combinatie met een statisch bepaald ontwerp.

De specificaties van een precisiemanipulator vereisen hoogfrequente trillingsmodes gecombineerd met elastische aandrijfmodes. De elastische aandrijfmodes zijn nodig om voldoende verplaatsing van +/- 10 μm met de typische lage kracht MEMS-actuatoren te verkrijgen. Daarom zijn de constructieprincipes, in het bijzonder statisch bepaald construeren, zo veel mogelijk toegepast. Echter, compromissen moesten gesloten worden tussen wat fundamenteel volgens constructieprincipes vereist was en wat haalbaar was om te fabriceren. Daarom zijn de elastische mechanismen gemodelleerd met in achtneming van niet-lineaire geometrische veranderingen. Ondanks dat het ontwerp relatief lange en dunne bladveren bevat is de eerste trillingsmode hoogfrequent met 3.8 kHz (bij geblokkeerde actuatoren). Echter, de fabricage in de stofarme ruimte vereiste meer tijd dan aanwezig in het project. Daardoor zijn slechts enkele stappen uit het manipulatorproces getest.

Het 3 maskerstappen fabricageproces voor een klemmechanisme dat gebaseerd is op het 5 maskerstappen proces om de manipulator te fabriceren, heeft als fabricage test gediend. Verder bevordert het klemmechanisme met vergrendeling de passieve stabiliteit van de manipulator. Het klemmechanisme maakt het daardoor mogelijk zonder elektrische spanning te klemmen op het moment dat de actuatoren de ingestelde positie bereikt hebben. Hierdoor is de beïnvloeding tussen de elektronenbundel van de TEM en de actuatoren van de manipulator sterk afgenomen. Tevens kan hierdoor geschakeld worden tussen elastische laagfrequente aandrijfmodes en hoogfrequente trillingsmodes door te klemmen tijdens een TEM opname. Het op MEMS-gebaseerde precisie klemmechanisme voor een relatief

grote klemkracht (0.5mN) is ontworpen, gemaakt en getest. De elastische deformatie van klemophanging is geoptimaliseerd om de positie van de manipulator tijdens het opvoeren van de klemkracht niet te beïnvloeden. Het oppervlak van het totale mechanisme is geoptimaliseerd door een balans te zoeken tussen het actuator oppervlak voor voldoende slag en kracht, en het oppervlak dat nodig is voor een hoge aandrijfcompliantie van het elastische mechanisme. Metingen hebben aangetoond dat het klemmechanisme in staat is een testactuator te klemmen, vast te houden zonder elektrische spanning en weer los te laten.

ABOUT THE AUTHOR

Dannis Brouwer was born on the 11th of July 1973 in Eindhoven. After attending two secondary schools, the United World College of South East Asia, Singapore and the Strabrecht College in Geldrop, the Netherlands, he successfully passed the pre-university education (VWO) exams in 1992.

He then embarked upon a study of mechanical engineering. During this time in Eindhoven, Dannis was also active in several functions within Squadra Veloce, the first student triathlon club of the Netherlands. With respect to sports, on more than one occasion he became student champion in the time trial discipline. At the end of 1998, Dannis received his Master's degree, after designing, building and testing a new viewfinder for a broadcast television camera for Philips Camera Systems in Breda. He expanded his technical knowledge by beginning a second Master's study about mechatronics at the Stan Ackermans Institute. In April 2001, Dannis completed his second Master's thesis, which concerned an active straight guidance for a lath using a laser as reference for Philips Center for Industrial Technology.

From May 2001 until February 2004, Dannis worked as a scientific employee for the Design Principles group of Philips Center for Industrial Technology. It was in this group that he met Herman Soemers, who later became his Ph.D. supervisor. In January 2003 a part time Ph.D. research, as a member of the MAMS project, was started at the University of Twente. However, in March 2004, after 14 months of working part time on his Ph.D. research, Dannis decided to continue his Ph.D. research full time. During this time, fundamental knowledge was gained on the principles of non-linear geometrical mechanisms, the behavior of micro systems and MEMS fabrication processes.

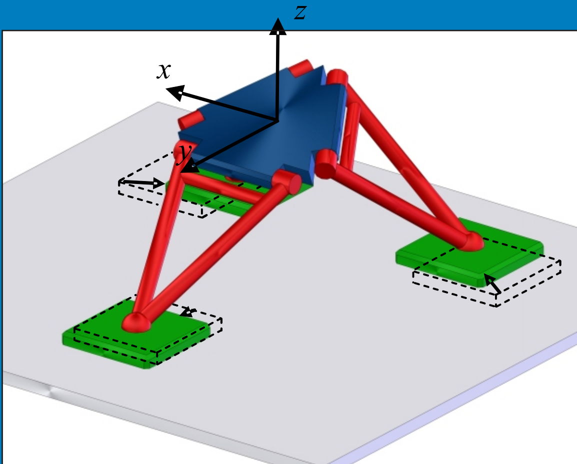

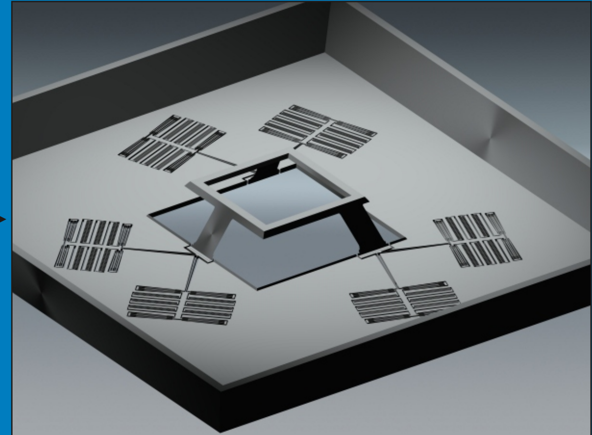

From Macro Kinematic Concept to Micro-Mechatronic Design

In the future, the precision manipulation of small objects will become more and more important for appliances such as data storage, micro assembly, sample manipulation in microscopes, cell manipulation, and manipulation of beam paths by micro mirrors. At the same time, there is a drive towards miniaturized systems. Therefore, Micro ElectroMechanical Systems (MEMS), a fabrication technique enabling micron sized features, has been researched for precision manipulation. MEMS devices comprise micro sensors, actuators, mechanisms, optics and fluidic systems. They have the ability to integrate several functions in a small package. Combining Design Principles, a mature design philosophy for creating precision machines, and MEMS fabrication, a technology for miniaturization, could lead to micro systems with deterministic behavior and accurate positioning capability. However, in MEMS design trade-offs need to be made between fabrication complexity and design principle requirements. This thesis describes a Micro-Mechatronic design of a six Degrees-of-Freedom MEMS-based Precision Manipulator. Principle solutions for the synthesis of exact kinematic constraint design and MEMS fabrication technology for multi DOFs precision manipulation in the micro domain will be derived.

ISBN 978-90-365-2510-7